Summer 7-29-2013

Electron Matter Optics of the Aharonov-Bohm and Stern-Gerlach Effects

Scot McGregor
University of Nebraska-Lincoln, scotm123456@hotmail.com

ELECTRON MATTER OPTICS OF THE AHARONOV-BOHM AND STERN-GERLACH EFFECTS

by

Scot Cameron McGregor

A DISSERTATION

Presented to the Faculty of

The Graduate College at the University of Nebraska

In Partial Fulfillment of Requirements

For the Degree of Doctor of Philosophy

Major: Physics and Astronomy

Under the Supervision of Professor Herman Batelaan

Lincoln, Nebraska

August, 2013

ELECTRON MATTER OPTICS OF THE AHARONOV-BOHM AND STERN-GERLACH EFFECTS

Scot Cameron McGregor, Ph.D.

University of Nebraska, 2013

Advisor: Herman Batelaan

Since the advent of quantum mechanics and the idea that massive particles exhibit wave properties, physicists have made efforts to make use of the short deBroglie wave length of matter waves for fundamental as well as practical studies. Among these are the precise measurements allowed by interference, diffraction, and microscopy as well as the study of more fundamental aspects of quantum theory such as the Aharonov-Bohm effects or the Stern-Gerlach effect, which are described below. However, in order to use matter waves to observe any of these effects it is necessary to produce and maintain coherence in the waves which are used for measurement. With a grasp of what coherence is and how it may be achieved and maintained one can move forward to study the interesting phenomena associated with coherent matter waves. More specifically in this work the interference and diffraction of electron matter waves are considered. The phenomena under consideration are those associated with the interaction of the electric charge and magnetic dipole moment of the electron with external fields and potentials while in the process of interfering or diffracting. Namely the focus of this dissertation is the Aharonov-Bohm effect, the Aharonov-Casher effect, and the Stern-Gerlach effect.

Additionally, a wide-angle electron beam-splitter capable of producing two centimeter beam separation at the detection plane is discussed. The beam-splitter utilizes a nanofabricated periodic grating in combination with a bi-prism element. Contrary to

devices utilizing only bi-prism elements, the use of the periodic grating causes amplitude, and not wave front, splitting. Even at maximum separation, beam profiles remain undistorted, providing evidence that coherence is intact. This is a step towards the realization of a large area electron interferometer using such a grating bi-prism combination. Such an interferometer could, in principle, be used to test the dispersionless nature of the Aharonov-Bohm effect. Work towards such an interferometer and possible future work are also discussed.

ELECTRON MATTER OPTICS OF THE AHARONOV-BOHM AND STERN-GERLACH EFFECTS

Scot Cameron McGregor, Ph.D.

University of Nebraska, 2013

Lay Abstract

Advisor: Herman Batelaan

The precision of a measurement is only as good as the smallest measurement available given the technique or device being used. For example a measurement with a ruler can only be as precise as the distance between neighboring marks. One way to make a more precise measurement than is possible with a ruler is by interference of waves. Interference is what happens when two waves are added together. The amplitude of the resulting wave is dependent on the relative displacement and amplitude of the two constituent waves. In other words the interference of waves of light or matter is the use of a wave as a ruler. This is an improvement over the conventional ruler because the wavelength of visible light is less than 1 micrometer. Going even further, the wavelength of electrons in our lab is typically on the order of one tenth of a nanometer. No conventional ruler could come close to that.

With such a fine ruler extremely precise measurements can be made using interference techniques. Additionally, with the use of electron interference can yield answers to fundamental questions as to the quantum mechanical nature of the electron. The electron has certain intrinsic properties. In a way it can be thought of as a tiny bar magnet with a nonzero net electric charge. These properties of the electron result in interesting quantum mechanical effects when the electron is bathed in or passes nearby an

electric or magnetic field. For example, if an electron passes near a solenoid (a coil of wire with a current passing through it) the electron wave is shifted. In principle the magnetic field is completely contained in the solenoid meaning the electron does not even need to pass through the field. This is known as the Aharonov-Bohm effect and is discussed in more detail in chapter 3. The purpose of this dissertation is to consider some possible causes and consequences of a few such quantum mechanical interactions.

Preface

Chapter 2 is the written portion of my comprehensive exam. The topic was received on February 21, 2013 to be turned in and defended on March 8, 2013 (due to scheduling conflicts the defense was postponed to March 15, 2013). The topic of the exam was as follows:

> What is the coherence length of electrons in a metallic structure and how can one measure this? This question can initially be addressed in general at a basic level; including a definition of coherence length and what decoherence processes are and do. The question should also be addressed with a focus on those electrons that can be photo-emitted. Techniques used in surface crystallography (see the book by L J Clarke, this will be provided for you) answer the above question for coherence lengths on the atomic length scale for photo-emission. Also see the following attached papers. However, it appears that a coherent electron emitter using coherence lengths at the hundreds of nanometers scale does not exist. A literature survey is necessary to establish if this statement is correct. What limits the scale? Is the coherence length not long enough, does the emission process reduce coherence, are the measurements techniques not scalable from the atomic regime to the nanoscale (or larger) regime, or is this a timely question and do you expect that current techniques allow one to address this question?

Chapter 3 has been published in *the New Journal of Physics* (S. McGregor, R. Hotovy, A. Caprez, and H. Batelaan, "On the relation between the Feynman paradox and the Aharonov-Bohm effects," New J. Phys. **14** 2012).

Chapter 4 has been accepted for publication as a section in the memorial book *In Memory of Akira Tonomura: Physicist and Electron Microscopist* in 2013.

Chapter 5 has been published in *the New Journal of Physics* (S. McGregor, R. Bach, and H. Batelaan, "Transverse quantum Stern-Gerlach magnets for electrons," New J. Phys. **13** 2011).

Chapter 6 is still in progress and will hopefully be submitted for publication in 2013.

Chapter 7 has been published in *Journal of Physics B: Atomic, Molecular and Optical Physics* (A. Caprez, R. Bach, S. McGregor, and H. Batelaan, "A wide-angle electron grating bi-prism beam splitter," J. Phys. B **42**, 165503 (2009))

We appreciate the support of the National Science Foundation and the Department of Education.

Table of Contents

List of Figures

Chapter 1 - Introduction

Chapter 2 - Source Coherence

List of Tables

Chapter 6 - Spin Dependent Two Color K-D Effects

Chapter 1 – Introduction

1. The Aharonov-Bohm Effect

Having been first predicted by Ehrenberg and Siday[1] and later appearing in a 1959 Physical Review by its namesake authors[2], the Aharonov-Bohm effect continues to inspire debate over its apparent consequences. The Aharonov-Bohm (A-B) effect states that as an electron passes a solenoid its wave function accumulates a phase shift due to its interaction with the magnetic vector potential. If an electron interferometer is constructed such that the two arms pass around a solenoid in which the magnetic field is completely contained a measureable phase difference between the two arms will accrue in spite of the fact that both arms pass through field free regions. The phase accumulated by an electron moving along a path through a magnetic vector potential is given by[2]

$$\varphi = -\frac{e}{\hbar}\int \vec{A}\cdot d\vec{x}, \tag{1}$$

where $\vec{A}$ is the magnetic vector potential, and e is the charge of the electron. Thus the phase difference between two paths which pass on either side of a solenoid may be computed by taking the difference between two such integrals resulting in the closed loop integral[2]

$$\Delta\varphi_{AB} = -\frac{e}{\hbar}\oint \vec{A}\cdot d\vec{x} = -\frac{e}{\hbar}\int \left(\nabla\times\vec{A}\right)\cdot d\vec{a} = -\frac{e}{\hbar}\int \vec{B}\cdot d\vec{a} = -\frac{e\Phi_B}{\hbar}, \tag{2}$$

where Φ_B is the magnetic flux enclosed between the two arms of the interferometer. This implies that there need only be a magnetic field present and that the electrons need not actually pass through it.

This effect was first observed by R. G. Chambers in 1960[3] in an experiment in which a tapered magnetic whisker was placed between the two arms of an electron bi-prism interferometer (see figure 1.1a).

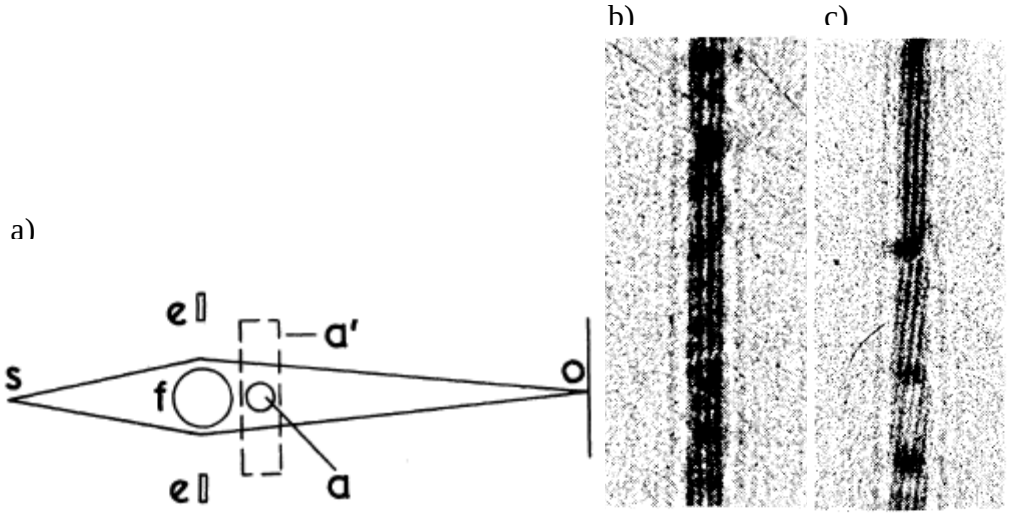

Figure 1.1

Chambers' Experimental Setup and Observation

a) Two arms of an electron interferometer propagate from source s around a bi-prism wire f, and magnetic whisker a to observation plane o. Upon measurement b) straight vertical fringes were observed in the shadow of the bi-prism in absence of the whisker while c) slanted fringes were seen with the whisker present. Images taken from Chambers' article[3].

Upon measurement straight vertical fringes were observed in the shadow of the bi-prism in absence of the whisker (figure 1.1b) while slanted fringes were seen with the whisker present (figure 1.1c). The magnetic flux enclosed in the whisker is a function of its thickness. Therefore, the slant in the fringes is due to the taper in the whisker giving a phase difference which is dependent upon which part of the whisker the two arms pass.

The A-B effect was again demonstrated in an experiment in 1986 conducted by Akira Tonomura[4] in which a loop of ferromagnetic material was enclosed by a superconductor thus eliminating the effect of stray magnetic fields.

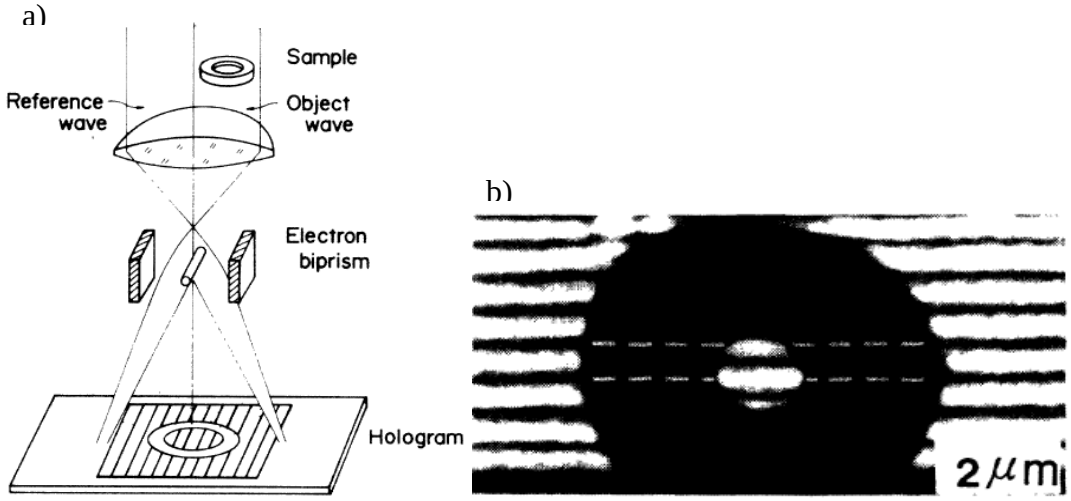

Figure 1.2

Tonomura's Experimental Setup and Observation

a) The object wave and reference wave interfere at the detection plane. Fringes corresponding to electrons that passed through the loop are compared to fringes that passed around. b) Dashed lines indicate the phase difference between the two parts of the object wave. Images taken from Tonomura's PRL[4].

As in Chambers' experiment Tonomura used an electron bi-prism interferometer to measure the A-B effect (see figure 1.2a). The portion of the electron beam passing through and immediately around the ferromagnetic loop is sent on one side of the bi-prism. This is referred to as the object wave. The part of the electron beam passing on the other side of the bi-prism is called the reference wave. The object and reference waves are brought together to interfere at the detector where the phase difference between electrons passing through the loop and those passing around may be observed.

In spite of the fact that the A-B effect has been beautifully demonstrated in experiments such as those shown above, it remains surrounded by controversy. When an electron passes a solenoid, the magnetic field produced by the moving particle exerts a force on the solenoid. Given that the electron is passing through a field free region it

would appear that the force is not reciprocated and Newton's third law is violated. However, it has been suggested by Boyer that Newton's third law can be invoked and that the back acting force on the electron provides a delay which exactly matches the quantum mechanical phase shift predicted by Aharonov and Bohm[5]. In a 2007 PRL by Caprez *et al.*[6] an experiment is described which tests this very claim.

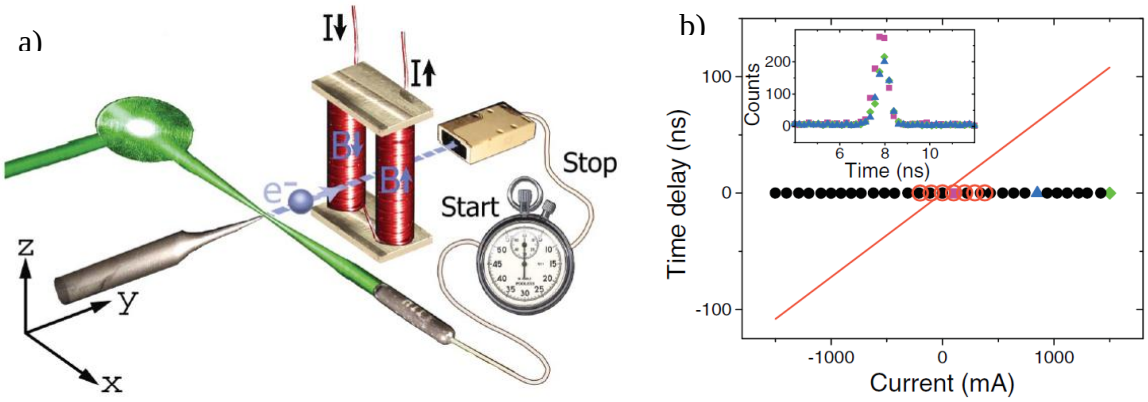

Figure 1.3

Macroscopic Test of the Aharonov-Bohm Effect

a) The time of flight of pulsed electrons passing between two solenoids is measured in order to test if there is a delay resulting from a force. b) Measurement over a range of currents indicates a time of flight which is independent of the current thus indicating the absence of a force. Images taken from PRL by Caprez *et al.*[6]

Pulsed electrons were sent between two current carrying solenoids and the time of flight of the electrons was measured (see figure 1.3a). This was done for a range of currents resulting and the measured time of flight for the electrons was compared to that which would be predicted assuming a classical force appropriate for an A-B phase shift (see figure 1.3b). The result was that the time of flight for the electrons was independent of the current in the solenoid thus seemingly disproving the notion that the A-B effect is a result of a classical force. Boyer responds to this result with the claim that the response of conduction electrons within the solenoid to a passing electron depends on the size of the

solenoid. Thus the lack of a time delay measured for a macroscopic solenoid does not necessarily indicate likewise for a microscopic solenoid[7]. One test which could possibly settle the debate is suggested by Anton Zeilinger[8] in which an A-B phase difference corresponding to a delay in excess of the coherence length of the electrons is applied to the two arms of an interferometer (see figure 1.4).

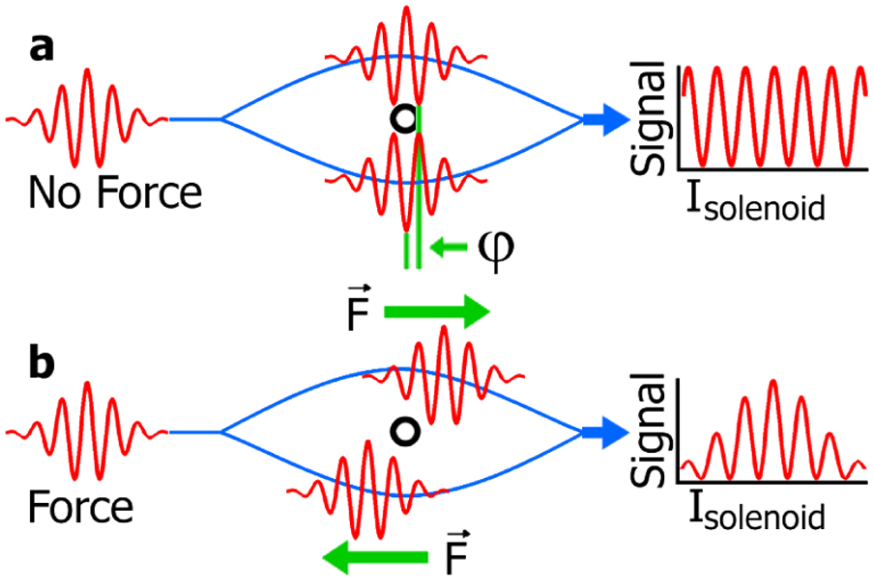

Figure 1.4

The A-B Effect: Phase or Force

a) If there is no force and the A-B effect is purely quantum mechanical then the phase can be increased indefinitely without loss of coherence. b) If the A-B effect is the result of a classical force then the interference pattern will lose contrast as the two arms will no longer be coherent with each other. Image taken from reference[6]

If the A-B effect is the result of a classical force then the interference pattern will lose contrast as the two arms will no longer be coherent with each other. Alternatively, if there is no force and the A-B effect is purely quantum mechanical then the phase can be increased indefinitely without lose of coherence. In such an experiment the presence or absence of a force would be demonstrated using a microscopic solenoid under conditions

in which the A-B phase difference could be measured directly. Steps have been taken toward constructing an interferometer capable of such an experiment and are discussed in chapters 7 and 8.

In chapter 7 a wide-angle electron beam-splitter capable of producing two centimeter beam separation at the detection plane is reported. The beam-splitter utilizes a nanofabricated periodic grating in combination with a bi-prism element. Contrary to devices utilizing only bi-prism elements, the use of the periodic grating causes amplitude, and not wave front, splitting. Even at maximum separation, beam profiles remain undistorted, providing evidence that coherence is intact. This is a step towards the realization of a large area electron interferometer using such a grating bi-prism combination. In chapter 8 an electron interferometer consisting of a field emission tip and a bi-prism wire is reported as work toward a grating bi-prism interferometer. Additionally, potential difficulties in constructing a grating bi-prism interferometer and possible future steps are discussed.

Furthermore, a defining property of the Aharonov-Bohm effect is its dispersionless nature. This means that the response of a matter wave to external potentials of the type used in the A-B effect is frequency or, equivalently, velocity independent. In the classical limit the dispersionless nature is often equated with the absence of forces. But how is the classical limit defined in the context of the A-B effect? This is the question addressed in chapter 4 where it is argued that the A-B physical system provides an interesting testing ground for the classical-quantum boundary.

2. The Aharonov-Casher Effect

Sometimes referred to as the dual of the A-B effect, the Aharonov-Casher (A-C) effect was first proposed in 1984[9] and describes the behavior of a neutron passing by a charged wire. The A-C effect states that a neutron passing a charged wire accumulates a phase shift due to the interaction between the motional electric dipole moment of the neutron with the electric field of the charged wire. The phase difference between two paths taken by neutrons passing on either side of a charged wire is given by[9] (in CGS units)

$$\Delta\varphi_{AC} = \frac{1}{\hbar}\oint\left(\frac{\vec{\mu}}{c}\times\vec{E}\right)\cdot d\vec{x} = \sigma\frac{4\pi\mu\Lambda}{\hbar c}, \tag{3}$$

where $\vec{\mu}$ is the magnetic moment of the neutron, $\sigma = 1$ or -1 for spin up or spin down, respectively. $\vec{E}$ and Λ are the electric field and linear charge density of the charged wire, respectively.

The A-C effect was first observed by Cimmino et al. in 1989[10] in an experiment in which neutrons were sent through a Mach-Zehnder interferometer consisting of three Bragg crystals (see figure 1.5).

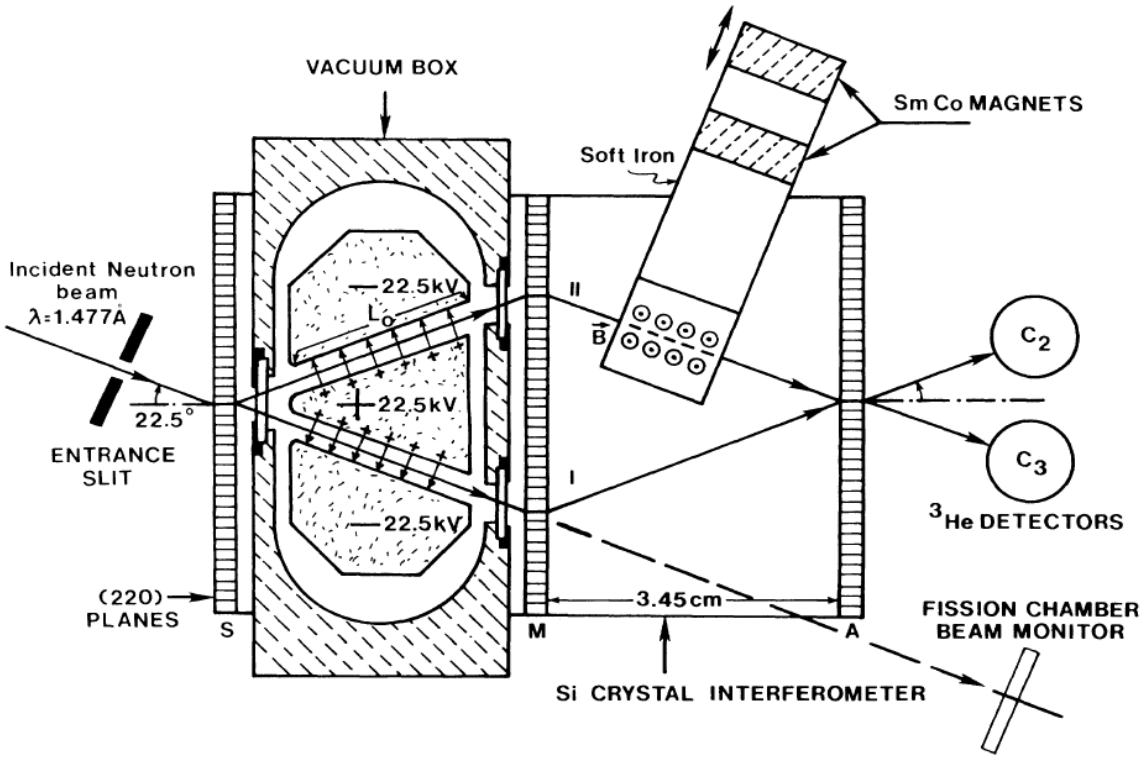

Figure 1.5

Experimental Setup for A-C Effect

Bragg diffracted neutrons are split into two beams which are sent through two sets of electrodes. The neutrons then diffract from a second Bragg crystal to be recombined onto a third thus completing a Mach-Zehnder interferometer. Measurements of count rate at C2 and C3 were used to determine the A-C phase difference. Image taken from reference[10].

As with the A-B effect, in spite of this demonstration of the A-C effect there is still some controversy regarding the underlying mechanism for the measured phase difference. Is it a classical force or a purely quantum mechanical phase shift? In this case the intuitive answer seems to be that a force causes the effect because the motional electric dipole is in fact bathed in a spatially dependent electric field. As with the Aharonov-Bohm effect the delay associated with a force predicted in this manner corresponds to exactly the same phase shift as that stated originally by Aharonov and Casher[11]. This, however, is not the

commonly accepted view of the effect. A Hamiltonian approach[12] as well as the approach which takes into account "hidden momentum"[13] suggest that given the symmetry along the spin quantization axis in the A-C system the force on the neutron is zero. These different perspectives on the A-C effect are discussed in chapter 3. Also in chapter 3, using the Euler-Lagrange equations it is predicted that in the case of unconstrained motion only one part of each system (A-B and A-C) accelerates, while momentum remains conserved. This prediction requires a time dependent electromagnetic momentum. For our analysis of unconstrained motion the A-B and A-C effects are then examples of the Feynman paradox which will be explained in chapter 3. In the case of constrained motion, the Euler-Lagrange equations give no forces in agreement with the generally accepted analysis. The quantum mechanical A-B and A-C phase shifts are independent of the treatment of constraint. Nevertheless, experimental testing of the above ideas and further understanding of A-B effects which is central to both quantum mechanics and electromagnetism may be possible.

3. The Stern-Gerlach Effect for Electrons

While examining the various aspects the A-B and A-C effects it is quite natural to consider the classical or quantum mechanical behavior of any system consisting of a charged particle or a magnetic moment bathed in an external field or potential. One such experiment of historical significance for the development of early quantum mechanics is the Stern-Gerlach (S-G) experiment. One of the most significant experiments in modern physics is that which was conducted by Otto Stern and Walter Gerlach in 1922 in which a beam of silver atoms was sent through an inhomogeneous magnetic field[14].

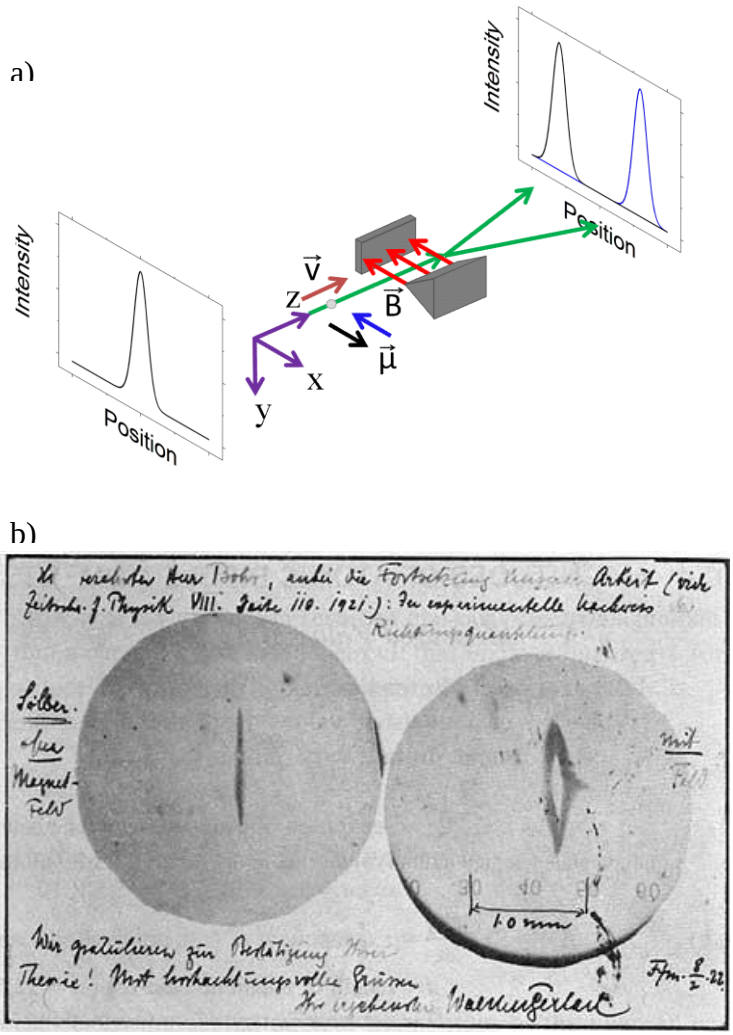

Figure 1.6

Stern-Gerlach Setup and Results

a) In the original Stern-Gerlach setup a beam of silver atoms propagated through an inhomogeneous magnetic field. The atoms were then split into two beams representing the two spin states of the electron. b) Images of two of the deposition detectors used in the Stern-Gerlach experiment are shown. The right and left images show the intensity profile of the silver atoms with and without the magnetic field, respectively. Image taken from reference[16]

The result was a separation of the beam into two distinct beams indicating the quantization of spin angular momentum of the 5s state electron of the silver atom[15] (see figure 1.6). This separation is due to the interaction between the magnetic moment of the

silver atom and the applied magnetic field. The force exerted on a magnetic dipole moment in an external magnetic field is $\vec{F} = \nabla\left(\vec{\mu} \cdot \vec{B}\right)$.

Even though this experiment was a demonstration of spin quantization for electrons bound to silver atoms, it cannot be used for a similar demonstration of spin quantization for free electrons. This is due to the inclusion of the charge of the electron and the consequence of the inclusion of Lorentz force in its interaction with the external field. In order for spin splitting to occur in the first place there must be a gradient in the magnetic field in the direction in which spin splitting is intended. However, a magnetic field with a gradient in only one direction is physically impossible. This can be seen by applying the Maxwell equations in free space (more specifically $\nabla \cdot \vec{B} = 0$).

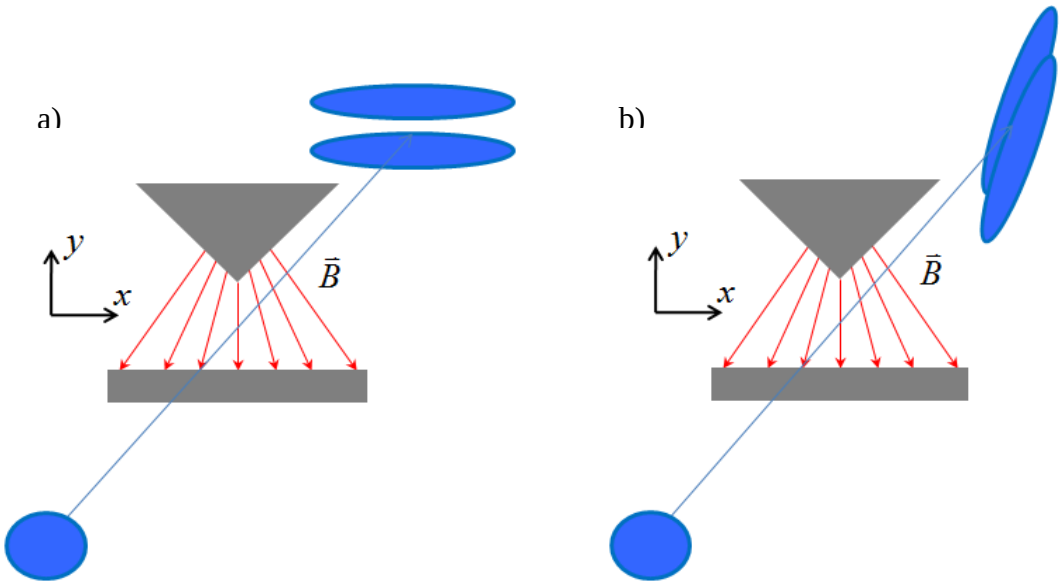

Figure 1.7

With and Without Lorentz Force

a) Without the Lorentz force an electron S-G apparatus would function in much the same way as the original setup but b) when included the gradient in the y-direction gives rise to blurring which makes the two spin states indistinguishable.

Consider an electron propagating in the z-direction through an inhomogeneous magnetic field (see figure 1.7b). Taking the y-direction as the spin quantization axis the spin dependent force acting on an electron passing through the center of the magnetic field is $\pm\mu\frac{\partial B_y}{\partial y}$. However, the spatial extent of the beam must be in excess of a certain size in accordance with the Heisenberg uncertainty principle and therefore must pass through more than just the center of the field. Additionally, Gauss' law for magnetic fields dictates that the gradient of the x component of the magnetic field in the x direction is given by $\frac{\partial B_x}{\partial x} = -\frac{\partial B_y}{\partial y}$. Because of this there is a spatially dependent y component of the Lorentz force (the same direction as the spin splitting force). The result is that the two spin states are blurred together and are no longer distinguishable. A more thorough and quantitative explanation is given by Kessler[17].

An alternative attempt at free electron spin separation was put forth by Brillouin in the form of the longitudinal S-G effect[18]. Brillouin's idea was to send a pulse of electrons through a current loop so that the resulting magnetic field is aligned with the direction of motion of the electrons (see figure 1.8).

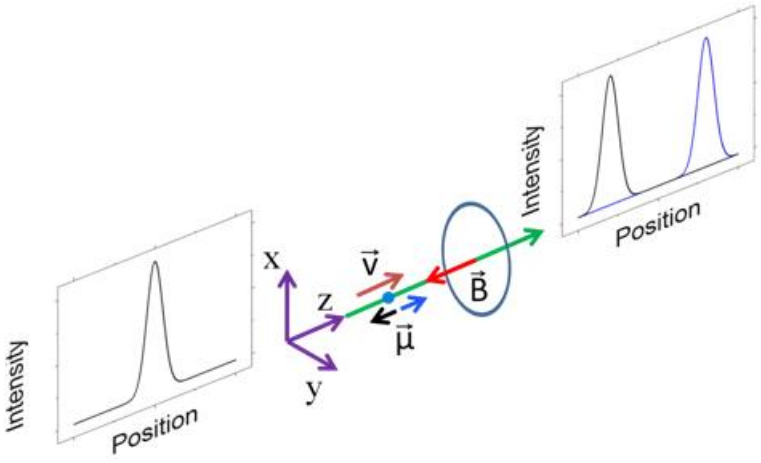

Figure 1.8

Longitudinal S-G Effect

A pulse of electrons sent through a current loop was expected to split longitudinally thus creating spin up and spin down pulses separated in time.

The difference in this case was that with the magnetic field and electron velocity aligned the Lorentz force would be eliminated. However, once again by considering classical trajectories it seems that this approach can be defeated. Given the finite spatial extent of the beam and the spatial dependence of all components of the magnetic field, some of the electrons will experience a transverse Lorentz force. These electrons will spiral through the current loop and experience a time delay which is dependent upon their initial position. Thus the pulses will broaden and become indistinguishable. Upon considering the above idea among others, Wolfgang Pauli stated at the 1930 Solvay conference that "it is impossible to observe the spin of the electron, separated fully from its orbital momentum, by means of experiments based on the concept of classical particle trajectories"[19,20]. This, however, begs the question: what about experiments based on the concept of quantum particle trajectories?

The first experiment of this kind was done by Hans Dehmelt's groupe and demonstrated what they called the continuous Stern-Gerlach effect[21]. With The use of a Penning trap, Dehmelt was able to observe the spin of an electron continuously for several minutes by measuring the cyclotron frequency of the trapped electron (see figure 1.9).

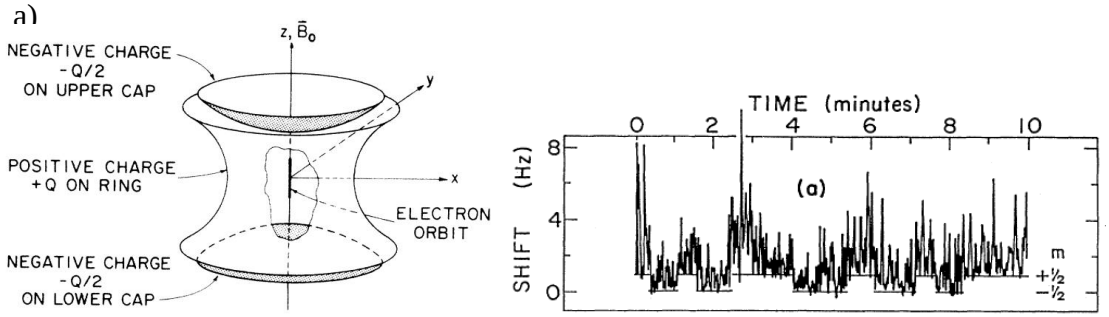

Figure 1.9

Continuous Stern-Gerlach Effect

a) Two negatively charged electrodes and a positively charged ring bathed in an external magnetic field are used to trap an electron. The resonant frequency of the trapped electron is then measured. b) Jumps in the baseline of shifts in the resonant frequency of the electron indicate spin flips. Images taken from reference[21]

The idea that the quantum mechanical behavior of the electron could allow for measurement of its spin was pushed further when the longitudinal Stern-Gerlach effect was analyzed fully quantum mechanically and was shown to be, in principle, possible[22]. Examples of thought experiments based on the quantum mechanical behavior of the electron with the intention of creating a transverse Stern-Gerlach effect are discussed in chapter 5. There it is shown that a magnetic phase grating composed of a regular array of microscopic current loops can separate electron diffraction peaks according to their spin states. The experimental feasibility of a diffractive approach is compared to that of an interferometric approach. We show that an interferometric arrangement with magnetic

phase control is the functional equivalent of an electron Stern-Gerlach magnet. Furthermore, the interaction between an electron and a laser field is analyzed quantum mechanically in chapter 6. There, an experimentally realizable scenario in which spin dependent effects of the interaction between the laser and electrons are dominant is predicted. The laser interaction strength and incident electron velocity are in the non-relativistic domain. This process potentially allows for spin separation of electrons and may thus be thought of as a laser induced Stern-Gerlach effect for electrons.

4. Coherence

While not yet stated explicitly, one common thread that runs throughout this chapter and the rest of this dissertation is quantum mechanical coherence. Each section so far has introduced certain features of the quantum mechanical behavior of electrons or, in the case of the A-C effect, neutrons. The manner in which these effects are proposed to be exhibited is through interference or diffraction. Given that a coherent beam is necessary to observe either of these phenomena it is worth considering what coherence is and how it may be lost before anything else. In chapter 2 qualitative as well as quantitative descriptions are given for coherence. Processes by which coherence can be lost and measured are discussed. A sufficiently coherent electron source is also important as well. Different types of electron sources are discussed as well as techniques of measuring the coherence of the free electrons at the source, conduction electrons within the source, and a possible connection between the two.

Chapter 2 – Source Coherence

1. Coherence

The scientific study and application of waves be they optical or material is contingent on an understanding of the concept of coherence. Coherence is a property of waves that is necessary for the observation of interference, a definitive phenomenon of waves, which is the superposition of waves with a known phase relation. The result of this superposition is a wave of greater or lesser amplitude depending on the phase difference. For the purpose of this chapter the focus will be on transverse spatial coherence rather than temporal coherence. Spatial coherence implies the ability to observe a time averaged interference between two spatially separated points on a wave front. When considering two different sources of light, a light bulb and a laser, one may observe exactly this phenomenon of coherence. In the case of the light bulb each point on the filament may be considered as an independent light source from which light is emitted with a random phase relationship with light emitted from any other point on the filament. The result is a wave front with a random spatially dependent phase. To see how this would result in reduced spatial coherence, consider making a copy of such a wave and superimposing it, with a transverse spatial shift, onto the original (see figure 2.1a). The result is that in some places constructive interference (i.e. resulting in increased amplitude) occurs while in other places destructive interference (i.e. cancellation of the two waves upon superposition) occurs. Since the light is spatially averaged over the detector one obtains reduced contrast in their interference fringes due to the averaging of constructive and destructive interference. If the length scale over which these random phase differences occur is small than the detector must be just as small in order to

distinguish regions where constructive interference occurs from regions of destructive interference. Alternatively if the two waves are shifted transversely relative to one another a distance which is small compared to this length scale than interference will occur over the entire wave front. As the transverse displacement of one copy relative to the other increases, the contrast decreases in the manner described above. It is in this manner that one may define the transverse coherence length. Additionally, if the phase difference between any two points on the wave front is sufficiently small compared to 2π than contrast will not be lost fully even if the two copies are transversely shifted a distance in excess of the length scale over which phase shifts occur.

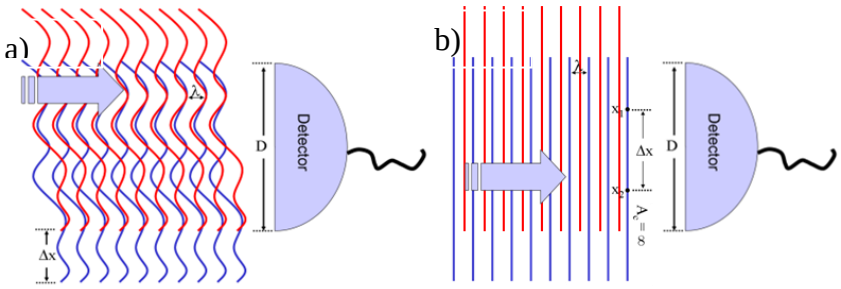

Figure 2.1

Coherence length and interference

a) A coherent wave with a random spatially dependent phase is copied, shifted, and superimposed with itself. b) A coherent plane wave such as that which is produced by a laser has a minimal if not nonexistent transverse spatially dependent phase. Copying and superimposing such a wave onto itself would result in interference contrast that is independent of the extent to which the waves are shifted transversely relative to one another. (Images taken from Wikipedia article: http://en.wikipedia.org/wiki/Coherence_(physics))

Alternatively, in the case of the laser, light is created via stimulated emission thus there is an imposed phase relation and the result is a plane wave (i.e. the wave fronts have minimal phase variation. See figure 2.1b). Because of the minimal or nonexistent

spatially dependent phase of the light produced by the laser, copying and superimposing such a wave onto itself would result in interference contrast that is independent of the extent to which the waves are shifted transversely relative to one another. If coherence is the extent to which two wave functions can interfere, then the coherence length is the largest distance between two points on a wave function which can interfere with one another. Thus, laser light is said to have a very large transverse coherence length.

One can see that the above statements may be made for any sort of wave for which the superposition principle holds. This would mean that the same principles hold for matter wave solutions of the Schrodinger equation. It is on the coherence and decoherence of electron matter waves that this chapter is intended to focus. Potential causes of decoherence in matter waves involve interactions with parts of the environment which would impart random phase shifts to the wave function. There have been many experiments demonstrating the loss of coherence in free propagating matter waves due to environmental interaction. Examples include coherence loss in matter waves due to interaction with light[2-4], scattering from molecules[5], or interaction of electrons with nearby materials[6] to name a few. Note that each of these interactions can be studied independently. That is if you can create a matter wave with enough coherence to observe interference fringes, then you can observe the loss of coherence by applying any one of these interactions independently.

An example of such an experiment by Hackermueller *et al.*[7] shows decoherence of a beam of C_{70} molecules by interaction with an Argon ion laser beam. To do this they sent their molecular beam first through the laser beam which resulted in the absorption of photons. The use of large molecules allowed for the absorbed energy to be distributed

amongst the many vibrational and rotational degrees of freedom of the molecules. Eventually a fraction of this absorbed energy is emitted as another photon. The kinetic energy of the molecule is changed and thus the time dependent phase factor $\exp(iEt/\hbar)$ is randomly affected with each absorption. The molecules were then sent through a three grating interferometer which is a means by which a beam can be split into two copies which are then overlapped. By varying the position of one of the gratings the overall phase difference between the two beams can be controlled. This allows the observer to measure interference fringes.

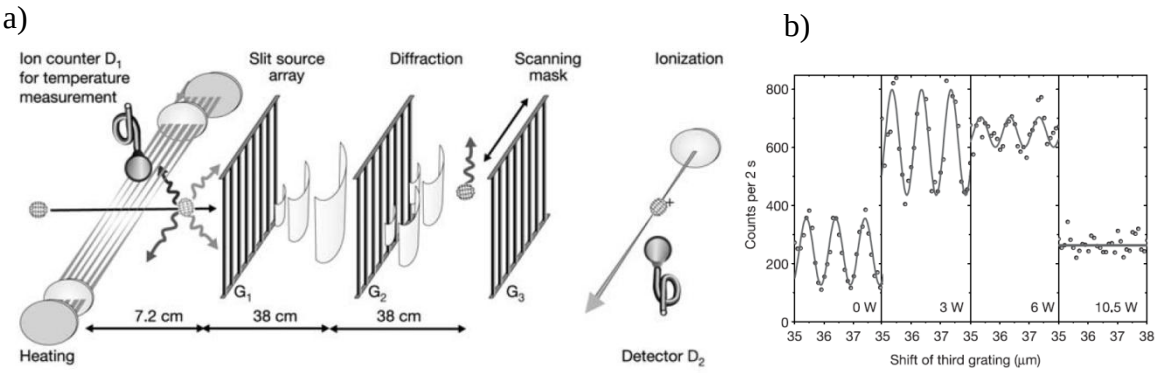

Figure 2.2

Decoherence of C_{70} beam by Photon Absorption

a) A beam of C_{70} molecules loses transverse coherence via absorption and emission of photons from an Argon ion laser. The molecular beam is then sent through a three grating interferometer. Interference fringes are measured by varying the position of the final grating which is used to control the phase between the two interfering wave functions. b) As the power output of the laser increases from 3W to 6W to 10.5W a decrease in fringe contrast is observed. (Images taken from Hackermueller *et al.*[7])

It is apparent from this example that if one wishes to conduct an experiment measuring interference fringes, one would do well to maximize the coherence width of the matter

wave used to measure interference. Applications for which a coherent source of matter waves is necessary are numerous[8-11].

2. Decoherence due to photoemission and field emission

All of the discussion thus far regarding decoherence of matter waves has been mainly focused on the decoherence of free waves to illuminate possible causes of decoherence. It would seem that any random interaction with the environment may result in decoherence. One potentially important factor in the coherence of an electron beam is the manner in which it is created. In order to examine this idea a little further, consider sources of free electrons. Two methods of producing a free electron beam are field emission, and photo emission. In the analysis of these two methods the electrons bound to the material are modeled as being contained within a finite square well. The highest energy that can be occupied by electrons at 0K is known as the Fermi energy.

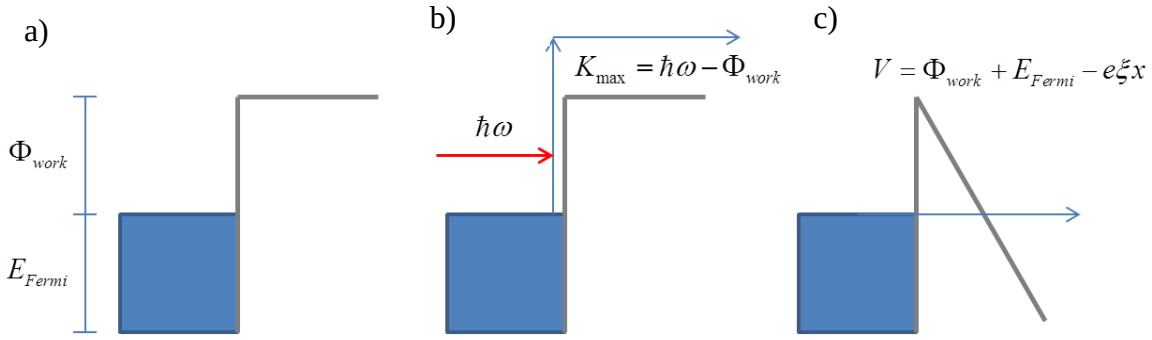

Figure 2.3

Photoemission and Field Emission

a) The model used for field emission of electrons consists of a finite square well in which electrons occupy energies up to the Fermi energy E_{fermi}. The energy difference between the top of the well and the Fermi energy is the work function Φ_{work}. b) Applying an electrostatic potential ξ to the material creates a potential that drops off linearly outside the surface of the material. This allows the electrons within the material to tunnel out through the surface.

The energy difference between the top of the well and the Fermi energy is called the work function (figure 2.3a).

In the case of photoemission electrons are liberated via the photoelectric effect[12]. In this process a photon is absorbed by an electron giving enough energy for the electron to go over its potential barrier (figure 2.3b). For a given photon frequency ω, the maximum kinetic energy $K_{\max}$ of the liberated photon is the difference between the energy of the photon $\hbar\omega$ and the work function Φ_{work} ($K_{\max} = \hbar\omega - \Phi_{work}$). In the case of field emission, an electric potential is applied to the material resulting in an electric field outside the surface of the conductor[13]. The corresponding electrostatic potential drops off linearly outside of the material which gives the electrons contained inside an opportunity to tunnel out through the surface (figure 2.3c). These effects may be taken in combination to produce coherent electron sources[14, 15].

One important question to ask is whether or not decoherence is a reversible process. The consensus view among in the literature seems to be that decoherence is an irreversible process by which the wave function interacts with an external system consisting of a large number of degrees of freedom[16-18]. That is significant because, if it is true, the process of removing electrons from metal can at best leave the coherence length of the electrons unchanged. The coherence length of free electrons just outside the metal surface is limited by the coherence length of the conduction electrons inside the metal. The assumed connection between emitted electrons and conduction electrons is based on claims in the literature that photoemitted electrons from metals originate entirely in the conduction band[19, 20] and that in the case of field emission the electrons with the highest energy (i.e. the ones at the top of the conduction band) are most likely to tunnel through

the barrier. In the interest of producing the most coherent source possible it would be worthwhile to consider which of these processes best maintains the coherence of the electrons as they are being liberated from the source. One way to determine the extent of decoherence upon field emission or photoemission is to compare the coherence length of the electrons at the source immediately after they have been freed to the coherence length of the conduction electrons that are still within the metallic structure. If one of the two processes yields a smaller change in coherence length then it is the best choice for a coherent source. In the next section I discuss one possible way of determining the coherence length of emitted electrons at the source and an example of a similar experiment performed in 2004 by B. Cho *et al*[21].

2.1. Coherence of free electrons at the source

It is clear from the above discussion that in order to perform any experiment involving interference of matter waves one must have a coherent source. In order to better understand the consequences of coherence length at the source it is necessary to work out a quantitative description of a partially coherent source. One common way for quantifying coherence is with the density operator which allows for full coherence, partial coherence, or complete incoherence. For a state vector $|\varphi\rangle$ the corresponding density operator would be $\rho = |\varphi\rangle\langle\varphi|$. If the state vector were a coherent superposition of states $|\psi\rangle = \frac{1}{\sqrt{2}}\left(|\varphi_1\rangle + |\varphi_2\rangle\right)$ it would be treated the normal way (just add up the states in superposition) and a density operator could be made of it.

$$\rho = |\psi\rangle\langle\psi| = \frac{1}{2}\left(|\varphi_1\rangle + |\varphi_2\rangle\right)\left(\langle\varphi_1| + \langle\varphi_2|\right) = \frac{1}{2}\left(|\varphi_1\rangle\langle\varphi_1| + |\varphi_2\rangle\langle\varphi_2| + |\varphi_1\rangle\langle\varphi_2| + |\varphi_2\rangle\langle\varphi_1|\right) \quad (1)$$

For an incoherent superposition the density operator is simply the weighted sum of the density operators corresponding to each of the states in the superposition.

$$\rho = \sum_n P_n \rho_n = \sum_n P_n \left|\varphi_n\right\rangle\left\langle\varphi_n\right| \tag{2}$$

Finally the probability of measuring a particular outcome of observable A can be found by computing a trace

$$P(a_n) = Tr\left\{\rho\left|a_n\right\rangle\left\langle a_n\right|\right\} \tag{3}$$

where $\left|a_n\right\rangle$ is an eigenstate of operator A. Taking the coherent state to be a Gaussian wave packet with a width equal to the coherence width of the source, it is possible to apply all of the above formalism to predict the outcome of an experiment with a partially coherent source. In order to write the density operator for the state at the source I must integrate the density operators corresponding to the coherent states

$$\rho = \int P_0(x_s)\left|\varphi(x_s,t)\right\rangle\left\langle\varphi(x_s,t)\right| dx_s \tag{4}$$

where x_s is the location of a fully coherent state at the source, and $P(x_s)$ is the probability density at the source. This is essentially the same as saying that my partially coherent source is actually the incoherent superposition of infinitely many fully coherent sources. In order to determine the probability density at the detector a trace is required.

$$P(x_d) = Tr\left\{\rho\left|x_d\right\rangle\left\langle x_d\right|\right\} = \int\left\langle x\right|\rho\left|x_d\right\rangle\left\langle x_d\right|x\rangle dx = \int\left\langle x\right|\rho\left|x_d\right\rangle\delta(x-x_d)\,dx = \left\langle x_d\right|\rho\left|x_d\right\rangle$$

$$= \left\langle x_d\right|\left[\int P_0(x_s)\left|\varphi(x_s,t)\right\rangle\left\langle\varphi(x_s,t)\right| dx_s\right]\left|x_d\right\rangle = \int P_0(x_s)\left\langle x_d\right|\left|\varphi(x_s,t)\right\rangle\left\langle\varphi(x_s,t)\right|\left.x_d\right\rangle dx_s$$

$$= \int P_0(x_s)\left|\varphi(x_s,x_d,t)\right|^2 dx_s \tag{5}$$

Here $\varphi(x_s, x_d, t)$ is the final wave function, having propagated it to the detector. $\varphi(x_s, x_d, t)$ is obtained using the free space propagator

$$\varphi(x_f, t_f) = \int U(x_f, t_f; x_i, t_i)\varphi(x_i, t_i)\, dx_i \tag{6}$$

$$U(x_f, t_f; x_i, t_i) = \left(\frac{m}{2\pi\hbar i(t_f - t_i)}\right)^{\frac{1}{2}} \exp\left(\frac{im(x_f - x_i)^2}{2\hbar(t_f - t_i)}\right) \tag{7}$$

where x_f, x_f, t_f, and t_f are the initial position, final position, initial time, and final time of the wave function being propagated. The probability integral basically amounts to the convolution of the final probability density of the fully coherent portion of the source with the initial probability density of my overall partially coherent source. This result was shown for optical microscopy and interferometry by Hopkins[22].

As an example of this calculation I chose a source with an overall intensity distribution and a coherence width defined by $P_0(x_s)$ and $\varphi(x_s, x, 0)$ as follows

$$P_0(x_s) = \frac{1}{\pi^{\frac{1}{2}}\Delta x_s} \exp\left(-\frac{x_s^2}{\Delta x_s^2}\right) \tag{8}$$

$$\varphi(x_s, x, 0) = \frac{1}{(\pi\Delta x^2)^{\frac{1}{4}}} \exp\left(-\frac{(x_s - x)^2}{2\Delta x^2}\right). \tag{9}$$

The electrons were then allowed to propagate to a double slit a distance of 5cm from whence they propagated another 50cm to the detection plane. The slits had a width of 200nm and center to center separation of 1μm. The width of the source was chosen as $\Delta x_s = 1\mu m$, and the energy of the electrons was chosen to be just over 2.5keV ($v = 3\times10^7\ m/s$). The FORTRAN code written to compute the diffraction pattern is

included in the appendix. Figure 2.4 shows the resulting diffraction pattern for coherence lengths of Δx =1nm, 300nm, 600nm, and 1μm. It is plainly visible that as the coherence width increases the contrast also increases. Note that by changing the center to center separation between the slits on can change the separation between the diffraction peaks without having to change anything about the initial state of the electron. It seems that this would change the range of coherence width over which a significant transition in contrast would occur. For example, putting the slits closer together would push the peaks further apart. It seems that this would allow for visible contrast at a lower coherence length.

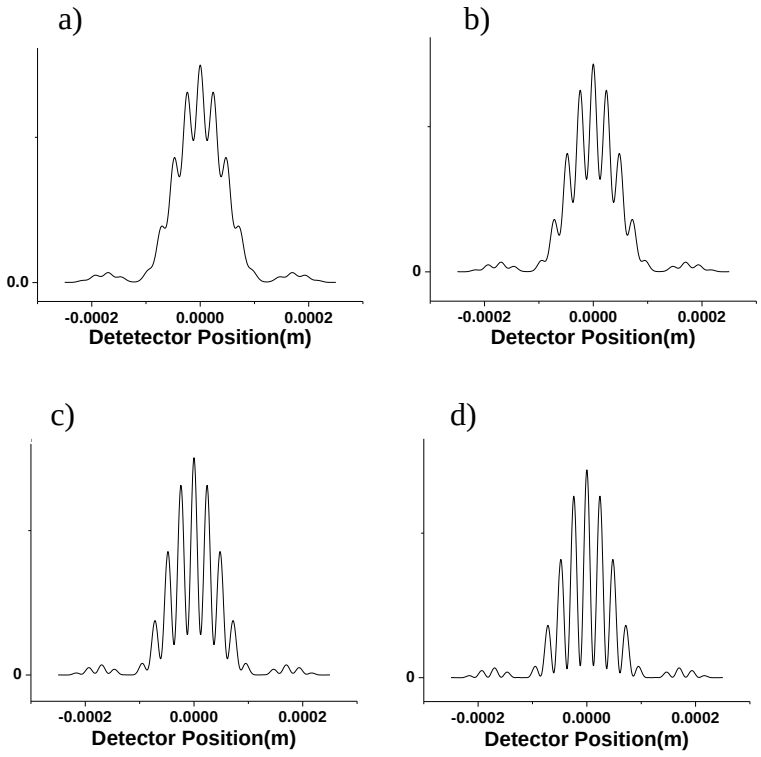

Figure 2.4

Double Slit Diffraction with Varying Source Coherence Length

The contrast increases with increasing coherence width. Shown here are plots of diffraction with coherence widths of a) 1nm b) 300nm d) 600nm and e) 1μm.

In the case of field emission an experiment to measure the transverse coherence length of electrons at the source has actually been done by B. Cho *et al*.[21] using a tungsten field emission tip, and a multiwalled carbon nanotube (MWCNT) bi-prism to form interference fringes. A tungsten tip with radius of hundreds of nanometers was positioned behind a MWCNT by distances ranging from 0.1mm to 10mm. The distance from the nanotube to the detector was 16.5cm (see figure 2.5a). Electrons of less than 100eV were used. The deformation of the electric field due to the presence of the grounded nanotube pulled the electrons on either side of the nanotube together to overlap on the detection screen.

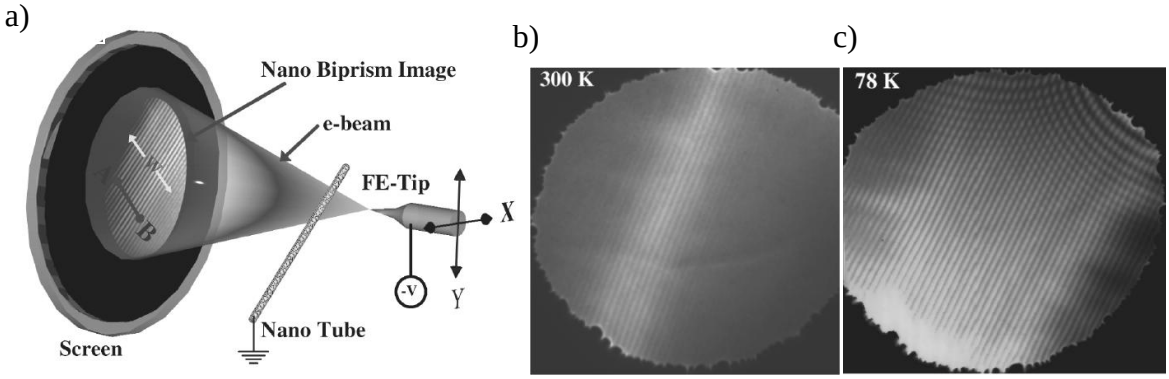

Figure 2.5

Tungsten FET/MWCNT Bi-Prism Source Coherence Measurement

a) The set up for the experiment by Cho et al. consisted of a tungsten field emission tip as an electron source, a MWCNT from which electrons diffracted, and a detection screen for measuring the diffraction pattern. Also shown here are examples of images taken at b) 300K and at c) 78K. (Images taken from B. Cho et al.[21])

Determination of the coherence length at the tip was done using a result by Pozzi[23] which states that the ratio of the coherence width to the overall beam width is constant throughout beam propagation. Based on the interference pattern measured at the detector the authors estimate the transverse coherence length of the electron source. At 300K and 78K the resulting coherence lengths were found to be 5-10nm and 35nm, respectively.

2.2. Coherence of electrons in a metallic structure

In order to determine the coherence length of electrons in a metallic structure one must first ask what dictates the coherence length of the conduction electrons within a metal. There are many interactions and system dependent factors which come into play such as electron-phonon interaction, electron-electron interaction, spin-orbit coupling, electron spin flip scattering, shape of the material (i.e. three dimensional bulk material, thin films, mesoscopic wires, nanostructures, quantum dots etc.), impurities, disorder in the material, superconductivity, etc[24-27]. The determination of the coherence length of electrons in metals has been an ongoing subject of research at least the last three decades[24]. Unlike the case of free propagating matter waves these interactions and systematic factors cannot be isolated. The strength of the coupling between the electrons in a metal and their environment is so strong and so much dependent on the specific details of the system that a general answer cannot be attained. In other words it is my impression that any model attempting to isolate any one of these interactions would not be representative of any real material and would therefore be meaningless. Therefore, in this section I discuss the ideas behind a common technique for measuring coherence length of conduction electrons as well as an example of a couple of experiments done to make such a measurement.

2.2.1. Weak localization and magnetoresistance

One of the most common techniques of measuring the coherence length of conduction electrons in metal is low field magnetoresistance. In order to make such measurements one must first understand the quantum corrections to conductivity. The following is a qualitative explanation of the quantum corrections to conductivity as seen

in[28-30]. Other, more precise theoretical approaches exist in the literature[31, 32]. To begin with this understanding it is necessary to start with the assumption that the conduction electrons are moving in a solid which has impurities randomly situated throughout. Electrons drifting through a metal structure can scatter from these as well as phonons, other electrons, etc. If we define the scattering rate from any one of these events as $1/\tau_i$ then it is assumed that the overall scattering rate is simply the sum of the rates associated with each type of scattering event $\sum_i 1/\tau_i$. The scattering time corresponding to elastic scattering events (electrons scattering from impurities) is denoted sans subscript as $1/\tau$. These are scattering events which do not change the energy of the electron and therefore do not affect the time dependent phase factor of the electrons wave function $\exp(iEt/\hbar)$. Since it is random variations in the phase of the electron which are said to give rise to decoherence, these elastic scattering events do not affect coherence. Alternatively inelastic processes (i.e. those by which the electrons kinetic energy is changed) such as electron-phonon or electron-electron scattering are denoted $1/\tau_\varphi$ where τ_φ is defined as the dephasing time (the time necessary for the electron to lose coherence). From here on in the discussion the assumption will be made that τ_φ is much greater than τ thus allowing paths over which the electrons can elastically scatter many times before losing their coherence.

More specifically the motion of the electron is described as diffusive. The elastic scattering of the electron results in the electron taking a random walk through the metal where each step takes the electron from one impurity to another. For an electron moving

during a time interval t the probability of finding that electron a distance r from where it started is given by

$$p(r,t) = (4\pi Dt)^{\frac{-d}{2}} \exp\left(\frac{-r^2}{4Dt}\right),\ r^2 = \sum_{i=1}^{d} x_i^2 \tag{10}$$

where $D = lv_F/d$ is the diffusion constant, $l = v_F\tau$ is the mean free path, v_F is the Fermi velocity, and d is the dimensionality of the system. It may seem strange to have anything other than 3 for the dimensionality of a real metal structure but for the purpose of analysis not shown here the dimensionality is defined in terms of the coherence length. A system has reduced dimensionality if one or more of its length scales b is small compared to the coherence length L_φ ($b \ll L_\varphi$). The width of the distribution is then given by

$\Delta r = \sqrt{Dt} = \sqrt{lv_F t/d} = \sqrt{l^2 t/d\tau} = l\sqrt{N/d}$ where $N = t/\tau$ is approximately the number of inelastic scattering events which have occurred in time t. This is basically the result of a classical description of an electron diffusively moving through a metallic structure. To find the probability of the electron going from one point to another it is only necessary to add the probabilities associated with each possible path between those two points. Using quantum mechanics, however, one must add the probability amplitudes associated with each path and square the sum in order to obtain a probability.

$$P_{classical} = \sum_i |A_i|^2 \tag{11}$$

$$P_{quantum} = \left|\sum_i A_i\right|^2 = \sum_i |A_i|^2 + \sum_{i \neq j} A_i A_j^* \tag{12}$$

Here A_i is the probability amplitude associated with a particular electron path. This is much like the Feynman path integral approach to quantum mechanics where the group of

all possible paths between two points consists of paths that connect impurities with straight lines. Now consider paths which are loops that start and stop at the same point (see figure 2.6).

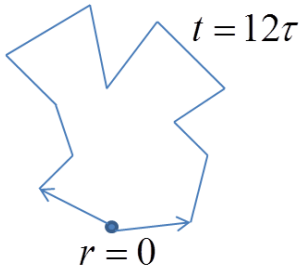

Figure 2.6

Weak Localization Loop

An electron going in a closed loop may go around the loop either clockwise or counterclockwise as shown in this example of a path that extends over 12 times the inelastic scattering time.

For such a loop the electron can go clockwise or counterclockwise, each way having the same probability amplitude.

$$P_{classical} = |A_1|^2 + |A_2|^2 = 2|A|^2 \tag{13}$$

$$P_{quantum} = |A_1 + A_2|^2 = |A_1|^2 + |A_2|^2 + A_1A_2^* + A_2A_1^* = 4|A|^2 \tag{14}$$

where A_1 and A_2 are the probability amplitudes of the two possible directions of the loop and $A_1 = A_2 = A$. With any trajectory that is a closed loop there are two identical paths which can be added in this way. This identical path pairing cannot be done so easily with paths that start and end at different points. Given that the specific path an electron takes is determined by inelastic scattering from randomly situated impurities and defects it is very unlikely that for such a path there is a different path which accumulates exactly the same phase. Because the probability of the electron returning to its origin is twice that which would be predicted classically, the electron will spend more time in the vicinity of the

origin and therefore the conductivity will be affected. This effect is called weak localization. Note that only paths within a certain length scale can be added coherently in this way. If the time taken to travel along a loop exceeds the dephasing time than the two possible paths will no longer be in a coherent superposition upon returning their starting point and thus cannot interfere. It is in this way that the coherence length $L_\varphi = \sqrt{D\tau_\varphi}$ becomes significant.

In order to see how this effect can be put to use, consider how a magnetic field affects this phenomenon. For this consideration a magnetic field is required such that $\Omega\tau \ll 1$ where $\Omega = \frac{eB}{m}$ is the cyclotron frequency. This limitation on the magnetic field is taken so that the electrons take between inelastic scattering events deviate minimally from being straight lines thus allowing for identical clockwise and counterclockwise loop trajectories to be taken. The inclusion of the magnetic field induces an additional phase shift on the electron due to the magnetic vector potential $\vec{A}$. This means including a phase factor on the probability amplitude for the closed loops under consideration. With the use of Stoke's theorem that phase factor can be written as

$$A \to A\exp\left(\frac{ie}{\hbar}\oint \vec{A}\cdot d\bar{x}\right) = A\exp\left(\frac{ie}{\hbar}\oint\left(\nabla\times\vec{A}\right)\cdot d\bar{a}\right)$$

$$= A\exp\left(\frac{ie}{\hbar}\oint \vec{B}\cdot d\bar{a}\right) = A\exp\left(\pm\frac{ie\Phi_B}{\hbar}\right) \qquad (15)$$

where Φ_B is the magnetic flux enclosed in the loop and the sign of the phase depends on the direction the electron took relative to the magnetic field to get around the loop. Since the phase shifts accumulated by the two paths are equal in magnitude and opposite in sign then the difference in phase is twice as much as the phase accumulated on an individual

path $\left(\Delta\phi = 2e\Phi_B/\hbar\right)$. The area of the loop is taken to be on the order of the square of the size of the diffusive probability distribution mentioned earlier $\left(\Delta r^2 = Dt\right)$. This leaves us with a phase difference of $\Delta\phi = 2e\Phi_B/\hbar = 2eBa/\hbar = 2eBDt/\hbar$ where a is the area of the loop. The effect of this phase shift can now be seen in the probability calculation made earlier.

$$P_{quantum} = \left|A_1 e^{i\Delta\phi/2} + A_2 e^{-i\Delta\phi/2}\right|^2 = \left|A_1\right|^2 + \left|A_2\right|^2 + A_1 A_2^* e^{i\Delta\phi} + A_2 A_1^* e^{-i\Delta\phi}$$

$$= 2\left|A\right|^2\left(1+\cos\left(\Delta\phi\right)\right) = 4\left|A\right|^2\cos^2\left(\frac{\Delta\phi}{2}\right) \qquad (16)$$

It is apparent from this expression that for the right value of the magnetic field the constructive interference which results in weak localization is switched over to destructive interference thus not permitting the formation of closed loops. The above expression for $P_{quantum}$ has a similar effect on the conductivity as the previous correction. The change in the number of electrons that return to their starting place must be opposite in sign to the change in number of electrons that do not. The difference here is that instead of increasing the probability of returning by adding $2\left|A\right|^2$, this probability is increased by adding $2\left|A\right|^2\cos\left(\Delta\phi\right)$.

With this result in hand it is possible to consider the magnetic field necessary to cause destructive interference and attempt to give credence to the stipulation made earlier on the magnetic field $\left(eB\tau/m \ll 1\right)$. Larger loops take longer to complete and have more magnetic flux enclosed, therefore not as much magnetic field strength is necessary for destructive interference. The longest loop which allows for interference can take no more

than τ_φ to complete. Therefore, the minimum magnetic field necessary to make the probability shown above equal to zero is

$$B_\varphi = \frac{\pi\hbar}{2eD\tau_\varphi} \tag{17}$$

Rearranging the diffusion constant as $D = \frac{\tau E_F}{dm}$ where E_F is the Fermi energy.

Substituting this into the above expression and solving for $\Omega\tau$ gives

$$\Omega\tau = \frac{eB_\varphi\tau}{m} = \frac{d\pi\hbar}{2E_F\tau_\varphi} \tag{18}$$

A portion of this expression can be recognized as the phase accumulated by an electron with the Fermi energy during the dephasing time which would be much greater than one $\left(E_F\tau_\varphi/\hbar \gg 1\right)$. Therefore it is possible to see the effect of the magnetic field this way without causing any significant bending of trajectories between inelastic scattering events (i.e. $\Omega\tau \ll 1$ holds).

If the time necessary for the phase difference $\Delta\phi$ to be of order 1 $\left(\tau_B = \hbar/2eBD\right)$ is much less than the dephasing time ($\tau_B \ll \tau_\varphi$ or alternatively $B \gg B_\varphi$) then the largest possible phase shift greatly exceeds 1. In this case the group of paths which form loops contain both constructive and destructive interference and the two effects average out, removing the localization phenomenon. Because of this, experimentalists can measure a magnetic field dependence in the conductivity and find a best fit using a theory of this kind to determine the coherence length. This Analysis can be pushed further to account for the effects of spin-orbit interaction, electron-electron interaction and so on. For the purpose of this chapter I will push this analysis no further. With an expression for the

conductivity an experimentalist can fit their resistance data to determine the dephasing time. This can be done at various temperatures in order to map out the dephasing time as a function of temperature.

2.2.2. Measurements of coherence length in mesoscopic metal wires

In a 2003 article by Pierre *et al.*[1] the phase coherence time was measured via low field magnetoresistance. These measurements were made specifically on silver, gold, and copper at various levels of impurity and at temperatures ranging from around 2K down to as little as 40mK. Samples were created using electron beam lithography. Such low temperatures were achieved with the use of a top loading dilution refrigerator. Resistance measurements were made using a four lead technique (see figure 2.7).

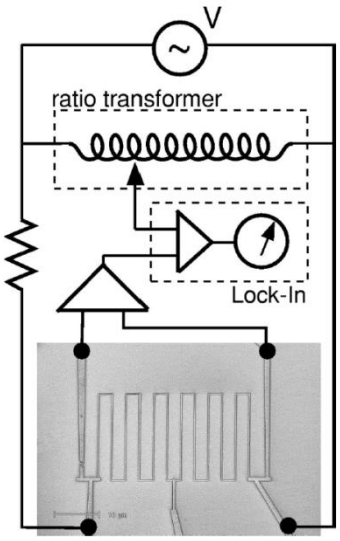

Figure 2.7

Experimental Setup for Coherence Measurement in Mesoscopic Metal Wires

A four lead technique was used to measure the magnetoresistance of the samples. Two leads were used to supply a current and two were used to measure the voltage drop across the sample. The measured voltage drop was compared to the signal taken directly from the power supply via a lock-in amplifier. (Image taken from Pierre *et al.*[1])

A power supply is used to drive an AC current through the sample via two of the leads while another pair of leads are used to measure the voltage difference across the sample. The voltage from the power supply is modified by a ratio transformer and is then compared to the voltage drop across the sample. This technique allows for measurements of very small variations in resistance of the sample. The use of this four lead technique instead of a standard resistance meter is so the leads do not contribute to the resistance being measured. A superconducting coil was used to generate the magnetic field. This field was applied perpendicular to the plane of the sample.

Figure 2.8a shows a list of the different samples as well as the following characteristic parameters: length l, thickness t, width w, Diffusion constant D, and

a)

Sample	Made at	L (μm)	t (nm)	w (nm)	R (kΩ)	D (cm^2/s)
Ag(6N)a	Saclay	135	45	65	1.44	115
Ag(6N)b	Saclay	270	45	100	3.30	70
Ag(6N)c	Saclay	400	55	105	1.44	185
Ag(6N)d	MSU	285	35	90	1.99	165
Ag(5N)a	Saclay	135	65	108	0.68	105
Ag(5N)b	Saclay	270	65	90	1.31	135
$Ag(5N)c_{Mn0.3}$	Saclay	135	65	110	0.47	150
$Ag(5N)d_{Mn1}$	Saclay	270	65	95	1.22	135
Au(6N)	MSU	175	45	90	1.08	135
Cu(6N)a	MSU	285	45	155	0.70	145
Cu(6N)b	MSU	285	20	70	7.98	60
Cu(6N)c	MSU	285	35	75	4.37	65
Cu(6N)d	MSU	285	20	80	8.50	50
Cu(5N)a	Saclay	270	45	110	1.68	70
Cu(5N)b	Saclay	270	45	100	0.95	160

b)

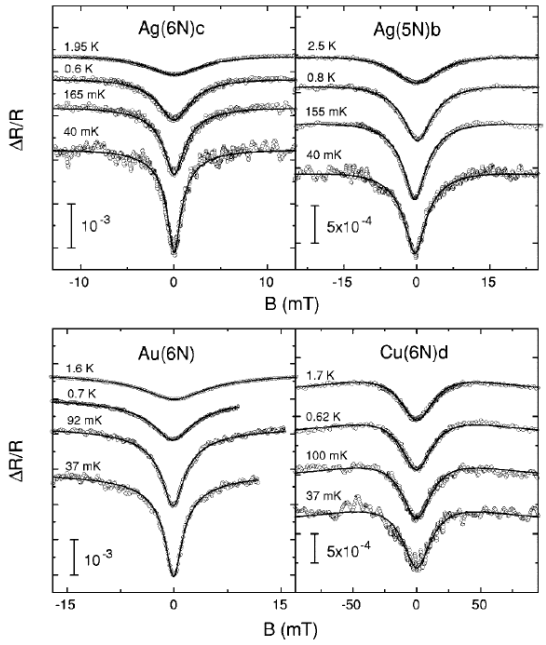

Figure 2.8

Wire Characteristics and Corresponding Magnetoresistance Measurements

a) All of the different samples are listed here along with their various characteristics. b) Magnetoresistance curves for four of the samples are shown here at various temperatures. The curves are offset vertically so that those of different temperatures can easily be seen. (Images taken from Pierre *et al.*[1])

resistance of the wire R. Figure 2.8b shows the measurements of magneto resistance made on 4 of the samples. The level of impurity in the samples is indicated by the numbers "5N" and "6N" which mean 99.999% pure and 99.9999% pure, respectively. In order to determine the dephasing time as a function of temperature, the authors fit their magnetoresistance data using an expression based on one dimensional weak localization theory which involves spin-orbit coupling

$$\frac{\Delta R}{R} = \frac{e^2 R}{\pi \hbar L}\left\{\frac{3}{2}\left[\frac{1}{L_\varphi^2}+\frac{4}{3L_{so}^2}+\frac{1}{3}\left(\frac{eBw}{\hbar}\right)^2\right]^{\frac{-1}{2}} - \frac{1}{2}\left[\frac{1}{L_\varphi^2}+\frac{1}{3}\left(\frac{eBw}{\hbar}\right)^2\right]^{\frac{-1}{2}}\right\} \tag{19}$$

where $L_{so} = \sqrt{D\tau_{so}}$ is the spin-orbit length which characterizes the strength of the spin-orbit coupling. The fit parameters taken were L_φ, w, and L_{so}. The width obtained as a result of fitting (denoted as w_{wl} in figure 2.9a) was obtained by taking the best fit of all data over the various temperatures. The fit width w_{wl} was compared to STM images and was always found to differ from the measured width by less than 15%. The spin orbit distance was determined based on a fit of the magnetoresistance at the highest temperature. Figure 2.9a shows the maximum dephasing time τ_φ obtained at the lowest temperature as well as the other two fitting parameters.

a)

Sample	τ_ϕ^{max} (ns)	L_{so} (μm)	w_{WL} (w) (nm)
Ag(6N)a	9↗	0.65	57 (65)
Ag(6N)b	12↗	0.35	85 (100)
Ag(6N)c	22↗	1.0	90 (105)
Ag(6N)d	12↗	0.82	75 (90)
Ag(5N)a	2.9	0.65	108 (108)
Ag(5N)b	3.5	0.75	82 (90)
Au(6N)	11↗	0.085	85 (90)
Cu(6N)a	0.45	0.67	155 (155)
Cu(6N)b	0.95	0.4	70 (70)
Cu(6N)c	0.2	0.35	75 (75)
Cu(6N)d	0.35	0.33	80 (80)
Cu(5N)a	1.8	0.52	110 (110)
Cu(5N)b	0.9	0.67	100 (100)

b)

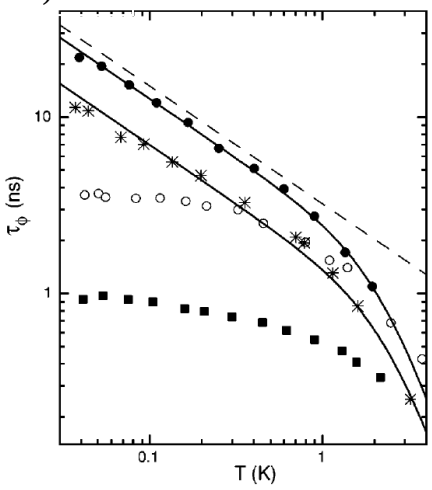

Figure 2.9

Inelastic Scattering Time for Mesoscopic Metal Wires (example 1)

a) Shown here are the maximum dephasing times for all the samples and the values of the fitting parameters L_{so} and w_{wl} as well as the measured width w. b) Four of the plots of the dephasing time as functions of temperature are shown here. The squares, stars, dark circles, and hollow circles represent copper Cu(6N)b, gold Au(6N), silver Ag(6N)c, and Ag(5N)b, respectively. (Images taken from Pierre *et al.*[1])

Figure 2.9b shows plots of τ_φ corresponding to copper Cu(6N)b, gold Au(6N), silver Ag(6N)c, and Ag(5N)b. Note that silver Ag(6N)c has both the largest dephasing time $\tau_\varphi^{\max} = 22ns$ and the largest diffusion constant $D = 0.0185 m^2/s$. Therefore, at the lowest temperature, the sample Ag(6N)c had the largest coherence length at $L_\varphi^{\max} = \sqrt{D\tau_\varphi^{\max}} \approx 20\mu m$. That certainly seems like a large number but figure 2.9b shows that the dephasing time drops precipitously with increasing temperature, losing almost two orders of magnitude with an increase of just over 1K in the case of Ag(6N)c. This would result in a loss of a factor of 10 on the coherence length putting it at roughly 2μm at just over 1K.

A similar experiment by S. Wind *et al.*[33] in which magnetoresistance measurements were made on aluminum and silver wires (purity levels were not specified). The wires had widths ranging from 35nm to 110nm (comparable to the widths in the previously mentioned experiment). These measurements revealed that for silver (again with the highest diffusion constant) the coherence length at 20K is already as low as 200nm (see figure 2.10b).

a)

Sample	W [a] (nm)	$R_\square$ [b] (Ω)	D [c] (cm^2/sec)
Al1*a*	35	1.8	39
Al1*b*	46	1.8	39
Al2*a*	40	1.4	49
Al2*b*	60	1.4	49
Al2*c*	62	1.4	49
Al2F	Film	1.3	53
Al3	110	1.1	63
Ag1	60	2.6	48
Ag2	100	1.5	85

b)

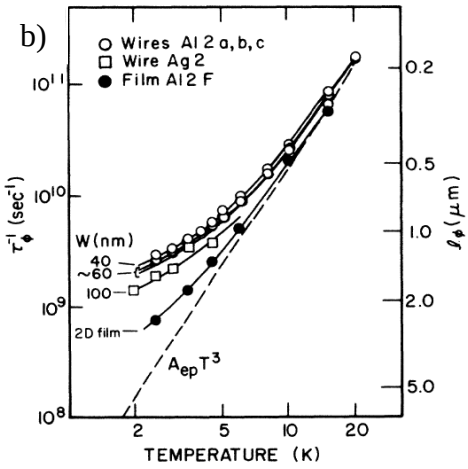

Figure 2.10

Inelastic Scattering Time for Mesoscopic Metal Wires (example 2)

a) Listed here are the samples measured along with the width, resistance, and diffusion constant for each wire. b) The dephasing time and coherence length for aluminum and silver wires as well as an aluminum film are plotted as functions of temperature. At 20K the coherence length reaches, at most, 200nm. (Image taken from S. Wind *et al.*[33])

3. Conclusion

A precipitous drop in coherence length of conduction electrons in silver from 20μm to 2μm as a result of increasing temperature from 40mK to just over 1K was shown in the data in section 3.3.1. Further data from that section showed coherence length of silver dropping further from about 2μm to 200nm for temperatures ranging from 2K to

20K. The data in section 2.1 showed that the coherence length of emitted electrons at the source (a tungsten field emission tip) falls from about 35nm to 5-10nm for temperatures increasing from 78K to 300K. They also claim that the "inelastic mean free path" of conduction electrons drops from 140nm to 16nm over that same range of increasing temperature, implying a connection between the coherence of emitted electrons and conduction electrons (the authors do not strictly define this term nor do they measure it themselves). That data along with the idea that decoherence is an irreversible process seems to suggest that the coherence of an electron source is limited by the strength of the environmental interactions taking place inside the conductor as a function of temperature. This data also seems to indicate the possibility that the coherence length of such a source could be dramatically improved by lowering the temperature. An experiment comparing the coherence length outside of the conductor to that of the conduction electrons could potentially determine which process most effectively maintains coherence. Such an experiment could also confirm the possibility that low temperatures dramatically improve the coherence of the source. Note that the assumption made thus far regarding the connection between emitted electrons and conduction electrons is based on claims in the literature that photoemitted electrons from metals originate entirely in the conduction band[19, 20] and that in the case of field emission the electrons with the highest energy (i.e. the ones at the top of the conduction band) are most likely to tunnel through the barrier.

While I could find nothing in the literature indicating a direct measurement of the coherence length of electrons photoemitted from a metal, it seems reasonable to expect a correlation between the between the coherence length of photo emitted electrons and conduction electrons given the implied correlation for field emitted electrons in the data

in section 2.1. It is also worth noting that one could predict an approximate lower limit to the coherence length of conduction electrons based on the uncertainty principle. Considering the simple model of electrons randomly walking from impurity to impurity the direction of the momentum of the conduction electrons would seem to be isotropic. Assuming the magnitude of the momentum to be approximately that of the Fermi energy the minimum uncertainty in position could be written as

$$\Delta x_{\min} = \frac{\hbar}{2\Delta p} \approx \frac{\hbar}{4p_F} = \frac{1}{4k_F} \tag{20}$$

Given that the typical Fermi wave number in metals[34] is on the order of $10^8 cm^{-1}$, the minimum coherence length would be approximately a quarter of an angstrom.

Future efforts could include attempts to work out detailed plans for measurement of coherence lost due to photoemission. The geometry of the metallic structure would have to be favorable for both magnetoresistance measurements as well as emission. Also, the use of a top loading dilution refrigerator is not practical for such an experiment. Such a device requires that the sample is buried inside a very complicated cryostat and as such is not accessible for photo emission (see figure 2.11). This seems to limit the temperatures that can be reached. One possible experiment may involve photoemission from a thin film held at liquid helium temperature (4.2K) with the use of a cold finger.

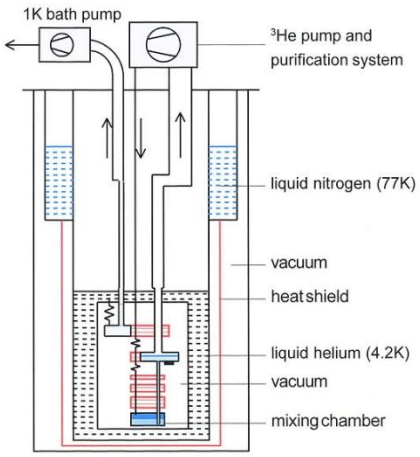

Figure 2.11

Schematic of Dilution Refrigerator

Shown here is a schematic diagram of a dilution refrigerator. The sample would be placed on the surface of the mixing chamber. (Image taken from Wikipedia article: http://en.wikipedia.org/wiki/Dilution_refrigerator

Judging from the plotted data presented by S. Wind *et al.*[33] the upper limit for the transverse coherence length of electrons emitted from a silver source at liquid helium temperatures would seem to be approximately 1μm (though this may be different for thin films). The calculation of the propagation of a partially coherent state made 2.1 neglected the decoherence processes that would occur at the double slit. These processes are known to reduce contrast[35] and must be accounted for. Alternatively, it may be possible to photoemit and look at the angular spread. The coherence length of the partially coherent state can be thought of as the uncertainty in position of its fully coherent constituent as described in section 2.1. The Heisenberg uncertainty principle $\left(\Delta x \Delta p \geq \hbar/2\right)$ tells us that the minimum angular spread can be determined by the uncertainty in position.

$$\Delta\theta \approx \frac{\Delta v}{v} = \frac{\Delta p}{p} \quad \Rightarrow \quad \Delta\theta \geq \frac{\hbar}{2p\Delta x} \tag{21}$$

Thus for a given coherence length the angular spread of the beam can be no less than a certain value. For example, in the calculation considered in section 2.1 the coherence length ranged from 1nm to 1μm. In that case the minimum angular spread would range from approximately 2mrad down to 2μrad. Of course, it also seems reasonable to consider repeating the experiment by B. Cho *et al*.[21] in section 2.1 but for photoemission instead of field emission.

Chapter 3 – The Relation Between the Feynman Paradox and Aharonov-Bohm Effects

1. Introduction

The question whether or not forces are present for physical systems that display the Aharonov-Bohm effect has been debated for decades. The general consensus is that there are no forces, which is considered to be a defining property of the famous effect. The best known version of the effect occurs when a current carrying solenoid (or more generally a magnetic flux) is enclosed by an electron interferometer. When the current is changed the consequence is that the observed electron fringes in the interferometer shift. Given that the solenoid is thought to produce no discernible magnetic (or electric) field external to its structure, and that is where the electron passes, there is no force on the electron. It is rare if not unique to encounter a response of a physical system without the presence of forces, which illuminates a part of the appeal of the A-B effect.

Central to A-B effects is the interaction between a magnetic moment and a charge. This interaction is associated with a classical relativistic paradox[1]. Recently[2], Aharonov and Rohrlich stated that: "The paradox is crucial to clarifying the entirely quantum interactions of "fluxons" and charges – the generalized Aharonov-Bohm effect.." The central problem to the paradox is the following. When a point charge moves in the vicinity of a tube that contains magnetic flux, the momentum in the electromagnetic field changes. Outside of the flux tube there is no electric or magnetic field and the charge does not change its momentum. The tube carries no net charge, may thus not experience a Lorentz force and appears not to change its momentum. These

cursory observations would, if true, violate momentum conservation and give the appearance that the A-B effect is paradoxical in nature.

In this chapter, we give a description of the magnetic A-B effect and its reciprocal[3] based on the Darwin Lagrangian. Our approach resolves the paradox, is consistent with all experiments to date, and can in principle be differentiated experimentally from previous theoretical approaches. We find that for constrained motion both parts of the physical system do not accelerate, consistent with the generally accepted prediction, however we also find that for unconstrained motion the magnetic part does accelerate and the charged part does not. The apparent violation of Newton's third law is typical for the "Feynman paradox." The relation between the Feynman paradox and Aharonov-Bohm effects has to our knowledge not been pointed out before. Building on the Feynman paradox the difference between constrained and unconstrained motion is delineated. We argue that the appropriate description of physical systems, which are used for demonstration of A-B effects, is not known to be constrained or unconstrained.

Feynman explains a paradox in his famous Lectures where two particles interact in such a way that the momentum of one particle changes by a certain amount that is not the same as the momentum change of the other particle[4]. The specific scenario is that two charged particles are placed on the x-axis, with one charged particle moving initially along the x-axis, while the other moves along the y-axis. From the Lorentz force it is clear that the magnetic part of the force is not balanced (figure 3.1a). A relativistic treatment of this problem does not change this conclusion[5]. This is indeed an example where the interpretation of Newton's third law as conservation of mechanical momentum (as opposed to canonical momentum) breaks down.

In this work, a Lagrangian approach is chosen. The Lagrangian offers ways to conveniently impose constraints on the particle motion. A Hamiltonian can be obtained from it that can be compared to other approaches[6]. Finally, a path integral method can be used to obtain the quantum mechanical phase shifts that can be compared to the known A-B and A-C phase shifts. For the interaction of charged particles no Lagrangian exists that is manifestly invariant and obeys Lorentz symmetry[7] to all orders in v/c. The Darwin Lagrangian is the best known choice that is valid to $(v/c)^2$. This approximation will turn out to be sufficient to treat the Feynman paradox and the A-B and A-C problem in such a way that momentum is conserved, the equations of motion for both parts of the system are obtained and the method used for all systems is the same. Note that the inclusion and the physical effect of higher order terms is potentially interesting but unknown.

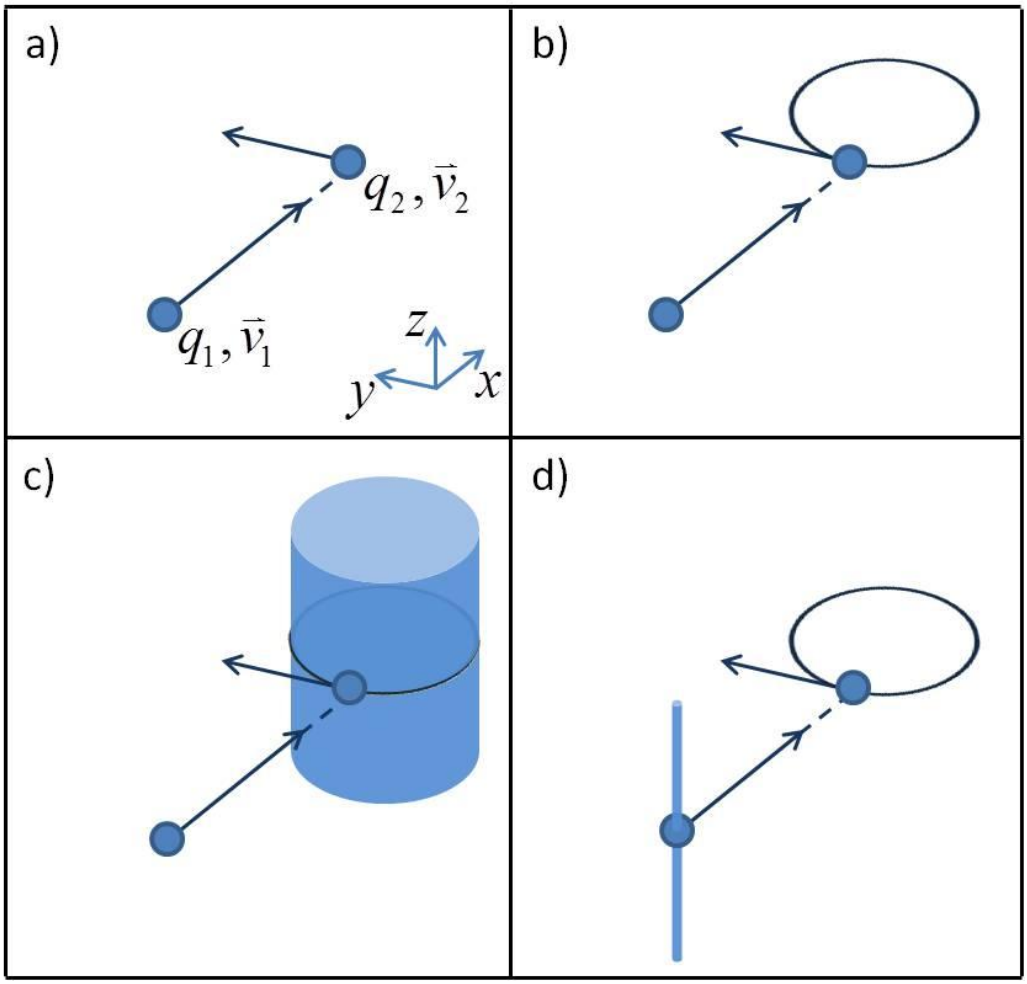

Figure 3.1

Build Up of Mott-Schwinger, Aharonov-Bohm, and Aharonov-Casher Systems

a) In the physical system presented in the Feynman paradox, particle 1 moves toward particle 2, and particle 2 moves with a velocity perpendicular to that of particle 1. The Lorentz Forces are not balanced in this case. b) The Mott-Schwinger system consists of a charged particle moving in the vicinity of a current loop[8,9]. The current loop may be thought of as many circulating charge elements. Consequently this system bears a resemblance to the Feynman system. c) In the case of the Aharonov-Bohm effect, a charged particle is moving near a current carrying solenoid. Here the solenoid is depicted as constructed from current loops as they appear in the Mott-Schwinger system. d) The Aharonov-Casher system involves a charged wire and a current loop. Similar to the solenoid in the Aharonov-Bohm system, the charged wire is shown as constructed from charged particles as in the Mott-Schwinger system.

2. Relativistic Classical Analysis

2.1. Preamble and assumptions: Building the physical systems

It is from the constituents of the physical system presented in the Feynman paradox (figure 3.1a) that the Mott-Schwinger system (figure 3.1b), the Aharonov-Bohm system (figure 3.1c), and the Aharonov-Casher system (figure 3.1d) can be constructed. The neutron in the Mott-Schwinger system can be modeled as a current loop. Such a loop may be thought of as many circulating charge elements. Thus, the transition from the Feynman paradox to the Mott-Schwinger system may be done by integration over the charges in the loop. Similarly a solenoid may be constructed via the addition of non-interacting current loops, and a charged wire constructed by addition of non-interacting point charges. Consequently, a transition from the Mott-Schwinger system to the Aharonov-Bohm or Aharonov-Casher systems may be done by integration of current loops or point charges, respectively.

In the construction phase the issue of constraints comes into play. The construction of the Mott-Schwinger system may be performed in two ways. Either the Lagrangian for the Feynman system can by integrated directly, or, alternatively, the forces resulting from the Lagrangian can be integrated. These two methods imply inherent assumptions regarding the freedom of the relative motion of the charges that constitute the current loop. If the forces resulting from the Lagrangian are integrated, the net force on the overall system, and thus the equation of motion of the current loop, is determined. Because the forces were computed without applying any restrictions to the relative motion, the charge elements are free to move independently (i.e. the motion of the charge elements is unconstrained). If, on the other hand, the Lagrangian is integrated

directly, the Euler-Lagrange equations give the equation of motion for the current loop. The derivatives of the Euler-Lagrange equations are taken with respect to the position and velocity of the current loop. This method stipulates that the charge elements move relative to each other in such a way that the initial shape of the charge distribution is preserved and the loop merely undergoes translation (i.e. the motion of the charge elements is constrained).

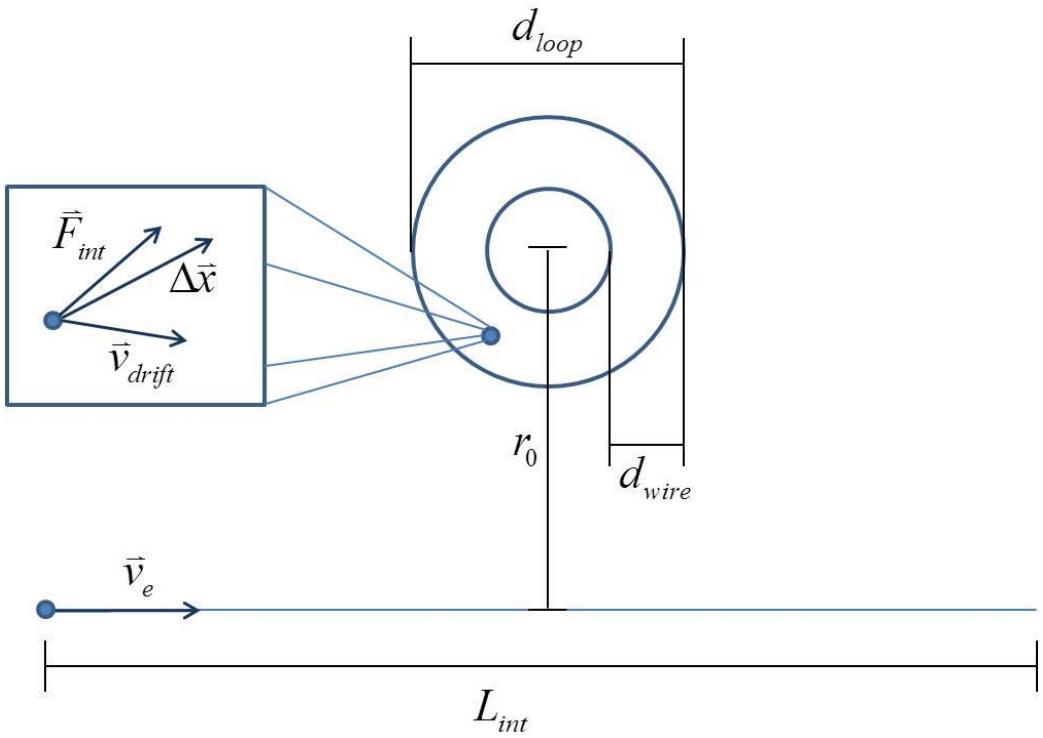

Figure 3.2

Motion of Conduction Electrons in Current Loop

An electron in a current loop with diameter d_{loop} and an electron passing at a distance r_0 interact via the Lorentz force. The electron in the loop experiences a force F_{int}. During the interaction time the electron in the loop moves a distance Δx. This movement is a combination of drift movement due to drift velocity v_{drift} and the displacement due to the Lorentz force.

It appears obvious that the motion of the conduction electrons in a solenoid should be treated as constrained. Simple estimates can be made to investigate this statement. Consider an electron passing a solenoid in a certain interaction time. During this time the motion of solenoidal conduction electrons can be investigated and their distance traveled can be compared to the solenoid wire thickness. If the distance traveled is much larger, then constraints are certainly important, while if the distance traveled is much shorter the roll that the constraints play is much less clear. Our argumentation hinges on the veracity of the latter and justifies the investigation of comparison of motion for unconstrained versus constrained systems. *We do not claim that the system is either*, but consider both fully unconstrained and constrained systems to be interesting limiting cases.

In A-B experiments such as the one by Mollenstedt and Bayh[10], the interaction time of an electron passing a solenoid at 40 keV is roughly 1 ps (see figure 3.2), assuming an interaction length of three times the loop diameter (3×36 μm). The electron velocity has a drift velocity of $v_{drift} = I/nAq = 80$ μm/s, where I is the current, n is the number of atoms per unit volume of the wire, A is the cross sectional area of the wire and q is the charge of an electron. The electron has a far larger thermal component $v_{thermal} = \sqrt{2k_B T/m_e} = 9.5\times10^5$ m/s. The thermal drift displacement during the interaction time is $\Delta x_{thermal}$ = 87 nm, which is much smaller than the solenoid wire diameter of 5 μm. The displacement of electrons within the coil due to the magnetic field of the passing electron Δx_{int} can also be approximately determined, by using the Lorentz force. The result is $\Delta x_{int} = 3.7\times10^{-20}$ m using the thermal velocity. Note that the inclusion of the effective electron mass of the Drude-Sommerfeld model has little effect on the estimates,

as the effective mass of a conduction electron in tungsten is only 2-3 times that of a free electron[11]. The potential which restricts the charge to the wire may be thought of as having negligible curvature over such small distances. Additionally, the centripetal force required for the electrons in the solenoid to move in a circle with a drift velocity of 80 μm/s is on the order of 10^{-34} N, whereas the Lorentz force due to the passing electron charge is on the order of 10^{-32} N. It appears reasonable to at least consider the scenario of unconstrained motion.

Objections can be raised to these estimates. For example, electron-phonon interaction may in principle lead to a back-action force. Another example is, that the interaction time is much slower than the plasmonic response time of tungsten (0.44 fs)[12]. This motivates the inclusion of electron-electron interaction within the wire during the interaction time. An interesting attempt has been made to include such interactions and some constraints[13], that support the controversial idea that both parts of the A-B system experience a force. However, arguably[14], a recent experiment may rule out the presence of force on the passing electron[15]. To date, no detailed models have been analytically or numerically solved, which motivates the study of the simpler case of constrained and unconstrained motion.

For neutrons in the A-C system this type of estimate gives a completely different result. The neutron could be modeled as a current loop of radius 10^{-15} m. (This simplistic classical model ignores quantum mechanical addition of quark angular momentum and magnetic moment). In order for such a loop to generate a magnetic moment of 10^{-26} J/T, the constituent charges would circulate with a period on the order of 10^{-23} s. The interaction time in the experiment by Werner *et al.*[16] was on the order of 10^{-5} s thus the

motion of the charged constituents of the neutron is constrained. For completeness it is still interesting to analyze the A-C system in terms of constrained and unconstrained motion as described above. Furthermore, A-C phase shift may be observable for other larger magnetic particles, for which the constraints are not clear.

A case has been made in favor of the effective presence of constraints on the basis of the following lemma: any finite stationary distribution of matter has zero total momentum[17]. The term "stationary" is defined by $\partial_0 T^{\mu\nu} = 0$, where $T^{\mu\nu}$ is the electromagnetic stress tensor. The assumption of a stationary distribution along with the conservation law $\partial_\mu T^{\mu\nu} = 0$ gives the result $\partial_j T^{j0} = 0$. Using the divergence theorem the total momentum may be written as a surface integral[18]

$$p^i = \frac{1}{c}\int T^{i0} d\tau = \frac{1}{c}\int \left[\partial_j \left(x_i T^{j0}\right) - x_i \partial_j T^{j0}\right] d\tau = \frac{1}{c}\oint x_i T^{j0} dS_j \,. \qquad (1)$$

The assumption of a finite distribution of matter ensures that the elements of the stress tensor must fall off as $1/r^{4+\delta}$ ($\delta \geq 0$). Consequently the above surface integral is zero, proving the lemma;

$$p^i = \frac{1}{c}\oint x_i T^{j0} dS_j = 0 \,. \qquad (2)$$

The presence of electromagnetic momentum for a stationary charge-current distribution, taken together with the validity of the lemma, demands that there is another opposite and equal form of momentum. This "hidden momentum" results from internal motion of a stationary system. One text-book example is that of a current carrying loop of wire, bathed in a uniform external electric field[19] (figure 3.3). Relevant for our present discussion, the electric field could be thought of as arising from the presence of a distant point charge.

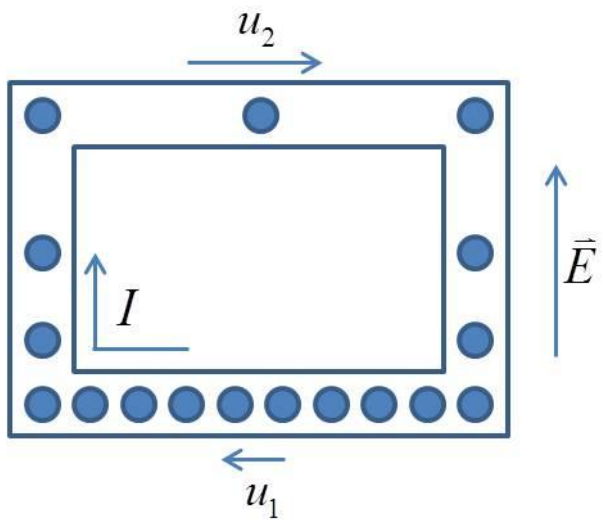

Figure 3.3

Hidden Momentum in Current Loop

A conducting loop with current circulating clockwise is immersed in an external homogeneous electric field directed toward the top of the page. The electric field accelerates the charges moving toward the top of the loop and decelerates those moving toward the bottom of the loop. Consequently there is a non-zero net relativistic total linear momentum of the charges contained in the loop[19]. This is the "hidden momentum" and it exactly cancels the momentum in the electromagnetic field.

The applied electric field $\vec{E}$ gives rise to a change in velocity of the charges as they move along the vertical segments of the loop. Consequently, the velocity of the charges moving in the bottom segment, u_1, is smaller than the velocity in the top section, u_2. The result is that the charges in the loop carry a net relativistic mechanical momentum equal and opposite to the electromagnetic field momentum[19]. Proponents of using hidden momentum for analysis of the A-B effects, claim that in the case of dynamic systems for which equations of motion are being calculated, the hidden momentum has a direct effect on the equation of motion of the object in question. In the case of a current loop passing a charged wire (A-C system) the "hidden momentum" goes directly into the equation of

motion so as to cancel the force on the loop. However, one should tread carefully when taking this approach considering that the lemma being applied requires a stationary system while the calculation of the equations of motion of a system requires the assumption of a non-stationary system. Such an analysis of the loop-wire system has been made with three different models of the current loop[17]: a gas of charged particles constrained to move inside a neutral tube, a gas of charged particles constrained to move inside a conducting tube, a charged (incompressible) fluid constrained to move inside a neutral tube. Although these analyses all predict zero forces, this is not a general property for unconstrained motion as shown by the counterexample given in our present analysis.

2.2. Unconstrained motion

In section 2.2.1 the force and the equations of motion for two interacting charged particles is derived from the Darwin Lagrangian for the Feynman problem (figure 3.1a). In the following two sections the force is integrated for charge and current distributions that are relevant for the Mott-Schwinger, and the A-B and A-C effects, respectively.

2.2.1. Equations of motion for two interacting charged particles using the Darwin Lagrangian

The Darwin Lagrangian[18] is given by

$$L = \frac{1}{2} m_1 v_1^2 + \frac{1}{2} m_2 v_2^2 - \frac{q_1 q_2}{r} + \frac{q_1 q_2}{2rc^2}\left[\vec{v}_1 \cdot \vec{v}_2 + \frac{(\vec{v}_1 \cdot \vec{r})(\vec{v}_2 \cdot \vec{r})}{r^2} \right], \tag{3}$$

where $\vec{r} = \vec{r}_1 - \vec{r}_2$. The vector potential and scalar potential for a moving charged particle are given by

$$\vec{A} = \frac{q}{2rc}\left[\vec{v} + \frac{\vec{r}(\vec{v} \cdot \vec{r})}{r^2} \right] \tag{4}$$

$$\varphi = \frac{q}{r}. \tag{5}$$

The Euler-Lagrangian equations of motion[20] are $\frac{d}{dt}\frac{\partial L}{\partial \vec{v}_1} = \frac{\partial L}{\partial \vec{r}_1}$ and $\frac{d}{dt}\frac{\partial L}{\partial \vec{v}_2} = \frac{\partial L}{\partial \vec{r}_2}$, where

$$\frac{d}{dt}\frac{\partial L}{\partial \vec{v}_1} = m_1\vec{a}_1 - \frac{q_1q_2(\vec{r}\cdot\dot{\vec{r}})}{2c^2r^3}\left[\vec{v}_2 + \frac{(\vec{v}_2\cdot\vec{r})\vec{r}}{r^2}\right] + \frac{q_1q_2}{2c^2r}\left\{\vec{a}_2 - \frac{2(\vec{v}_2\cdot\vec{r})(\vec{r}\cdot\dot{\vec{r}})\vec{r}}{r^4} + \frac{\left[(\vec{a}_2\cdot\vec{r}) + (\vec{v}_2\cdot\dot{\vec{r}})\right]\vec{r} + (\vec{v}_2\cdot\vec{r})\dot{\vec{r}}}{r^2}\right\}$$

$$= m_1\vec{a}_1 + \frac{q_1q_2}{2c^2r}\left\{\vec{a}_2 - \frac{(\vec{r}\cdot\dot{\vec{r}})\vec{v}_2}{r^2} - \frac{3(\vec{v}_2\cdot\vec{r})(\vec{r}\cdot\dot{\vec{r}})\vec{r}}{r^4} + \frac{\left[(\vec{a}_2\cdot\vec{r}) + (\vec{v}_2\cdot\dot{\vec{r}})\right]\vec{r} + (\vec{v}_2\cdot\vec{r})\dot{\vec{r}}}{r^2}\right\} \tag{6}$$

$$\frac{d}{dt}\frac{\partial L}{\partial \vec{v}_2} = m_2\vec{a}_2 + \frac{q_1q_2}{2c^2r}\left\{\vec{a}_1 - \frac{(\vec{r}\cdot\dot{\vec{r}})\vec{v}_1}{r^2} - \frac{3(\vec{v}_1\cdot\vec{r})(\vec{r}\cdot\dot{\vec{r}})\vec{r}}{r^4} + \frac{\left[(\vec{a}_1\cdot\vec{r}) + (\vec{v}_1\cdot\dot{\vec{r}})\right]\vec{r} + (\vec{v}_1\cdot\vec{r})\dot{\vec{r}}}{r^2}\right\} \tag{7}$$

$$\frac{\partial L}{\partial \vec{r}_1} = \frac{q_1q_2}{r^3}\vec{r} + \frac{q_1q_2}{2c^2}\left[\frac{-(\vec{v}_1\cdot\vec{v}_2)\vec{r}}{r^3} - \frac{3(\vec{v}_1\cdot\vec{r})(\vec{v}_2\cdot\vec{r})\vec{r}}{r^5} + \frac{(\vec{v}_1\cdot\vec{r})\vec{v}_2 + (\vec{v}_2\cdot\vec{r})\vec{v}_1}{r^3}\right] \tag{8}$$

$$\frac{\partial L}{\partial \vec{r}_2} = -\frac{q_1q_2}{r^3}\vec{r} - \frac{q_1q_2}{2c^2}\left[\frac{-(\vec{v}_1\cdot\vec{v}_2)\vec{r}}{r^3} - \frac{3(\vec{v}_1\cdot\vec{r})(\vec{v}_2\cdot\vec{r})\vec{r}}{r^5} + \frac{(\vec{v}_1\cdot\vec{r})\vec{v}_2 + (\vec{v}_2\cdot\vec{r})\vec{v}_1}{r^3}\right]. \tag{9}$$

Taking the conditions which define the Feynman paradox (figure 3.4)

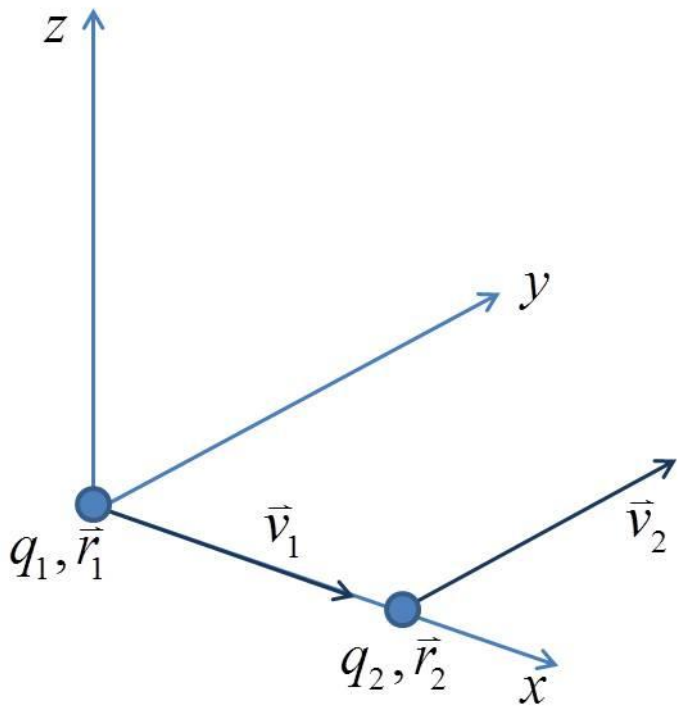

Figure 3.4

The Feynman Paradox

The coordinate system used for the analysis of the Feynman paradox (see text) is given.

$$\vec{r}_1 = \vec{0},\ \vec{r}_2 = r\hat{x}$$

$$\vec{v}_1 = v\hat{x},\ \vec{v}_2 = v\hat{y}$$

$$q_1 = q_2,\ m_1 = m_2$$

$$\vec{r} = -r\hat{x},\ \dot{\vec{r}} = v(\hat{x} - \hat{y}),\ \hat{r} = -\hat{x}. \tag{10}$$

The equations of motion obtained for particle 1 are

$$a_{1x} = \frac{-\frac{q^2}{mr^2}\left[\left(1+\frac{v^2}{2c^2}\right)+\frac{q^2}{mc^2 r}\left(1-\frac{v^2}{c^2}\right)\right]}{1-\frac{1}{m^2}\left(\frac{q^2}{c^2 r}\right)^2} \approx -\frac{q^2}{mr^2}\left(1+\frac{v^2}{2c^2}\right) \tag{11}$$

$$a_{1y} = \frac{-\frac{q^2 v^2}{mc^2 r^2}}{1-\frac{1}{4m^2}\left(\frac{q^2}{c^2 r}\right)^2} \approx -\frac{q^2 v^2}{mc^2 r^2}\,, \tag{12}$$

and for particle 2

$$a_{2x} = \frac{\frac{q^2}{mr^2}\left[\left(1-\frac{v^2}{c^2}\right)+\frac{q^2}{mc^2 r}\left(1+\frac{v^2}{2c^2}\right)\right]}{1-\frac{1}{m^2}\left(\frac{q^2}{c^2 r}\right)^2} \approx \frac{q^2}{mr^2}\left(1-\frac{v^2}{c^2}\right) \tag{13}$$

$$a_{2y} = \frac{\frac{v^2}{2m^2 r}\left(\frac{q^2}{c^2 r}\right)^2}{1-\frac{1}{4m^2}\left(\frac{q^2}{c^2 r}\right)^2} \approx 0\,. \tag{14}$$

The approximation in equations (11)-(14) is obtained by expansion to first order in $q^2/mc^2 r$ under the assumption that $q^2/mc^2 r \ll v^2/c^2$. This is valid if the paths of the charged particles are approximately straight. A small deflection implies that the potential energy of the particle is always less than the kinetic energy (i.e. $q^2/r < mv^2/2$). Alternatively, the relativistic equation of motion is given by the Lorentz force law

$$\vec{F} = q\left(\vec{E} + \frac{1}{c}\vec{v}\times\vec{B}\right). \tag{15}$$

Expanding the Lorentz force in this equation to second order in v/c leads to the equations of motion:

$$a_{1x} = -\frac{\gamma q^2}{mr^2} \approx -\frac{q^2}{mr^2}\left(1+\frac{v^2}{2c^2}\right) \tag{16}$$

$$a_{1y} = -\frac{\gamma q^2 v^2}{mc^2 r^2} \approx -\frac{q^2 v^2}{mc^2 r^2} \tag{17}$$

$$a_{2x} = \frac{q^2}{\gamma^2 m r^2} = \frac{q^2}{m r^2}\left(1 - \frac{v^2}{c^2}\right) \tag{18}$$

$$a_{2y} = 0\,, \tag{19}$$

which agree with the Darwin Lagrangian approach as well as Feynman's resolution of the paradox[5] in the non-relativistic limit. As Feynman points out, Newton's third law does not hold for mechanical momentum; however the consideration of the change of electromagnetic momentum ensures the conservation of total and canonical momentum. Note that the use of the Darwin Lagrangian is a superfluous step. We could have limited ourselves to the forces occurring in the relativistic equation of motion. However, for a consistent treatment of the unconstrained and constrained motion an identical starting point is favored. For unconstrained motion we can now proceed to integrate over the forces acting on the constituent particles of an extended body.

2.2.2. Charged particle and current loop

The forces in a system consisting of two interacting point charges have now been determined. A system of a point charge and a loop consisting of many mutually non-interacting point charges can now be constructed by direct integration over the forces. Consider a system consisting of a charged particle moving in the x direction in the vicinity of a current loop of radius ε centered at the origin (figure 3.5).

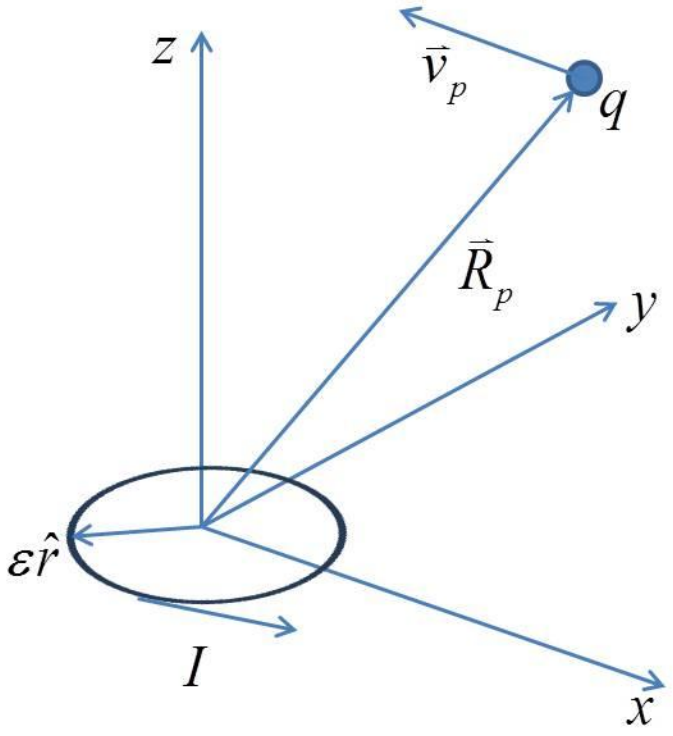

Figure 3.5

The Mott-Schwinger System

The coordinate system for the analysis of a charged particle interacting with a current loop (see text) is given.

$\vec{R}_q = \left(x_q, y_q, z_q\right)$ is the position of the charged particle relative to the center of the loop, q is the charge, $\vec{v}_p$ is the velocity of the particle, and I is the current. The force on the current loop due to the charged particle in the limit $\varepsilon \to 0$ is

$$\vec{F}_\mu = \frac{1}{c}\int \vec{J} \times \vec{B} d\tau = \frac{\mu q v_q}{c R_q^3}\left[\frac{3\left(x_q y_q \hat{x} + y_q^2 \hat{y} + y_q z_q \hat{z}\right)}{R_q^2} - \hat{y}\right]. \qquad (20)$$

The force on the moving charge due to the current loop is

$$\vec{F}_q = \frac{q}{c}\vec{v}_q \times \vec{B} = \frac{\mu q v_q}{c R_q^3}\left[\frac{3\left(z_q^2 \hat{y} - y_q z_q \hat{z}\right)}{R_q^2} - \hat{y}\right], \tag{21}$$

where the magnetic moment is denoted by μ. Note that the forces are not equal and opposite after integration and thus total mechanical momentum is not conserved similar to the Feynman paradox. The same procedure will now be followed for the Aharonov-Bohm and Aharonov-Casher systems (figure 3.1c and 2.1d).

2.2.3. Aharonov-Bohm and Aharonov-Casher systems

The forces involved in the Aharonov-Bohm (figure 3.1c) and Aharonov-Casher (figure 3.1d) systems can be determined by integration of the forces obtained for the loop/charge. For the A-B system the connection between the loop magnetic moment and the solenoid is made by substituting a differential magnetic moment element of the solenoid for the magnetic moment of the current loop:

$$\vec{\mu} \to \frac{c\Phi_B}{4\pi}\hat{z}dz_\mu, \tag{22}$$

where Φ_B is the magnetic flux in the solenoid. The charged particle is assumed to move in the x-direction. By integrating equation (21) the force on the charged particle is

$$\vec{F}_q = \int_{solenoid} d\vec{F}_q = 0. \tag{23}$$

This is obvious given that the particle is propagating through a region where there are no electric or magnetic fields. By integrating equation (20) the force on the solenoid is

$$\vec{F}_s = \int_{solenoid} d\vec{F}_\mu = \frac{q\phi_B v_q}{2\pi}\left\{\frac{2\left(x_q - x_s\right)\left(y_q - y_s\right)\hat{x} - \left[\left(x_q - x_s\right)^2 - \left(y_q - y_s\right)^2\right]\hat{y}}{\left[\left(x_q - x_s\right)^2 + \left(y_q - y_s\right)^2\right]^2}\right\}. \tag{24}$$

For the A-C system the connection between charged particle and the wire was made by substituting a differential charge element of the wire for the charge of the particle:

$$q \to \lambda dz_q \,. \tag{25}$$

By integrating equation (21) the force on the wire is

$$\vec{F}_w = \int_{wire} d\vec{F}_q = 0 \tag{26}$$

and by integrating equation (20) the force on the current loop is

$$\vec{F}_\mu = \int_{wire} d\vec{F}_\mu = \frac{2\lambda\mu v_w}{c}\left\{\frac{2\left(x_w - x_\mu\right)\left(y_w - y_\mu\right)\hat{x} - \left[\left(x_w - x_\mu\right)^2 - \left(y_w - y_\mu\right)^2\right]\hat{y}}{\left[\left(x_w - x_\mu\right)^2 + \left(y_w - y_\mu\right)^2\right]^2}\right\}. \tag{27}$$

As stated in the introduction it is unreasonable to describe the motion of constituents of a neutron as unconstrained during the typical interaction times for A-C experiments. Moreover, the above simplistic reasoning foregoes the interesting physics that underlies the understanding of the neutron's magnetic moment as the sum of the magnetic moment of its parts and dynamics[21]. Nevertheless, for completeness in our present argument, the unconstrained model is considered in the context of the A-C physical system, and hopefully highlights the disparity in the nature of the solenoidal versus the neutron's magnetic moment. In this point of view Aharonov and Casher's realization that a neutron passing by a charged wire accumulates a phase shift that can be interpreted as the reciprocal of the A-B effect is both beautiful and surprising.

In each of these systems one object feels a force while the other does not. This again is a system which exhibits the qualitative feature of the underlying Feynman system that total mechanical momentum is not conserved.

2.3. Constrained motion

In the following sections the integrated Lagrangian will be used to obtain the equations of motion for the Mott-Schwinger, A-B and A-C systems. The derivatives in the Euler Lagrange equation will be made with respect to coordinates that describe the motion of complete objects, such as the current loop in the Mott-Schwinger system. This constrains the motion of the charge elements in the loop to experience the same acceleration.

2.3.1. Integration of the Lagrangian

An alternative to the unconstrained method of analysis described above for the Mott-Schwinger system (figure 3.1b) is the approach of assuming that the charge elements within the loop are fixed relative to one another and must accelerate identically along with a coordinate defining the location of the loop. This can be done by two possible methods. By the first method, the vector potential of the moving charge, appropriate for the Darwin Lagrangian, is taken to determine the resulting magnetic field. The vector potential and magnetic field of the moving charge are

$$\vec{A}_q = \frac{q}{2rc}\left[\vec{v}_q + \frac{\vec{r}\left(\vec{v}_q \cdot \vec{r}\right)}{r^2}\right] \tag{28}$$

$$\vec{B}_q = \vec{\nabla} \times \vec{A}_q = \frac{q}{c}\frac{\vec{v}_q \times \vec{r}}{r^3}\,. \tag{29}$$

The magnetic and electric fields are coupled to the magnetic dipole and relativistic electric dipole to obtain the Lagrangian

$$L = \frac{1}{2}m_q v_q^2 + \frac{1}{2}m_\mu v_\mu^2 + \vec{\mu}\cdot\vec{B} + \vec{d}\cdot\vec{E}$$

$$= \frac{1}{2} m_q v_q^2 + \frac{1}{2} m_\mu v_\mu^2 + \frac{q}{c} \frac{\vec{\mu} \cdot \left[\vec{v}_q \times \left(\vec{r}_\mu - \vec{r}_q \right) \right]}{\left| \vec{r}_\mu - \vec{r}_q \right|^3} + \frac{q}{c} \frac{\left(\vec{v}_\mu \times \vec{\mu} \right) \cdot \left(\vec{r}_\mu - \vec{r}_q \right)}{\left| \vec{r}_\mu - \vec{r}_q \right|^3}$$

$$= \frac{1}{2} m_q v_q^2 + \frac{1}{2} m_\mu v_\mu^2 + \frac{q}{c} \frac{\left(\vec{v}_\mu - \vec{v}_q \right) \cdot \left[\vec{\mu} \times \left(\vec{r}_\mu - \vec{r}_q \right) \right]}{\left| \vec{r}_\mu - \vec{r}_q \right|^3}. \tag{30}$$

The second method is integration of the vector potential over the charges in the current loop. Integration of the vector potential (equation (23)) as it appears in the Darwin Lagrangian (equation (3)) for a current loop with no net charge gives

$$\vec{A}_\mu = \frac{\vec{\mu} \times \vec{r}}{r^3} \tag{31}$$

$$\varphi_\mu = \frac{1}{c} \vec{v}_\mu \cdot \vec{A}_\mu = \frac{\vec{v}_\mu \cdot \left(\vec{\mu} \times \vec{r} \right)}{cr^3}. \tag{32}$$

Coupling these potentials to the point charge gives the Lagrangian

$$L = \frac{1}{2} m_q v_q^2 + \frac{1}{2} m_\mu v_\mu^2 + \frac{q}{c} \vec{v}_q \cdot \vec{A}_\mu - q\varphi_\mu$$

$$= \frac{1}{2} m_q v_q^2 + \frac{1}{2} m_\mu v_\mu^2 + \frac{q}{c} \frac{\vec{v}_q \cdot \left[\vec{\mu} \times \left(\vec{r}_q - \vec{r}_\mu \right) \right]}{\left| \vec{r}_q - \vec{r}_\mu \right|^3} - \frac{q}{c} \frac{\vec{v}_\mu \cdot \left[\vec{\mu} \times \left(\vec{r}_q - \vec{r}_\mu \right) \right]}{\left| \vec{r}_q - \vec{r}_\mu \right|^3}$$

$$= \frac{1}{2} m_q v_q^2 + \frac{1}{2} m_\mu v_\mu^2 + \frac{q}{c} \frac{\left(\vec{v}_\mu - \vec{v}_q \right) \cdot \left[\vec{\mu} \times \left(\vec{r}_\mu - \vec{r}_q \right) \right]}{\left| \vec{r}_\mu - \vec{r}_q \right|^3}. \tag{33}$$

These two methods give the same result due to the symmetry under permutation of particles of the Darwin Lagrangian and therefore only one should be taken for the computation of the equations of motion to avoid double counting. Applying the Euler-Lagrange equations gives

$$\frac{d}{dt} \frac{\partial L}{\partial \vec{v}} - \frac{\partial L}{\partial \vec{r}} = 0 \tag{34}$$

$$m_\mu \vec{a}_\mu = -\frac{q}{c}\left\{\frac{\left(\vec{v}_\mu - \vec{v}_q\right)\times\vec{\mu}}{\left|\vec{r}_\mu - \vec{r}_q\right|^3} + \frac{3\left[\left(\vec{r}_\mu - \vec{r}_q\right)\cdot\vec{\mu}\right]\left[\left(\vec{r}_\mu - \vec{r}_q\right)\times\left(\vec{v}_\mu - \vec{v}_q\right)\right]}{\left|\vec{r}_\mu - \vec{r}_q\right|^5}\right\} \tag{35}$$

$$m_q \vec{a}_q = \frac{q}{c}\left\{\frac{\left(\vec{v}_\mu - \vec{v}_q\right)\times\vec{\mu}}{\left|\vec{r}_\mu - \vec{r}_q\right|^3} + \frac{3\left[\left(\vec{r}_\mu - \vec{r}_q\right)\cdot\vec{\mu}\right]\left[\left(\vec{r}_\mu - \vec{r}_q\right)\times\left(\vec{v}_\mu - \vec{v}_q\right)\right]}{\left|\vec{r}_\mu - \vec{r}_q\right|^5}\right\}. \tag{36}$$

These forces are equal in magnitude and opposite in direction and thus conserve total mechanical momentum. Therefore this cannot be characterized as a Feynman type paradox.

The forces acting on the individual components of the A-B (figure 3.1c) and A-C (figure 3.1d) systems can be determined by integrating the Mott-Schwinger Lagrangian (equation (30) or (33)). The Lagrangian obtained for the A-B system is

$$L = \frac{1}{2}m_s v_s^2 + \frac{1}{2}m_q v_q^2 + \frac{q\Phi_B}{2\pi}\frac{\left(\vec{v}_q - \vec{v}_s\right)\cdot\left[\hat{z}\times\left(\vec{r}_q - \vec{r}_s\right)\right]}{\left(x_q - x_s\right)^2 + \left(y_q - y_s\right)^2} \tag{37}$$

$$= \frac{1}{2}m_q v_q^2 + \frac{1}{2}m_s v_s^2 + \frac{q}{c}\left(\vec{v}_q - \vec{v}_s\right)\cdot\vec{A}_s. \tag{38}$$

Likewise, the Lagrangian obtained for the A-C system is

$$L = \frac{1}{2}m_\mu v_\mu^2 + \frac{1}{2}m_w v_w^2 + \frac{2\lambda}{c}\frac{\left(\vec{v}_w - \vec{v}_\mu\right)\cdot\left[\vec{\mu}\times\left(\vec{r}_w - \vec{r}_\mu\right)\right]}{\left(x_w - x_\mu\right)^2 + \left(y_w - y_\mu\right)^2} \tag{39}$$

$$= \frac{1}{2}m_\mu v_\mu^2 + \frac{1}{2}m_w v_w^2 + \frac{1}{c}\left(\vec{v}_\mu - \vec{v}_w\right)\cdot\left(\vec{\mu}\times\vec{E}_w\right). \tag{40}$$

In both cases application of the Euler-Lagrange equations of motion gives zero force acting on both elements of both the A-B and A-C systems.

The predictions for the unconstrained motion are very different from the predictions of the constrained motion (the latter coinciding with generally accepted one).

Can these two methods be distinguished by comparing their predicted phase shifts to the experimentally measured phase shifts?

3. Quantum mechanical phase shifts

3.1. Constrained

To compute the quantum mechanical phase shift for the charged particle and the neutron in the A-B and A-C effects, respectively, a closed loop path integral over time is taken for the Lagrangian described for constrained motion. The phase for the constrained case is the generally accepted one and only a brief summary is given in this section. In these calculations the charged wire and the solenoid are taken to be stationary ($v_w = v_s = 0$). Using the Lagrangian given by equation (38) the A-B phase is

$$\varphi_{AB} = \frac{1}{\hbar}\oint\left(\frac{1}{2}m_q v_q^2 + \frac{q}{c}\vec{v}_q \cdot \vec{A}_s\right)dt = \frac{q\Phi_B}{\hbar c}, \tag{41}$$

which has been experimentally verified[10,22-24]. Using the Lagrangian given by equation (40) the A-C phase is

$$\varphi_{AC} = \frac{1}{\hbar}\oint\left(\frac{1}{2}m_\mu v_\mu^2 + \frac{1}{c}\vec{v}_\mu \cdot \left(\vec{\mu}\times\vec{E}_w\right)\right)dt = \frac{4\pi\lambda\mu}{\hbar c}. \tag{42}$$

In either case the first term in the Lagrangian, ($mv^2/2$), does not contribute to the phase. There is no force acting on the charged particle or the neutron and the effects are true A-B effects. An experimental test of the Aharonov-Casher effect by Werner *et al.*[6] is in agreement with the standard quantum mechanical prediction, where the experimental to theoretical ratio is given by $\varphi_{AC}^E / \varphi_{AC}^T = 1.46 \pm 0.35$.

3.2. Unconstrained

In the path integral formulation[25] the wavefunction is propagated with the kernel, $K(b,a)=\exp\left(\frac{i}{\hbar}\int_{t_a}^{t_b} L dt\right)$, where L is the classical Lagrangian. For a free particle the Kernel is $\exp\left(\frac{i}{\hbar}\int \vec{p}\cdot d\vec{r}\right)$, where $p=mv$. Formally, the initial wave function should now be constructed and propagated. However, for the purpose of understanding the measured phase shift in an interferometer it is customary to consider the effect on plane waves. In this case the phase shift is given by $\frac{1}{\hbar}\int_{t_a}^{t_b} L dt=\frac{1}{\hbar}\int_{t_a}^{t_b}(p\dot{x}-H)dt$, where p is the canonical momentum $p=mv+qA$. In the case that the Hamiltonian is time independent the phase shift becomes $\frac{1}{\hbar}\int_{x_a}^{x_b}\vec{p}\cdot d\vec{x}$ [26].

For unconstrained motion in the case of the A-B effect the phase may therefore be written as follows

$$\varphi_{total}=\frac{1}{\hbar}\int \vec{p}\cdot d\vec{x}=\frac{1}{\hbar}\int\left(m\vec{v}+\sum q\vec{A}_j\right)\cdot d\vec{x}$$

$$=\frac{1}{\hbar}\int\left(m\vec{v}+q\sum\vec{A}_j\right)\cdot d\vec{x}=\frac{1}{\hbar}\int\left(m\vec{v}+q\vec{A}_s\right)\cdot d\vec{x} \qquad (43)$$

where $\vec{A}_s$ is the vector potential generated by the solenoid and $\vec{A}_j$ is the vector potential generated by the charges that constitute the solenoid. This is identical to the phase integral for the A-B effect in the case of constrained motion.

In the case of the A-C effect considering unconstrained motion as argued above is unreasonable. However, the existence of a larger particle with a magnetic moment cannot be excluded. Such a particle may have constituents that are best described by

unconstrained motion. In our model, there are different forces acting on such constituents. How is the path integral phase shift defined for a composite object if the constituents experience different forces? The physical picture is that if the interaction does not lead to a change of the internal quantum states then the two arms of the interferometer remain indistinguishable. The measured phase shift reflects only the effect in the center of mass coordinate or external quantum state. If the internal quantum states do change then the contrast of the interferometer may be reduced. The initial wavefunction for an unconstrained composite particle with N mutually non-interacting constituents can be written as a product state of plane waves, $\psi_C = \prod_{j=1}^{N} \exp\left(i\,\vec{p}_j \cdot \vec{R}_j / \hbar\right)$.

The phase accumulated by each plane wave along a path is $\varphi = \frac{1}{\hbar}\int \vec{p} \cdot d\vec{x}$ and thus the phase of the composite wavefunction ψ_C picks up an overall phase factor of $\exp\left(\frac{i}{\hbar}\sum\int \vec{p}_j \cdot d\vec{x}\right)$. This phase factor may be rewritten in terms of the total force, $\vec{F}_{total}$, on the current loop as computed in section 2.2.3.,

$$\varphi_{total} = \frac{1}{\hbar}\sum\int \vec{p}_j \cdot d\vec{x} = \frac{1}{\hbar}\int\left(\sum \vec{p}_j\right)\cdot d\vec{x} = \frac{1}{\hbar}\int\left[\sum\left(\vec{p}_{0j} + \int \vec{F}_j dt\right)\right]\cdot d\vec{x}$$

$$= \frac{1}{\hbar}\int\left(\sum \vec{p}_{0j}\right)\cdot d\vec{x} + \frac{1}{\hbar}\int\left[\int\left(\sum \vec{F}_j\right)dt\right]\cdot d\vec{x}\,.$$

$$= \frac{1}{\hbar}\int\left(\sum \vec{p}_{0j}\right)\cdot d\vec{x} + \frac{1}{\hbar}\int\left[\int \vec{F}_{total} dt\right]\cdot d\vec{x} \qquad (44)$$

Note that the composite particle has no charge and the qA term does not contribute to the phase. Integration of the total force (equation (27)) along a straight path gives the total phase

$$\varphi_{total} = \frac{1}{\hbar}\int\left(\sum \vec{p}_{0j}\right)\cdot d\vec{x} + \frac{2\pi\lambda\mu}{\hbar c}\, sign\left(y_{\mu} - y_{w}\right). \tag{45}$$

The difference in phase between the two paths is $\Delta\varphi_{total} = \frac{4\pi\lambda\mu}{\hbar c}$, which is the appropriate AC phase shift. Thus the constrained and unconstrained method cannot be distinguished by inspecting the phase.

4. Comparison to previous analyses

4.1. Hidden momentum

The approach taken by Vaidman[17] as applied to the A-C system is one in which internal motion of the system manifest itself in "hidden momentum" which affects the motion of the neutron. The time derivative of this "hidden momentum" or the hidden force, as one may refer to it, is applied directly to the equation of motion

$$m\vec{a} = \frac{d\vec{p}}{dt} - \frac{d\vec{p}_{hid}}{dt}. \tag{46}$$

As mentioned above the justification for the use of the hidden momentum comes from a lemma that states that for stationary and finite current and charge distributions the total momentum is zero. A non-zero value of the electromagnetic field momentum than implies the presence of a hidden momentum of equal magnitude and opposite in direction:

$$\vec{p}_{hid} = -\frac{1}{c^2}\int \varphi\vec{J}d\tau = -\frac{1}{4\pi c}\int \vec{E}\times\vec{B}d\tau = -\vec{p}_{em}, \tag{47}$$

where φ is the electrostatic potential of the charged wire and $\vec{J}$ is the current density of the loop. The electric potential and current density result in an electric field $\vec{E}$ and

magnetic field $\vec{B}$, respectively. Thus the equation of motion explicitly depends on the change of the electromagnetic field momentum,

$$m\vec{a} = \frac{d\vec{p}}{dt} + \frac{d}{dt}\left[\frac{1}{4\pi c}\int \vec{E}\times\vec{B}d\tau\right]. \tag{48}$$

The equation of motion for a current loop in the Aharonov-Casher system (figure 3.1d) determined by direct application of this method is

$$m\vec{a} = \frac{d\vec{p}}{dt} - \frac{d\vec{p}_{hid}}{dt} = \vec{\nabla}\left(\vec{\mu}\cdot\vec{B}\right) - \frac{1}{c}\frac{d}{dt}\left(\vec{\mu}\times\vec{E}\right)$$

$$= -\frac{1}{c}\vec{\nabla}\left[\vec{\mu}\cdot\left(\vec{v}\times\vec{E}\right)\right] - \frac{1}{c}\frac{d}{dt}\left(\vec{\mu}\times\vec{E}\right)$$

$$= -\frac{1}{c}\left[\left(\vec{\mu}\cdot\vec{\nabla}\right)\left(\vec{v}\times\vec{E}\right) - \left(\vec{v}\cdot\vec{\nabla}\right)\left(\vec{\mu}\times\vec{E}\right)\right] - \frac{1}{c}\left(\vec{v}\cdot\vec{\nabla}\right)\left(\vec{\mu}\times\vec{E}\right)$$

$$= -\frac{1}{c}\left(\vec{\mu}\cdot\vec{\nabla}\right)\left(\vec{v}\times\vec{E}\right). \tag{49}$$

This acceleration is zero for the geometry of the Aharonov-Casher effect. Thus the force on both objects in the Aharonov-Casher system is zero, by this method.

However, for the Feynman paradox the equations of motion do not depend on the change of the electromagnetic field momentum. The inclusion of electromagnetic field momentum solves the paradox by offering a third physical entity that carries a changing momentum[5], while the forces on both objects are not zero, contrasting the Vaidman analysis of the Aharonov-Casher system. Why is there a difference between the two analyses? The reason is that the Feynman paradox concerns a physical system that is not a stationary charge distribution and the Lemma does not hold. The question for the A-C system is than if it is well represented by a stationary charge and current distribution. Clearly, the neutron passes by the charged wire and formally, the A-C system is not

represented by a stationary distribution. The result that our constrained description gives is the same as the Vaidman approach, while it is interesting to consider the unconstrained result in relation to the Feynman paradox.

4.2. Newton's third law

The approach taken by Boyer is documented in a series of papers that extend over several decades[13,14,27,28], and argue that the Aharonov-Bohm effects are accompanied by a force. This point of view conflicts the generally accepted interpretation of the A-B effect. We will limit ourselves to comment on two of the more recent papers in this series. Boyer considers a charged particle passing by a solenoid (represented by a line of magnetic dipoles) and calculates the Lorentz force on the solenoid[13]. This force is the same as that given in section 2.2.3 (equation (24)) and Boyer's work motivated that part of our calculation. Boyer continues his argument by invoking Newton's third law and noticing that the back-acting force on the electron causes a displacement that through a semi-classical argument gives exactly the Aharonov-Bohm phase shift. It is remarkable that such an argument can be given that provides exactly the necessary force, in view of the observation that an unperturbed solenoid has no external electromagnetic fields. The argument hinges on three assumptions. First the force on the solenoid is the total force that acts on the solenoid, second Newton's third law holds, and third the semi-classical approximation is valid. Our work shows that the total force on the solenoid depends on the presence or absence of constraints. Additionally, Feynman's paradox illustrates that Newton's third law is not generally valid. (Boyer argues in another paper in 2002 that the electromagnetic momentum is conserved during the interaction[13]). Finally it is interesting to note that Boyer's force is dispersionless, implying that the group velocity of a

wavepacket in a semiclassical approximation does not change. All these issues are interesting in their own right, and warrant further discussion. Additional forces in this context have been predicted to exist by Anandan[29,30].

In a paper that comments on our experimental demonstration of the absence of force for a charged particle passing a solenoid[14], Boyer argues that charged particles in a solenoid that mutually interact and experience friction can provide a back-action on the passing particle. This line of reasoning considers a model that is more complex than the ones considered previously and in this dissertation, because mutual interaction between the constituents of magnetic dipoles are excluded.

4.3. Hamiltonian approach

An analysis based on a Hamiltonian approach by Werner and Klein[6] has been done to determine the force on the neutron in the Aharonov-Casher system (figure 3.1d). The Hamiltonian used was

$$H = \frac{p^2}{2m} - \frac{1}{mc}\vec{\mu}\cdot\left(\vec{E}\times\vec{p}\right). \tag{50}$$

A direct application of Hamilton's equations of motion gives

$$\dot{\vec{r}} = \frac{\partial H}{\partial \vec{p}} \tag{51}$$

$$\dot{\vec{p}} = -\frac{\partial H}{\partial \vec{r}} \tag{52}$$

$$m\ddot{\vec{r}} = -\frac{1}{c}\left(\vec{\mu}\cdot\vec{\nabla}\right)\left(\vec{v}\times\vec{E}\right). \tag{53}$$

In the Aharonov-Casher geometry the electric field has no spatial dependence in the direction of the magnetic moment, therefore, the force on the neutron is zero, by the above prescription. Note that this approach does not describe a closed system as it is a

single particle Hamiltonian. Because this approach is that of an open system it does not address conservation of momentum. Thus, the criterium that total momentum must be conserved cannot be applied to this approach as a test of the validity of the Hamiltonian. Furthermore, this Hamiltonian is equivalent to our Lagrangian (equation (40)) for a stationary wire. Using the vector identity $(a\times b)\cdot c = a\cdot(b\times c)$ the equivalence is found:

$$L = \frac{1}{2}mv^2 + \vec{d}\cdot\vec{E} = \frac{1}{2}mv^2 + \frac{1}{c}(\vec{v}\times\vec{\mu})\cdot\vec{E} \tag{54}$$

$$\vec{p} = \frac{\partial L}{\partial \vec{v}} = m\vec{v} + \frac{1}{c}\vec{\mu}\times\vec{E} \tag{55}$$

$$H = \vec{p}\cdot\vec{v} - L = \frac{1}{2m}\left(\vec{p} - \frac{1}{c}\vec{\mu}\times\vec{E}\right)^2 \approx \frac{p^2}{2m} - \frac{1}{mc}\vec{p}\cdot(\vec{\mu}\times\vec{E}). \tag{56}$$

This Hamiltonian can thus be classified as describing a constrained system as described in section 2.3.1.

4.4. Aharonov and Rohrlich

In their 2005 book, "Quantum Paradoxes: Quantum Theory for the Perplexed", Aharonov and Rohrlich discuss various momentum terms that can make up for the changing momentum in the electromagnetic field and ultimately conserve momentum. The missing momentum is stated to be the relativistic momentum of the charged particles which give rise to the magnetic flux. The contribution of the Lorentz force to the momentum conservation is ignored. The statement that "We move it [passing particle] as slowly as we like, so that the charge scarcely induces a magnetic field…" does not address this issue. Although the magnetic field and thus the Lorentz force scale linearly with velocity, the momentum exchange is independent of velocity as the interaction time scale inversely with velocity. In this chapter it is shown that (in the unconstrained

description) the change of momentum due to the Lorentz force is identical in magnitude to the change of momentum in the electromagnetic field.

5. Conclusion

The relation between the Feynman paradox and the AB-effects is that an unconstrained treatment of the AB-effects share with the Feynman paradox the property that momentum is stored in the electromagnetic field during the interaction, and consequently that the forces on the two interacting mechanical parts of the system are not balanced. This implies that one part of the system experiences a force, which is a prediction that is in stark contrast with the usual understanding of AB-effects. In the constrained description the AB-effects are very different than the Feynman paradox. In this description, the usual prediction is made that both mechanical parts do not experience a force. Both of these scenarios are limited to the case that constituents that make up the magnetic moment are assumed not to interact. Given the limited theoretical scope of the theoretical claims, experiments are important. However, as we will indicate now, there are very few options within reach of present technology.

An experiment to test for the force on an electron in the Aharonov-Bohm system (figure 3.1c) has been conducted by our group (see Caprez *et al.*). In that experiment a time delay was measured for an electron passing between two solenoids[15]. The time required for the electron to pass from source to detector was found to be independent of the magnetic flux contained in the solenoids and thus it appears that the Aharonov-Bohm phase shift cannot be explained by a classical force on the electron. However, it has been pointed out that in this case a macroscopic solenoid was used and the qualitative characteristics of the system, such as whether or not there is a measurable delay,

potentially depend on the size of the solenoid[14]. For larger solenoids the interaction time is greater than the plasma oscillation period. This is the case for all experimental tests of the A-B effect so far, and as such the force experiment and phase experiments are performed in the same regime. The issue considered in this chapter is a different one. The above experiment does not discriminate between the unconstrained and constrained description.

For the Aharonov-Bohm system, an experiment to detect the predicted force on the solenoid (as predicted by the unconstrained model) appears impossible given the necessity to detect the force of a single electron on a macroscopic object.

Although experiments have been done to show the Aharonov-Casher phase shift, no experiments have tested for the presence of a force on the neutron. However, for the molecule Thallium Fluoride the phase shift was shown to be independent of velocity[31] which is a feature associated with the dispersionless nature of the A-B effect and provides a link to the absence of force[32-34]. The interaction between the applied electric field and the magnetic moment of the fluoride nucleus was responsible for the phase shift. Given the small size of a nucleus, or even an atom or molecule that may be used in such type of experiments, the circulation time for constituent charges that produce the magnetic moment is much less than the interaction time. It is likely then that the system must be modeled by constrained motion. Consequently, our present analysis would predict that there is, in fact, no force acting on the interfering particle, consistent with the Thallium Fluoride experiment.

Similarly, due to the small size of the neutron, the Mott-Schwinger effect for neutron scattering of nuclei is not a physical system that can provide an interesting test

between the constrained and unconstrained description. On the other hand if the magnetic moment is present in a physical system that has a size between that of a neutron and a solenoid, the unconstrained description may be appropriate while still allowing an observation of the motion of the magnetic moment. Even, this scenario is plagued with an additional difficulty. For a finite system of charge and current distribution the electric and magnetic fields must approach zero at large distances from the charges and currents. Consider a charge and current loop that scatter from each other. When the charge and current loop are far apart the electromagnetic field momentum tends to zero. The total mechanical momentum must thus be identical for the final and initial state and Newton's third law holds. These statements imply that there is no difference between the constrained and unconstrained approach as far as momentum exchange is concerned. This statement may appear to be at odds with our above argumentation, but is not. The result of the imbalance of forces, and the violation of Newton's third law during the interaction at close proximity of the two interacting parts of the system, is a displacement for the final states, not a momentum exchange. This is not a general property, but can be shown in the impulse approximation for our unconstrained (equation (20)) and constrained force (equation (35)) by integrating the force over time for a straight path. Effects that depend on the differential cross section, such as the Sherman function for the Mott-Schwinger effect, are thus not expected to depend on the effective constraint in such a classical treatment.

Although, testing of unconstrained forces for A-B systems appears to be out of reach, a test of the Feynman paradox may be possible with current technology. Such a test would provide the first demonstration of the violation of Newton's third law (as it

applies to the instantaneous conservation of mechanical momentum). Consider two electrons that are cross fired at each other. The capability to generate femtosecond electron pulses from nanoscale sources[35-37] gives control over the initial conditions of the trajectories that these electrons will follow. For electrons of about 1 keV energy the point of closest approach is on the order of microns. The capability to influence the motion of electrons in flight with a focused, pulsed laser may provide a means to make a "movie" of the electrons' trajectory. If momentum is stored in the electromagnetic field as Feynman states then controlling and monitoring both electron trajectories should reveal this behavior. Even with current technology, this is a major experimental challenge and perhaps explains why the Feynman paradox has never been demonstrated.

Chapter 4 – Do Dispersionless Forces Exist?

1. Introduction

The Aharonov-Bohm effect is well known because it is thought to establish that the vector potential can cause measurable effects even when the fields (and thus the forces) are zero. It thus elevates the relevance of the vector potential from being a helpful mathematical construct to that of having direct physical reality associated with it. To highlight this it is interesting to combine two experimental results. The first is the demonstration of the Aharonov-Bohm effect. Tonomura's experiment[2] is not the first to do this, but certainly one of the most elegant ones. The second is the demonstration that forces are absent.[3]

An opposing view on the Aharonov-Bohm effect was provided in the previous decade. A force was proposed to explain the Aharonov-Bohm effect.[4] The *x*-component of the Lorentz force on the solenoid with cross-sectional area A and magnetic field B_0 is given by the expression

$$F_{sol}^{x} = \frac{B_0 A v_0}{4\pi c} \frac{4 x_e y_e}{\left(x_e^2 + y_e^2\right)^2}, \tag{1}$$

where v_0 is the electron velocity along the *x*-direction and x_e and y_e are the *xy*-coordinates of the charge relative to the solenoid's *z*-axis. The supposed back-action force of the solenoid on the electron provided by Newton's third law can be integrated to yield a relative displacement between electrons passing on opposite sides of the solenoid of $\Delta x = eB_0 A/mv_0$. In a semi-classical approximation $\Delta\varphi = k\Delta x$. This phase turns out to be equal to the well-known Aharonov-Bohm phase shift $\Delta\varphi = eB_0 A/\hbar$. It should be emphasized that the fact that such a force can be formulated at all, is very surprising in

view of the generally accepted interpretation of the effect. The proposed force was predicted to give rise to a time delay for electrons passing by a solenoid. This time delay was shown experimentally not to occur in the second experiment mentioned above and thus it may appear that this discussion is over. It is the purpose of this chapter to revisit that apparent conclusion.

2. Statement of the problem

To start the discussion it may be useful to delineate between the classical, semi-classical and quantum-mechanical parts of the predictions. In the classical description it is noted that the force (1) has components along the direction of motion and thus may cause a time delay as compared to the free electron's motion. The delay can be estimated by making the impulse approximation. This means that we assume that the change in velocity is small compared to the electron's initial velocity v_0 and compute the displacement Δx. The semi-classical part consists of guessing what the associated phase shift is. A reasonable guess would be the use the phase factor e^{ikx} associated with a plane wave and assume that this factor changes by $e^{ik\Delta x}$. The quantum mechanical part is most readily attained by using the path integral approach and the phase shift accumulated over the electron's path as it passes by a solenoid is calculated as

$$\Delta\varphi_{AB} = \frac{e}{\hbar}\int_C \vec{A}\cdot d\vec{l} = \frac{e}{\hbar}\int \vec{B}\cdot d\vec{S}. \qquad (2)$$

At this point it may appear convenient to simply rely on the fact that quantum mechanics is a superior theory, encompasses classical mechanics, and ignore the classical and semi-classical arguments. Such a convenient argument would neither do justice to the

correspondence principle nor to the main reason why the A-B effect is famous as pointed out above. The question remains how to deal with classical forces in a quantum mechanical context.

2.1. Classical-Quantum deflection in a magnetic field

To answer this question it is perhaps useful to consider the simple deflection of an electron passing through a homogeneous magnetic field. Classical mechanics provides an answer that agrees with observation. Consider an electron entering a region with a homogeneous magnetic field (Figure 4.1). The electron's velocity v is at right angle with the magnetic field. The classical deflection angle θ is given by

$$\theta = \Delta v / v = qvB\Delta t / mv = qBL / mv.$$

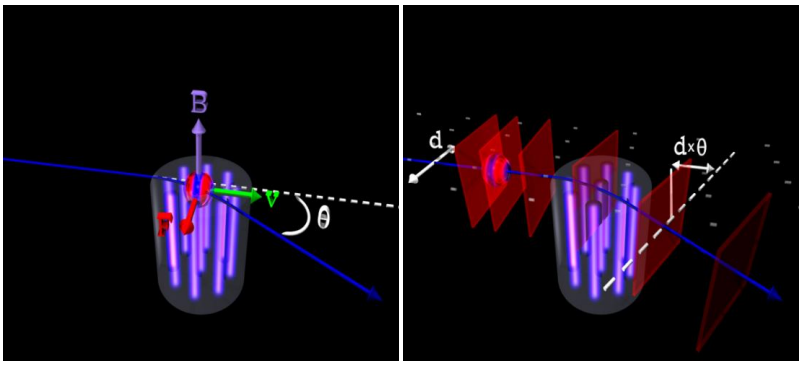

Figure 4.1

Deflection of Electrons in a Magnetic Field

Left: Electrons deflect by an angle θ after travelling through a region of space with a homogeneous magnetic field *B* and experiencing a Lorentz force *F*. Right: An electron wave accumulates a spatially dependent phase shift after travelling through a region of space with a spatially dependent vector potential. This deflects the electron wave by an angle θ.

Associated with the electron is a quantum mechanical wave. For a plane wave in free space the wave planes are at right angles to the direction of motion of the electron. If

the planes of the wave tilt then the electron is deflected. Consider planes of constant phase of the wave while propagating through the homogeneous magnetic field.

The phase difference φ accumulated over the width *d* of a section of a plane wave, determines the tilt of the wavefront. The Lagrangian is given by $L = 1/2\, m_e \dot{\vec{x}}^2 + q\vec{A}\cdot\dot{\vec{x}}$. The phase shift is $\varphi = 1/\hbar \int L dt = 1/\hbar \int qA dy \approx qAL/\hbar$ for a vector potential that corresponds to a homogeneous magnetic field $A_y = \int B_z dx \approx B_z \Delta x = B_z d$ in the z-direction. A wavefront section with a width *d* tilts by an angle $\theta = \left(\lambda_{dB}\varphi/(2\pi)\right)/d$, where λ_{dB} is the electron's de Broglie wavelength. This can be rewritten as $\theta = \Delta L/d = \left(\lambda_{dB}\varphi/(2\pi)\right)/d = \left(\lambda_{dB}\left(qB_z dL/\hbar\right)/(2\pi)\right)/d = qB_z L/mv$ and it is clear that the quantum and classical deflection are identical. In other words, the quantum-classical correspondence demands the presence of the phase shift.

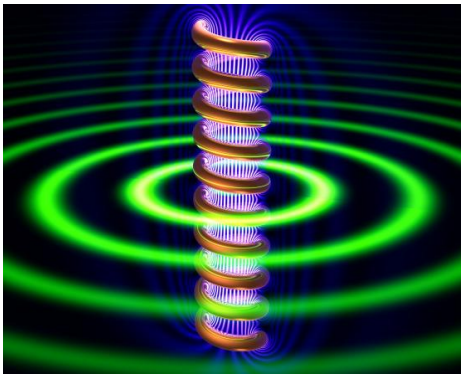

Figure 4.2

Magnetic Field and Vector Potential of a Solenoid

An example of a current carrying solenoid with magnetic field lines (blue) and equi-(vector) potential lines (green) (see also cover article of reference[1] .

The phase shift can be generalized for an arbitrary path to $\varphi = 1/\hbar \int q\vec{A} \cdot d\vec{l}$. For a closed path this is the A-B phase shift $\varphi = 1/\hbar \int_C q\vec{A} \cdot d\vec{l}$. Thus it can be said that the deflection of a charged particle in a magnetic field is caused by the A-B phase shift. This should not be confused with the A-B effect which occurs when paths are considered through regions of space where the magnetic field is zero as would be the case when the solenoid in figure 4.2 would be extended in length to infinity. Returning to the main question, one should note that although the identical classical and quantum prediction may be pleasing this should not be mistaken for the classical quantum correspondence.

2.2. Classical-Quantum correspondence

The correspondence principle demands that there is some limiting procedure by which one can recover from the quantum mechanical description the classical description. It is traditional to associate large quantum numbers or physically large systems with such a limit.[5] The textbook observation that Gaussian wave packets for particles of macroscopic mass (associated with large systems) have immeasurable small position and velocity spread is correct but does not represent an appropriate classical limit, after all, a wave packet for a large mass particle could still interfere with itself (in an interferometer type arrangement) and exhibit quantum mechanical behavior. Thus one would not expect a large mass to present a truly appropriate classical limit. Instead the capability to interfere must be removed. But what is the detailed description of this coherence removal? One could add an overall random phase factor to the wave packet, or one could instead add a random phase factor to each frequency component. Both modifications approach the classical limit in that the particle loses the capability to interfere with itself, but more than one choice is possible. One could attempt to describe the detailed

underlying interaction with the environment. For example, large molecules lose their capability to interfere with themselves by interaction with a thermal background providing evidence for decoherence theory as a means to connect the quantum and classical world. This has been demonstrated in a beautiful controlled coherence experiment by the Arndt group in Vienna.[6] In this experiment it is thought that thermal excitations of internal molecular quantum states and thermal emission make the arms of the interferometer (in principle) distinguishable and thus taking a partial trace over the environment removes coherence. In the present context of the discussion of what types of forces exist, it is the external quantum states that are relevant. In the next section the problem of coherence is defined mathematically at a basic level.

3. Complete Coherence and Incoherence

Suppose we would like to experimentally test that quantum mechanics correctly describes a free particle. A short pulse could be made and its propagation studied. It is sufficient to investigate the propagation of two frequency components. Consider two plane waves of equal amplitude propagating along the positive *x*-axis with velocities $v+\Delta v$ and $v-\Delta v$. The wavefunction can be written as the sum of the two frequency components,

$$\psi(x,t)=\psi_{E_1}(x,t)+\psi_{E_2}(x,t)$$

$$=\frac{1}{2}\sqrt{2}e^{i\left(\frac{2\pi m(v-\Delta v)}{h}x-\frac{\pi m(v-\Delta v)^2}{h}t\right)}+\frac{1}{2}\sqrt{2}e^{i\left(\frac{2\pi m(v+\Delta v)}{h}x-\frac{\pi m(v+\Delta v)^2}{h}t\right)} \quad (3)$$

This wavefunction can be rewritten as the product of the frequency carrier and the envelope,

$$\psi(x,t)=\frac{1}{2}\sqrt{2}e^{i\left(\frac{2\pi m(v)}{h}x-\frac{\pi m(v)^2}{h}t\right)}\left(e^{i\left(\frac{2\pi m\Delta v}{h}(x-vt)+O((\Delta v)^2\right)}+e^{i\left(\frac{2\pi m\Delta v}{h}(x-vt)+O((\Delta v)^2\right)}\right), \quad (4)$$

where the former has a phase velocity of *v*/2 and the latter travels at the group velocity of *v*, but only when the two components are coherently added. The probability distribution $\psi^*(x,t)\psi(x,t)$ follows the group velocity according to $x=vt,$ in "correspondence" with the classical prediction. Such an argument can be generalized to a wave packet. If an interaction causes a phase shift that affects each frequency (or equivalently velocity) component in the same way; $\psi(x,t)=\psi_{E_1}(x,t)e^{i\varphi}+\psi_{E_2}(x,t)e^{i\varphi},$ then (3) and (4) are only modified by an overall phase factor that does not change the probability distribution. Thus dispersionless interactions do not cause a deviation from the classical path; hence we can state that a dispersionless interaction is associated with the absence of force.

If we assume that an underlying physical decoherence process removes all coherence then we can construct a density matrix and add $\psi_{E_1}(x,t)$ and $\psi_{E_2}(x,t)$ completely incoherently in an attempt to take a classical limit:

$$\rho=\left|\psi_{E_1}(x,t)\right\rangle\left\langle\psi_{E_1}(x,t)\right|+\left|\psi_{E_2}(x,t)\right\rangle\left\langle\psi_{E_2}(x,t)\right|. \quad (5)$$

Rewriting the density matrix as a product of the carrier wave and its envelope is now not possible. Instead we can calculate how the expectation value of the position propagates in time. The result is ill-defined because the expectation value for plane waves is ill-defined. This very basic simple step failed, and serves to illustrate that taking classical limits may be hard with and even without forces. Perhaps, we should not care about the correspondence principle and only demand that our best theory matches our experimental outcomes, and not that it should first match a presumably worse theory. So,

let's next attempt to circumvent the classical limit and simply calculate the velocity dependence of the phase shift in the absence of force and when the force given by (1) is present.

4. Velocity dependent Phase shift with and without Forces

Using the path integral formulation of quantum mechanics, the phase shift is given by

$$\varphi = 1/\hbar \int L dt = 1/\hbar \int (1/2\, m_e \dot{\vec{x}}^2 + q\vec{A}\cdot\dot{\vec{x}}) dt, \tag{6}$$

where the integral is to be taken along a classical path that starts at (x_A, t_A) and ends at (x_B, t_B). For a particle that travels along a classical path that is free from any force, this expression can be simplified to

$$\varphi_{free} = 1/\hbar \int (1/2\, m_e \dot{\vec{x}}\cdot + q\vec{A}\cdot) d\vec{x} = \frac{\pi(x_B - x_A)}{\lambda_{dB}} + 1/\hbar \int q\vec{A}\cdot d\vec{x}, \tag{7}$$

where the first term is similar to what is expected from the Huygens' principle for matter waves[7] except for a missing factor of two. It is straightforward to show that the factor of two can be recovered by considering only phase differences between paths that start and stop at the same time. The second term yields a phase that is velocity independent, and is thus dispersionless as expected.

For a particle that travels along a classical path that experiences a force given by (1), this expression has to be explicitly calculated. For the present discussion it will suffice to make a very crude approximation. Noting that the force is anti-symmetric under parity in x, a simple piecewise constant force (Figure 4.3) is considered that modifies the velocity to $v - \Delta v$ when $x < 0$, and $v + \Delta v$ when $x > 0$.

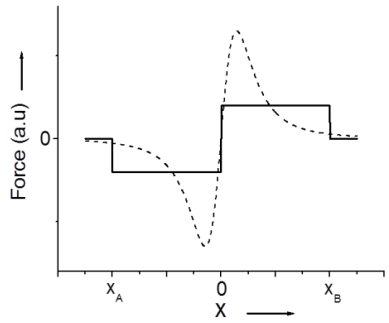

Figure 4.3

Lorentz Force on a Solenoid Due to a Passing Electron

The x-dependence of the force given by equation (1) is given (dashed line). A crude estimate (solid line) is used to estimate the phase dependence on velocity.

Further, consider a particle that starts at location $x_A = -L/2$ and ends at $x_B = L/2.$ In this case the phase shift can be approximated by

$$\varphi_{force} = \frac{\pi(0 - x_A)m(v - \Delta v)}{h} + \frac{\pi(x_B - 0)m(v + \Delta v)}{h} + 1/\hbar \int q\vec{A} \cdot d\vec{x}$$

$$= \frac{\pi(x_B - x_A)}{\lambda_{dB}} + 1/\hbar \int q\vec{A} \cdot d\vec{x}, \qquad (8)$$

which is identical to the phase shift for the free particle. The reason that the result with force is not the same as the semi-classical phase $e^{ik\Delta x}$ is caused by the demand that the path has the same start and stop time as in free particle case. A key feature of the force is that it is linear in the velocity itself, which results in a phase that is velocity independent. *In other words it appears possible to construct forces that are dispersionless.*

5. Approximately dispersionless

If the magnitude of the force is large in the sense that the change in velocity Δv is not small compared to the initial velocity v, then the demand that the start and end time should not change leads to dispersion. In specific, for the conditions

$(v-\Delta v_1)t_1+(v+\Delta v_2)t_2 = x_B - x_A$ and $t_1+t_2 = t_B - t_A$, the decrease in velocity for the region $x<0$ does not equal the increase in velocity in the region $x>0$. The result is that the cancelation of the Δv terms in (8) is removed, which results in a velocity dependent phase shift in (8). This leads to a time delay and it may be possible to falsify such a prediction experimentally with a refined version of the experiment reported in Ref. 3.

6. Summary and Conclusion

To identify if there is a force, one can measure a time delay of a pulse or a deflection of a beam of particles. This experimental definition appears to be very clear. But can we conclude that if there is no deflection or delay that no forces acted? This is not obvious. Nevertheless, that is the operational definition for the claim that the Aharonov-Bohm effect occurs in the absence of any force. A counter argument based on the non-zero force (1) is hard to rule out. In our first attempt to do so (section 3) by demanding that the correspondence principle should hold, we find that it is hard to find an appropriate classical limit. In our second attempt to rule out this force (section 4) it turns out to be dispersionless. However, dispersionless interaction is considered to be a defining property of the A-B effect. This leads to the question raised in the title: "Do dispersionless forces exist?" A potential way to resolve this issue presents itself when one realizes that the force is only dispersionless for small changes in velocity. A re-analysis of the experimental data for small delays may rule out the approximately dispersionless forces. A complicating factor for large changes in velocity is the issue to what extent decoherence and "the classical limit" can be avoided for such conditions.

Chapter 5 – Transverse Quantum Stern-Gerlach Magnets for Electrons

1. Introduction

Since Stern and Gerlach were able to separate the spin states of an unpolarized beam of silver atoms[1], one may ask, "Can the same experiment be done with electrons?" In the 1930 Solvay Conference, Bohr and Pauli rejected four proposals regarding the separation of spin states for free electrons. Pauli's claim was that "it is impossible to observe the spin of the electron, separated fully from its orbital momentum, by means of experiments based on the concept of classical particle trajectories"[2,3]. An argument against the splitting of a free electron beam with a Stern-Gerlach magnet is that Lorentz forces will blur the effect of the spin-splitting forces.

The implications of the Bohr and Pauli statement have found their way into many contemporary textbooks[4-9] and have been interpreted to imply that the construction of an electron Stern-Gerlach magnet is impossible. In this chapter I do not address Bohr and Pauli's dictum, but instead explore the possibility of an electron Stern-Gerlach magnet by considering *quantum trajectories*. That is, take advantage of the quantum mechanical nature of the electron to force it into a motional quantum state in which spin splitting is possible. Such an idea has already been put forth for the longitudinal Stern-Gerlach magnet, for which the spin-splitting is in the direction of motion[10]. For the longitudinal case the motion is appropriately described by Landau states. These purely quantum mechanical motional states can be used to sidestep the issue of blurring due to the magnetic forces[10]. However, the question whether a quantum mechanical transverse Stern-Gerlach magnet exists for electrons has to our knowledge never been addressed.

For the transverse case the spin splitting is at normal angles to the direction of propagation of the electron, just as it is for the usual silver atom case. A transverse electron Stern-Gerlach magnet may provide an alternative technique to the production of polarized electron beams as compared to the usual optically pumped Ga-As sources[11]. The existence of a tranverse Stern-Gerlach magnet (in addition to the earlier proposed longitudinal Stern-Gerlach magnet) addresses another of the four proposals rejected by Bohr and Pauli. This sheds insight on finding a currently unknown dictum such as: "It is possible to observe the spin of the electron, separated fully from its orbital momentum, by means of experiments based on the concept of *quantum* particle trajectories."

In this chapter our main focus is on the fundamental question if a transverse Stern-Gerlach magnet for electrons is possible in principle. To this end quantum mechanical motion is considered. The hallmark for quantum mechanical interference is that a final coherent state will be reached by at least two indistinguishable paths. The general idea is that along those paths a different spin dependent phase is applied to the electrons in each path. Upon recombination, a spin dependent interference pattern will form. The techniques proposed for beam separation are diffraction with a magnetic phase grating (section 2) and interferometry with controlled Aharonov-Bohm and magnetic phases (section 3).

2. Stern-Gerlach Diffraction

2.1. Magnetic Phase Grating

In Stern and Gerlach's original experiment a beam of Silver atoms was passed through a magnetic field gradient (Figure 5.1a).

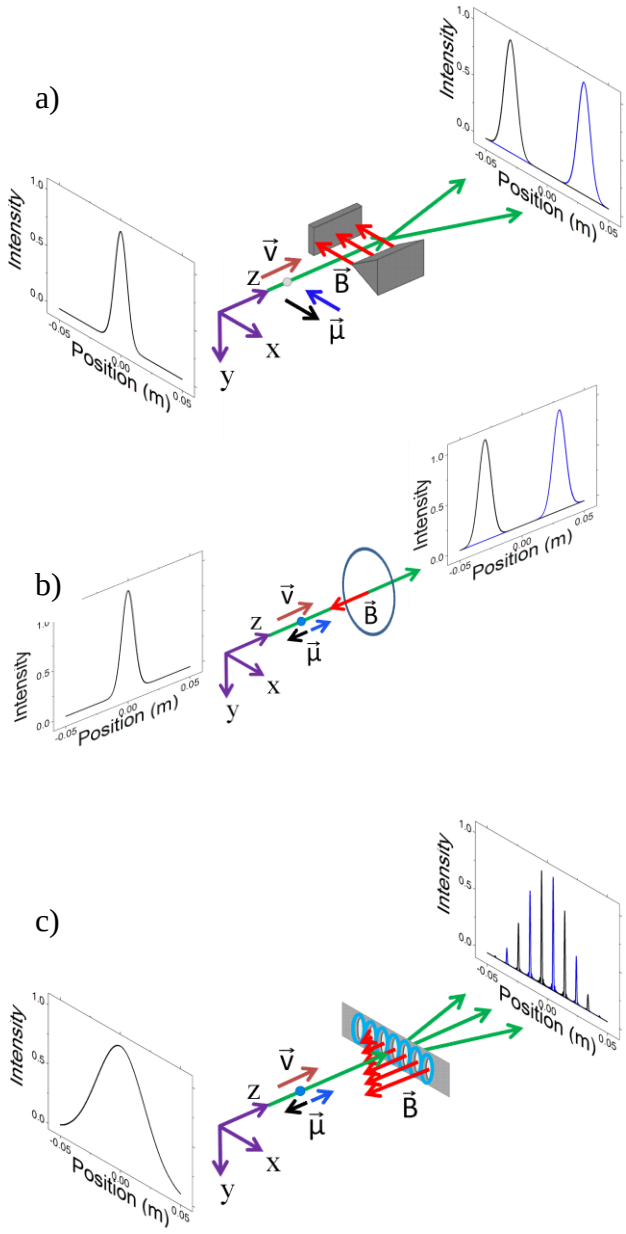

Figure 5.1

Stern-Gerlach Systems

a) In the original Stern-Gerlach experimental setup[1] a beam of silver atoms was split transversally to its direction of motion by an inhomogeneous magnetic field. b) The longitudinal Stern-Gerlach magnet, originally conceived by Brillouin[12] and criticized by Pauli[2,3], was reinstated by Batelaan and Gay[10,13]. Electrons passing through a current carrying loop obtain an additional spin dependent

phase due to the interaction energy of the magnetic moment of the electron and the magnetic field applied by the loop. Spin forward/backward electrons are delayed/advanced in an arrangement that is a longitudinal Stern-Gerlach magnet (i.e. the splitting is along the direction of motion). c) A Quantum mechanical transverse Stern-Gerlach magnet for electrons is proposed in this chapter. Current-carrying loops are placed in front of the slits of a grating in order to impart a phase on passing electrons which depends on the spin of the electrons as well as which slit they pass through. This causes the diffraction peaks for spin forward to be shifted oppositely to spin backward peaks, transverse to the direction of motion.

The magnetic moments $\vec{\mu}$ of the atoms were directed transverse to the electron velocity $\vec{v}$ and (anti-)parallel to the magnetic field $\vec{B}$. The resulting classical motion of the atoms is governed by the interaction between the quantized spin and magnetic field. The outcome is a beam that has been fully separated according to spin state.

For electrons the original Stern-Gerlach arrangement would not work due to strong Lorentz forces. Brillouin proposed to use a longitudinal field (Figure 5.1b) so that Lorentz forces could be neglected[12]. Pauli noted that although the spin states will be pushed apart by the inhomogeneous field of the Stern-Gerlach magnet, they will be blurred by a Lorentz force as a result of the gradient in the magnetic field orthogonal to the gradient which is necessary for the splitting of the spins in the first place. The presence of the orthogonal field gradient is a consequence of Maxwell's equation that dictates that the divergence of the magnetic field be zero. Batelaan *et al.*[13] found a mistake in Pauli's proof, but an analysis based on classical trajectories (with Landau state initial conditions) showed that the effect of Lorentz forces and spin forces were at best of the same strength, in keeping with the dictum of Bohr and Pauli. However, a fully quantum mechanical analysis[10], found that complete spin splitting is indeed possible due

to quantization of orbital motion of Landau states. This scheme works when the width of the diffraction limited electron beam is matched to the width of the lowest Landau state.

The new physical arrangement that discussed in this section (Figure 5.1c), is electrons passing through a grating where the applied magnetic field for each grating slit can be controlled separately. The quantization axis is chosen along the direction of motion. The electron velocity is parallel to the applied magnetic fields to avoid Lorentz forces, as in Brillouin's case. The motion must be treated quantum mechanically given that diffraction is a quantum phenomenon.

Currents in each loop are chosen in such a way that the magnetic field increases from one loop to the next in a stepwise manner across the grating (Figure 5.1c). The magnetic field created by each loop induces a phase due to the $-\vec{\mu}\cdot\vec{B}$ interaction energy between the magnetic moment of the electron $\vec{\mu}$ and the applied field $\vec{B}$. This results in a phase shift for electrons that also increases in a stepwise manner. The phase shift difference for adjacent loops is chosen to be constant. The induced phase shifts for forward and backward spins are of opposite sign (Figure 5.2).

Diffraction has the following general features. If the phaseshift in each slit is spatially dependent and identical then the envelope is determined by that spatial dependence, while the individual diffraction peaks' shape and position is unaffected. If the phaseshift in each slit is spatially uniform but varies from slit to slit the diffraction envelope is unaffected but the diffraction peaks shift, transverse to the direction of motion. The latter applies to the described physical system, which I refer to as a "magnetic phase grating."

According to Feynman's path integral formalism of quantum mechanics[14], the phase accumulated by an electron as it propagates along a path is given by the time integral of the Lagrangian[5] divided by Planck's constant;

$$\varphi = \frac{1}{\hbar}\int\left(\frac{p^2}{2m} + \vec{\mu}\cdot\vec{B} + q\vec{v}\cdot\vec{A}\right)dt. \tag{1}$$

The phase shift due to p^2 (i.e. the first term in equation 1) equals $2\pi L/\lambda_{dB}$ in free space, where L is the length of the path and λ_{dB} is the deBroglie wavelength of the electrons. The phase due to the vector potential $\vec{A}$ (i.e. the third term in equation 1) is discussed in detail in section 2.2.

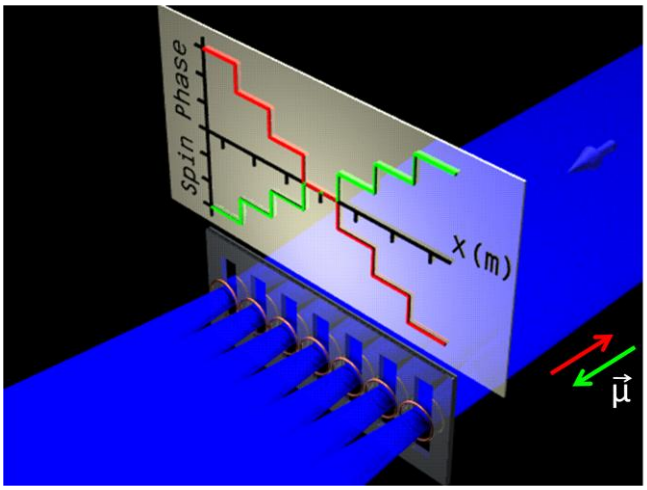

Figure 5.2

Magnetic Phase Grating

Electrons pass through current carrying loops just after diffracting from the grating. The loops impart a phase which is spatially dependent in a stepwise manner. Each increment on the vertical axis is a π/2 phase shift and each mark on the horizontal axis indicates the location of a slit.

The on-axis magnetic field for a loop of radius R [15] is

$$\vec{B} = B_0\frac{R^3}{\left(z^2+R^2\right)^{3/2}}\hat{z}, \tag{2}$$

where B_0 is the magnitude of the magnetic field at the center of the loop and $\hat{z}$ is directed along the axis. Performing the path integral over a straight trajectory along the $\hat{z}$ -axis gives a phase shift

$$\varphi(x) = \frac{1}{\hbar}\int_{-\infty}^{\infty} \vec{\mu}\cdot\vec{B}(x)\ dt = \pm\frac{\mu B_0 R^3 \sum_n H\left[x-\left(n-1/2\right)d\right]}{\hbar v_e}\int_{-\infty}^{\infty}\frac{1}{\left(z^2+R^2\right)^{3/2}}\ dz$$

$$= \pm 2\frac{\mu B_0 R \sum_n H\left[x-\left(n-1/2\right)d\right]}{\hbar v_e}, \tag{3}$$

where v_e is the electron velocity, μ is the electron's magnetic moment, d is the grating's period, $n = 0, \pm 1, \pm 2, \ldots$ labels the slit, and x is the coordinate parallel to the grating. The "$\pm$" sign in the second equality is due to considering spin up and down along the magnetic field direction. The Heaviside function $H(x)$ is used to get an increasing stepwise function. The amplitude modulation imposed by the grating to an incident plane wave is

$$A(x) = \frac{1}{N}\sum_n \left\{ H\left[x-\left(nd+\frac{1}{2}w\right)\right] + H\left[x-\left(nd-\frac{1}{2}w\right)\right]\right\}, \tag{4}$$

where w is the slit width and N the total number of slits. The wave function after interaction with the grating is $\psi_{grating} = A(x)e^{i\varphi(x)}$, where φ and A are given by equations 3 and 4. Using the path integral formulation the final quantum wave function at the detection plane is given by[16]

$$\psi_{detect}(x_d) = \int_{-\infty}^{\infty} K_{x_g \to x_d}\left(x_g, x_d\right)\psi_{grating}\left(x_g\right)dx_g, \tag{5}$$

where x_g and x_d are the position at the grating and the detector, respectively, $\psi_{grating}$ is the wave function immediately after the grating, and $K_{x_g \to x_d}$ is the free space propagator

$$K_{x_g \to x_d} = \exp\left[\frac{i2\pi}{\lambda_{dB}}\sqrt{\left(x_d - x_g\right)^2 + l^2}\right], \tag{6}$$

where λ_{dB} is the de Broglie wavelength and l is the distance from the grating to the detector. After the wave function is propagated the probability distribution is $P\left(x_d\right) = \left|\psi_{detect}\left(x_d\right)\right|^2$. Figure 5.3a, b, and c show diffraction patterns corresponding to increasing magnetic field strengths. The velocity of the electrons is chosen to be 10^5 m/s, the period of the grating is 200 nm, the slit width is 15 nm, there are 25 slits each with a magnetic coil, and the distance from the grating to the detector is 53 cm. The parameters are motivated by experiments[17] except for the very low electron velocity. For now, Lorentz forces are ignored and the magnetic field is assumed to be uniform over the area of each slit, to simplify the exposition of the basic idea.

For zero currents the electrons will simply diffract from the grating (Figure 5.3a). When the current is increased, the two spin components each separate into a comb of diffraction peaks (Figure 5.3b). For maximum spin separation, the necessary phase jump needed between adjacent slits is $\pi/2$ (Figure 5.3c). The result is a spin dependent displacement of the diffraction peaks within the diffraction envelope. The spin forward electrons are displaced in an opposite direction as compared to the spin backward electrons. The spin components are completely separated and motivate the nomenclature "Quantum Stern-Gerlach Magnet".

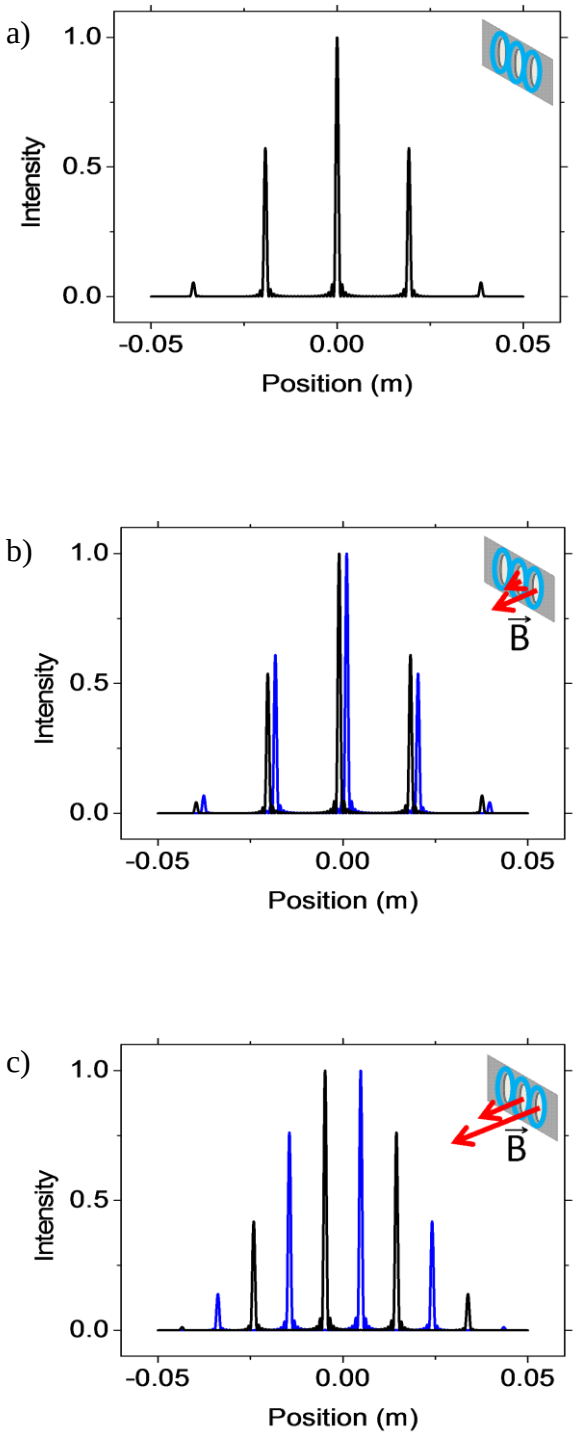

Figure 5.3

Spin Dependent Electron Diffraction Patterns at Varying Magnetic Field Strengths Without Lorentz Blurring

a) A familiar diffraction pattern is obtained when no magnetic field is applied. b) A diffraction pattern with resolvable spin splitting is shown, when the magnetic field increment for adjacent slits is 1.8T. c) A diffraction pattern is shown when the magnetic field increment is 8.5T which shows maximum splitting. The phase shift between neighboring slits is $\pi/2$.

It is interesting to compare the above scenario to a *blazed* magnetic phase grating (for a regular blazed grating see[18]) to the above discussed *stepped* magnetic phase grating. A blazed magnetic phase grating shifts the diffraction envelope in a spin dependent manner while leaving the peak position unaffected. The affected envelope is representative of the single slit diffraction pattern. Now the Bohr and Pauli argument applies directly; for a wide single slit where diffraction is small, the Lorentz force broadens the beam and overshadows the spin splitting. For a narrow single slit the Lorentz force can be reduced, but diffraction dominates the electron motion. Constructing a grating out of many such slits adds diffraction peaks, but as mentioned above, these are not affected by spin. Thus, any such blazed grating Stern-Gerlach scheme is doomed to fail as either Lorentz forces or diffraction dominate the spin splitting effect, not allowing for full separation of the spin states.

2.2. Lorentz blurring and spin flipping

Given that Lorentz blurring is at the heart of the argument set forth by Bohr and Pauli, it is important to include the Lorentz blurring in the calculation. In order to determine the effects of the Lorentz force, the phase accumulated along a path is computed for an electron passing through the current carrying loop (Figure 5.4a). (Note that the path is not assumed to be straight but the classical trajectory obtained from solving the equation of motion, as appropriate for the path integral). This phase can be

used in the path integral calculation to determine the effect of Lorentz blurring on the interference pattern. The phase was calculated as a function of initial position for the electrons along the x-axis (Figure 5.4b). The final value of spin phase (due to the $-\vec{\mu}\cdot\vec{B}$ term) and Lorentz phase (due to the $q\vec{v}\cdot\vec{A}$ term) are calculated separately. The equations of motion[15] used for these trajectories are

$$\frac{d\vec{v}}{dt}=\frac{q}{\gamma m}\left[\vec{E}+\vec{v}\times\vec{B}-\frac{1}{c^2}\vec{v}\left(\vec{v}\cdot\vec{E}\right)\right]+\nabla\left[\vec{\mu}\cdot\vec{B}+\frac{1}{c^2}\left(\vec{v}\times\vec{\mu}\right)\cdot\vec{E}\right]$$

$$\frac{d\vec{\mu}}{dt}=\frac{q}{m}\vec{\mu}\times\left[\left(\frac{g}{2}-1+\frac{1}{\gamma}\right)\vec{B}-\frac{1}{c^2}\left(\frac{g}{2}-1\right)\frac{\gamma}{\gamma+1}\vec{v}\left(\vec{v}\cdot\vec{B}\right)-\frac{1}{c^2}\left(\frac{g}{2}-\frac{\gamma}{\gamma+1}\right)\left(\vec{v}\times\vec{E}\right)\right] \qquad (7)$$

$$\gamma=\frac{1}{\sqrt{1-v^2/c^2}},$$

where $\vec{E}$ is electric field, g is the gyromagnetic ratio, and c is the speed of light. For our purposes $g=2$, $\gamma=1$, and $\vec{E}=0$ thus reducing the above equations to the following:

$$\frac{d\vec{v}}{dt}=\frac{q}{m}\vec{v}\times\vec{B}+\frac{1}{m}\nabla\left(\vec{\mu}\cdot\vec{B}\right)$$

$$\frac{d\vec{\mu}}{dt}=\frac{q}{m}\vec{\mu}\times\vec{B}. \qquad (8)$$

The vector potential used is

$$A_x=\frac{-B_0R^3y}{2\left(R^2+x^2+y^2+z^2\right)^{\frac{3}{2}}}$$

$$A_y=\frac{B_0R^3x}{2\left(R^2+x^2+y^2+z^2\right)^{\frac{3}{2}}}$$

$$A_z = 0, \tag{9}$$

which is a valid approximation to second order in the position coordinates near the axis of the coil[15]. Figure 5.4b and c are calculated for a B_0 value of 8.5 T (to get a phase shift of $\pi/2$ for an interaction time of 0.8 ns). For the calculation in figure 5.3 the spin phase is assumed to be uniform across each individual slit. This assumption is not used for the results in figure 5.4b and c. With initial conditions varying over a span of 15 nm, the spin forward and backward phase varies by less than 1%. It is apparent from figure 5.4b that the Lorentz phase will have a negligible influence on the spin splitting due to the fact that the difference in Lorentz phase accumulated by the two spin states is small compared to $\pi/2$. It does, however, have a parabolic shape. This is of little significance, though, as modulation of the shape of the phase in this way only effects the shape of the single slit envelope and leaves the position and width of the much narrower diffraction peaks unaltered thus in no way affecting the possibility of spin splitting (Figure 5.4c).

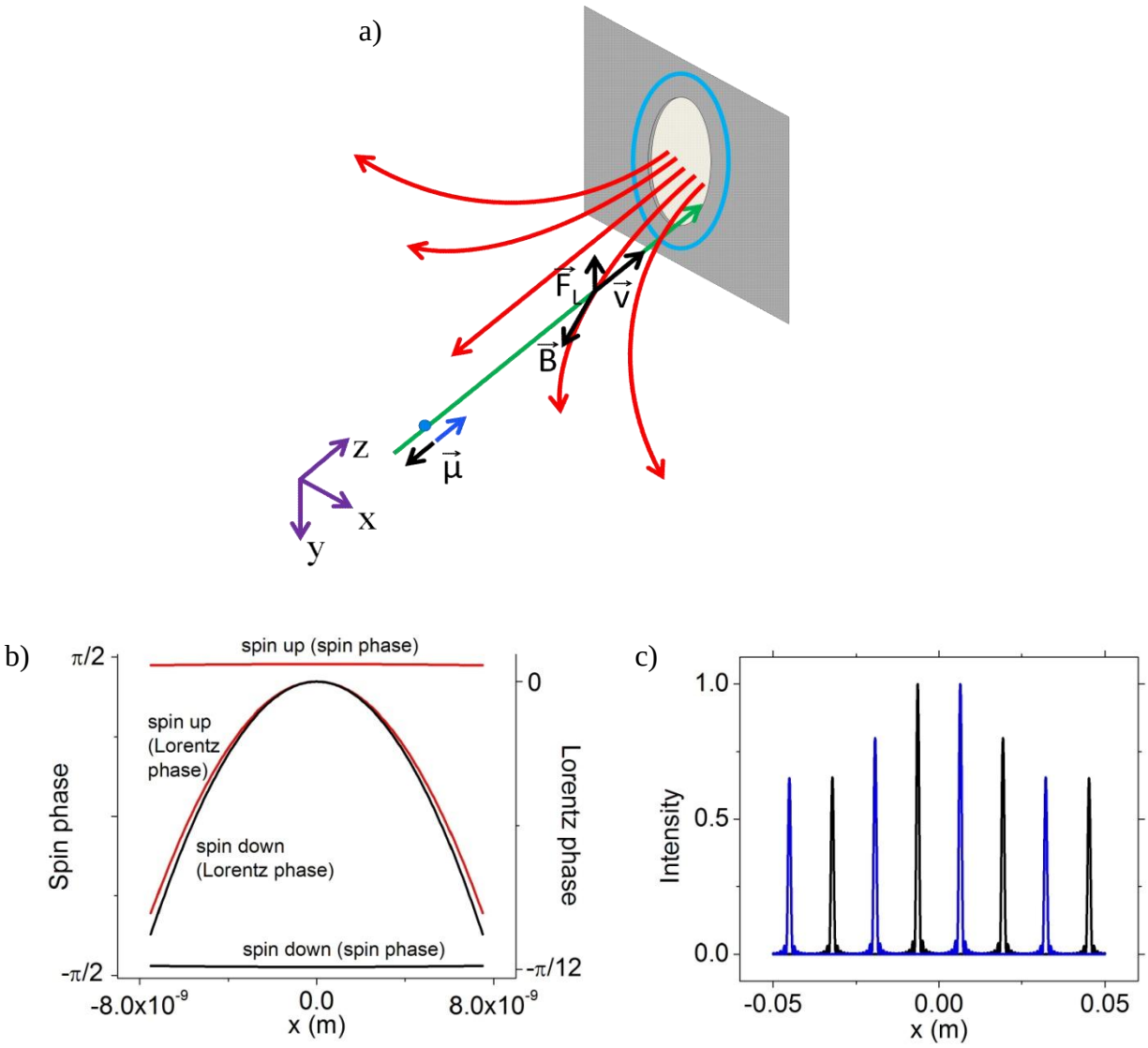

Figure 5.4

Lorentz Blurring

a) An electron entering a slit off-center experiences a Lorentz force and therefore accumulates a (Lorentz) phase accordingly. b) The spin phase due to the magnetic interaction term $-\vec{\mu}\cdot\vec{B}$, is calculated along a path for electrons passing through a current-carrying loop as a function of initial position in x. It is approximately uniform. The Lorentz phase shift due to the interaction term $\vec{v}\cdot\vec{A}$, associated with the Lorentz force, is given for both spin states. The Lorentz phase shift difference between both spin states, is much smaller than the spin phase difference for all x (note the separate scales on the vertical axes). c) Spin splitting with the inclusion of Lorentz blurring, i.e., the spin

dependent parabolic phase shift at each slit due to the Lorentz phase is taken into account in a fully quantum mechanical path integral calculation. The envelope of the diffraction pattern is modified, while the width and location of the individual diffraction peaks is not. Spin splitting remains in spite of the Lorentz force.

One as of yet unmentioned assumption is the absence of spin flipping. If the probability of spin flipping is large then even when the diffraction peaks are maximally separated, the peaks are not spin polarized as many of the electrons will have spin flipped. To estimate the spin flip probability the final orientation of the spin is calculated. Ehrenfest's theorem yields the time evolution of the quantum mechanical expectation value of the magnetic moment of an electron in a uniform magnetic field:

$$\frac{d\langle\vec{\mu}\rangle}{dt} = \frac{q}{m}\langle\vec{\mu}\rangle \times \vec{B}. \tag{10}$$

Therefore, the expectation value of the magnetic moment has the same time dependence as the solution to the classical equation of motion (Eq.8). The magnetic moment is calculated for a path passing through the current carrying loop. The relative variation of the magnetic moment is very small. It can be shown by integration that the final value of the z-component only varies about 0.08% over a range of initial positions of 15 nm thus illustrating the negligible probability of spin flipping, and justifying the use of equation 10.

Another effect that in principle contributes to the phase shift is image charge interaction[16,17]. Image charge can affect the electron trajectory as well as time evolution of the magnetic moment (see equation 7). Effects on the electron trajectory are the same for each slit and as such affect only the envelope, therefore not affecting the spin splitting in any way. Also, any spin evolution terms which depend on the electric field are

proportional to $1/c^2$ and are therefore very small compared to an already spin evolution in the magnetic field.

While the above arguments demonstrate that the transverse spin splitting of a free electron beam is, in principle, possible, it is, by the means described in this chapter, not experimentally feasible due to the large magnetic fields and low energy electrons. These problems can possibly be addressed in a number of ways. The demand for high magnetic fields can be reduced by applying the spin dependent phase modulo 2π. In the configuration described above the spin dependent phase follows the pattern 0, $\pi/2$, π, $3\pi/2$, 2π, $5\pi/2$, and so on. If those values are taken modulo 2π the pattern would simply repeat the values 0, $\pi/2$, π, $3\pi/2$ allowing for lower magnetic fields in many of the coils. Second, the length of the region in which the electron has appreciable interaction with the magnetic field can be increased. This can be done by replacing the loop by a solenoid. Doing so would allow for a combination of lower magnetic fields and higher electron energy. The small separation of the slits makes this even with modern nano-fabrication technology a very challenging proposition.

3. Stern-Gerlach Interference

3.1. Magnetic Phase Interferometer

Consider the interferometer shown in figure 5.5. In such an interferometer an electron beam is split into two beams. Each beam passes through a solenoid. After the beams pass through the solenoids they are recombined and interference fringes are observed.

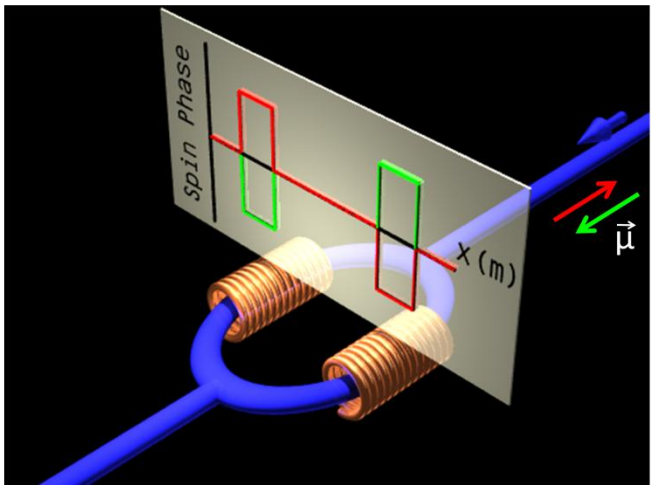

Figure 5.5

Magnetic Phase Interferometer

An electron interferometer with a solenoid around each arm creates a spin dependent phase difference between the two arms. The graph indicates the phase accumulated by the electrons as they pass through the solenoids. The green and red curves represent spin up and down respectively. It is proposed that this arrangement will control the electron polarization of the output, as explained below.

The solenoids are set up to create magnetic fields of equal magnitude but opposite direction which are parallel to the direction of motion of the electrons to reduce Lorentz forces. When the magnetic field is turned on the fringes corresponding to spin forward electrons will shift one way and the fringes corresponding to spin backward electrons will shift the other way. Here a solenoid 1 cm long with a radius of 1 mm is considered. A 1 micron diameter beam of electrons enters the solenoid at $5\text{x}10^6$ m/s. Here the following vector potential is used

$$A_x = \frac{\mu_0 K R^2 y}{4\left(R^2 + x^2 + y^2\right)}\left(\frac{z - L/2}{\sqrt{R^2 + x^2 + y^2 + \left(z - L/2\right)^2}} - \frac{z + L/2}{\sqrt{R^2 + x^2 + y^2 + \left(z + L/2\right)^2}}\right)$$

$$A_y = \frac{\mu_0 K R^2 x}{4\left(R^2 + x^2 + y^2\right)}\left(\frac{z + L/2}{\sqrt{R^2 + x^2 + y^2 + \left(z + L/2\right)^2}} - \frac{z - L/2}{\sqrt{R^2 + x^2 + y^2 + \left(z - L/2\right)^2}}\right)$$

$$A_z = 0. \tag{11}$$

The vector potential for a solenoid with length L was constructed by integrating the vector potential in the continuous limit of a series of loops (Eq. 9)[15]. In these equations μ_0 is the permeability of free space, K is the surface current density in the solenoid, and R is the radius of the solenoid. The spin dependent phase was integrated along the classical curved path (Figure 5.6a) and found to be uniform across the solenoid (Figure 5.6b). The Lorentz phase was, as before, quadratic in initial position but not dependent on spin (Figure 5.6b). These calculations were made for a solenoid with a modest surface current density equal to 7100 A/m which gives the spin forward electrons passing through the solenoid a phase shift of π/2.The probability of spin flipping is low ($< 3\times10^{-7}$) in this case as it was in the example of the magnetic phase grating.

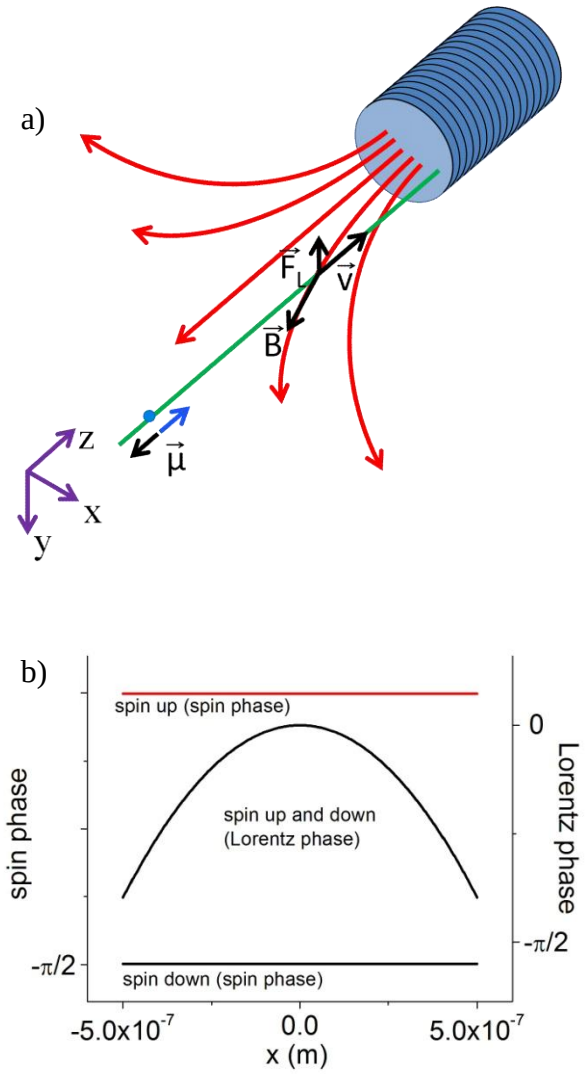

Figure 5.6

Lorentz Blurring for a Solenoid

a) An electron entering the solenoid off-center experiences a Lorentz force and therefore accumulates a (Lorentz) phase accordingly. b) The spin phase term is uniform across the solenoid in the region of interest, as in the previous case involving the phase grating. The Lorentz phase term is quadratic and spin independent, as in the previous case involving the phase grating.

3.2. Grating Bi-Prism Interferometer

Consider a wide angle beam splitter consisting of a grating and a bi-prism wire such as the one described by Caprez *et al.*[19]. Figure 5.7 depicts a setup using this beam splitter to separate (albeit not fully) spin states interferometrically.

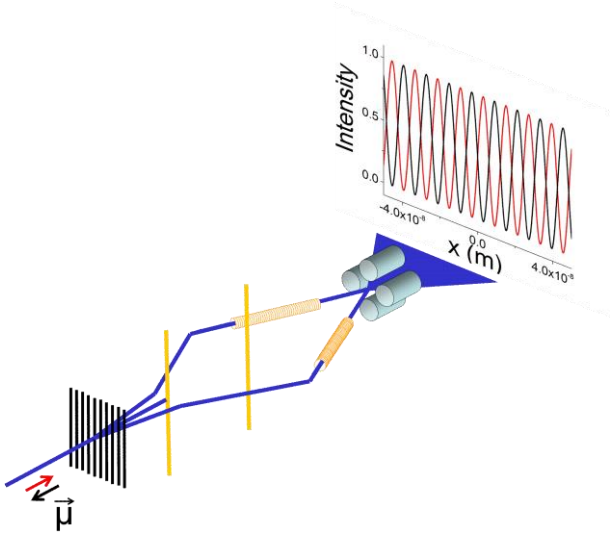

Figure 5.7

Grating Bi-Prism Interferometer

An electron beam passes through a grating. The zero order and the two first order diffracted beams are shown. The first bi-prism wire blocks the zero order while pushing the two first order beams away from each other. The second biprism brings the two first order beams back together. They pass through solenoids on their way to the quadrupole lens where the image of the fringes is magnified and projected onto the detection plane. Near-field interference patterns for spin-up and spin-down states (red and black) are shifted with respect to each other.

The interferometer shown above consists of a grating, two bi-prisms, two solenoids, an electrostatic quadrupole lens, and a spatial detector. The zero diffraction order is blocked by the first bi-prism wire. A negative voltage is applied to the first bi-prism to push the two first diffraction orders away from each other. This is necessary to create space for the solenoids. A positive voltage is applied to the second bi-prism to bring the two beams

back together. The two beams pass through solenoids as they approach a quadrupole lens which magnifies the interference pattern. By applying a current to the solenoids, a spin dependent phase difference is created between the two arms of the interferometer. This would result in opposite fringe shifts for spin up as compared to spin down electrons.

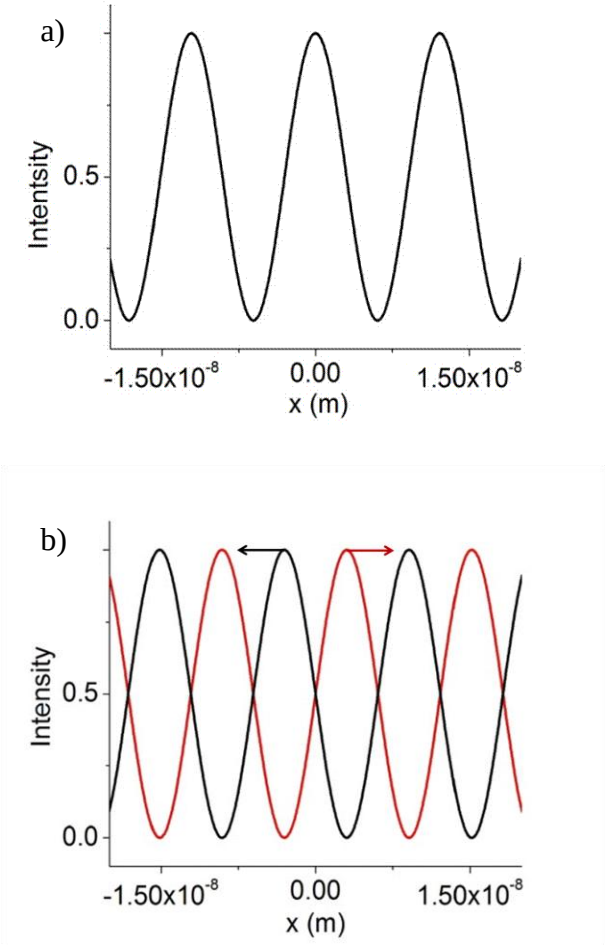

Figure 5.8

Near Field Fringes

a) Interference fringes are calculated with no current in the solenoids. b) Interference fringes are calculated with each solenoid carrying a surface current density of 3550 A/m. The arrows show the direction that the fringes shift for each spin state as the current is increased.

Figure 5.8a depicts the interference fringes with no current being applied to the solenoids. Figure 5.8b shows a similar fringe pattern but this time with a surface current density of 3550 A/m, the current required for a $\pi/4$ magnitude phase shift in each arm. This result is obtained from a full path integral simulation including a biprism and two beams propagating through finite length solenoids (including Lorentz blurring). This scenario is more feasible (than the example of the phase grating) as a large separation between the arms of the interferometer allows for larger coils to be inserted.

3.3. Mach-Zehnder Interferometer

To achieve full spin splitting, consider a Mach-Zehnder interferometer that consists of two sets of unfocused counter propagating laser beams and three bi-prism wires (Figure 5.9)[20] in a similar configuration as the previous example. The electrons Bragg scatter from the laser beams as described by Freimund *et al.*[21]. Two balanced electron beams emerge from a perfect Bragg crystal. In between the two arms of the interferometer a solenoid is placed perpendicular to the electron beams, which provides an Aharonov Bohm phase shift[22]. The purpose of this phase shift is to balance the electron intensity of the two interferometer output beams. A solenoid in each interferometer arm provides a spin dependent phase shift causing an electron polarization of the two outputs.

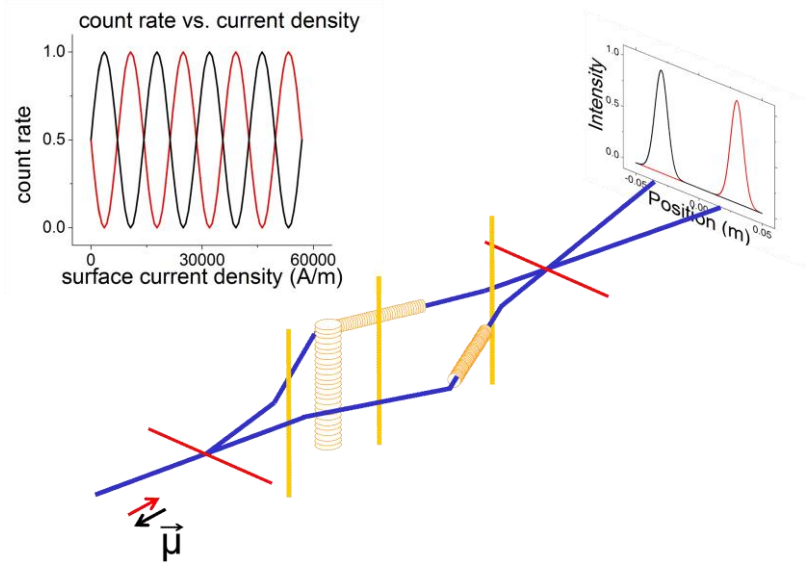

Figure 5.9

Mach-Zehnder Interferometer

The interferometer consists of two sets of counter propagating laser beams (horizontal red lines) and three bi-prism wires. A solenoid enclosed by the two interferometer arms creates an Aharonov-Bohm phase shift to balance the interferometer (see text). Solenoids are placed around each arm to create a spin dependent phase shift which polarizes the two outputs of the interferometer. The graph shown is the result of a path integral calculation of the count rate in one of the arms as a function of current density in the solenoids. The two curves are the count rates of the two spin states.

As with the grating bi-prism interferometer example (section 3.2) the large separation allows for long interaction times thus minimizing the necessary magnetic field as well as allowing for higher energy electrons. For this configuration a path integral computation yields the probability for spin-forward and spin-backward detection as a function of the current in the two solenoids, taking into account Lorentz blurring (Figure 5.9). *Complete separation of the two spin states in two beams is obtained (Figure 5.9 inset) as one would hope to get for a perfect electron Stern-Gerlach magnet.*

A quantum optical analysis of this system based on two momentum states and two spin states yields the same result. Consider an unpolarized input state with a downward component of momentum (Figure 5.10) described by the density operator

$$\rho_{initial} = \frac{1}{2}\left(|+\rangle_{-}\langle +|_{-} + |-\rangle_{-}\langle -|_{-} \right). \tag{12}$$

Where a "+" or "−" inside the bras and kets indicates spin forward or backward while a "+" or "−" subscript indicates an upward or downward component of momentum (as related to figure 5.10).

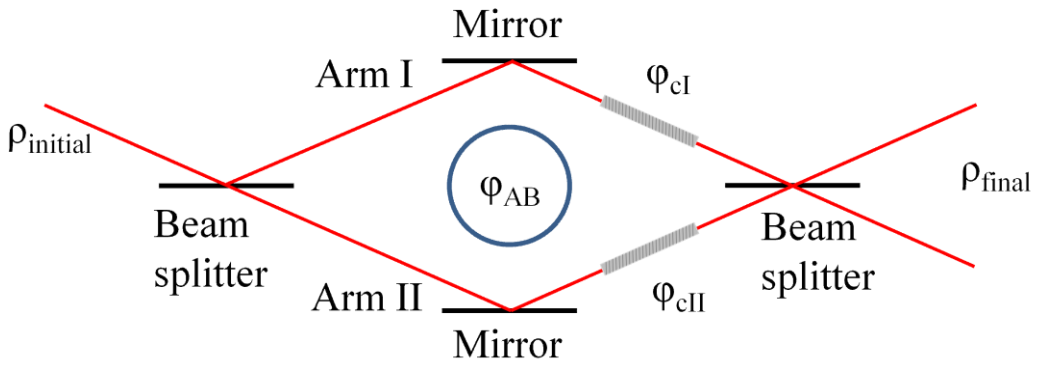

Figure 5.10

Interferometer Schematic

The operational elements of the Mach-Zehnder interferometer are indicated (for a detailed description see text).

The effect of the beamsplitter described by

$$|+\rangle_{-} \xrightarrow{BS} \frac{\sqrt{2}}{2}\left(i|+\rangle_{+} + |+\rangle_{-}\right)$$

$$|+\rangle_{+} \xrightarrow{BS} \frac{\sqrt{2}}{2}\left(i|+\rangle_{-} + |+\rangle_{+}\right), \tag{13}$$

is independent of spin. The effect of the mirror described by

$$\left|+\right\rangle_{-} \xrightarrow{M} i\left|+\right\rangle_{+}$$

$$\left|+\right\rangle_{+} \xrightarrow{M} i\left|+\right\rangle_{-}, \tag{14}$$

is also independent of spin. The AB phase shift and the phase shift given by the coils is dependent upon which arm of the interferometer the electrons go through. The arms are labeled I and II to track these phase shifts. The phase shifts given by the coils are chosen to be of equal magnitude and opposite sign. In arm I, the phase shift given by the coil and the AB phase shift are given by

$$\left|+\right\rangle_{-} \xrightarrow{Coil} \exp\left(i\varphi_c\right)\left|+\right\rangle_{-}$$

$$\left|-\right\rangle_{-} \xrightarrow{Coil} \exp\left(-i\varphi_c\right)\left|-\right\rangle_{-}$$

$$\left|+\right\rangle_{-} \xrightarrow{AB} \exp\left(i\varphi_{AB}/2\right)\left|+\right\rangle_{-}, \tag{15}$$

and in arm II these phase shifts are given by

$$\left|+\right\rangle_{+} \xrightarrow{Coil} \exp\left(-i\varphi_c\right)\left|+\right\rangle_{+}$$

$$\left|-\right\rangle_{+} \xrightarrow{Coil} \exp\left(i\varphi_c\right)\left|-\right\rangle_{+}$$

$$\left|+\right\rangle_{+} \xrightarrow{AB} \exp\left(-i\varphi_{AB}/2\right)\left|+\right\rangle_{+}, \tag{16}$$

where the AB phase shift is spin independent. The resulting output density operator is

$$\rho_{final} = \frac{1}{8}\left\{\exp\left[-i\left(\varphi_c + \varphi_{AB}/2\right)\right]\left(\left|+\right\rangle_{+} + i\left|+\right\rangle_{-}\right) + i\exp\left[i\left(\varphi_c + \varphi_{AB}/2\right)\right]\left(\left|+\right\rangle_{-} + i\left|+\right\rangle_{+}\right)\right\}$$

$$\times\left\{\exp\left[i\left(\varphi_c + \varphi_{AB}/2\right)\right]\left(\left\langle+\right|_{+} - i\left\langle+\right|_{-}\right) - i\exp\left[-i\left(\varphi_c + \varphi_{AB}/2\right)\right]\left(\left\langle+\right|_{-} - i\left\langle+\right|_{+}\right)\right\}$$

$$+\frac{1}{8}\left\{\exp\left[i\left(\varphi_c - \varphi_{AB}/2\right)\right]\left(\left|-\right\rangle_{+} + i\left|-\right\rangle_{-}\right) + i\exp\left[-i\left(\varphi_c - \varphi_{AB}/2\right)\right]\left(\left|-\right\rangle_{-} + i\left|-\right\rangle_{+}\right)\right\}$$

$$\times\left\{\exp\left[-i\left(\varphi_c-\varphi_{AB}/2\right)\right]\left(\langle-|_+-i\langle-|_-\right)-i\exp\left[i\left(\varphi_c-\varphi_{AB}/2\right)\right]\left(\langle-|_--i\langle-|_+\right)\right\}. \quad (17)$$

The probability of finding each spin state in each output is

$$P_{++}=\langle+|_+\rho_{final}|+\rangle_+=\frac{1}{2}\sin^2\left(\varphi_c+\varphi_{AB}/2\right)$$

$$P_{-+}=\langle-|_+\rho_{final}|-\rangle_+=\frac{1}{2}\sin^2\left(\varphi_c-\varphi_{AB}/2\right)$$

$$P_{+-}=\langle+|_-\rho_{final}|+\rangle_-=\frac{1}{2}\cos^2\left(\varphi_c+\varphi_{AB}/2\right)$$

$$P_{--}=\langle-|_-\rho_{final}|-\rangle_-=\frac{1}{2}\cos^2\left(\varphi_c-\varphi_{AB}/2\right). \quad (18)$$

A non-zero AB-phase shift ($\varphi_{AB}=\pi/2$) together with a non-zero spin dependent phase shift ($\varphi_c=\pi/4$) is required to obtain complete spin-splitting; $P_{++}=P_{--}=\frac{1}{2}$, $P_{+-}=P_{-+}=0$.

4. Conclusion

The question: "Is it possible to observe the spin of the electron, separated fully from its orbital momentum, by means of experiments based on the concept of *quantum* particle trajectories" is addressed. As this applies to Stern-Gerlach "magnets" the answer is affirmative. For the longitudinal case this has been analyzed previously[10], while in this chapter a transverse case is analyzed. The arrangement is not optimized for practical applications; magnetic Bragg crystals would be interesting to study in this context. Nevertheless, the logical argument is made for a scenario, where the physical elements have been individually realized. The answer to the above question appears to be: "Yes". For example, spin can by observed, fully separated from its orbital momentum, by energy

jumps associated with spin flips, in the lowest quantum motional states (cyclotron and magnetron)[23]. Dehmelt has observed such spin flips[23] for individual electrons, and attacked Bohr and Pauli's dictum[24] suggesting the above formulated general rule.

Chapter 6 – Spin Dependent Two Color K-D Effects

1. Introduction

The capability to control electrons with laser light has been demonstrated with the higher light intensities that are provided by pulsed lasers[1, 2]. In some of the first experiments, continuous electron beams were used so that most electrons were not affected by the light[1]. More recently, pulsed electrons have also been affected by pulsed laser light[3, 4]. As more variations of pulsed electron sources that are synchronous with pulsed lasers are becoming available[5, 6], proposals have appeared that use such technology to control electron motion[7, 8]. As also table-top relativistic laser intensities are becoming more and more accessible, it is timely to consider the weaker interaction of electron spin with laser light. Recently, it was predicted that X-ray laser light could be used to affect the electron spin of a beam of relativistic free electrons[9], which is relevant to the newest X-ray laser facilities. More generally, electron spin control can provide an additional control to ultrafast electron diffraction[10, 11] and ultrafast electron microscopy[12, 13], similar to the non-pulsed version of spin-polarized low energy electron microscopy[14] (SPLEEM). For SPLEEM, GaAs polarized electron sources are used. However it is not clear what technology will be used for polarization control of femtosecond electron beams. In addition to its technological appeal, spin control may provide (through the spin-statistics connection) an opportunity to investigate quantum degeneracy in multi-electron pulses[15]. In view of these developments, we investigate the influence of visible light on the spin of non-relativistic electrons.

We report on an electron laser configuration for which the spin dependent interaction is small, but dominant in the optical to near infrared domain. Specifically, a

well collimated electron beam is cross-fired perpendicularly with two counter-propagating laser beams (figure 6.1) with frequencies ω and 2ω ($\lambda = 2\pi c/\omega = 1\mu m$). The polarization of the two beams is linear and orthogonal to the electron beam propagation axis. For this configuration the regular Kapitza-Dirac effect[16] is absent due to the choice of widely separated frequencies, while the two-color Kapitza-Dirac effect[17] is absent because the electron velocity is chosen perpendicular to the laser polarization. The dominant interaction that remains is an interaction that scatters the electron beam by four momenta recoils and simultaneously flips the electron spin. The spin-flip probability for non-relativistic intensities is small, but within reach of current technology.

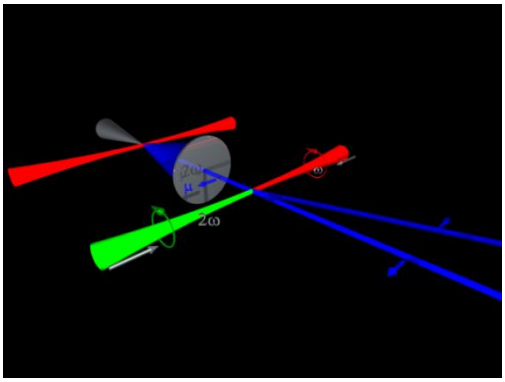

Figure 6.1

Two Color K-D Effect with Circular Polarization

An electron pulse is generated from a field emission tip that is illuminated with a femtosecond laser[5]. The electron pulse is collimated (blue beam) and cross fired with two counter propagating laser pulses of frequency ω (red) and 2ω (green). Some electrons receive photon recoils of 4 $\hbar k$ while simultaneously flipping their spin (blue arrows) for appropriate chosen light polarization (see text for details).

The probability increases for increasing intensity and an extension beyond the scope of the present paper to relativistic intensities (for example using the type of analysis used in reference[9]) in the same frequency regime appears interesting.

A spin-dependent scattering could be used as an electron spin analyzer. To analyze the spin-polarization of a non-relativistic femtosecond electron pulse no readily accessible techniques are available[18]. Techniques for non-pulsed beams include Mott scattering[19], optical polarimetry[20], Rb spin-filter[21] and others. The most well-known and widely used Mott scattering requires currents exceeding 1 pA[22]. This current is usually not available for femtosecond electron pulses, so steady state methods do not easily transfer to pulsed scenarios. Relativistic polarized pulse electron bunches in accelarators can be analyzed with Compton polarimetry[23]. However, their spin analyzing power drops off sharply with the relativistic gamma-factor. Femtosecond non-relativistic pulsed polarized electron sources are under development[24-26] and it is expected that analysis of their polarization will be needed. In general pulsed polarized electron sources are of interest for the broad area of spin physics[27].

The question may arise if such an optical control/analysis of electron spin is possible at all for non-relativistic electron motion. After all, Pauli pointed out that electrons cannot be polarized using ideas based on classical electron trajectories[28-34], as in a Stern-Gerlach device, even when the spin is treated quantum mechanically. This may appear to imply that the result obtained in this work could be ruled out based on a general principle. An earlier study based on classical mechanics for the physical system studied in this paper, indeed revealed no spin interaction[35]. Given that our current analysis is

based on perturbative quantum mechanics of the electron motion Pauli's objection is circumvented.

2. Perturbation Theory

The non-relativistic interaction Hamiltonian can be obtained by minimal substitution and considering the interaction of the electron dipole with the field[36],

$$H_{\text{int}} = -\frac{q}{2m}\left(\vec{p}\cdot\vec{A}+\vec{A}\cdot\vec{p}\right)+\frac{q^2A^2}{2m}-\vec{\mu}\cdot\vec{B}. \quad (1)$$

Here, the coupling of the motional electric dipole moment with the electric field is negligible, q and m are the electron charge and mass respectively, p is the momentum, A the vector potential, mu the electro's magnetic moment, and B the magnetic field. The Hamiltonian can couple the states

$$|\psi\rangle = |n\hbar k_z, \hbar k_x, m_s\rangle. \quad (2)$$

The first entry in the definition of state vector of the electron defines the component of the electron momentum in the z-direction (i.e. aligned with the laser propagation), the second entry sets the electron momentum in the x-direction, and the third entry sets the quantum number corresponding to the projection of electron spin along the z-axis. The integer *n* in the first entry is defined in anticipation of photon absorption and emission resulting in discrete changes of the electron momentum in terms of multiples of photon recoils, $\hbar k_z$. The Bragg condition leads to energy and momentum conservation for changes of the z-component of the electron momentum from $n\hbar k_z$ to , while the x-component remains unchanged[16].

The $\frac{q^2A^2}{2m}$ term in the Hamiltonian is responsible in first order time-dependent perturbation theory for the regular K-D effect[16], the terms $\frac{q^2A^2}{2m}$ and $\frac{q}{m}\vec{p}\cdot\vec{A}$ together lead in second order perturbation to the two-color K-D effect[17], while the terms $\frac{q^2A^2}{2m}$ and $\vec{\mu}\cdot\vec{B}$ in second order perturbation yield spin dependent scattering that is the main focus of our current study.

Only processes which conserve energy in the laser field are considered in the perturbative approach. That this is valid is not obvious and needs to be justified. Below we report on a relativistic classical calculation that shows that for our parameters the change in the electron velocity along the direction of the laser propagation direction is limited to the order of a photon recoil. Our parameters are carefully choice to avoid transverse acceleration and thus the weak spin-dependent scattering can become the dominant effect. Details of these choices are discussed below. The question whether or not an electron can be accelerated by laser fields has been debated for decades. In spite of the Lawson-Woodward theorem[37] it has been shown, that energy gain by laser interaction is possible for high energy electrons interacting with a tightly focused laser[38], and very recently even for approximately plane waves[39]. Our parameters do not satisfy the Lawson-Woodward criteria as the fields are not infinite in extent, the electron energy is not relativistic, and the ponderomotive potential is not negligible. The reason that the electron's velocity in the laser propagation direction change little is that the electron and counter propagating laser pulses are timed such that the ponderomotive force from both

pulses cancels. Our relativistic simulation does show that the longitudinal velocity can change significantly (see below).

To prevent a potentially dominant spin-independent scattering from overwhelming the weaker spin-dependent scattering, the physical parameters need to satisfy further criteria. At a laser intensity of 10^{19} W/m^2, an electron in a ponderomotive potential undergoes acceleration of up to 10^{22}m/s^2. The Larmor radiation rate at this acceleration, gives rise to a photon emission probability of 10^{-2} in an interaction time of 10 ps. However, these photons are emitted in a large solid angle, give an average recoil in the laser propagation direction that is zero, and thus do not overwhelm the spin-dependent scattering.

We now continue with the explicit calculation of the spin-dependent perturbation term. In order to test whether or not spin-dependent scattering is plausible, perturbation theory was used to analyze each term in the interaction Hamiltonian in search of one term which would connect an initial spin state with a spin-flipped final state. For the purpose of this investigation we began with the vector potential corresponding with two circularly polarized laser beams which are counter-propagating along the z-axis,

$$\vec{A} = -\frac{A_0}{2\sqrt{2}}\exp\left(\frac{-t^2}{\tau^2}\right)\left(a_L e^{i(kz-\omega t)}\left(\hat{x}+i\hat{y}\right)+a_L^{\dagger}e^{-i(kz-\omega t)}\left(\hat{x}-i\hat{y}\right)\right)$$

$$-\frac{A_0}{2\sqrt{2}}\exp\left(\frac{-t^2}{\tau^2}\right)\left(a_R e^{-i2(kz+\omega t)}\left(\hat{x}+i\hat{y}\right)+a_R^{\dagger}e^{i2(kz+\omega t)}\left(\hat{x}-i\hat{y}\right)\right). \qquad (3)$$

The choice of using raising and lowering photon number operators is made to facilitate the selection of particular processes and is not essential. The calculations done in this section could have been done with classical fields to the same effect. The laser propagating in the direction of the positive z-axis has frequency ω and the laser

propagating in the direction of the negative z-axis has frequency 2ω. Both beams have spin $\hbar$ in the direction of the positive z axis. The magnetic dipole moment operator may be written in terms of the Pauli spin operator as $\vec{\mu} = \frac{-2\mu_B}{\hbar}\vec{S}$ where μ_B is the Bohr magneton. The $\frac{q}{m}\vec{p}\cdot\vec{A}$, $\frac{q^2A^2}{2m}$, and $\vec{\mu}\cdot\vec{B}$ terms in the interaction Hamiltonian are

$$\frac{q}{2m}\left(\vec{p}\cdot\vec{A}+\vec{A}\cdot\vec{p}\right) = -\frac{qA_0}{2\sqrt{2}m}\exp\left(\frac{-t^2}{\tau^2}\right)\left(a_L e^{i(kz-\omega t)} + a_L^{\dagger}e^{-i(kz-\omega t)}\right)p_x$$

$$-\frac{qA_0}{2\sqrt{2}m}\exp\left(\frac{-t^2}{\tau^2}\right)\left(a_R e^{-i2(kz+\omega t)} + a_R^{\dagger}e^{i2(kz+\omega t)}\right)p_x \qquad (4)$$

$$\frac{q^2A^2}{2m} = \frac{q^2A_0^2}{8m}\exp\left(\frac{-2t^2}{\tau^2}\right)\left[a_L a_L^{\dagger} + a_R a_R^{\dagger} + a_L a_R^{\dagger}e^{i(3kz+\omega t)} + a_R a_L^{\dagger}e^{-i(3kz+\omega t)}\right]$$

$$+\frac{q^2A_0^2}{8m}\exp\left(\frac{-2t^2}{\tau^2}\right)\left[a_L^{\dagger}a_L + a_R^{\dagger}a_R + a_L^{\dagger}a_R e^{-i(3kz+\omega t)} + a_R^{\dagger}a_L e^{i(3kz+\omega t)}\right] \qquad (5)$$

$$\vec{\mu}\cdot\vec{B} = \frac{\mu_B A_0 k}{\sqrt{2}\hbar}\exp\left(\frac{-t^2}{\tau^2}\right)\left[\left(a_L e^{i(kz-\omega t)} - 2a_R e^{-i2(kz+\omega t)}\right)S_+ + \left(a_L^{\dagger}e^{-i(kz-\omega t)} - 2a_R^{\dagger}e^{i2(kz+\omega t)}\right)S_-\right], \qquad (6)$$

where $S_+ = \frac{\hbar}{2}\left(\sigma_x + i\sigma_y\right)$ and $S_- = \frac{\hbar}{2}\left(\sigma_x - i\sigma_y\right)$ are the electron spin raising and lowering operators. The presence of the electron spin raising and lowering operators are a consequence of the choice of polarization. These operators can be used to connect initial and final states with different spin and therefore justify the choice of polarization in the search for spin-flip processes.

The first order probability amplitude is

$$C_{fi} = \frac{-i}{\hbar}\int_{-\infty}^{\infty} H_{\text{int}}^{fi}(t')dt'. \qquad (7)$$

where $H_{\text{int}}^{fi} = \langle f | H_{\text{int}} | i \rangle$. For spin-flip processes it is necessary to consider terms in the $\vec{\mu} \cdot \vec{B}$ part of the Hamiltonian as those contain the spin raising and lowering operators which are necessary to connect initial and final states with different spin in the matrix element. On examination of the $\vec{\mu} \cdot \vec{B}$ term it is apparent that such a first order process must be either single photon absorption or single photon emission because the terms in $\vec{\mu} \cdot \vec{B}$ each contain only one photon number operator. Single photon processes are impossible because they cannot simultaneously conserve momentum and energy. It is therefore necessary to consider second order perturbation theory.

Using second order perturbation theory, the probability amplitude, C_{fi}, for transition between the initial (i) and final (f) states is found by summing over the intermediate state (m) for the 2nd and 3rd terms in the interaction Hamiltonian (Eq. 3,4)

$$C_{fi} = \frac{-1}{\hbar^2} \sum_m \int_{-\infty}^{\infty} \int_{-\infty}^{t'} H_{\text{int}}^{fm}(t') H_{\text{int}}^{mi}(t'') dt'' dt' . \tag{8}$$

The matrix elements H_{int}^{mi} and H_{int}^{fm} correspond to transitions from the initial state to the intermediate state and from the intermediate state to the final state, respectively. For example, let us take $|N_\omega, N_{2\omega}, 2\hbar k, \uparrow\rangle$ and $|N_\omega + 2, N_{2\omega} - 1, -2\hbar k, \downarrow\rangle$ as initial and final states, respectively, where the first quantum number is the photon number for frequency ω, the second quantum number is the photon number for frequency 2ω, the third quantum number indicates the transverse momentum of the electron, and the arrow indicates the spin state of the electron. The wave function of the electron is a plane wave $\exp\left(i\left(\vec{k}_e \cdot \vec{x} - \omega_e t\right)\right)$ where $\vec{k}_e$ and ω_e are the wave number and frequency of the electron,

respectively. The $\frac{-\mu_B A_0 k}{\sqrt{2}\hbar} a_L^\dagger e^{-i(kz-\omega t)} S_-$ operator in the $\vec{\mu}\cdot\vec{B}$ term and the $\frac{q^2 A_0^2}{8m} a_R a_L^\dagger e^{-i(3kz+\omega t)}$ in the $\frac{q^2 A^2}{2m}$ term may be used to connect these two states.

$$H_{\text{int}}^{mi}(t) = \frac{-\mu_B A_0 k}{\sqrt{2}\hbar} \exp\left(\frac{-t^2}{\tau^2}\right) \left\langle N_\omega + 1, N_{2\omega}, \hbar k, \downarrow \left| a_L^\dagger e^{-i(kz-\omega t)} S_- \right| N_\omega, N_{2\omega}, 2\hbar k, \uparrow \right\rangle$$

$$= \frac{-\mu_B A_0 k\sqrt{N+1}}{\sqrt{2}} \exp\left(\frac{-t^2}{\tau^2}\right) \exp\left(i\left(\omega_{mi} + \omega\right)t\right) \quad (9)$$

$$H_{\text{int}}^{fm}(t) = \frac{q^2 A_0^2}{8m} \exp\left(\frac{-2t^2}{\tau^2}\right) \left\langle N_\omega + 2, N_{2\omega} - 1, \hbar k, \downarrow \left| a_R a_L^\dagger e^{-i(3kz+\omega t)} \right| N_\omega + 1, N_{2\omega}, \hbar k, \downarrow \right\rangle$$

$$= \frac{q^2 A_0^2 \sqrt{N(N+2)}}{8m} \exp\left(\frac{-2t^2}{\tau^2}\right) \exp\left(i\left(\omega_{fm} - \omega\right)t\right), \quad (10)$$

where $N_{2\omega} = N_\omega = N$, $\omega_{mi} = \omega_m - \omega_i$ is the frequency difference between the initial and intermediate states, and $\omega_{fm} = \omega_f - \omega_m$ is the frequency difference between the intermediate and final states. The probability amplitude for this process may therefore be written as

$$C_{fi} = \frac{\mu_B q^2 k A_0^3 N^{3/2}}{8\sqrt{2}m\hbar^2} \int_{-\infty}^{\infty} \int_{-\infty}^{t'} \exp\left[i\left(\left(\omega_{fm} - \omega\right)t' + \left(\omega_{mi} + \omega\right)t''\right)\right] \exp\left(\frac{-2t'^2 - t''^2}{\tau^2}\right) dt'' dt', \quad (11)$$

where $\sqrt{N(N+1)(N+2)} \approx N^{3/2}$. It is apparent from this example that for the Hamiltonian given above there are only particular states that lead to a non-zero probability amplitude and identify the possible processes. Processes in which one of the lasers has no net change in photon number or processes in which the net change in photon number is identical for both lasers cannot simultaneously conserve momentum and energy[9]. Therefore, within the Bragg regime[16], spin flips are allowed for initial and final

electron momentum states with $-2\hbar k$ and $2\hbar k$ using the $\vec{\mu}\cdot\vec{B}$ and $\frac{q^2A^2}{2m}$ terms. All possible amplitudes corresponding to different intermediate states for processes involving a $-4\hbar k$ momentum kick with a spin flip from $\uparrow$ to $\downarrow$ are added together to determine the overall amplitude for the process;

$$C_{fi}=\frac{\mu_B q^2 k A_0^3}{8\sqrt{2}m\hbar^3}\int_{-\infty}^{\infty}\int_{-\infty}^{t'}\left\langle N_\omega+2,N_{2\omega}-1,-2\hbar k,\downarrow\left|a_R a_L^\dagger e^{-i(3kz+\omega t)}\right|N_\omega+1,N_{2\omega},\hbar k,\downarrow\right\rangle$$

$$\times\exp\left(i\omega_{fm}t'\right)\exp\left(\frac{-2t'^2}{\tau^2}\right)$$

$$\times\left\langle N_\omega+1,N_{2\omega},\hbar k,\downarrow\left|a_L^\dagger e^{-i(kz-\omega t)}S_-\right|N_\omega,N_{2\omega},2\hbar k,\uparrow\right\rangle\exp\left(i\omega_{mi}t''\right)\exp\left(\frac{-t''^2}{\tau^2}\right)dt''dt'$$

$$+\frac{\mu_B q^2 k A_0^3}{8\sqrt{2}m\hbar^3}\int_{-\infty}^{\infty}\int_{-\infty}^{t'}\left\langle N_\omega+2,N_{2\omega}-1,-2\hbar k,\downarrow\left|a_L^\dagger a_R e^{-i(3kz+\omega t)}\right|N_\omega+1,N_{2\omega},\hbar k,\downarrow\right\rangle$$

$$\times\exp\left(i\omega_{fm}t'\right)\exp\left(\frac{-2t'^2}{\tau^2}\right)$$

$$\times\left\langle N_\omega+1,N_{2\omega},\hbar k,\downarrow\left|a_L^\dagger e^{-i(kz-\omega t)}S_-\right|N_\omega,N_{2\omega},2\hbar k,\uparrow\right\rangle\exp\left(i\omega_{mi}t''\right)\exp\left(\frac{-t''^2}{\tau^2}\right)dt''dt'$$

$$+\frac{\mu_B q^2 k A_0^3}{8\sqrt{2}m\hbar^3}\int_{-\infty}^{\infty}\int_{-\infty}^{t'}\left\langle N_\omega+2,N_{2\omega}-1,-2\hbar k,\downarrow\left|a_L^\dagger e^{-i(kz-\omega t)}S_-\right|N_\omega+1,N_{2\omega}-1,-\hbar k,\uparrow\right\rangle$$

$$\times\exp\left(i\omega_{fm}t'\right)\exp\left(\frac{-t'^2}{\tau^2}\right)$$

$$\times\left\langle N_\omega+1,N_{2\omega}-1,-\hbar k,\uparrow\left|a_R a_L^\dagger e^{-i(3kz+\omega t)}\right|N_\omega,N_{2\omega},2\hbar k,\uparrow\right\rangle\exp\left(i\omega_{mi}t''\right)\exp\left(\frac{-2t''^2}{\tau^2}\right)dt''dt'$$

$$+\frac{\mu_B q^2 k A_0^3}{8\sqrt{2}m\hbar^3}\int_{-\infty}^{\infty}\int_{-\infty}^{t'}\left\langle N_\omega+2,N_{2\omega}-1,-2\hbar k,\downarrow\left|a_L^\dagger e^{-i(kz-\omega t)}S_-\right|N_\omega+1,N_{2\omega}-1,-\hbar k,\uparrow\right\rangle$$

$$\times \exp\left(i\omega_{fm}t'\right)\exp\left(\frac{-t'^2}{\tau^2}\right)$$

$$\times\left\langle N_\omega+1, N_{2\omega}-1, -\hbar k, \uparrow \left| a_L^\dagger a_R e^{-i(3kz+\omega t)} \right| N_\omega, N_{2\omega}, 2\hbar k, \uparrow \right\rangle \exp\left(i\omega_{mi}t''\right)\exp\left(\frac{-2t''^2}{\tau^2}\right)dt''dt' \quad (12)$$

The integrals were calculated numerically and the results are shown in column 2 of table 6.1. Similarly there are two integrals representative of two processes by which the electron can receive a spin flip from $\uparrow$ to $\downarrow$ with no net momentum kick from only one of the lasers that must be summed coherently.

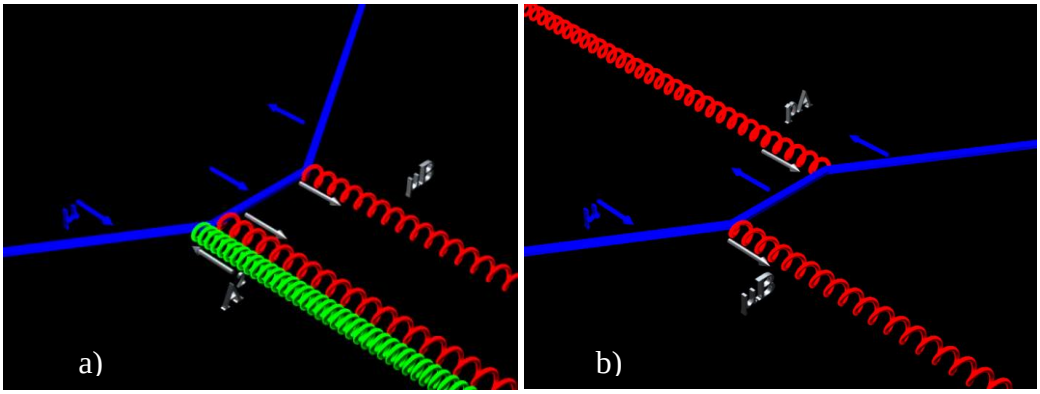

Figure 6.2

Spin Flip Kick and Depolarizer

a) An example is shown of three photon process by which the electron receives a spin flip and a momentum kick by absorbing one 2ω photon and emitting two ω photons. The first process shown represents an absorption and emission of a 2ω photon and a 1ω photon, respectively, indicating the use of the A^2 term of the Hamiltonian. The second process shown represents an emission of a 1ω photon, indicating the use of the μB term of the Hamiltonian. b) An example is shown of two photon process by which the electron receives a spin flip without an overall deflection by emitting and absorbing photons from the same laser. The first process shown represents an emission of a photon, indicating the use of the μB term of the Hamiltonian. The second process shown represents an absorption of a photon, indicating the use of the pA term of the Hamiltonian.

Such an event may flip a spin of an electron that already received a momentum kick and spin flip, and thus undo the effect we are interested in. The laser considered for this calculation was the ω frequency laser in the above expression for $\vec{A}$. The results of the calculations are shown in column 1 of table 6.1.

	Depolarizer	Spin-dependent effect	Two-color KD-effect
Intensity	$10^{18}\,W/m^2$	$10^{18}\,W/m^2$	$10^{15}\,W/m^2$
Velocity	$10^{7}\,m/s$	$10^{7}\,m/s$	$10^{7}\,m/s$
Wavelength	$1064nm$	$1064nm$	$1064nm$
Interaction Time	$100\,ps$	$100\,ps$	$100\,ps$
Probability	0.00576	0.001277	7.424×10^{-4}
Proportionality	$P=\alpha I^2v^2\lambda^2\tau^2$	$P=\alpha I^3\lambda^4\tau^2$	$P=\alpha I^3v^2\lambda^6\tau^2$
α	5.0912×10^{-21}	9.9638×10^{-14}	5.1167×10^{-7}

Table 6.1

Process Parameters and Probabilities

The probability of a two photon spin flip, a three photon spin flip (with circularly polarized light), or a two color K-D momentum kick (with linearly polarized light) is given as functions of laser intensity, electron velocity, laser wavelength, and interaction time.

Given the numbers in table 6.1 it appears that an interaction in which an electron spin flip due to laser interaction is possible but these are only representative of a small a relatively small number of potentially relevant scattering events that may take place in the physical scenario described above. With only this information we cannot know that the spin dependent effect is dominant. It is therefore necessary to compute the spin flip probability in a manner which incorporates all possible interactions described by the Hamiltonian and conceive of a physical scenario in which a spin flip is dominant.

3. Alternative Processes

In the previous section the focus was on particular perturbative terms. Here a more systematic approach is followed in which alternative processes are considered. Ignoring specific choices of the physical parameters, in first order perturbation theory three matrix elements $H_{fi}^{j} \equiv \langle f | H^{j} | i \rangle$ are possible (see Eq. 5), where the operators are $H^{1} = q^{2}A^{2}/2m$, $H^{2} = q\vec{p}\cdot\vec{A}/m$, and $H^{3} = \vec{\mu}\cdot\vec{B}$. At this point we consider as before two counter propagating laser pulses that are cross-fired with an electron, and the frequency of both fields is given by ω_1 and ω_2. The probability amplitude (Eq.6) is rewritten as $C_{fi}^{j} \equiv \left\| H^{j} \right\| f_{fi}^{j}(\tau)$, where the magnitude in decreasing order is given by $\left\| H^{1} \right\| \equiv q^{2}A_0^{2}/2m$, $\left\| H^{2} \right\| = q\vec{p}\cdot\vec{A}_0/m$, and $\left\| H^{3} \right\| = \vec{\mu}\cdot\vec{B}_0/m$, with $B_0 = kA_0$. The value of the amplitude (Eq. 5) can be approximated (see Appendix) by

$$C_{fi}^{j} \approx \left\| H^{j} \right\| \tau/\hbar . \tag{13}$$

The amplitude $C_{fi}^{j=1}$ is non-zero for $\omega_1 = \omega_2$ with an initial and final state choice of $-\hbar k$ and $\hbar k$. This process is the well-known KD-effect[16], conserves energy and momentum, and is a two-photon process. The number of photons in a process can be recognized by inspecting the power of the field. From equation (11) the probability of scattering is given by $(q^{2}A_0^{2}\tau/2m\hbar)^{2}$ in agreement with previous work[2, 16].

Energy and momentum can also be conserved for $C_{fi}^{j=1}$ when $\omega_1 \neq \omega_2$. However, when $\omega_1 = 2\omega_2$, for example, the electron needs to move relativistically at steep angles with respect to the laser propagation direction. The amplitudes C^{2} and C^{3} involve the interaction with one photon, which is kinematically not allowed.

In second order perturbation theory all combinations of two terms of H^j need to be considered. The matrix elements $H_{fmi}^{jj'} \equiv \langle f | H^j | m \rangle \langle m | H^{j'} | i \rangle$ give rise to a probability amplitude $C_{fmi}^{jj'} \equiv \| H^j \| \| H^{j'} \| g_{fmi}^{jj'}(\tau)$. The value of the amplitude (Eq. 9) can be approximated (see Appendix) by

$$C_{fmi}^{jj'} \approx \| H^j \| \| H^{j'} \| \frac{\tau}{\omega \hbar^2} \frac{\hbar k}{mc} \ . \tag{14}$$

The term $C_{fmi}^{j=1,j'=1}$ for $\omega_1 = 2\omega_2$ (where ω_1 comes from one direction and ω_2 from the other (see figure 6.1)) does not conserve energy and momentum, unless the initial and final state are identical. It is thus possible that our wanted spin-dependent kick is followed by this process. However, this term does not couple spin or momentum and will not dilute our process of interest.

The second order term $C_{fmi}^{j=1,j'=2}$ for $\omega_1 = 2\omega_2$ is the regular two-color KD-effect[17]. From equation (12) the probability of scattering is given by $\left(kq^3 A_0^2 \vec{p} \cdot \vec{A}_0 \tau / 2m^3 \omega \hbar c \right)^2$ in agreement with previous work[17]. To suppress this term, $\vec{p}$ is chosen perpendicular to $\vec{A}$. This also implies that $C_{fmi}^{j,j'=2} = 0$. The next term to consider is $C_{fmi}^{j=1,j'=3}$. That is the term of interest of this paper (see the derivation in the previous section). The last second order perturbative term, $C_{fmi}^{j=3,j'=3}$, can only conserve energy and momentum when the momentum and spin state is unchanged, and thus will not be observable in a scattering experiment.

Higher order processes are are worth considering as well despite the fact that it seems likely that they will be negligible compared to the spin dependent process of interest. For example third order perturbation theory might be expected to result weaker

processes than lower order perturbative processes, however, the combination of three strong matrix elements (i.e. matrix elements computed from the $q^2A^2/2m$ term of the Hamiltonian) might provide stronger scattering than our spin-dependent scattering term that has one strong and one weak matrix element. To consider the effects of all higher order processes a numerical integration of the Schrödinger equation was performed.

4. Numerical integration of Schrödinger's equation.

The numerical simulation written by Wayne Cheng-Wei Huang is to verify that the perturbation expansion analysis does not introduce incorrect results by limiting which processes are considered. The electron scattering to different states of momentum and spin are calculated by numerically solving the Pauli equation. Initially, the electron state is a plane wave described by

$$|\psi(t=0)\rangle = |k_x, k_z, s\rangle \tag{15}$$

where k_z and $|s\rangle$ indicate the initial state of the electron by specifying the z component of momentum and spin, respectively, and N is the normalization factor. The electron then passes through the two-color light $\vec{A}(z,t) = \vec{A}_R(z,t) + \vec{A}_L(z,t)$, which is composed of two light fields coming from opposite directions,

$$\vec{A}_L(z,t) \simeq 2A_L e^{-(t/\tau)^2} \cos(k_L z - \omega_L t)\ \hat{\varepsilon}_L,$$

$$\vec{A}_R(z,t) \simeq 2A_R e^{-(t/\tau)^2} \cos(k_R z + \omega_R t)\ \hat{\varepsilon}_R. \tag{16}$$

The frequency of one light field is $\omega_L = \omega_0$ and the frequency of the other light is $\omega_R = 2\omega_0$. The field polarization is described by the unit vector $\hat{\varepsilon}$ in the $\mathrm{x\text{-}y}$ plane. Because the light field has no spatial dependence in the x-direction, the electron is scattered to multiple $|k_z\rangle$ states, while the $|k_x\rangle$ state stays intact,

$$|\psi(t)\rangle = \sum_{n,j} C_{n,j}(t) e^{i\omega_n t} |k_x, k_z + k_n, s_j\rangle, \tag{17}$$

where $\omega_n = \hbar\left[k_x^{\,2} + \left(k_z + k_n\right)^2\right]/2m_e$, and $k_n = nk_0 = n\omega_0/c$. In order to calculate the scattering coefficients $C_{n,s}$, we solve for the Pauli equation,

$$H' = \left(\frac{p_x^{\,2}}{2m_e} + \frac{p_z^{\,2}}{2m_e} - \frac{q_e}{m_e}A_x p_x + \frac{q^2}{2m_e}(A_x^{\,2} + A_y^{\,2})\right) \otimes I_s - \frac{\hbar q_e}{2m_e}\left(B_x \otimes \sigma_x + B_y \otimes \sigma_y\right), \tag{18}$$

where I_s is a 2×2 identity matrix and σ_i are the Pauli matrices. The Hamiltonian can be decomposed into an unperturbed part,

$$H_0 = \left(\frac{p_x^{\,2}}{2m_e} + \frac{p_z^{\,2}}{2m_e}\right) \otimes I_s, \tag{19}$$

and a perturbation part,

$$H' = \left(-\frac{q_e}{m_e}A_x p_x + \frac{q^2}{2m_e}(A_x^{\,2} + A_y^{\,2})\right) \otimes I_s - \frac{\hbar q_e}{2m_e}\left(B_x \otimes \sigma_x + B_y \otimes \sigma_y\right). \tag{20}$$

Given the scattered electron state as shown above, the Pauli equation can be simplified to

$$\frac{d}{dt}C_{m,i}(t) = -\frac{i}{\hbar}\sum_{n,j} H'_{2(m-1)+i,2(n-1)+j} C_{n,j}(t) e^{i\omega_{mn}t}, \tag{21}$$

where $\omega_{mn} = \omega_m - \omega_n$ and

$$H'_{2(m-1)+i,2(n-1)+j} = \langle k_x, k_m, s_i | H' | k_x, k_n, s_j\rangle$$

$$= -\frac{q_e \hbar k_x}{m_e}\langle k_m | A_x | k_n\rangle + \frac{q^2}{2m_e}\langle k_m | \left(A_x^{\,2} + A_y^{\,2}\right) | k_n\rangle$$

$$-\frac{\hbar q_e}{2m_e}\left(\langle k_m | B_x | k_n\rangle\langle s_i | \sigma_x | s_j\rangle + \langle k_m | B_y | k_n\rangle\langle s_i | \sigma_y | s_j\rangle\right). \tag{22}$$

When calculating for the matrix element, it is convenient to use the formula,

$$\langle k_m \mid e^{\pm ik_0} \mid k_n \rangle = \delta_{m,n\pm 1}. \tag{23}$$

The above calculations were performed with the initial electron state given by $k_z = 2\hbar k_0$ and $|s\rangle = |\hbar/2\rangle$. The initial electron velocity was 10^7m/s and the lasers were polarized in the y direction. The probability of the spin dependent scattering process as computed by the above method with the same process computed by perturbation theory are shown in figure 6.3 demonstrating good agreement between the two methods. Additionally, the two color K-D effect and as well as the regular K-D effect (for $\omega_L = \omega_R$) are plotted for comparison.

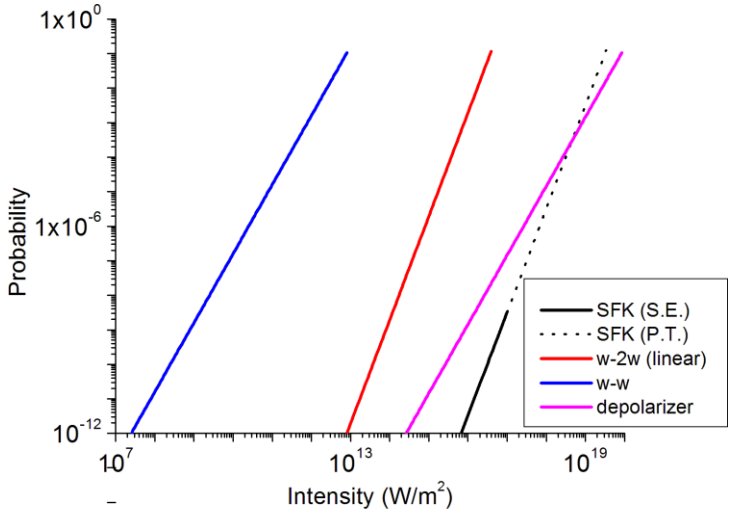

Figure 6.3

Probability vs. Intensity

The probability of the spin flip kick scattering process as computed by the above method (SFK(S.E.)) with the same process computed by perturbation theory (SFK(P.T.)) are shown demonstrating good agreement between the two methods. Additionally, the two color K-D (w-2w(linear)) effect, the regular K-D (w-w) effect (for $\omega_L = \omega_R$), and the depolarizer are plotted for comparison.

The probability of the spin dependent process of interest is about 0.01 at 10^{19}W/m^2. This exceeds the depolarizing process by about an order of magnitude thus making the diluting effect of the latter negligible (i.e. of the electrons which undergo the spin flip kick process, only approximately 1 in 10^3 will return to spin up). The implications of a comparative analysis of the $\omega-\omega$ and $\omega-2\omega$ K-D effects with the spin flip momentum kick process are discussed in the discussion section of this paper.

The probability associated with final momentum states having z components of $p_z = n\hbar k_0$ for $n=-7$ through 7 are shown in figure 6.4 for spin up and spin down. These values were computed for a laser intensity of 10^{18}W/m^2.

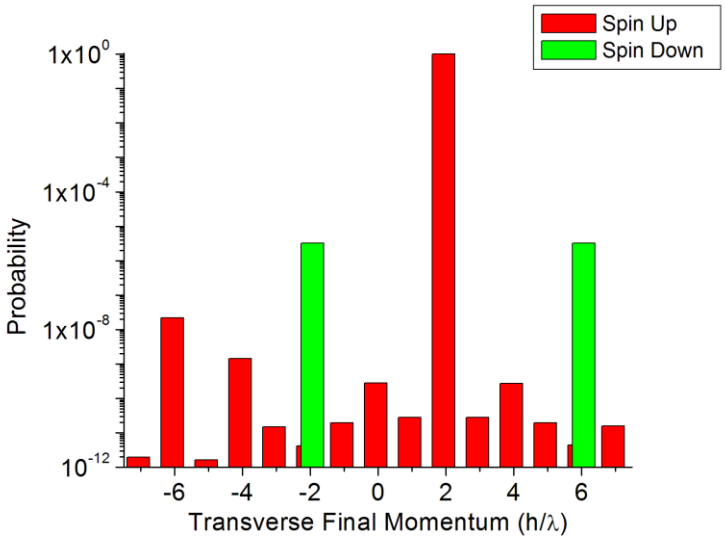

Figure 6.4

Final State Probability Distribution

The probability associated with final momentum states having z components of $p_z = n\hbar k_0$ for $n=-7$ through 7 are shown for spin up and spin down.

At this intensity it is clear that the spin flip kick process of interest is dominant over all non-trivial processes. Here there is no worry of accidentally excluding some other

potentially larger process because the direct integration of the Schrödinger equation implies the inclusion of all orders. According to this computation, at $10^{18}W/m^2$ the probability of the spin flip kick is a little more than 10^{-6}, confirming again the perturbative calculation shown in figure 6.3. One possible concern is the validity of the assumption that the motion induced within the laser field is non-relativistic. This is addressed in the next section.

5. Relativistic Classical Simulation

In order to assess if some of the assumptions made are valid relativistic classical electron trajectories were computed by Professor Bradley Shadwick. The particular assumptions are: *i*) the electrons do not reflect from the ponderomotive barrier presented to the electron by the laser light, *ii*) the electrons do not reach relativistic factors γ that strongly exceed 1, and *iii*) the electron are not deflected transversally by much more than the deflection produced by the spin-dependent scattering (i.e., four photon recoils). It is important to validate these assumptions in order to give credence to the calculations made thus far. Predictions that have been made in the previous sections were based on non-relativistic quantum mechanics. This requires sufficiently low velocity electrons throughout the interaction with the laser field. Additionally scattering from the ponderomotive potential will result in broadening of the diffraction peaks. If the maximum deflection due to ponderomotive scattering exceeds that of the spin dependent scattering, the peak corresponding to the effect of interest will be resolved. Finally, if the electron is reflected back from whence it came, it cannot pass through the laser and arrive at the detector.

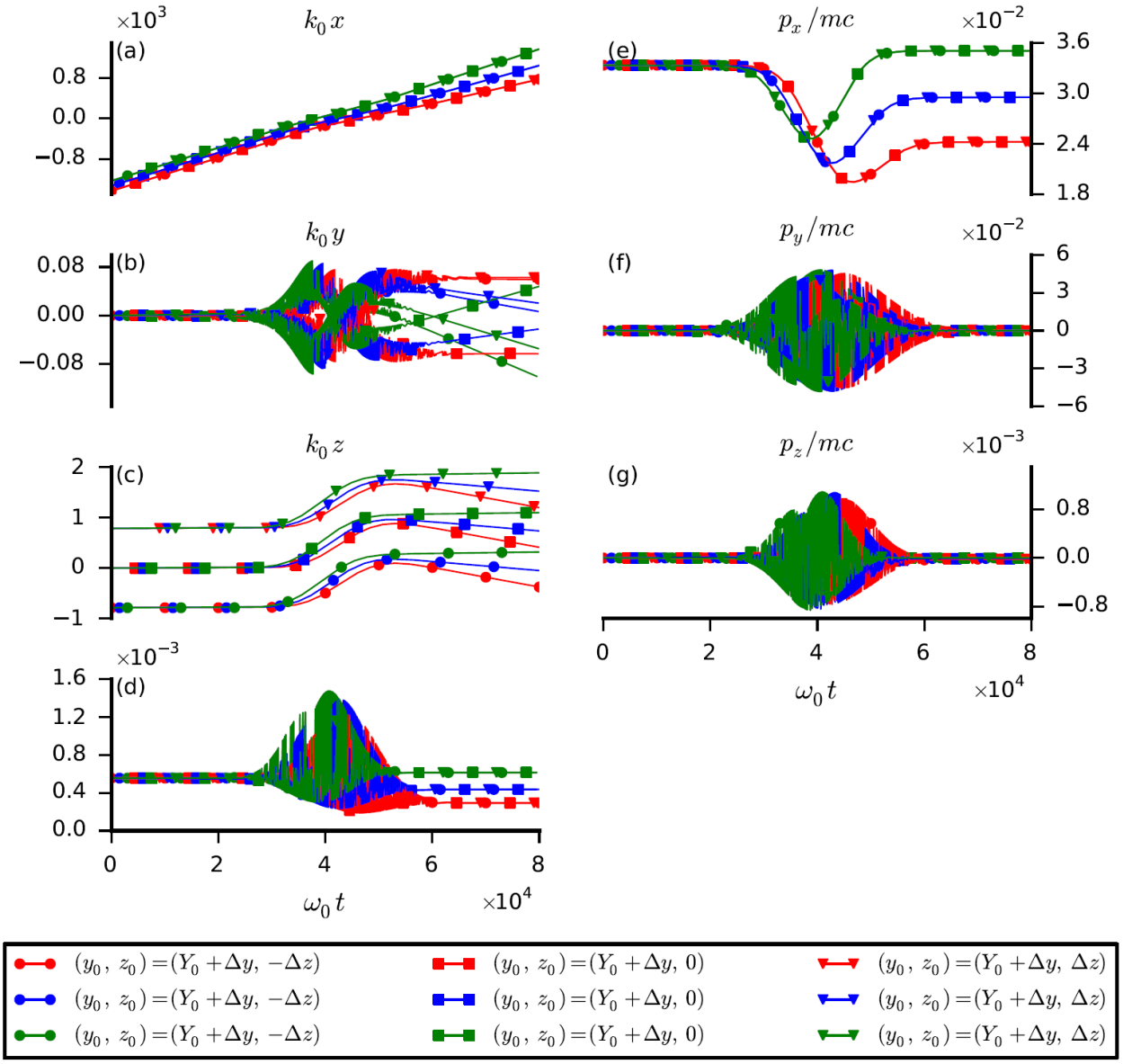

Figure 6.5

Relativistic Classical Trajectories

Shown here is the time dependence of the position of the electron a) k_0x, b) k_0y, c) k_0z; momentum of the electron e) p_x/mc, f) p_y/mc, g) p_z/mc; and d) the relativistic factor γ-1. Each is shown for different initial positions.

The relativistic equations of motion are solved numerically for a single electron traversing counter-propagating laser pulses. The electron momentum and position evolve according to

$$\frac{d\vec{p}}{dt} = q\left(\vec{E} + \vec{v} \times \vec{B}\right), \tag{24}$$

$$\frac{d\vec{r}}{dt} = \vec{v}, \tag{25}$$

where q and m are, respectively, the charge and mass of the electron, $\vec{p} = \gamma m \vec{v}$, $\gamma^2 = 1 + p^2/m^2c^2$, and the electric and magnetic fields are evaluated at the location of the electron. The laser pulses, taken to be described by the lowest order paraxial Gaussian mode[40], are polarized in the y-direction, propagate in the z-direction and have a 100μm spot size at the focus. The pulse propagating in the positive z-direction has frequency ω_0 corresponding to a wavelength of 1μm with a peak value of the vector potential given by $qA/mc^2 = 0.03$ $\left(I_{\omega_0} = 1.24 \times 10^{19}\, W/m^2\right)$ while the pulse propagating in the negative z-direction has frequency $2\omega_0$ with peak value of the vector potential given by $qA/mc = 0.02$ $\left(I_{2\omega_0} = 2.20 \times 10^{19}\, W/m^2\right)$. For both laser pulses, the vector potential has the Gaussian temporal profile $\exp\left[-\left(z - ct\right)^2/\tau^2\right]$ with $\tau = 10\, ps$. The laser pulses are initialized such that they reach the focus at $z = 0$ at $\omega_0 t = 4000$. The electron is initially propagating in the positive x-direction with a velocity $v_0 = c/30$. The sensitivity of the deflection to initial conditions can be seen by examining trajectories over a set of initial conditions. Initially, we take y = 0 and (x, z) from the set of nine pairs $\left[X_0 - \Delta x, X_0, X_0 + \Delta x\right] \times \left[-\Delta z, 0, \Delta z\right]$, where $k_0 X_0 = 4000\, v_0/c$, $k_0 \Delta x = 100$, and

$k_0 \Delta z = \pi/4$. The value for X_0 is chosen such that, in the absence of an interaction with the laser field, the electron would arrive at the origin at the same instant that the laser pulses reach focus and have maximal overlap. The value of Δx is chosen to be comparable the laser spot size, and Δz is chosen comparable to the laser wavelength. All computations are performed in dimensionless variables using ω_0 and $k_0 = \omega_0/c$ to set the temporal and spatial scales while mc is used for the momentum scale.

The top three panels in the left (right) column of figure 6.5 indicate the electron position (momentum) as is propagates through the laser pulses. Panel (b) and (f) show that as the electron is present in the laser field it performs an oscillatory motion, which is due to the electric part of the laser field. Panel (a) and (e) show that the ponderomotive potential affects the electron motion in the forward direction, and validates assumption *i*). Panel (c) and (g) show that the magnetic part of the Lorentz force causes an oscillatory motion. Panel (d) shows that the gamma factor does not strongly deviate from one at any time, validating assumption *ii*). Panel (c) also shows that the transverse deflection reaches maximum values of $4\hbar k$ (which occurs at $k_0 \Delta z = \pi/4$), validating assumption *iii*).

From this analysis it is possible to deduce what the limitations are in a demonstration of the spin dependent effect. While the intensity of the lasers is not limited by the demand of keeping the electron trajectory non-relativistic it is limited by deflection. While the transverse ponderomotive scattering in this case is sufficiently low an increase in intensity would lead to increased deflection pushing the broadening of diffraction peaks to an unacceptable level.

6. Discussion

It appears there is a window of parameter values where spin-dependent scattering of laser light with electrons is dominant. However, in a real experiment spurious effects can be present and overwhelm the process of interest. Three of such effects are now discussed. With short pulses the frequency distribution of one laser beam (centered around ω) could be broadened so that it has a nonzero value at the peak of the distribution of the counter-propagating laser beam (centered around 2ω). Since the regular (ω-ω) K-D effect[2] is so much stronger than the effects considered in this paper, one may wonder if it will overshadow our effect in spite of the fact that the two frequencies are an octave apart. If 10ps pulses of light with 1064nm wavelength are used, than the difference between the two frequencies is about 10^4 times the uncertainty of each distribution. This leads to negligible effect for a Lorentzian (or Gaussian) spectral distribution of the laser. The regular K-D effect is thus sufficiently reduced by the separation of the frequencies.

In practice, the 2ω laser beam may be generated by up-conversion and result two co-propagating beams that need to be separated optically. If this is not done the regular K-D effect will still be present. Dichroic mirrors and filtering can be used to provide separation of the two frequencies. Our analysis indicates that the ratio of the first order over a second order process (Eq. 11 and 12) is given by $\left(\left\| H^{j'} \right\| \frac{1}{\omega\hbar} \frac{\hbar k}{mc} \right)^{-1}$. For the spin dependent coupling $\left\| H^{j'} \right\| \approx \mu B$ and an intensity of 10^{19}W/m^2 this is about 10^6. To suppress the regular K-D effect by this much an isolation in intensity of 10^{-6} is thus required.

The strong regular two-color K-D effect is suppressed by the choice that the laser polarization is perpendicular to the electron velocity, because this K-D effect has $\left\| H^{j'} \right\| \approx \frac{q}{m} \vec{p} \cdot \vec{A}$ term in the Hamiltonian. However the polarization angle or electron beam direction may be misaligned. The ratio of the regular two-color K-D effect over the spin-dependent K-D effect is $\frac{q}{m} \vec{p} \cdot \vec{A} / \mu B$, which equals about 10^5. Since the amplitude of the regular effect is proportional to $\cos\theta$, where θ is the angle between the electron velocity and the laser polarization, than angle should be aligned better than $0.01\,\text{mrad}$ from the perpendicular.

The three spurious effects given above can be discriminated against as they have distinguishing features which can isolate them from the spin-dependent scattering term of interest. The spin-dependent effect is not velocity dependent nor polarization angle dependent in contrast to the two color K-D effect. It can also be distinguished from the regular K-D effect by the different intensity dependence.

It is important to note that the effect discussed in this paper differs from the relativistic effect proposed by Ahrens *et al.*[9] in more ways than one. In the paper by Ahrens *et al.* the frequency of the two laser beams is the same, the laser light has a photon energy of 3.1keV, and the 176keV electrons are incident at an angle that is far from perpendicular to the lasers.

Given the wavelength dependence of the two and three photon effects it is tempting to consider lowering the frequency of the lasers to dramatically boost the probability. If the wavelength is increased the focal width too will increase which eventually will result in a wavelength dependent interaction time. Assuming an

interaction time that is proportional to wavelength, the two photon effect and the three photon effect become proportional to λ^4 and λ^6, respectively. While the ratio of the probabilities remains the same in this case the two effects become more strongly wavelength dependent by an added factor of λ^2 thus increasing the benefit of a longer wavelength.

It is apparent from the numbers presented in Table 6.1 that with the right parameters the probabilities of the two photon and three photon effects are comparable. Since the probability of a spin flip with no momentum kick due to the two photon process is the same for both spin states regardless of input angle this effect can be thought of as a depolarizer. If a polarized beam of electrons propagates through a laser field some of the electrons will not flip, some will flip once, while others will flip more than once. The output electron beam will be depolarized to some extent which depends on the intensity of the laser field. This could potentially be a problem. If the three photon process is used to create a polarized electron beam, that beam could be depolarized by the very same set of counter propagating lasers before it has a chance to exit the field. With such an experiment in mind, it is therefore necessary to set the parameters such that the probability associated with the two photon process is small compared to the probability associated with the three photon process.

7. Conclusion

In this paper we have shown that a dominant spin dependent K-D effect is possible, given the appropriate laser configuration. This effect could be used as an ultrafast spin polarized electron source or to analyze such a source. Applications include ultrafast electron diffraction, and ultrafast electron microscopy as well as more

fundamental physics studies looking into what the dominant interactions in multi-electron pulse or whether the control and analysis of femtosecond electron polarization affect X-ray production in relativistic Compton scattering.

Chapter 7 - A Wide-Angle Electron Grating Bi-Prism Beam-Splitter

1. Introduction

For the past half-century, electron interferometers have been used for both fundamental physics as well as more applied areas.[1] The shorter de Broglie wavelength of electrons provides electron interferometers with a much finer measuring "comb" than their optical counterparts. The electron's charge also provides for strong coupling to its environment. This combination has made electron interferometers a powerful tool for the study of fundamental physics. The first electron interferometer was constructed using metallic crystals as diffractive elements in 1953.[2, 3] Shortly afterwards, an interferometer using a bi-prism wire in lieu of metallic crystals was demonstrated in 1955.[4] All subsequent devices fell into these two basic types until recently, when interferometers using nanofabricated gratings were realized in 2006.[5-7]

More recently, applications of large area interferometers have become of interest, spurring further development of electron matter optics elements. For instance, determining the electron forward scattering amplitude with atoms or molecules by placing a gas cell in one arm of the interferometer requires large beam separation.[8] Also, the separation distance controls decoherence induced by nearby surfaces and relates to studies of the quantum-classical boundary.[9] A large area electron interferometer may also be the first step towards a proposed novel method of high-sensitivity rotation sensing using an charged particle interferometer enclosed in a Faraday cage.[10] The application which the authors are pursuing is a test of the dispersionless nature of the Aharonov-

Bohm effect.[11] Such a test requires placing a large solenoid between the arms of an interferometer.

As a first step towards this goal, high-quality electron diffraction from a nanofabricated grating has been demonstrated[12]. To ensure that the diffracted beams are also coherent, our group has also previously demonstrated a three grating Mach-Zehnder interferometer.[5] However, the small separation between the electron beams (3 μm) does not allow for objects to be placed between, or in, one of the interferometer arms. In this chapter the construction of a large angle beam-splitter composed of a nanofabricated grating in conjunction with a bi-prism wire is reported.

2. Experimental Setup

A schematic of the experimental setup is shown in Figure 7.1. A Kimball Physics EGG-3101 electron gun was used as a thermionic source at an energy of 7.5 keV with an estimated ΔE of 1 eV. All electron optics elements aside from the electron gun are rigidly mounted on a rail system. Two layers of magnetic shielding inside the vacuum system enclose the rail system. The inside layer is grounded at a single point to minimize eddy currents and thus provide shielding to oscillating magnetic fields. An external Faraday cage provides shielding from stray electric fields. A 2 μm diameter molybdenum circular aperture at a distance of 12 cm from the electron gun provides beam collimation. A second identical aperture 18 cm behind the first further narrows beam divergence. The beam is incident on a 100 nm periodicity nanofabricated grating situated 7 cm from the second aperture. The grating used is identical to those used by Gronniger *et al*.[5] The spatial transverse coherence length of the electron beam incident

on the grating is estimated to be 750 nm, based on the ratio of diffraction order separation to beam width and grating periodicity.[12]

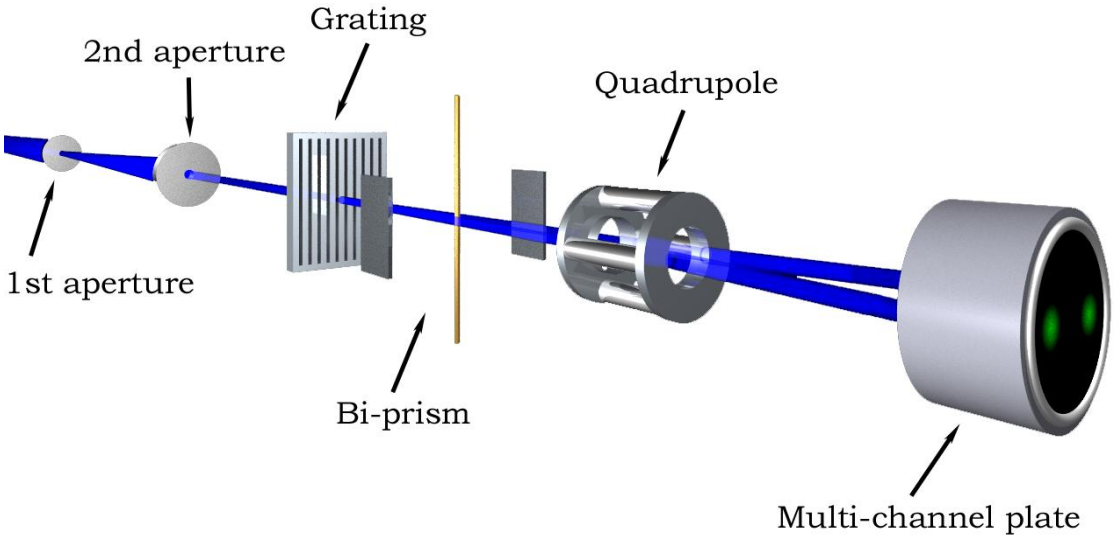

Figure 7.1

Schematic of Experimental Set-Up

Two apertures collimate an electron beam. A grating then coherently splits the beam. The zero order diffraction beam is blocked by the bi-prism wire, while the dominant first order beams pass on either side. The wire increases the beam separation without broadening, while the quadrupole magnifies the entire diffraction pattern. A multi-channel plate and a fluorescent screen are used to image the pattern.

As the beam encounters the grating it undergoes diffraction, with the angles at which maxima occur given by

$$n\lambda_{dB} = d\sin(\theta_n), \tag{1}$$

where n is the order number, λ_{dB} is the de Broglie wavelength of the electrons, d the grating periodicity, and θ_n is the diffraction angle. The quality of the diffraction pattern is good, and similar gratings have produced resolved orders out to the positive and

negative 21st order .[12] In this study use is made of the positive and negative 1st order beams. The diffracted beam is aligned such that the 0th order is centered on, and thus mostly blocked, by the bi-prism wire.

The wire is placed at a distance of 5.5cm from the grating. The mount for the wire is shown in Figure 7.2.

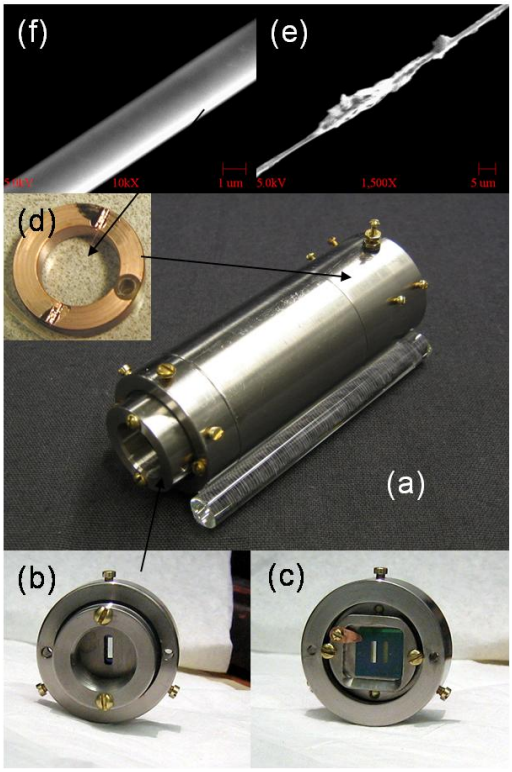

Figure 7.2

Grating Bi-Prism Electron Beam-Splitter

The titanium 3 cm diameter mount (a) holds the grating mount (b,c) and the copper coated Ultem bi-prism mount (d). The front view of the grating mount (b) shows the centered opening that the electrons are incident upon. The back view of the grating mount (c) shows the gold coated SiN 100 nm periodicity grating. Care should be taken to select the bi-prism wire. Electron microscope images of bad coating run (e) and good coating run (f) are shown.

The wire itself is composed of a quartz glass fiber that has been coated with gold via sputtering to a thickness of approximately 100 nm. The quartz fiber is produced by

rapidly expanding a rod of quartz that has been melted. A similar technique for wire production is described by Hibi and Yada.[13] The resulting thin thread is then mounted on an electrically insulating ring (composed of Ultem). The diameter of the wire for the data in this work is 5 μm.

A voltage V_{bp} applied to the bi-prism wire gives a potential surrounding the wire which can be approximated as[1]

$$V(r) = V_{bp} \frac{\ln\left(r/R_{el}\right)}{\ln\left(R_{bp}/R_{el}\right)}, \tag{2}$$

where r is the radial distance from the wire, R_{bp} the radius of the wire, and $R_{el} = 6\,\text{mm}$ is the distance from the wire to the grounded electrode. The potential given by Eq. (2) results in a deflection, which for small angles is[1]

$$\delta = \frac{\pi e V_{bp}}{2E_{el} \ln\left(R_{bp}/R_{el}\right)}, \tag{3}$$

where E_{el} is the kinetic energy of the electron beam, expressed in eV. The deflection angle is therefore independent of the radial distance of the beam from the bi-prism. A negative voltage applied to the wire increases the angle between the first order beams.

A set of deflection plates is placed 4 cm downstream from the bi-prism. An electrostatic quadrupole situated 7 cm behind the bi-prism provides an optional magnification of the diffraction pattern and deflected beams. The detector consists of microchannel plates (MCP) in combination with a phosphor screen, and is located 38 cm beyond the quadrupole. At 7.5 keV, the adjacent diffraction peaks are separated by 75 μm (at the detection screen). The peak width is determined by the transverse coherence length[12], and expected to be 10 μm.

3. Path Integral Calculation

The theoretical description of the physical system is based on Feynman's path integral formulation.[14] Propagation from an initial wave function given by $\Psi_i(x)$, to the final wave function $\Psi_f(x)$, in the path integral formulation is given by

$$\Psi_f(x) = \int K_{i\to f}(x', x)\Psi_i(x')dx'. \tag{4}$$

The coordinate system is chosen so that the incident electron beam is aligned along the z-axis, while the slits and grating are parallel to the x-axis. The kernel in Eq. (4) is given by

$$K_{i\to f}(x', x) = \exp\left(iS(x, x')/\hbar\right), \tag{5}$$

where S is the classical action. For our system the wave function propagates in free space between the planes where the slits, grating, bi-prism and detector are located. For that part of the propagation the action simplifies to

$$S(x, x') = 2\pi l(x, x')/\lambda_{db}. \tag{6}$$

The length of a straight individual Feynman path $l(x, x') = \sqrt{(x-x')^2 + (z-z')^2}$ is measured from some point (x', z') on a plane to a point (x, z) on a subsequent plane, and λ_{db} is the deBroglie wavelength of the matter wave.

At these planes, the wave function is modified in the following way:

$$\Psi_{plane,out}(x) = A(x)\exp(i\varphi(x))\Psi_{plane,in}(x). \tag{7}$$

For example, at the slit plane the amplitude of the wave function is modified by

$$A_{slit}(x) = H(x + w/2)\cdot H(-x + w/2), \tag{8}$$

where w is the slit width and H is the Heaviside function, while the phase is unaffected ($\varphi(x)=1$). For the detailed description of the effect of a grating see Barwick *et al.*[15] For this chapter the description of the bi-prism needs to be added. The bi-prism blocks the electron over its width:

$$A_{bp}(x) = H(-x - R_{bp}) + H(x - R_{bp}). \tag{9}$$

The electrons that pass the bi-prism accumulate a phase shift. This phase shift is due to the bi-prism potential given by Eq. (2). To apply Eq. (7), the phase shift that is caused by the electron passing through this potential is given by

$$\varphi_{bp}(x) = \frac{e}{\hbar v}\int_{-\infty}^{\infty} V(r(x,z))dz, \tag{10}$$

where v is the electron velocity. This integral diverges; however only local phase differences accumulated for trajectories at different distances from the wire are relevant. Setting the global phase equal to zero at $x=0$ gives

$$\varphi_{bp}(x) = \frac{e\pi}{\hbar v}\frac{V_{bp}}{\ln(R_{bp}/R_{el})}x. \tag{11}$$

Consecutive application of Eqs. (4) and (7) yields the wave function at the detection plane, from which the probability distribution of the diffraction pattern can be found directly:

$$P_{\det}(x) = |\Psi(x)|^2. \tag{12}$$

4. Results

A diffraction pattern with a quadrupole setting producing a magnification of 16X, and zero voltage on the bi-prism, is shown in the graph of Figure 7.3a. The magnification factor is determined by comparing the measured peak positions to those

given by Eq. (1). The shadow of the bi-prism wire blocks most of the zero order diffraction peak which is centered around 0 mm in the graph. The 1^{st}, 3^{rd}, and 5^{th} diffraction orders are visible on the left and right hand side of the bi-prism shadow. As expected, the even orders are suppressed as a result of using a grating with an open fraction of 50%.[15] The solid line is the result of a path integral simulation written by Roger Bach. The simulation result is scaled by the magnification factor. The result of the simulation is fully left-right symmetric, while the data is not. For example, an offset in the bi-prism position can cause the asymmetry in the 0 order remnant. As the voltage on the bi-prism wire is increased to -20 and -40 volts, the beam separation between the negative and positive diffraction orders increases, while the distance between orders of the same sign does not increase (see Figure 7.3 b and c). This indicates, as expected, that the bi-prism deflection angle does not depend on the distance that the electron passes from the bi-prism wire.

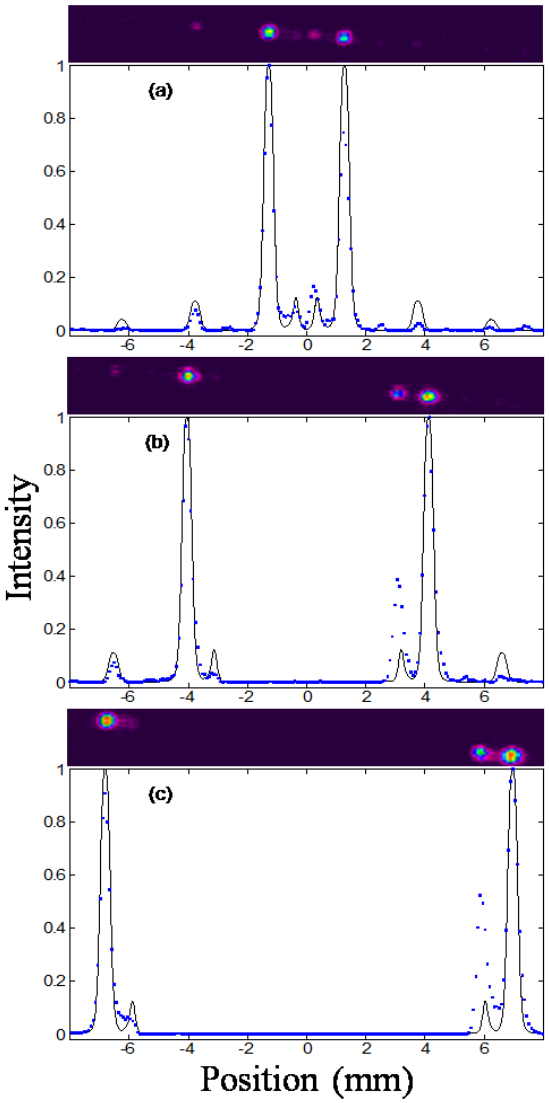

Figure 7.3

Diffraction Patterns at Different Bi-Prism Voltages

The photographed image of an electron diffraction pattern and the associated line graph are shown for bi-prism voltages of (a) 0V (b) -20V (c) -40V. Experimental data (blue dots) and a path integral calculation (solid line) are compared. The zero order diffraction peak is mostly blocked by the bi-prism wire. The diffraction peak separation and width do not substantially change as the bi-prism voltage is increased.

To investigate if the grating-bi-prism is a useful beam splitter for a large angle electron interferometer, the beam separation needs to be sufficiently large without

causing significant beam distortion. A full interferometer would require a second bi-prism wire and/or grating to be installed after the first one to redirect the electron beams towards each other. To reach a separation of 1 mm between the electron interferometer arms at the second bi-prism in our device, a bi-prism voltage of 400 V was required (The observed separation at the detection screen is about 1 cm with the quadrupole turned off). The geometric separation at the second bi-prism is $\frac{5cm}{L} \times 1cm$, where L is the distance between the first bi-prism and the detection screen. Such a separation is a ten-fold increase as compared to any previous electron interferometer design.[1, 16] To test if there is beam distortion at such large bi-prism voltages, the quadrupole magnification needs to be large enough such that the width of the diffracted beams exceed the spatial resolution of the detector system.

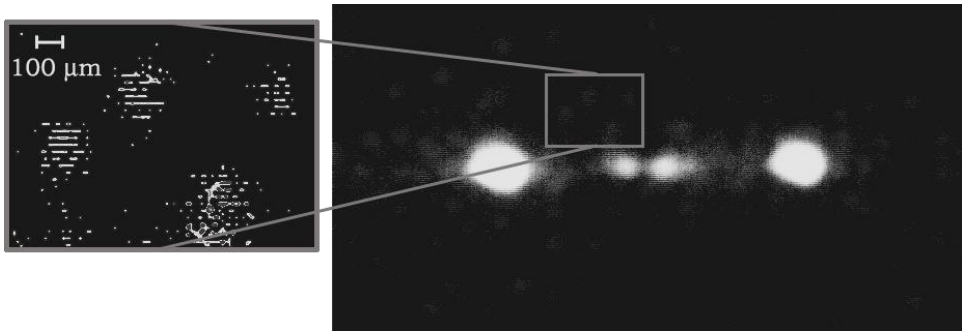

Figure 7.4

Electron Spot Size

An image of an electron diffraction pattern is shown. In the background, fluorescent spots due to single electrons are visible. The width (FWHM) of the single electron spots is in the 100-150 □m range, showing that the spatial resolution of the apparatus exceeds the diffraction order width.

The spatial resolution of our detection system (including camera) was about 100-150 μm as determined from the observed size of individual electron hits (Figure 7.4). To account for this, the simulation includes a convolution with a Gaussian width of 150 μm.

The quadrupole increases the beam width to exceed this value. Additionally, moderate electrostatic lensing at the second collimating aperture was added to obtain good agreement between the measured and simulated diffraction peak widths (Figures 7.3 and 6.5). The lensing was incorporated in the simulation by adding a parabolic phase shift over the width of the second aperture. The width of the observed diffraction orders is about 375 μm.

In Figure 7.5a the measured beam width is shown as a function of applied bi-prism voltage. The major feature is that the beam becomes narrower at larger bi-prism voltages. It is important to note that the combined effect of the bi-prism voltage and quadrupole magnification are large enough to shift the electron beam off the detection plate. To overcome this difficulty, the deflection plate in front of the quadrupole was used to keep the position of the beam at the same spot on the detection plate. The beam narrows by about 100 μm at bi-prism settings of ±400 V. The same narrowing can be obtained in our simulation by adjusting the lensing strength of the parabolic potential. The maximum phase shift needed to obtain such a narrowing is about π radians (Figure 7.5b). This phase shift is small enough to permit interferometry. Moreover, it is likely that the phase shift distortion caused by the bi-prism is much smaller. Reflection symmetry in a plane through the bi-prism wire and parallel to the incident electron beam, demands that $V(x) = V(-x)$, where x is orthogonal to the plane. This means that lensing for electrons passing on the left ($x < 0$) or right ($x > 0$) of the wire is the same. For our data the polarity of the bi-prism voltage is switched for the negative first order diffraction beam (which passes on the left) as compared to that for the positive first order diffraction beam (which passes on the right). The lensing, if caused by the bi-prism, should thus be

of opposite sign; broadening for negative bi-prism voltages and narrowing for positive bi-prism voltages. This is not observed, and the phase shift distortion is likely due to other electrostatic elements such as the quadrupole.

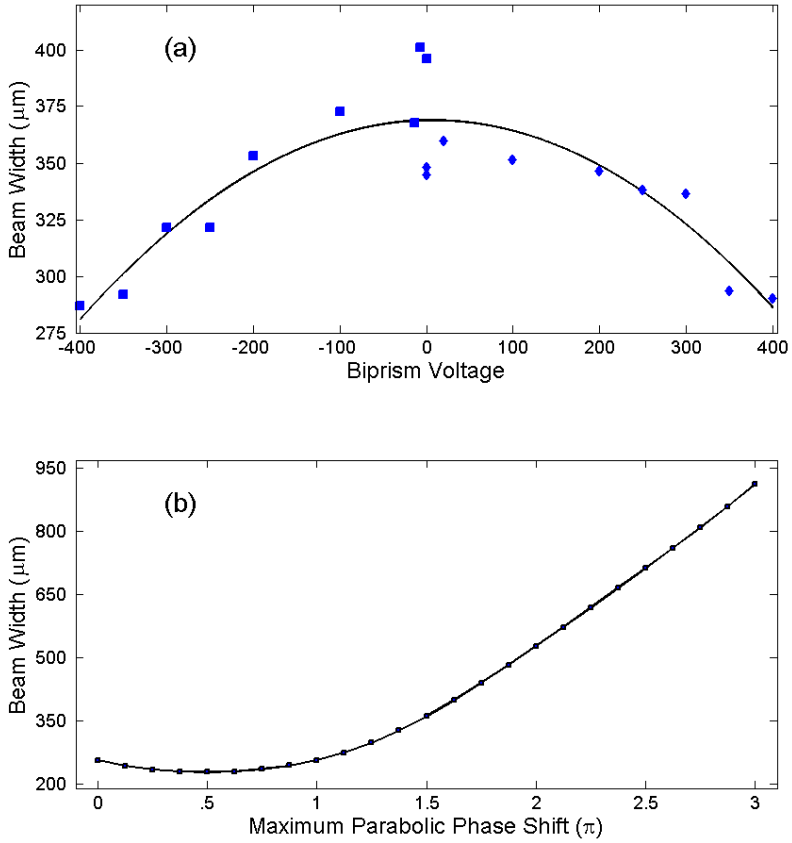

Figure 7.5

Phase Distortion Estimation

(a) The measured diffraction beam width as a function of the bi-prism voltage is shown. The beam narrows by about 100 μm. (b) A simulation of beam width variation due to a parabolic potential is given. The parabolic potential is applied across the electron beam. The edge of the beam accrues the maximum phase shift. As the potential strength and thus the maximum phase shift are changed, the beam width varies. Starting at a width of about 375 μm, a width reduction of 100 μm requires a phase shift of about π radians.

5. Conclusion

As the beam-splitting device presented here is a novel combination of previously developed techniques; a material grating and bi-prism, it is useful to compare benefits and drawbacks with other beam splitting techniques used for electron interferometers. The three-grating Mach-Zehnder interferometer presented in Gronniger *et al*[5] achieves a maximum beam separation of 3 μm with a grating spacing of 2.5 cm. By comparison, our device can easily attain a distance of 1 mm between beams at a distance of 5 cm behind the bi-prism wire. In order for a three-grating setup to achieve the same separation the distance between the gratings would need to be approximately 4 m, as there is no beam adjustability present. Moreover, it has been shown that dephasing occurs at the 2nd grating at lower electron energies.[5] The three grating interferometer loses contrast below energies of 5 keV. For a bi-prism interferometer it is known that at energies below 1 kV, the interference contrast reduces sharply.[17] The cause of this behavior is possibly due to a combination of increased sensitivity to external fields, mechanical alignment details and interaction with nearby surfaces. It has been shown that decoherence can be caused by a purposefully introduced metallic surface near the electron paths in a bi-prism electron interferometer.[9, 18] Bi-prism wires provide metallic surfaces with a close proximity to the electrons. In the operation of bi-prism electron interferometers, great care is used to select a high quality wire.

The idea of a hybrid grating bi-prism beam-splitter based interferometer is that the grating will provide some initial distance between the diffracted electron beams and the bi-prism wire to reduce decoherence, while keeping the adjustability provided by the potential on the wire to enable a large beam-splitting angle. Difficulties in the grating bi-

prism approach to interferometry include its sensitivity to mechanical alignment. For example, a slight displacement of the bi-prism wire so that it is not situated in the middle between the two diffraction orders will, upon recombination of the two electron beams, lead to slightly different path length. If these exceed the longitudinal coherence, no fringes will be observed. This difficulty and others is discussed in more detail in the next chapter.

Electron interferometers utilizing bi-prism filaments have been used extensively in the past 50 years in a wide variety of tasks, and as such are a proven technology. The principal difference of these types of devices from material gratings is that bi-prisms cause wavefront splitting of the electron beam, while gratings are amplitude splitting devices. Amplitude splitting creates two copies of the incident beam, which are then propagated in space. Wavefront splitting simply divides one wavefront into two, thus the spatial coherence of the original electron wave must exceed the bi-prism wire diameter to allow the two divided wavefronts to interfere when recombined later. Additionally, since the bi-prism is placed directly in the path of the wavefront, surface effects due to the wire are more pronounced than in our device where the beams are spatially separated from the bi-prism. Furthermore, the largest beam separation bi-prism interferometers obtain is about 120 μm[1, 16]. The question of how large a beam separation in an interferometer can be achieved using material gratings is an open one. However, a grating-bi-prism combination seems more suited to explore this than the use of multiple gratings given its ability to produce relatively large separation distances in a small apparatus size, as discussed above.

Chapter 8 - A Field Emission Tip Bi-Prism Interferometer

1. Introduction

The work discussed in chapter 7 was intended to be the first steps toward a new type of interferometer. An interferometer which consists of a grating to generate two beams by amplitude splitting (the two first order diffracted beams), and a bi-prism to pull them back together. Figure 8.1 shows the design of the interferometer. The beam first travels through two collimating apertures. It is then sent through a grating which splits up the beam into diffraction orders. The zero order is blocked by the bi-prism and the two first order beams are pulled together by the bi-prism wire. The interference pattern is then magnified by two quadrupole lenses and projected onto a multichannel plate with a phosphor screen where the pattern can be observed. An overview and the testing of each experimental component made during the effort to measure interference fringes with this device are thoroughly documented in the dissertation of Adam Caprez[1]. This effort did not successfully produce interference. In order to investigate the potential difficulties the system was simplified to consist only of a field emission tip, a bi-prism wire, and two quadrupole lenses (i.e. the same set up as depicted in figure 8.1b but with the grating removed and the 25μm slit replaced with a 250μm aperture). Because the grating has been removed the two arms are generated by splitting the beam with the bi-prism wire. Once the beam is separated by wave front splitting, the two halves are pulled together by the bi-prism. Such an interferometer has been created and fringes have been observed. This may allow for improvement of the system as a useful precursor to the grating bi-prism interferometer. In this chapter the production of the bi-prism, successful

measurement of fringes with the tip bi-prism setup, and potential solutions for the grating bi-prism interferometer are discussed.

a)

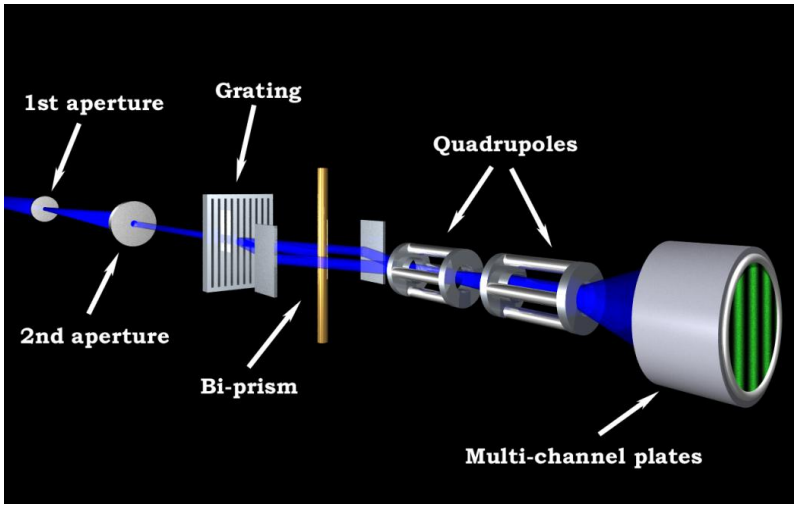

b)

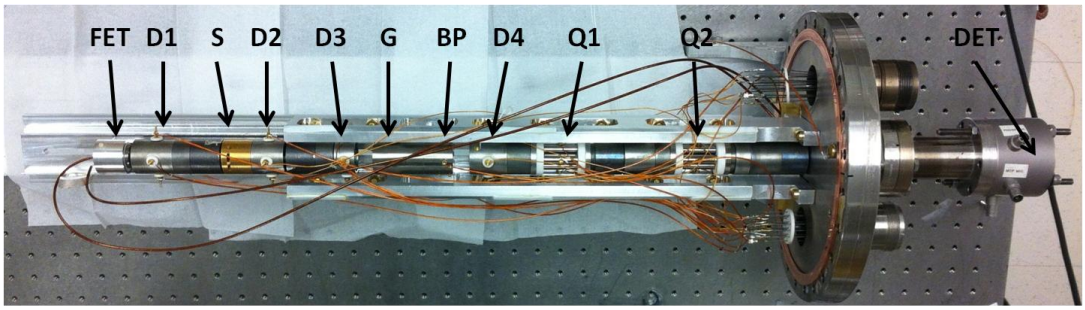

FET - field emission tip
D1 - deflection plates
S - 25μm slit
D2 - deflection plates
D3 - deflection plates
G - 100nm periodicity grating
BP - biprism wire
D4 - deflection plates
Q1 - quadrupole lens
Q2 - quadrupole lens
DET - detector

Figure 8.1

Grating Bi-prism Setup

a) The experimental set up for potential new type of interferometer shown here consists of a grating to generate two beams by amplitude splitting, and a bi-prism to pull them back together. (Image taken from[1]) b) Shown here is an image of the current experimental apparatus with all of the components labeled.

2. Bi-prism wire

One critical aspect of this experiment is the bi-prism wire. At this point it is worthwhile to outline the manufacture of the bi-prism and discuss some of the difficulties therein. The first step in the process of making the bi-prism to melt hollow glass rods using an oxy-acetylene torch.

Figure 8.2

Quartz Rods

Quartz glass rods were melted to produce a thin fiber which was then coated and used as a bi-prism.

Before opening the tanks the adjustment screws and torch valves should be closed (turn adjustment screws clockwise to open and counterclockwise to close). After opening the tank valves the adjustment screws can be opened and to set the pressure in the gas line. The settings that were used for bi-prism production were 20 psi in the oxygen line and 5 psi in the acetylene line before opening either of the torch valves. When opening the torch valves the acetylene line should be opened sufficiently. A flame that is too mild

does not burn as efficiently and visibly spews smoke and soot which is not the case with a hotter flame. The fact that for hotter flames the smoke and soot is significantly diminished does not mean that it is completely gone and as such it would be worthwhile to consider cleaner burning fuel. It doesn't matter how clean the room is if the flame itself introduces dirt.

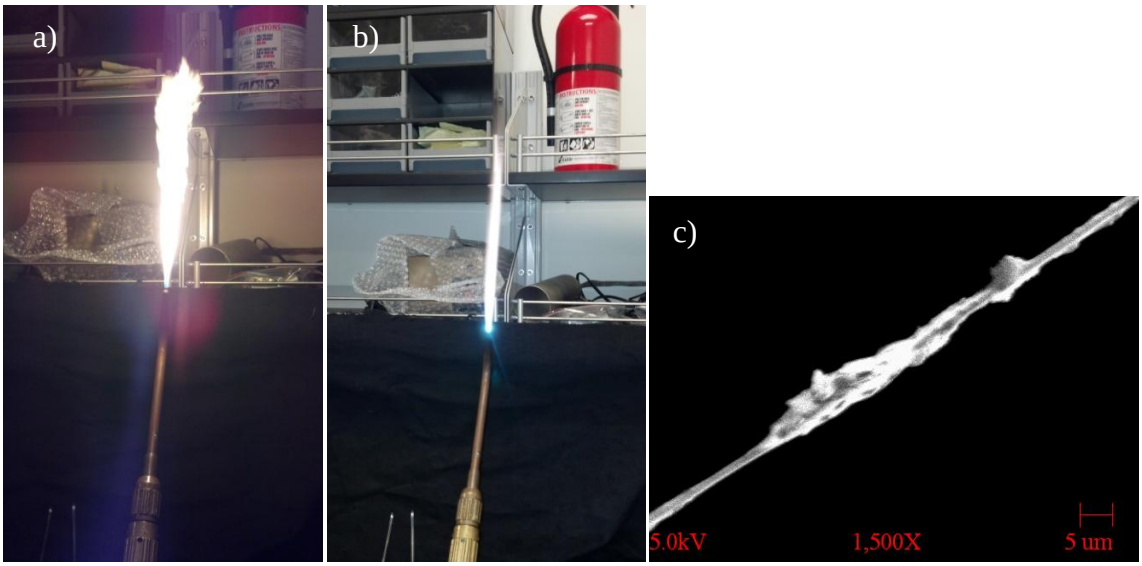

Figure 8.3

Torch and Dirty Wire

a) Immediately after ignition the torch has a significant enough flame as not to spew smoke and soot. b) After careful adjustment of the oxygen and acetylene the flame has turned blue with a bright blue cone at its base of approximately 1cm. c) An SEM image of a contaminated bi-prism wire is shown here.

After the torch has been ignited the oxygen and acetylene valves are slowly adjusted such that the flame turns blue with a bright blue cone at its base on the order of about 1cm in length. The bright blue cone is the hottest spot in the flame and is the point where the glass is melted. The larger part of the flame is usually set to be around a foot in length. When the quartz glass is placed in the flame the end of the glass begins to melt. Two

pieces are then melted together and then pulled apart rapidly to produce a thin strand of quartz glass. The target fiber is less than 1μm in diameter and is thus very difficult to see. A black backdrop and a collimated light source were set up in order to make it a little easier to spot the thin strand.

a) b)

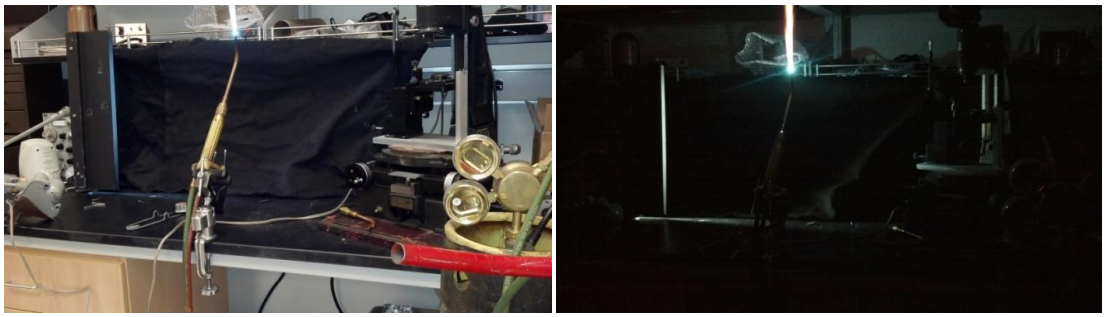

Figure 8.4

Setup for Bi-Prism Construction

a) The setup used for quartz fiber production consists of the oxy-acetylene torch, a black backdrop and collimated light source to improve visibility, and a microscope and translation stages for mounting the fiber. b) shown here is the setup in the darkened conditions in which fibers were made. All light is removed except for the collimated lamp and the torch.

Identifying the appropriate width strands is a matter of experience. However, it is worth noting that when looking for submicron width strands if the fiber is easily visible it is too thick. The ideal strand is very difficult to see even from just the right angle with just the right lighting. Once the fiber is made it must then be captured with a fork.

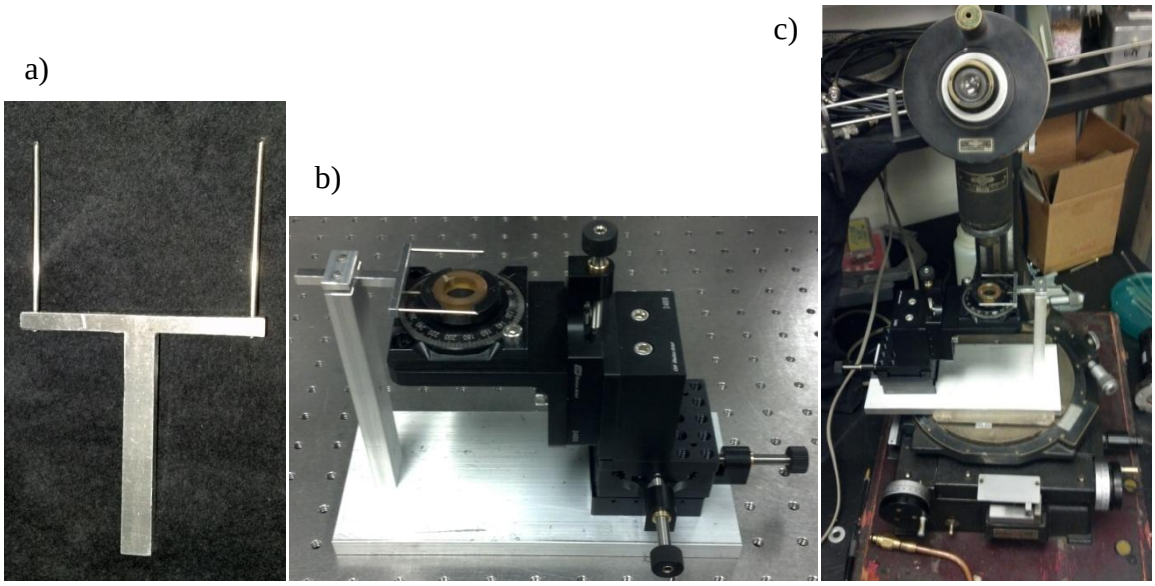

Figure 8.5

Microscope Setup for Wire Mounting

a) A fork was used to capture the thin quartz glass fiber. b) The fork is then placed in the mounting apparatus where the fiber is then placed on an ultem ring. c) The fiber is placed on the ultem ring under a microscope.

After the fiber has been captured on the fork it can then be mounted to an ultem ring via the three dimensional translation stage shown in figure 8.5b. This is done under a microscope. The lighting in figure 8.5c is not ideal for mounting the fiber. A bright lamp would normally be placed next to the microscope and the angle adjusted until the fiber becomes visible. The fiber is aligned with notches in the ultem ring by translation and rotation. Once the fiber is placed on the ultem ring it is glued into place with silver paint (Ted Pella, Inc. “Leitsilber” conductive silver cement). After the fiber is mounted and glued in place it is then coated via sputtering. When coating the ring and fiber the sputtering machine is set for a 100nm layer of gold. This may seem thick but we are uncertain as to the uniformity of the layer. After having been coated the wires are then lowered into the mount with another translation stage.

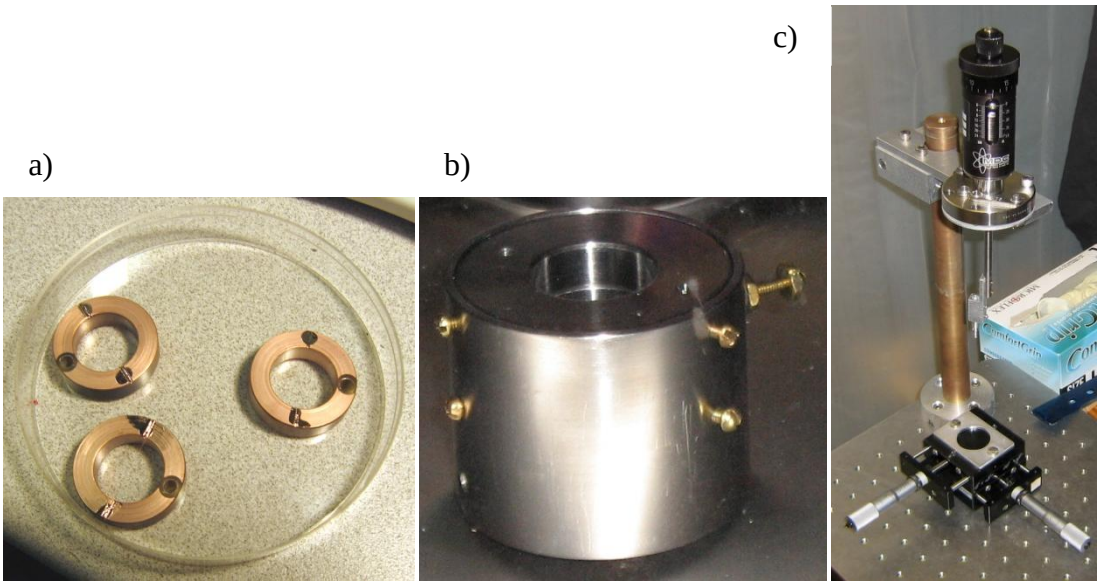

Figure 8.6

Example Bi-Prisms, Mount, and Mounting Translation Stage

a) Ultem rings are with fibers are shown here after having been coated with gold. b) The bi-prism is held in the mount shown here. c) When the bi-prism is mounted the lid of the mount is removed and the ring is lowered in using a translation stage. (images taken from reference[1])

3. Potential difficulties

In order for the field emission tip bi-prism interferometer to function the bi-prism has to pull the two arms of the interferometer together while satisfying certain conditions. This action must sufficiently preserve coherence in the two halves remaining halves of the beam. The wire must have a diameter less than the coherence width of the beam at the wire so that the two halves may be coherent with one another. The deflection of the two halves must be sufficiently constant (i.e. small enough noise on the power supply and small enough vibration of the wire relative to the beam). The wire must be sufficiently aligned with the beam so that differences in the phase shift accumulated during deflection of each half do not exceed the longitudinal coherence length of the beam.

Preservation of the coherence of the beam may be dependent on contact potentials or image charge effects. An analysis of these effects has been done by Barwick *et al*[2]. This analysis was done by calculating the phase accumulated by electron interaction with image charges within the two nearest grating bars in addition to the phase accumulated due to interaction with a random potential generated by the contact between neighboring crystals of different orientation within the grating surface. In figure 8.7a an image of the Si_3N_4 substrate used by Barwick *et al*[2] is shown. The authors suggest that the protrusions visible in figure 8.7a could lead to contact potentials. Figure 8.7b shows one of the thicker wires which was coated with gold. Note that the larger protrusions on the gold wire have a similar spacing as those on the Si_3N_4 substrate. In the case of the gratings this does not prevent the observation of a diffraction pattern but it does lead to broadening.

a) b)

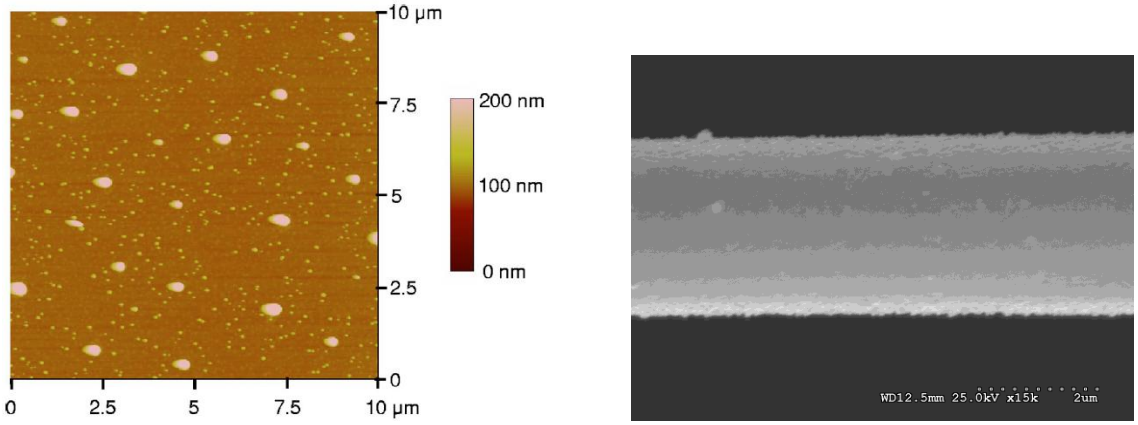

Figure 8.7

Si_3N_4 substrate and Bi-Prism SEM image

a) The Si_3N_4 substrate used by Barwick *et al*[2] is shown. The authors suggest that the protrusions shown here could lead to contact potentials. b) One of the thicker wires which was coated with gold is shown here.

The extent of the broadening of the diffracted beam is dependent on the material with which the substrate is coated. The data shown by Barwick *et al*[2] demonstrates that of the materials studied, a Nickel coating has the least effect on the breadth of the beam. Bearing this in mind it seems worthwhile to consider a Nickel coating for future attempts at bi-prism production.

The constancy of the deflection of the electrons by the bi-prism depends on the position of the wire relative to the two arms and the voltage applied to the wire. For small angles the deflection of an electron beam by a bi-prism wire is

$$\delta = \frac{\pi e V_{bp}}{2E_{el} \ln\left(\frac{R_{bp}}{R_{el}}\right)} \tag{1}$$

where V_{bp} is the voltage applied to the bi-prism, E_{el} is the kinetic energy of the electrons in eV, R_{bp} is the radius of the bi-prism wire, and R_{el} is the distance from the wire to the grounded electrode. With this deflection angle the phase accumulated can be approximated as

$$\varphi = \frac{2\pi x}{\lambda}\delta = \frac{\pi^2 e x V_{bp}}{\lambda E_{el} \ln\left(\frac{R_{bp}}{R_{el}}\right)} \tag{2}$$

where x is the distance from the bi-prism at the point of closest approach. This would imply that a time dependent change in the position of the electrons relative to the wire $\Delta x(t)$ would give rise to a time dependent change in phase $\Delta\varphi(t)$. With 10^7m/s electrons, a 1μm diameter wire, 0.51m between the wire and the detector, 0.31m between the source and the wire, and 1cm distance between the wire and the grounded electrode, the variation of the position of the wire relative to the beam should be $\Delta x \ll 14\mu m$ in

order to have $\Delta\varphi \ll \pi$. This is important because a phase difference of π would move the fringes such that a maximum would move to where a minimum was previously located. If this movement were oscillatory and faster than the measurement time then the fringe contrast would disappear. This is of was of some concern for us since mechanical pumps which supply pressurized air for the building are located at the end of the hall on our floor and they tend to make the walls in the basement shake. Measurements were made of the vibration of a wall in our lab relative to the optical table on which the system was sitting. These measurements were done using an optical interferometer (see figure 8.8).

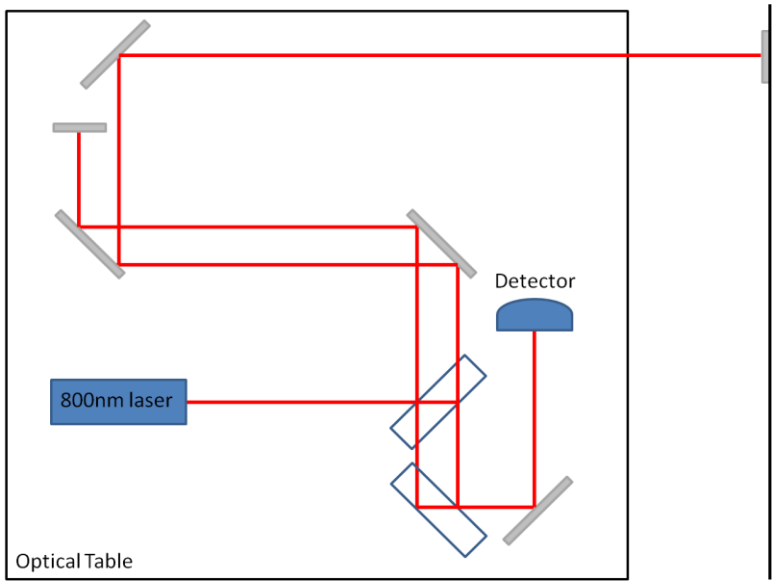

Figure 8.8

Schematic of Optical Interferometer

To use the optical interference to measure the vibration of the wall relative to the optical table 800nm wavelength light is first reflected from the front and back surfaces of a piece of glass to create two beams. One of these two beams is reflected back onto itself by a mirror on the table while the other is reflected back by a retroreflector on the wall. The two beams are recombined at a second piece of glass and measured by a photodetector.

Typical measurements gave a vibration of less than 10μm at a frequency of 13.7Hz when any of the air handling pumps are on. According to specifications the horizontal and vertical resonance frequencies of the optical table are 1.5Hz and 1.1Hz, respectively. In each case for the measured frequency the table damps vibrations by a factor of less than 0.01 for vertical transmission and less than 0.1 for horizontal transmission. Thus for this vibration the transmitted oscillation is less than 1μm.

In the same way that vibration of the wire causes a relative phase difference between the arms of the interferometer a static displacement which puts the wire out of alignment will result in a difference in the path length for electrons going on either side of the wire. If this difference in path length exceeds the longitudinal coherence length then interference will not be observed. In an article by Kiesel *et al.*[3] a coherence of 90nm was reported ($\Delta E = 0.13eV,\ \ E = 900eV$). Taking this value as an example and using equation (2), in order for the phase difference between the two arms to be much less than the coherence length the offset of the wire must be much less than 17.6mm. In order for this to be problematic the width of the beam would have to be on the order for the wire to be so far off center to generate such a phase difference in two interfering paths (see figures 8.9a and b).

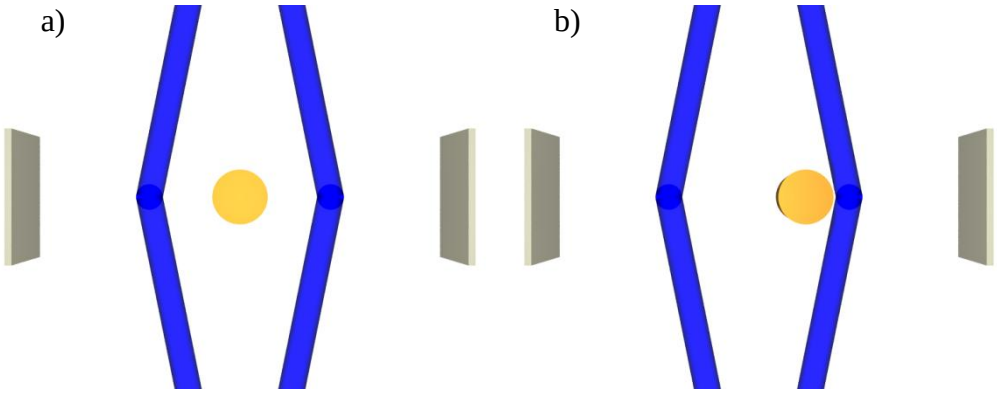

Figure 8.9

Bi-Prism Displacement

a) An electron bi-prism wire is deflecting two electron paths to interfere on a detection screen. b) Because the deflection angle is independent of distance from the bi-prism the deflection angle of the two paths is the same even when the wire is shifted to the right (image a taken from[1]).

Such a large variation is of little concern given that for a tip bi-prism interferometer it is only necessary to overlap paths of grazing incidence on either side of the wire. For a grating bi-prism interferometer in which the two paths shown in figure 8.9 represent the two first order diffraction beams this might matter because the interfering paths are further apart from each other for some freedom of the position of the wire between them. Additionally, the larger angle of deflection for the grating bi-prism setup implies an increased phase shift due to displacement of the wire. A more detailed discussion of the grating bi-prism setup is given in the concluding section of this chapter.

It is also necessary that the source maintain sufficient coherence and brightness. In a report on the progress of electron and ion interferometry[4] Hasselbach states that for tip bi-prism interferometers it is beneficial to use a single crystal tungsten field emission tip with a radius of curvature of about 50 nm and (3 1 0), (1 0 0) or (1 1 1) orientation in order to obtain a high emission in axial direction of the single crystal. We do use field

emission tips that are on the order of 100nm in diameter but have not attempted this experiment with single crystal tips (see figure 8.10[5]).

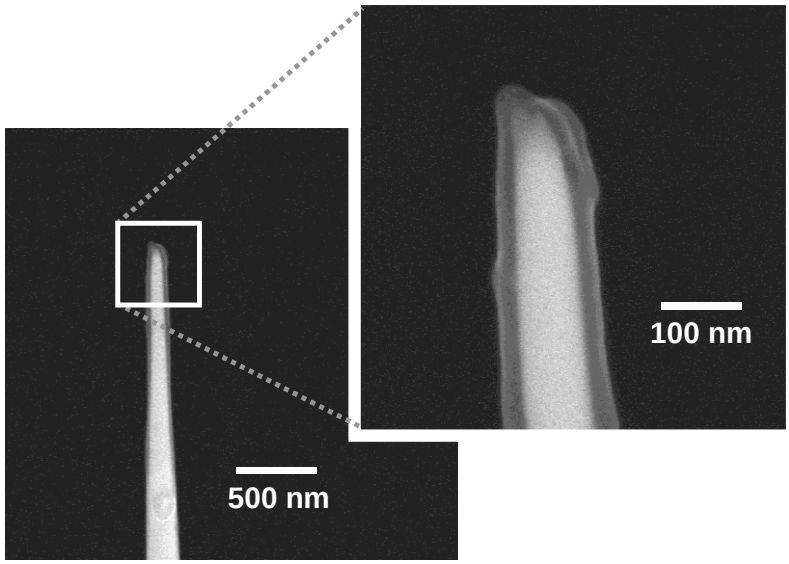

Figure 8.10

Field Emission Tip SEM Image

Shown here is an example of a tungsten field emission tip made in our lab with a diameter of less than 100nm (Image taken from[5]).

4. Measurement

In the interest of narrowing the search for fringes it is worthwhile to obtain an approximate value for the width of the fringes and the necessary voltage of the bi-prism wire to obtain those fringes. If two overlapping plane waves have been deflected by an angle δ in opposite directions the width w of the resulting interference fringes can be approximated as $w = \frac{\lambda}{2\sin(\delta)} \approx \frac{\lambda}{2\delta}$ where λ is the wavelength (see figure 8.11).

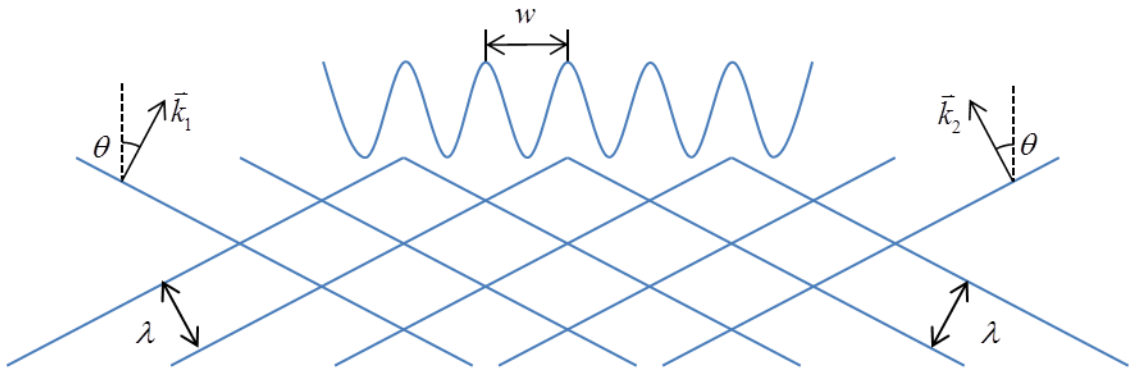

$$\vec{k}_1 = k_x\hat{x} + k_y\hat{y}$$
$$\vec{k}_2 = -k_x\hat{x} + k_y\hat{y}$$

$$\left|\varphi(\vec{r})\right|^2 = \left|\varphi_1(\vec{r}) + \varphi_2(\vec{r})\right|^2 = \left|\exp\left[i\left(k_x x + k_y y\right)\right] + \exp\left[i\left(-k_x x + k_y y\right)\right]\right|^2$$
$$= \left|2\cos\left(k_x x\right)\exp\left(ik_y y\right)\right|^2 = 4\cos^2\left(k_x x\right) = 2\left(1 + \cos\left(2k_x x\right)\right)$$

$$w = \frac{\pi}{k_x} = \frac{\lambda}{2\sin\theta} \approx \frac{\lambda}{2\theta}$$

Figure 8.11

Interfering Plane Waves

Two waves with wavelength λ have been deflected in opposite directions by an angle θ. The width of interference fringes is w.

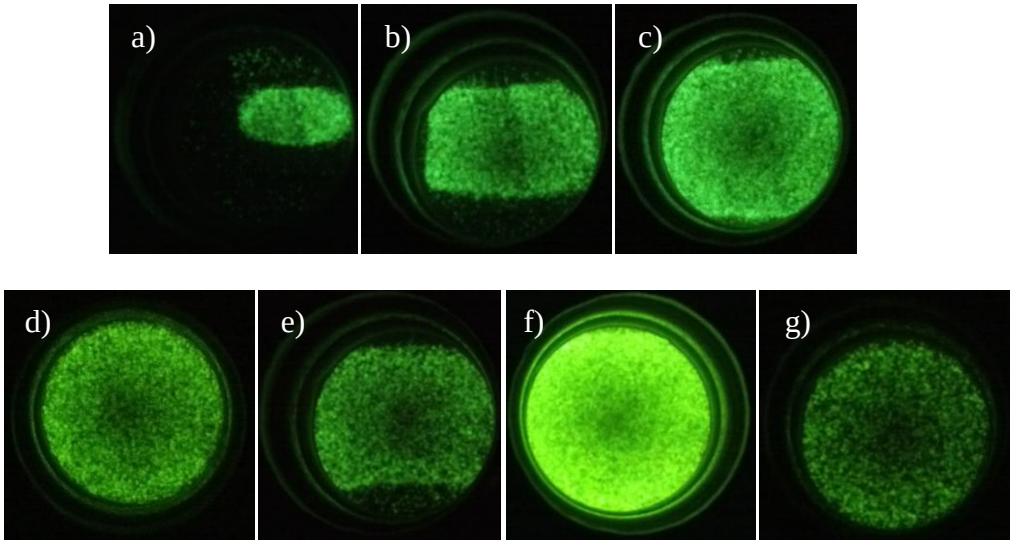

Figure 8.12

Quadrupole Magnification Images

The image of the electrons on the detector is shown here with a quadrupole voltage of a) 10V, b) 20V, c) 30V, d) 40V, e) 100V, f) 500V, and g) 800V.

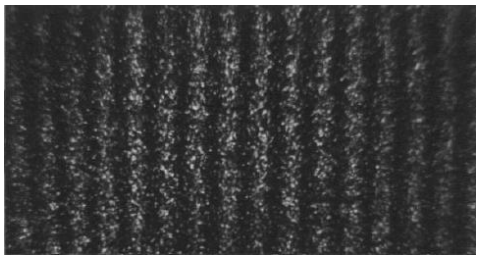

Figure 8.13

Hasselbach's Fringes

The intensity of these bi-prism interference fringes measured by Hasselbach[6] seems to indicate that our intensity should be sufficient at all of the magnifications shown in figure 8.12.

Assuming a wire diameter of 1μm, a wire to detector distance of approximately 0.51m, and $10^7\ m/s$ electrons $\left(\lambda \approx 7.27\times10^{-11} m\right)$ the fringe spacing for the minimum deflection angle to overlap the grazing electrons on either side of the wire is roughly 37μm. This corresponds to a bi-prism voltage of about 4.6mV. This would be easily visible with one hundred times magnification. In reference[1] a magnification of 10,000 is reported for 7.5keV electrons with the use of two quadrupole lenses (600V on the first and 200V on the second). A magnification of a few hundred should be easily within reach with the current configuration.

Attempts were made to find interference fringes at quadrupole voltages of 10V, 20V, 30V, 40V, 100V, 500V, and 800V using 1230eV electrons. In these attempts the bi-prism was left off as the diffraction pattern should be visible even with no voltage on the bi-prism. In figure 8.12a a faint shadow of the bi-prism can be seen at the center of the oval. The beam profile eventually exceeds the size of the detector at 40V. At 100V on the quadrupole the top and bottom edges of the beam profile become visible again. This is because the top and bottom poles of the quadrupole have a negative voltage. This initially

magnifies an inverted image but at higher voltage the electrons are pushed back together and the image shrinks and then expands at yet higher voltages. Figure 8.13 shows a low intensity bi-prism interference pattern measured by Hasselbach[6]. It is apparent that even at such low intensities the interference pattern is clearly visible. The intensity obtained at each magnification shown in figure 8.12 should be sufficient to observe interference fringes.

Furthermore it is possible to estimate the necessary quadrupole voltage required for observing fringes based on trajectory of electrons in the quadrupole fields[7]. The trajectories of electrons as they pass through the quadrupole are given by

$$x(z) = x_1 \cos(kz) + \frac{1}{k}\tan(\alpha_1)\sin(kz)$$

$$\tan(\alpha(z)) = \frac{dx}{dz} = -x_1 k \sin(kz) + \tan(\alpha_1)\cos(kz)$$

$$y(z) = y_1 \cosh(kz) + \frac{1}{k}\tan(\beta_1)\sinh(kz)$$

$$\tan(\beta(z)) = \frac{dy}{dz} = -y_1 k \sinh(kz) + \tan(\beta_1)\cosh(kz) \qquad (3)$$

$$k^2 = \frac{2Vq}{G_0^2 m v_z^2} \qquad (4)$$

Where V is the quadrupole voltage, q is the charge $(q = -e)$, v_z is the forward component of electron velocity, x_1 and y_1 represent the position of the electron at the entrance of the quadrupole, α_1 and β_1 are the angles of the trajectory of the electron entering the quadrupole, and the separation and size of the poles is specified by G_0 (see figure 8.14).

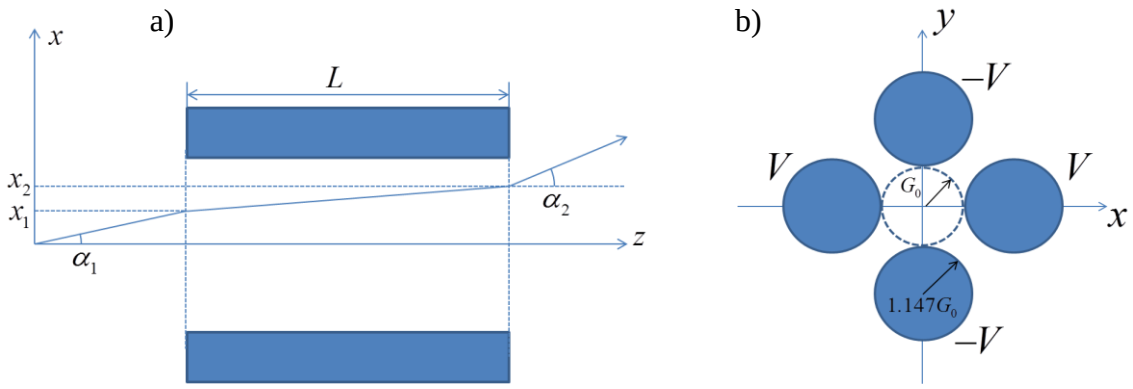

Figure 8.14

Schematic of Electrostatic Quadrupole Lens

a) Electrons enter the quadrupole at position x_1 with angle α_1 and exit at position x_2 and α_2. b) The separation and size of the poles is specified by G_0 and V is the voltage applied to the quadrupole.

Electrons exit the quadrupole at position x_2 and y_2 with angle α_2 and β_2. If the electrons propagate a distance d in the z direction to go from the quadrupole to the detector the position at the detector is

$$x_{\text{det}} = x_2 + d\tan(\alpha_2)$$

$$y_{\text{det}} = y_2 + d\tan(\beta_2) \tag{5}$$

From this the approximate magnification of the image at the front of the quadrupole can be determined. For 1.23keV electrons a magnification of 200 can be achieved with a quadrupole voltage of about 200V (assuming $\alpha_1 \approx 0$, and $\beta_1 \approx 0$).

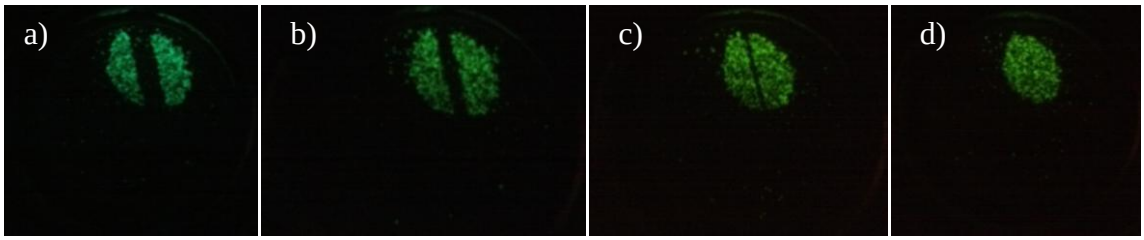

Figure 8.15

Beam Profile at Different Bi-Prism Voltages

Images of the beam profile were taken with an electron energy of 1230eV, a quadrupole voltage of 10V, and bi-prism voltages of a) 5V, b) 3V, c), 1V, and d) 0V.

In a series of images taken of the electron beam at different bi-prism voltages (see figure 8.15) it is clear that the shadow of the bi-prism appears to be slanted to the left and the beam profile has a different shape as compared to that of figure 8.12. The change in the shape of the beam profile may be in part due to the difference in the voltage applied to the field emission tip mount. In order to control the emission current separately from the electron energy the field emission tip is mounted in a container that is kept at an electrostatic potential (Figure 8.15 shows a schematic of the mount). During the measurements shown in figure 8.12 the quadrupole voltage was increased to 1000V. An image at this magnification was not recorded because at such high magnification a current is required which damages the tip and results in source instability. Consequently a higher potential difference is required to obtain emission. When beginning the measurements for figure 8.12 the voltage required to obtain emission was approximately 300V. After the measurements were completed the necessary voltage was roughly 500V. This means that in order to have an electron energy of 1230V the emission was previously initiated at a mount voltage of approximately 900V whereas after the measurements for figure 8.12 were completed a voltage of about 700V would be necessary.

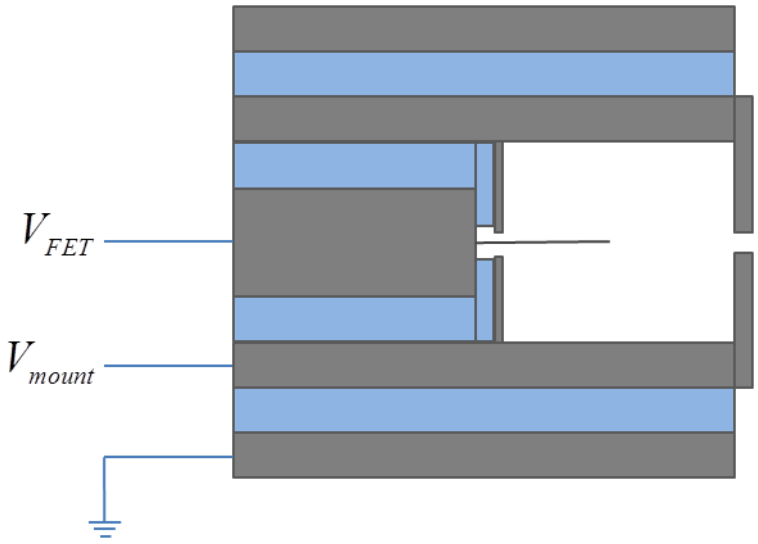

Figure 8.16

Schematic of Field Emission Tip Mount

Shown here is a cross section of the field emission tip mount as seen from the side. Each layer from top to bottom is a cylinder. The outermost layer is grounded and the inner most cylinder which holds the field emission tip is kept at the potential V_{FET} which sets the energy of the electrons. In between these two is the cylinder which partially creates a cavity surrounding the tip which is kept at a voltage V_{mount}. It is the difference between V_{FET} and V_{mount} which sets the emission current. The blue layers represent electrical insulation between the conducting layers.

This change in voltage of the mount chamber may have an effect on the beam profile due to fields near the exit aperture. Since this lensing occurs before the beam reaches the bi-prism it seems unlikely that it would affect the shape of the shadow of the bi-prism or that of the fringes. The slant in the image may also be due to aberrations of the quadrupole lens possibly due to the electrons entering the lens slightly off axis at an angle. Better alignment of the quadrupole lenses may be necessary to obtain interference fringes.

This slant could be much more severe at higher magnification due to the fact that magnification in one direction is much larger than in the other. The above expressions (Equations 3 and 5) for the trajectory of the electrons were used to determine the approximate magnification of the quadrupole lens. The magnification was plotted from 0V to 800V (see figure 8.17).

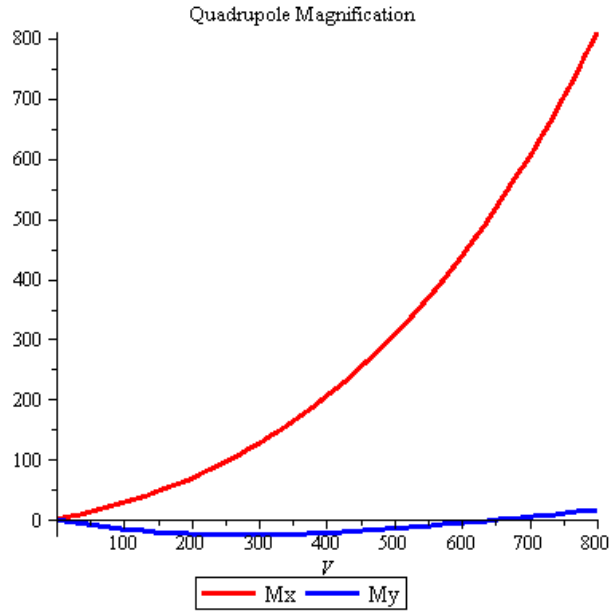

Figure 8.17

Quadrupole Magnification

The magnification in the y-direction is much less than in the x-direction for a single quadrupole. It is thus necessary to use two oppositely polarized quadrupoles to achieve approximately the same level of magnification in both directions.

This difference in magnification may make it impossible to observe fringes and thus it may be necessary to apply both quadrupole lenses with opposite polarization to obtain comparable magnification in both directions. A search for fringes was made with this in mind resulting in the images seen in figure 8.18.

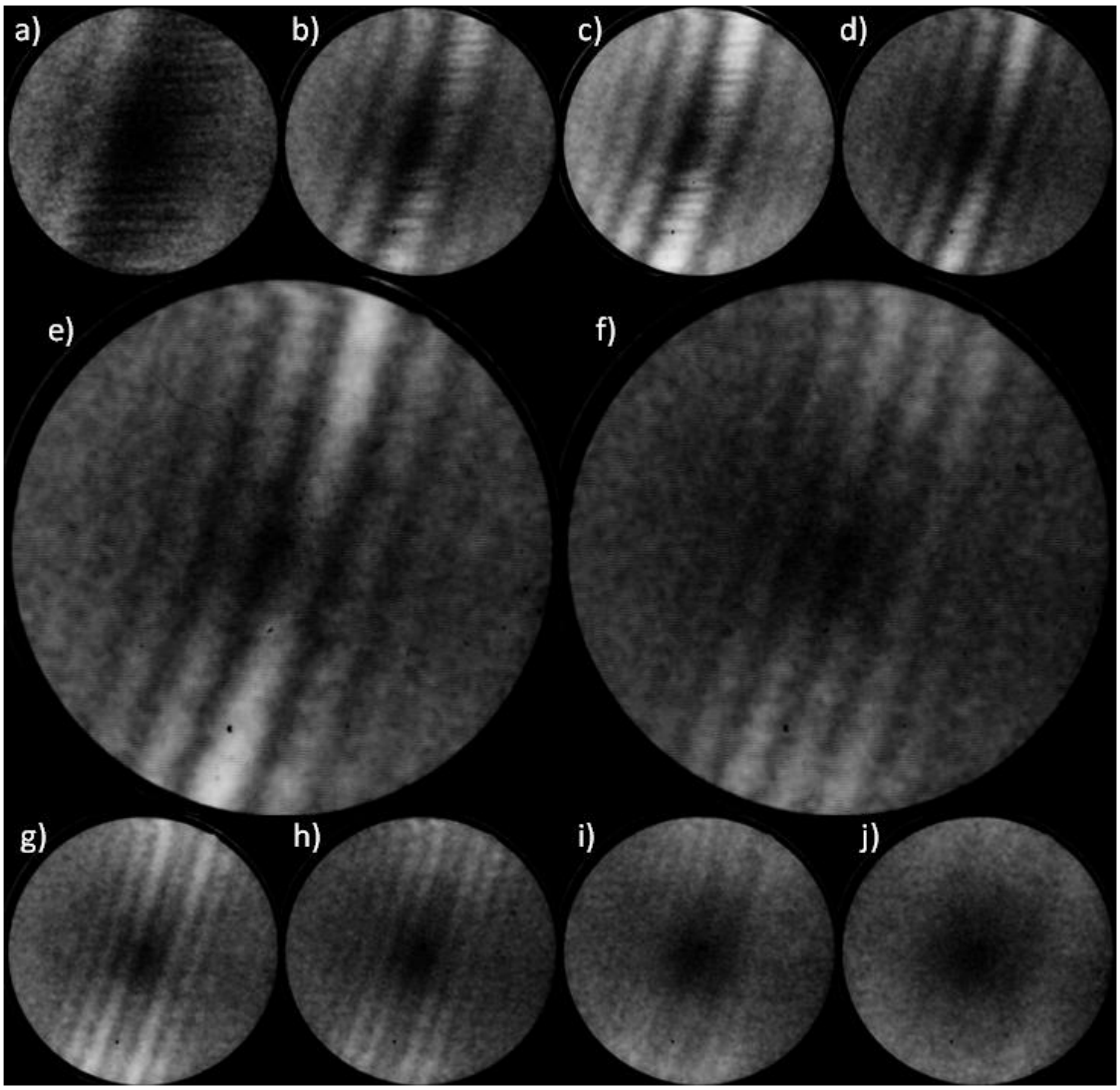

Figure 8.18

Tip Bi-Prism Fringes 1

Interference fringes were measured with 100V on the first quadrupole and 50V on the second quadrupole, and 1.23keV electrons. Shown here are the images with bi-prism voltages of a) -125mV, b) -16mV, c) 0V, d) 37mV, e) 61mV, f) 114mV, g) 138mV, h) 154mV, i) 192mV, and j) 261mV.

Images were taken for bi-prism voltages ranging from -125mV to 261mV with 100V on the first quadrupole and 50V on the second quadrupole and 1.23keV electrons. As the bi-prism voltage is increased the two arms are pulled together decreasing the fringe spacing until gradually the fringes completely fade away. This loss of contrast is due to the finite

transverse coherence length of the electrons. The dark spot in the center is simply where the multichannel plate detector has been worn out due to extended use. Additionally, data was taken with 80V on the first quadrupole and 50V on the second with bi-prism voltages ranging from -270V to 97V (see figure 8.19).

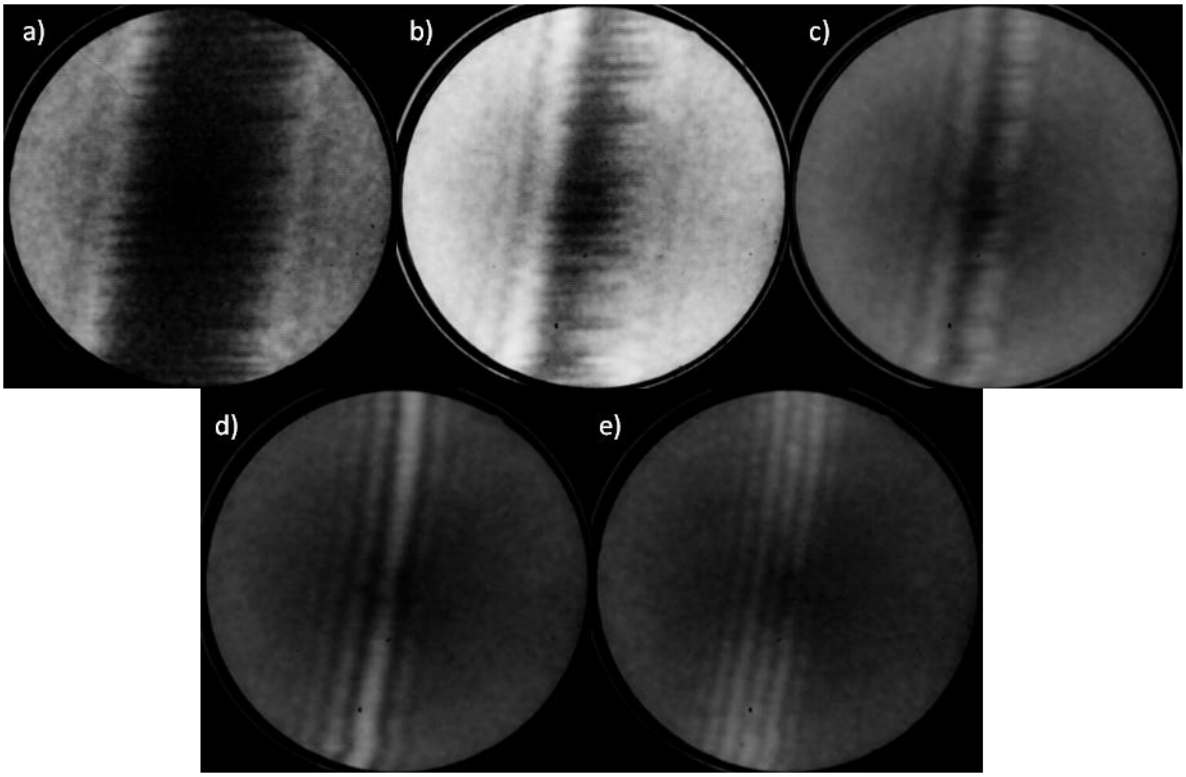

Figure 8.19

Tip Bi-Prism Fringes 2

Interference fringes were measured with 80V on the first quadrupole and 50V on the second quadrupole, and 1.23keV electrons. Shown here are the images with bi-prism voltages of a) -270mV, b) -121mV, c) -47mV, d) 28mV, and e) 97mV.

In the second data set the fringes have smaller spacing due to the decreased quadrupole voltage. Also the slant on the fringes is decreased in the second set as compared to the first. This slant is presumably due to a misalignment between the beam and the

quadrupole and thus lower quadrupole voltage would have less of an image distorting effect.

5. Conclusion

An electron interferometer consisting of a field emission tip and a bi-prism wire has been created as a first step toward a grating bi-prism interferometer. With this step completed it is now possible to attempt to optimize the parameters of the former set up in order to optimize the probability of success of the latter. With 1.23keV electrons the expected fringes in the grating bi-prism interferometer will have a smaller periodicity. Assuming a 100nm periodicity grating is set 5.5cm behind the bi-prism the distance from the bi-prism to the first order diffracted beams is approximately 15μm. With a distance of approximately 0.51m from the bi-prism to the detector the fringe spacing should be about 577nm at the detector (as compared to 18μm for the current setup with 1.23keV electrons and a bi-prism wire of approximately 1μm diameter). The increased bi-prism deflection angle will create an increased sensitivity to bi-prism position due to the previously mentioned dependence of the phase shift of an arm on its distance from the bi-prism. For the above parameters the necessary deflection angle should be about 30μrad. This must be taken in addition to the angle at which the two first order diffracted beams approach the bi-prism which is 350μrad. Thus the overall deflection that must be provided by the bi-prism is 380μrad. To do this a bi-prism voltage of 2.95V is necessary. This increased voltage puts a tighter restriction on the vibration of the wire. With 1.23keV electrons in the current grating bi-prism setup a bi-prism movement of 46nm would produce a π phase shift in each of the two arms and thus any vibration of the wire must be significantly less than 46nm. Similarly, a greater restriction will be placed on the alignment of the bi-prism

as described in section 3. Taking again as an example the same longitudinal coherence length of 90nm as described in the article by Kiesel *et al.*[3], a displacement of the bi-prism relative to the center of the two first order beams of approximately 119μm would generate a phase difference between the two arms of one coherence length. Thus the wire must be centered between the two arms to better than 119μm. Fortunately, since the distance between the two first orders at the bi-prism is approximately 31μm, just getting the bi-prism between the two arms at all will do. Therefore, centering the zero order beam on the bi-prism should be more than sufficient.

Additionally the stability of each of the power supplies may be critical to the success of a grating bi-prism interferometer. Fluctuations in voltages applied to the bi-prism, deflection plates, or quadrupole lenses could cause a displacement in fringes thus making them difficult or impossible to detect. Further consideration needs to be given to the stability of each power supply. The alignment of the quadrupole lenses with the grating and the bi-prism is also potentially important and a technique which allows for universal rotational alignment of each component of the system is a future objective worth considering.

Chapter 9 - Conclusion

The main effort of the work presented in this dissertation was to take steps toward the eventual realization of a test of the dispersionless nature of the Aharonov-Bohm effect through classical and quantum mechanical theoretical analysis as well as progress in the experimental development of a novel electron interferometer. By considering the theoretical aspects of interactions of electrons with externally applied fields and potentials we have probed some of the controversial questions surrounding the Aharonov-Bohm effect. Is this effect a purely quantum mechanical phase or is it the result of a force? What is the nature of the quantum/classical boundary in light of this consideration? Furthermore we have considered similar scenarios in which properties of the electron are manifested in thought experiments based purely on quantum mechanical behavior (i.e. the Stern-Gerlach effects discussed in chapters 5 and 6). In chapters 7 the development of a grating bi-prism beamsplitter is presented as the first step toward a grating bi-prism interferometer. Finally, a working field emission tip bi-prism interferometer is reported in chapter 8 along with some suggestions as to future work to move forward with the grating bi-prism interferometer.

There are multiple potentially interesting future projects inspired by the conclusions drawn in the chapters of this dissertation. The first demonstration of a transverse Stern-Gerlach experiment for free electrons would be quite interesting in its own right in addition to having applications to spin-polarized electron research. The manipulation of electron spin via laser light could also have meaningful applications. The necessary technology for these to pursuits exists and they are shown to be, in principle, possible.

Given that the Feynman paradox seems to be at the heart of the controversy surrounding the Aharonov-Bohm and Aharonov-Casher systems, an experimental demonstration of the Feynman system, while experimentally very difficult, could be revealing. Such an experiment may be possible in which an electron pulse is sent past an oscillating atomic force microscopy cantilever held at an electric potential. In such a scenario the electrons and the cantilever tip are intended to represent q_2 and q_1 in figure 3.1 depicting the Feynman paradox. Measurement of displacement and delay could give information regarding the forces exerted on the electron by the cantilever.

Finally, in the interest of producing the most coherent source possible it is worthwhile to consider the use of a cold source as described in chapter 2 in order to improve the coherence width of emitted electrons at the source. Given the data shown in that chapter it seems possible to create a source of silver with a coherence width of as much as a micron at liquid helium temperatures. This potentially has a large positive impact on the results of any interference or diffraction experiment that uses non-atomic nanoscale sources.

Appendix A - FORTRAN Codes

A1 - Partially coherent source propagation

A state with partial spatial coherence is propagated through a double slit to a detector. This is done by taking a fully coherent Gaussian wave packet and propagating it to the detector and integrating the resulting probability distribution in a convolution with the initial partially coherent probability distribution. The details of this calculation are described analytically in chapter 2 section 2.1 and the results of this calculation are plotted in figure 2.4.

```
program simulation
use msimsl
implicit none

integer nslitpoints,ndet,num1,num2,num3,ns
real*8 v,vp,L1,L2,t1,t2,d1,d2,w,hbar,x,xd,xs,P,pi,delta
real*8 dxslit,wdet,dxdet,m,ws,dxsource,ptotal,g
complex(8) i,f,cwave,U


open(unit=30,file="probability dist.dat")



hbar = 1.0546d-34
m = 9.11d-31
v = 3d7                 !2562.1875 eV
vp = v/2d0          !phase velocity
L1 = 0.05d0         !distance from source to grating
L2 = 0.5d0          !distance from grating to detector
t1 = L1/vp          !propagation time for distance L1
t2 = L2/vp
d1 = 200d-9         !width of each slit
d2 = 1d-6           !the center to center distance between slits
w = 1d-6            !width of source (delta is the coherence width)
pi = 3.14159d0

i = (0,1)

!xs = 0d0
delta = 1000d-9     !coherence width

nslitpoints = 50    !number of points integrated in each slit is
                    !2*nslitpoints + 1
```

```
dxslit = d1/(2d0*nslitpoints) !distance between integration
                              !points on slit

ndet = 300              !number of points on detector 2*ndet + 1
wdet = 5d-4             !width of detector
dxdet = wdet/(2d0*ndet) !distance between points on detector

ns = 500                !number of coherent sources summed up is
                        !2*ns + 1

ws = 5d0*w              !integration width for convoluting final
                        !probability with source
dxsource = ws/(2d0*ns)

do num2 = -ndet,ndet
      xd = num2*dxdet

      Ptotal = 0d0
      do num3 = -ns,ns

      xs = num3*dxsource

      !integration of double slit
      cwave = (0d0,0d0) !coherent wavefunction at detector
            do num1 = -nslitpoints,nslitpoints
                  !first slit
                  x = d2/2d0 + num1*dxslit


                  !wavefunction just before grating
                  f = (pi**0.5d0*(delta +                      &
                       i*hbar*t1/(m*delta)))**(-0.5d0)         &
                       *cdexp(-(x - xs)**2d0/(2d0*delta**2d0*   &
                       (1d0 + i*hbar*t1/(m*delta**2d0))))

                  !free space propagator
                  U = (m/(2d0*pi*hbar*i*t2))**0.5d0*     &
                       cdexp(i*m*(x - xd)**2d0/(2d0*hbar*t2))

                  cwave = cwave + f*U*dxslit


                  !second slit
                  x = -d2/2d0 + num1*dxslit


                  !wavefunction just before grating
                  f = (pi**0.5d0*(delta +                  &
                       i*hbar*t1/(m*delta)))**(-           &
                       0.5d0)*cdexp(-(x - xs)**2d0/        &
                        (2d0*delta**2d0*(1d0 +             &
                       i*hbar*t1/(m*delta**2d0))))




                  !free space propagator
```

```
                        U = (m/(2d0*pi*hbar*i*t2))**0.5d0*        &
                             cdexp(i*m*(x - xd)**2d0/(2d0*hbar*t2))

                        cwave = cwave + f*U*dxslit

                  enddo

                  P = dfloat(dconjg(cwave)*cwave)

                  g = 1d0/(w*(pi)**0.5d0)*dexp(-xs**2d0/(w**2d0))
                  Ptotal = Ptotal + P*g*dxsource

            enddo


            write(6,*) num2
            write(30,999) xd,Ptotal

      enddo



999   Format(E12.6,x,E12.6)

      stop
    end
```

A2 - Stern-Gerlach diffraction I

A Plane wave is propagated through a grating and a diffraction pattern is calculated. This is done with an additional phase applied in each slit in a stair step pattern resulting from the interaction of the magnetic moment of the passing electrons with the applied magnetic field as described in section 2.1 of chapter 5. This also includes a phase in each slit which has a quadratic spatial dependence to account for the Lorentz force on the electrons passing through the grating. The result of this calculation is plotted in figure 5.3 without the quadratic phase.

```
program prog
implicit none


real*8 Pi,lambda,L,Fi,Fr,dx,a,xi,xj,d,W,dx1,dx2,dx3,P,QP,phi
integer Ng1,Ng2,Nd,i,j,k,s
Pi=3.14d0
lambda=7.274d-9
L=0.53d0  !distance from grating to detector
d=80d-9   !width of slit
W=0.1d0   !width of detector

Ng1=10
Ng2=1000
Nd=10000

QP=3.75d15        !factor for quadratic phase

dx1=d/(2d0*Ng2+1d0)  !delta x for riemann sum
dx2=W/(2d0*Nd+1d0)  !resolution of detector
dx3=200d-9              !grating periodicity

open(unit=29,file="intensity1.dat")
open(unit=30,file="intensity2.dat")
open(unit=31,file="phase.dat")

do s=0,1

      do i=-Nd,Nd
            Fi=0d0
            Fr=0d0

            do k=-Ng1,Ng1
                  do j=-Ng2,Ng2
```

```
                              xj=j*dx1+k*dx3
                              xi=i*dx2

                              Fi=Fi+sin((2d0*Pi/lambda)*((xi-       &
                                 xj)**2d0+L**2d0)**0.5d0-           &
                                 k*QP*(j*dx1)**2d0+k*(-1d0)**s*(Pi/2))

                              Fr=Fr+cos((2d0*Pi/lambda)*((xi-       &
                                 xj)**2d0+L**2d0)**0.5d0-           &
                                 k*QP*(j*dx1)**2d0+k*(-1d0)**s*(Pi/2))

                        enddo
                  enddo
                  P=(Fi**2d0+Fr**2d0)/((2d0*Ng1+1d0)*(2d0*Ng2+1d0))
                  if(s .EQ. 0)then
                        write(29,999) xi,P
                  elseif(s .EQ. 1)then
                        write(30,999) xi,P
                  endif
            enddo

      enddo

999 format(E12.6,x,E12.6)

      close(29)
      close(30)
      close(31)

      end program prog
```

A3 - Stern-Gerlach diffraction phase

The phase is computed electrons in classical trajectories propagating through a current loop. This program is used to determine quadratic factor on spatially dependent Lorentz phase. Additionally, the final position, velocity, and magnetic moment values for each trajectory as well as time dependent taken along specific individual trajectories are computed. The phase resulting from the calculation is plotted in figure 5.4b.

```
      program simulation
      use msimsl
      implicit none


      INTEGER    MXPARM, N,zend
      PARAMETER  (MXPARM=50, N=9,zend=100)
C                                  SPECIFICATIONS FOR LOCAL VARIABLES
      INTEGER    IDO, j, jend,z,s,send,A,i
      REAL*8       PARAM(MXPARM), T, TEND, TOL, Y(N)
      real*8       tstep,endoftime,xSTEP, endofspace,magmoment
      real*8         temp1,temp2,temp3,temp4,temp,factor


      real*8 omega,Bx,By,Bz,dBxdt,dBydt,dBzdt
      common /par/ omega,Bx,By,Bz,dBxdt,dBydt,dBzdt

      real*8         dphi,dphiP,dphiMUB,dphiVA
      real*8         phi,phiP,phiMUB,phiVA(-(zend+2):zend),Q(-
(zend+2):zend)
      common /par/ dphi,dphiP,dphiMUB,dphiVA,A

      External FCN
      open(unit=30,file="trajectory.dat")
      open(unit=31,file="velocity.dat")
      open(unit=32,file="magnetic moment.dat")
      open(unit=33,file="mmx.dat")
      open(unit=34,file="x velocity.dat")
      open(unit=35,file="omega.dat")
      open(unit=36,file="B field.dat")
      open(unit=37,file="dphi.dat")
      open(unit=38,file="dphiP.dat")
      open(unit=39,file="dphiMUB.dat")
      open(unit=40,file="dphiVA.dat")
      open(unit=41,file="phi.dat")
      open(unit=42,file="factor.dat")


c                                  Summations of B-Fields
```

```
!     do A=6,12
C                                SPECIFICATIONS FOR SUBROUTINES

      send=1
      magmoment=9.27d-24
      do s=0,send

!           zend=100
!           endofspace=7.5d-9
!           xSTEP = endofspace/zend
!           do z=-zend,zend

C                                Set initial conditions


                  T = 0.0d0
                  Y(1) = 7.5d-9 !z*xSTEP
                  Y(2) = 0.0d0
                  Y(3) = 0.0d0
                  Y(4) = 0.0d0
                  Y(5) = -4.0d-5
                  Y(6) = 1.0d5
                  Y(7) = 0.0d0
                  Y(8) = 0.0d0
                  Y(9) = (1-2*s)*magmoment

                  temp1=0d0
                  temp2=0d0
                  temp3=0d0
                  temp4=0d0



C
c                    Set error tolerance
                  TOL = 5.0d-12
C                                Set PARAM to default
                  CALL SSET (MXPARM, 0.0, PARAM, 1)
C                                Select absolute error control
                  PARAM(10) = 1.0d0
c                                             Set max iterations
                  PARAM(4)=1d8
C                                Print header

                  IDO = 1
                  jend=20000
                  endoftime=8.0d-10  !2.0d-10
                  tSTEP = endoftime/jend
                  do j=1,jend+1

                        TEND = (j)*tstep
c                       write(6,*) tend
                        CALL dIVPRK (IDO, N, FCN, T, TEND, TOL, PARAM,
Y)
```

```
!                       temp1=temp1+dphiVA
!                       temp2=temp2+dphiMUB
!                       temp3=temp3+dphiP
!                       temp4=temp4+dphi


c                       WRITE (6,'(10E12.3)') T, Y(1), Y(2), Y(3)
&
c                             ,Y(4), Y(5),Y(6),Y(7),Y(8),Y(9)
                        WRITE (30,998) T, Y(1), Y(3), Y(5)
                        WRITE (31,998) T, Y(2), Y(4), Y(6)
                        WRITE (32,998) T, Y(7), Y(8), Y(9)
c                   WRITE (37,999) T, dphi
c                   WRITE (38,999) T, dphiP
c                   WRITE (39,999) T, dphiMUB
c                   WRITE (40,999) T, dphiVA
c                   WRITE (35,999) T, omega
                    WRITE (36,996) T, Bx,By,Bz,dBxdt,dBydt,dBzdt
c                   WRITE (33,999) T,'    ', Y(7)

C                                   Final call to release workspace
c                   write(6,*) tend,y(2)

                    enddo

!                   phiVA(z)=temp1
!                   phiMUB=temp2
!                   phiP=temp3
!                   phi=temp4

!                   phiVA(-zend-2)=0d0
!                   phiVA(-zend-1)=0d0
!                   Q(z)=0.5d0*(phiVA(z)-2d0*phiVA(z-1)+phiVA(z-
2))/xSTEP**2d0

!                   !write(6,*)  z*xSTEP,phiVA,phiMUB,phiP            !s,
!                   write(30,998) z*xSTEP, Y(1), Y(3), Y(5)           !s,
!                   write(31,998) z*xSTEP, Y(2), Y(4), Y(6)           !s,
!                   write(32,998) z*xSTEP, Y(7), Y(8), Y(9)           !s,
!                   WRITE (41,994) z*xSTEP, phiVA,phiMUB,phiP,phi     !s,

c                   write(6,*) s,z,(0.5d0)*(9.11D-      &
c                         31)*(Y(2)*Y(2)+Y(4)*Y(4)      &
c                         +Y(6)*Y(6))-(0.5d0)*(9.11D-   &
c                         31)*(1.874d7)*(1.874d7)       &
      ido=3
                    CALL dIVPRK (IDO, N, FCN, T, TEND, TOL, PARAM, Y)
!           enddo
!     enddo

!     temp=0d0
!     do i=-(zend-2),zend
!           temp=temp+Q(i)
      enddo
!     factor=temp/(2d0*zend-1)

!     write(42,999) A*8.5d0,factor
```

```
!     write(6,*) A,factor

!     enddo

      close (30)
      close (31)
      close (32)
      close (33)
      close (34)
      close (35)
      close (36)
      close (37)
      close (38)
      close (39)
      close (40)
      close (41)
      close (42)

994   Format(E12.6,x,E12.6,x,E12.6,x,E12.6,x,E12.6)
995   Format(I5,x,E12.6,x,E12.6,x,E12.6,x,E12.6,x,E12.6)
996   Format(E12.6,x,E12.6,x,E12.6,x,E12.6,x,E12.6,x,E12.6,x,E12.6)
997   Format(I5,x,E12.6,x,E12.6,x,E12.6,x,E12.6)
998   Format(E12.6,x,E12.6,x,E12.6,x,E12.6)
999   Format(E12.6,x,E12.6)

      stop
      end



      Subroutine FCN (N, T, Y, YPRIME)
C                                  SPECIFICATIONS FOR ARGUMENTS
      INTEGER    N,A
      REAL*8     T, Y(N), YPRIME(N)
      real*8     m,q,dBxdx,dBxdy,dBxdz,dBydx,dBydy,dBydz,dBzdx
      real*8     dBzdy,dBzdz,Bo,R,L,d,j,W,hbar,Ax,Ay,Az,dt

      real*8     dphi,dphiP,dphiMUB,dphiVA
      real*8     omega,Bx,By,Bz,dBxdt,dBydt,dBzdt
      common /par/ omega,Bx,By,Bz,dBxdt,dBydt,dBzdt
      common /par/ dphi,dphiP,dphiMUB,dphiVA,A


      q=1.6D-19
      m=9.11D-31
      L=250.0D-9
      R=100.0d-9 !200.0D-9
      Bo=8.5d0 !A*8.5d0
      !d =L/(2d0*W+1.0d0)
      W=50d0
      hbar=1.054572d-34
      dt=4.0d-15

      Ax=-Bo*R**3d0*Y(3)/(2d0*(R**2d0+Y(1)**2d0+            &
         Y(3)**2d0+Y(5)**2d0)**(3d0/2d0))
```

```
Ay=Bo*R**3d0*Y(1)/(2d0*(R**2d0+Y(1)**2d0+        &
   Y(3)**2d0+Y(5)**2d0)**(3d0/2d0))

Az=0.0d0


Bx=3d0*Bo*R**3d0*Y(1)*Y(5)/(2d0*(R**2d0+         &
   Y(1)**2d0+Y(3)**2d0+Y(5)**2d0)**(5d0/2d0))

By=3d0*Bo*R**3d0*Y(3)*Y(5)/(2d0*(R**2d0+         &
   Y(1)**2d0+Y(3)**2d0+Y(5)**2d0)**(5d0/2d0))

Bz=Bo*R**3d0*(2d0*R**2d0-Y(1)**2d0 -             &
   Y(3)**2d0+2d0*Y(5)**2d0)/(2d0*                 &
   (R**2d0+Y(1)**2d0+Y(3)**2d0+Y(5)**2d0)**(5d0/2d0))


dBxdx=3d0*Bo*R**3d0*Y(5)*(R**2d0-4d0*Y(1)**      &
      2d0+Y(3)**2d0+Y(5)**2d0)/                  &
      (2d0*(R**2d0+Y(1)**2d0+Y(3)**2d0+Y(5)**2d0)**(7d0/2d0))

dBxdy=-15d0*Bo*R**3d0*Y(3)*Y(5)*Y(1)/(2d0*(R**2d0+Y(1)**    &
      2d0+Y(3)**2d0+Y(5)**2d0)**(7d0/2d0))

dBxdz=3d0*Bo*R**3d0*Y(1)*(R**2d0+Y(1)**2d0+Y(3)**2d0-4d0*Y(5)  &
**2d0)/(2d0*(R**2d0+Y(1)**2d0+Y(3)**2d0+Y(5)**2d0)**(7d0/2d0))


dBydx=-15d0*Bo*R**3d0*Y(3)*Y(5)*Y(1)/(2d0*       &
      (R**2d0+Y(1)**2d0+Y(3)**2d0+Y(5)**2d0)**(7d0/2d0))

dBydy=3d0*Bo*R**3d0*Y(5)*(R**2d0+Y(1)**2d0 -                  &
      4d0*Y(3)**2d0+Y(5)**2d0)/(2d0*(R**2d0+Y(1)**2d0+Y(3)**  &
      2d0+Y(5)**2d0)**(7d0/2d0))

dBydz=3d0*Bo*R**3d0*Y(3)*(R**2d0+Y(1)**2d0+Y(3)**2d0-4d0*Y(5)  &
   **2d0)/(2d0*(R**2d0+Y(1)**2d0+Y(3)**2d0+Y(5)**2d0)**(7d0/2d0))


dBzdx=-3d0*Bo*R**3d0*Y(1)*(4d0*R**2d0-Y(1)**2d0-       &
      Y(3)**2d0+4d0*Y(5)**2d0)/(2d0*(R**2d0+Y(1)       &
      **2d0+Y(3)**2d0+Y(5)**2d0)**(7d0/2d0))

dBzdy=-3d0*Bo*R**3d0*Y(3)*(4d0*R**2d0-Y(1)**2d0-       &
      Y(3)**2d0+4d0*Y(5)**2d0)/(2d0*(R**2d0+Y(1)**     &
      2d0+Y(3)**2d0+Y(5)**2d0)**(7d0/2d0))

dBzdz=-3d0*Bo*R**3d0*Y(5)*(2d0*R**2d0-3d0*Y(1)**                &
      2d0-3d0*Y(3)**2d0+2d0*Y(5)**2d0)/(2d0*(R**2d0+Y(1)**      &
      2d0+Y(3)**2d0+Y(5)**2d0) **(7d0/2d0))



dBxdt= Y(2)*dBxdx+Y(4)*dBxdy+Y(6)*dBxdz

dBydt= Y(2)*dBydx+Y(4)*dBydy+Y(6)*dBydz
```

```
      dBzdt= Y(2)*dBzdx+Y(4)*dBzdy+Y(6)*dBzdz

      omega=(((dBxdt)**2d0+(dBydt)**2d0+(dBzdt)**2d0)                &
            /(Bx**2d0+By**2d0+Bz**2d0))**(1d0/2d0)

      dphi=dphiP-dphiMUB-dphiVA

      dphiP=(1/hbar)*(1d0/2d0)*m*(Y(2)**2d0+Y(4)**2d0+Y(6)**2d0)*dt

      dphiMUB=-(1/hbar)*(Y(7)*Bx+Y(8)*By+Y(9)*Bz)*dt

      dphiVA=-(q/hbar)*(Y(2)*Ax+Y(4)*Ay+Y(6)*Az)*dt



      YPRIME(1) = Y(2)
      YPRIME(2) = (q/m)*(Y(4)*Bz-Y(6)*By)+(1/m)*             &
                  (Y(7)*dBxdx+Y(8)*dBydx + Y(9)*dBzdx)


      YPRIME(3) = Y(4)
      YPRIME(4) = (q/m)*(Y(6)*Bx-Y(2)*Bz)+(1/m)*             &
                   (Y(7)*dBxdy+Y(8)*dBydy + Y(9)*dBzdy)

      YPRIME(5) = Y(6)
      YPRIME(6) = (q/m)*(Y(2)*By-Y(4)*Bx)+(1/m)*             &
                  (Y(7)*dBxdz + Y(8)*dBydz +Y(9)*dBzdz)

      YPRIME(7) = (q/m)*(Y(8)*Bz-Y(9)*By)

      YPRIME(8) = (q/m)*(Y(9)*Bx-Y(7)*Bz)

      YPRIME(9) = (q/m)*(Y(7)*By-Y(8)*Bx)



c     WRITE (6,'(10E12.3)') T, Y(1), Y(2), Y(3), Y(4),    &
c              Y(5),Y(6),Y(7),Y(8),Y(9)

c     write(6,*) 'I made it here in function'
      RETURN
      END
```

A4 - Stern-Gerlach diffraction II

As in Appendix A2 a diffraction pattern is computed for a grating with a phase shift applied at each slit. In this case the strength of the quadratic phase is determined by the code in appendix A3. The result of this calculation may be seen in figure 5.4c.

```
program prog
implicit none


real*8 Pi,lambda,L,Fi,Fr,dx,xi,xj,d,W,dx1,dx2,dx3,P,QP(-12:12)
real*8 num,dr
integer Ng1,Ng2,Nd,i,j,k,s,NL

Pi=3.14d0
lambda=7.274d-9
L=0.53d0          !distance from grating to detector
d=100d-9 !30d-9   !80d-9 !width of slit
W=0.1d0           !width of detector



Ng1=12            !2d0*Ng1+1d0=number of slits
Ng2=1000
Nd=10000
NL=10             !number of loops


QP(0)=0d0
QP(1)=-3.73942d14
QP(2)=-8.90381d14
QP(3)=-1.62568d15
QP(4)=-1.92626d15
QP(5)=-2.49739d15
QP(6)=-2.75875E15
QP(7)=-3.11299E15
QP(8)=-3.43515E15
QP(9)=-3.59395E15
QP(10)=-3.97919E15
QP(11)=-4.01898E15
QP(12)=-4.39362E15


QP(-1)=-3.73942d14
QP(-2)=-8.90381d14
QP(-3)=-1.62568d15
QP(-4)=-1.92626d15
QP(-5)=-2.49739d15
QP(-6)=-2.75875E15
QP(-7)=-3.11299E15
QP(-8)=-3.43515E15
```

```
      QP(-9)=-3.59395E15
      QP(-10)=-3.97919E15
      QP(-11)=-4.01898E15
      QP(-12)=-4.39362E15


      dx1=d/(2d0*Ng2+1d0) !delta x for riemann sum
      dx2=W/(2d0*Nd+1d0)  !resolution of detector
      dx3=150d-9          !grating periodicity
      dr=2.0d-6           !space between neighboring loops

      open(unit=29,file="phase1.dat")
      open(unit=30,file="phase2.dat")
      open(unit=31,file="intensity1.dat")
      open(unit=32,file="intensity2.dat")

      do s=0,1
            do i=-Nd,Nd
                  Fi=0d0
                  Fr=0d0

                  do k=-Ng1,Ng1
                        do j=-Ng2,Ng2

                              xj=j*dx1+k*dx3
                              xi=i*dx2


      Fi=Fi+sin((2d0*Pi/lambda)*((xi-xj)**2d0+L**2d0)**           &
            0.5d0 - QP(modulo(k,4))*(j*dx1)**2d0-(1d0-2d0*s)*     &
            modulo(k,4)*Pi/2d0)

      Fr=Fr+cos((2d0*Pi/lambda)*((xi-xj)**2d0+L**2d0)**           &
            0.5d0 - QP(modulo(k,4))*(j*dx1)**2d0-(1d0-2d0*s)*     &
            modulo(k,4)*Pi/2d0)


                        enddo
                  enddo
                  P=(Fi**2d0+Fr**2d0)/((2d0*Ng1+1d0)*(2d0*Ng2+1d0))
                  if(s .EQ. 0)then
                        write(31,999) xi,P
                  elseif(s .EQ. 1)then
                        write(32,999) xi,P
                  endif
            enddo

      enddo

999 format(E12.6,x,E12.6)
      close(29)
      close(30)
      close(31)
      close(32)
      end program prog
```

A5 - Stern-Gerlach interference phase

This code accomplishes ultimately the same goal as the one in A3 except it is done with a solenoid for analysing the Stern-Gerlach interferometers as described in section 3 of chapter 5. The results of this calculation are plotted in figure 5.6b.

```
      program simulation
      implicit none


      INTEGER    MXPARM, N,zend
      PARAMETER  (MXPARM=50, N=9,zend=150)
!                                SPECIFICATIONS FOR LOCAL VARIABLES
      INTEGER    IDO, j, jend,z,s,send,A,i
      REAL*8     PARAM(MXPARM), T, TEND, TOL, Y(N)
      real*8     tstep,endoftime,xSTEP, endofspace,magmoment
      real*8     temp1,temp2,temp3,temp4,temp,factor


      real*8     omega,Bx,By,Bz,dBxdt,dBydt,dBzdt
      common /par/ omega,Bx,By,Bz,dBxdt,dBydt,dBzdt

      real*8       dphi,dphiP,dphiMUB,dphiVA
      real*8       phi,phiP,phiMUB,phiVA(-(zend+2):zend)
      real*8       Q(-(zend+2):zend)

      common /par/ dphi,dphiP,dphiMUB,dphiVA,A

      External FCN
      open(unit=30,file="trajectory.dat")
      open(unit=31,file="velocity.dat")
      open(unit=32,file="magnetic moment.dat")
      open(unit=33,file="mmx.dat")
      open(unit=34,file="x velocity.dat")
      open(unit=35,file="omega.dat")
      open(unit=36,file="B field.dat")
      open(unit=37,file="dphi.dat")
      open(unit=38,file="dphiP.dat")
      open(unit=39,file="dphiMUB.dat")
      open(unit=40,file="dphiVA.dat")
      open(unit=41,file="phi.dat")
      open(unit=42,file="vA quad factor.dat")


!     do A=0,80
!     write(6,*) A

      send=1
      magmoment=9.27d-24
      do s=0,send
```

```
!     zend=150
!     endofspace=0.5d-6
!     xSTEP = endofspace/zend
!     do z=-zend,zend

!                                Set initial conditions


      T = 0.0d0
                  Y(1) = 0.5d-6 !z*xSTEP
                  Y(2) = 0.0d0
                  Y(3) = 0.0d0
                  Y(4) = 0.0d0
                  Y(5) = -0.01d0          !-2.3425d-5
                  Y(6) = 5d6          !1.874d7
                  Y(7) = 0.0d0
                  Y(8) = 0.0d0
                  Y(9) = (1-2*s)*magmoment

                  temp1=0d0
                  temp2=0d0
                  temp3=0d0
                  temp4=0d0



!
!                    Set error tolerance
                  TOL = 5.0d-12
!                               Set PARAM to default
                  CALL SSET (MXPARM, 0.0, PARAM, 1)
!                               Select absolute error control
                  PARAM(10) = 1.0d0
!                                          Set max iterations
                  PARAM(4)=1d8
!                               Print header


                  IDO = 1
                  jend=10000  !150000 !1000000
                  endoftime=4d-9
                  tSTEP = endoftime/jend
                  do j=1,jend+1

                        TEND = (j)*tstep
!                       write(6,*) tend
!                       write(6,*) 'I made it here'
                        CALL dIVPRK (IDO, N, FCN, T, TEND, TOL,   &
                                     PARAM, Y)

                        temp1=temp1+dphiVA
                        temp2=temp2+dphiMUB
                        temp3=temp3+dphiP
                        temp4=temp4+dphi


!                       write(6,*) 'I made it here'
```

```
!            WRITE (6,'(10E12.3)') T, Y(1), Y(2), Y(3), Y(4),     &
!                                  Y(5),Y(6),Y(7),Y(8),Y(9)


                        WRITE (30,998) T, Y(1), Y(3), Y(5)
                        WRITE (31,998) T, Y(2), Y(4), Y(6)
                        WRITE (32,998) T, Y(7), Y(8), Y(9)
!                       WRITE (37,999) T, dphi
!                       WRITE (38,999) T, dphiP
!                       WRITE (39,999) T, dphiMUB
!                       WRITE (40,999) T, dphiVA
!                       WRITE (35,999) T, omega
                        WRITE (36,996) T, Bx,By,Bz,dBxdt,dBydt,dBzdt
!                       WRITE (33,999) T,'    ', Y(7)

!                                 Final call to release workspace
!                       write(6,*) tend,y(2)

                  enddo

!                 phiVA(z)=temp1
!                 phiMUB=temp2
!                 phiP=temp3
!                 phi=temp4

!                 phiVA(-zend-2)=0d0
!                 phiVA(-zend-1)=0d0
!                 Q(z)=0.5d0*(phiVA(z)-2d0*phiVA(z-1)+phiVA(z-
2))/xSTEP**2d0


!                 write(6,*)  s,z*xSTEP,phiVA(z),phiMUB,phiP
!                 write(30,997) s,z*xSTEP, Y(1), Y(3), Y(5)
!                 write(31,997) s,z*xSTEP, Y(2), Y(4), Y(6)
!                 write(32,997) s,z*xSTEP, Y(7), Y(8), Y(9)
!                 WRITE(41,995) s,z*xSTEP, phiVA(z),phiMUB,phiP,phi

!                 write(6,*) s,z,(0.5d0)*(9.11D-                   &
!                             31)*(Y(2)*Y(2)+Y(4)*Y(4)             &
!                             +Y(6)*Y(6))-(0.5d0)*(9.11D-31)*      &
!                             (1.874d7)*(1.874d7)
      ido=3
                  CALL dIVPRK (IDO, N, FCN, T, TEND, TOL, PARAM, Y)
!           enddo

!           temp=0d0
!           do i=-(zend-2),zend
!                 temp=temp+Q(i)
!           enddo
!           factor=temp/(2d0*zend-1)


!           write(42,999) A*7112.999d0/10d0,factor



!           write(6,*) A,factor
```

```
      enddo

!     enddo

      close (30)
      close (31)
      close (32)
      close (33)
      close (34)
      close (35)
      close (36)
      close (37)
      close (38)
      close (39)
      close (40)
      close (41)
      close (42)

994   Format(I5,x,E12.6,x,E12.6)
995   Format(I5,x,E12.6,x,E12.6,x,E12.6,x,E12.6,x,E12.6)
996   Format(E12.6,x,E12.6,x,E12.6,x,E12.6,x,E12.6,x,E12.6,x,E12.6)
997   Format(I5,x,E12.6,x,E12.6,x,E12.6,x,E12.6)
998   Format(E12.6,x,E12.6,x,E12.6,x,E12.6)
999   Format(E12.6,x,E12.6)

      stop
      end



      Subroutine FCN (N, T, Y, YPRIME)
!                                 SPECIFICATIONS FOR ARGUMENTS
      INTEGER    N,A
      REAL*8     T, Y(N), YPRIME(N)
      real*8     m,q,dBxdx,dBxdy,dBxdz,dBydx,dBydy,dBydz,dBzdx
      real*8     dBzdy,dBzdz,Bo,R,L,d,j,W,hbar,Ax,Ay,Az,dt,K,muo

      real*8     dphi,dphiP,dphiMUB,dphiVA,bignum1,bignum2
      real*8     omega,Bx,By,Bz,dBxdt,dBydt,dBzdt,c1,c2,c3,z1,z2
      common /par/ omega,Bx,By,Bz,dBxdt,dBydt,dBzdt
      common /par/ dphi,dphiP,dphiMUB,dphiVA,A


      q=1.6D-19
      m=9.11D-31
      K=7112.999d0            !A*7112.999d0/10d0  !surface current
density
      R=1d-3                  !radius of solenoid
      L=0.01d0                !length of solenoid
      muo=4d0*3.14d0*1d-7     !permeability of free space
      hbar=1.054572d-34
      dt=4.0d-13

      c1=R**2d0+Y(1)**2d0+Y(3)**2d0
      c2=c1+(Y(5)+L/2d0)**2d0
```

```
      c3=c1+(Y(5)-L/2d0)**2d0

      z1=Y(5)+L/2d0
      z2=Y(5)-L/2d0

      Ax=(muo*K*R**2d0*Y(3)/(4d0*c1))*(z2/c3**0.5d0-z1/c2**0.5d0)

      Ay=-(muo*K*R**2d0*Y(1)/(4d0*c1))*(z2/c3**0.5d0-z1/c2**0.5d0)

      Az=0.0d0


      Bx=-(muo*K*R**2d0*Y(1)/(4d0*c1))*(1d0/c2**0.5d0*                &
          (1d0-z1**2d0/c2)-1d0/c3**0.5d0*(1d0-z2**2d0/c3))

      By=-(muo*K*R**2d0*Y(3)/(4d0*c1))*(1d0/c2**0.5d0*                &
          (1d0-z1**2d0/c2)-1d0/c3**0.5d0*(1d0-z2**2d0/c3))

      Bz=(muo*K*R**2d0/(4d0*c1))*(2d0*(z1/c2**0.5d0-                  &
         z2/c3**0.5d0)*(1d0-(Y(1)**2d0+Y(3)**2d0)/c1)-                &
         (Y(1)**2d0+Y(3)**2d0)*(z1/c2**1.5d0-z2/c3**1.5d0))

      bignum1=-(muo*K*R**2d0/(4d0*c1))*(1d0/c2**0.5d0*                &
               (1d0-z1**2d0/c2)-1d0/c3**0.5d0*(1d0-z2**2d0/c3))

      dBxdx=bignum1-2d0*Y(1)*Bx/c1-                                   &
            (muo*K*R**2d0*Y(1)**2d0/(4d0*c1))*                  &
            (3d0*(z1**2d0/c2**2.5d0-                            &
            z2**2d0/c3**2.5d0)-(1d0/c2**1.5d0-1d0/c3**1.5d0))

      dBxdy=-2d0*Y(3)*Bx/c1-(muo*K*R**2d0*Y(1)*Y(3)/(4d0*c1))*    &
            (3d0*(z1**2d0/c2**2.5d0 -                           &
            z2**2d0/c3**2.5d0)-(1d0/c2**1.5d0-1d0/c3**1.5d0))

      dBxdz=3d0*(muo*K*R**2d0*Y(1)/(4d0*c1))*((z1/c2**1.5d0-      &
            z2/c3**1.5d0)-(z1**3d0/c2**2.5d0-z2**3d0/c3**2.5d0))

      dBydx=dBxdy

      bignum2=-(muo*K*R**2d0/(4d0*c1))*(1d0/c2**0.5d0*(1d0-         &
              z1**2d0/c2)-1d0/c3**0.5d0*(1d0-z2**2d0/c3))

    dBydy=bignum2-2d0*Y(3)*By/c1 - (muo*K*R**2d0*Y(3)**2d0/(4d0*c1))* &
            (3d0*(z1**2d0/c2**2.5d0 - z2**2d0/c3**2.5d0)-(1d0/c2**    &
            1.5d0-1d0/c3**1.5d0))

      dBydz=3d0*(muo*K*R**2d0*Y(3)/(4d0*c1))*((z1/c2**1.5d0-          &
            z2/c3**1.5d0)-(z1**3d0/c2**2.5d0-z2**3d0/c3**2.5d0))


      dBzdx=dBxdz

      dBzdy=dBydz

      dBzdz=-(dBxdx+dBydy)
```

```
      dBxdt= Y(2)*dBxdx+Y(4)*dBxdy+Y(6)*dBxdz

      dBydt= Y(2)*dBydx+Y(4)*dBydy+Y(6)*dBydz

      dBzdt= Y(2)*dBzdx+Y(4)*dBzdy+Y(6)*dBzdz

      omega=(((dBxdt)**2d0+(dBydt)**2d0+(dBzdt)**2d0)/(Bx**2d0+     &
            By**2d0+Bz**2d0))**(1d0/2d0)

      dphi=dphiP+dphiMUB+dphiVA

      dphiP=(1d0/hbar)*(1d0/2d0)*m*(Y(2)**2d0+Y(4)**2d0+Y(6)**2d0)*dt

      dphiMUB=(1d0/hbar)*(Y(7)*Bx+Y(8)*By+Y(9)*Bz)*dt

      dphiVA=(q/hbar)*(Y(2)*Ax+Y(4)*Ay+Y(6)*Az)*dt



      YPRIME(1) = Y(2)
      YPRIME(2) = (q/m)*(Y(4)*Bz-                              &
                  Y(6)*By)+(1/m)*(Y(7)*dBxdx+Y(8)*dBydx+Y(9)*dBzdx)


      YPRIME(3) = Y(4)
      YPRIME(4) = (q/m)*(Y(6)*Bx-                              &
                  Y(2)*Bz)+(1/m)*(Y(7)*dBxdy+Y(8)*dBydy+Y(9)*dBzdy)

      YPRIME(5) = Y(6)
      YPRIME(6) = (q/m)*(Y(2)*By-                            &
                  Y(4)*Bx)+(1/m)*(Y(7)*dBxdz+Y(8)*dBydz+Y(9)*dBzdz)

      YPRIME(7) = (q/m)*(Y(8)*Bz-Y(9)*By)

      YPRIME(8) = (q/m)*(Y(9)*Bx-Y(7)*Bz)

      YPRIME(9) = (q/m)*(Y(7)*By-Y(8)*Bx)



!     WRITE (6,'(10E12.3)') T, Y(1), Y(2), Y(3), Y(4),           &
!           Y(5),Y(6),Y(7),Y(8),Y(9)

      RETURN
      END
```

A6 - Stern-Gerlach grating-biprism interferometer

A beam of electrons is propagated from a point source to a collimating aperture and then to a grating from which it diffracts. The resulting first order diffracted beams are propagated to a bi-prism wire such that one passes on each side of the wire. The bi-prism pulls the two beams together at which point they pass through solenoids, acquiring spin dependent phase shifts. The two beams are then propagated to the detector where a probability distribution is calculated. The result of this calculation is plotted in figure 5.8a with no spin dependent phase shift and 8b with a spin dependent phase shift of magnitude $\pi/4$ in each arm.

```
program prog
implicit none

parameter(Nbp=5000,Ns=1000,Nd=10000) !Ng1=100,Ng1c=3
!parameter(gratingnumber=4)
real*8 Pi,lambda,dx,d,dx1,dx2,dx3,dx4,hbar,q,m,L1,L2
real*8 Rbp,Rel,Eel,alpha,Vbp,Wbp,Ws,Wa,xbp
real*8 P1(-Nd:Nd,0:1),Fr1(-Ns:Ns)
real*8 L3,Fr2(-Nbp:Nbp,0:1,0:1),Fi2(-Nbp:Nbp,0:1,0:1)
real*8 x2(-Nbp:Nbp),x3(-Nd:Nd),xg
real*8 Ki,Kr,Fi1(-Ns:Ns),x1(-Ns:Ns),A,P2(-Nbp:Nbp,0:1,0:1)
real*8 P3(-Ns:Ns)
real*8 L4,xs,xa,phi,muo,mu,L,Ko,v,Fr3(-Nd:Nd,0:1)
real*8 Fi3(-Nd:Nd,0:1),xd,Wd
integer nums,numk,Nbp,i,j,k,Ns,Na,spin,Nd,Nbpr,N

Pi=3.14d0
hbar=1.054572d-34  !hbar in J*s
Rbp=2d-6
q=-1.6d-19
m=9.1094d-31
L1=0.25d0  !distance from FET to aperture
L2=0.005d0 !distance from aperture to solenoid
L3=0.01d0  !distance from solenoid to biprism
L4=0.5d0   !distance from biprism to detector
L=0.01     !length of solenoid
Ko=3556.45 !0.1 times the necessary surface current density for
           !pi/2 phase shift
v=5d6
muo=4d0*Pi*1d-7
mu=9.27d-24
lambda=2d0*Pi*hbar/(m*v)
```

```
d=0.003d0  !seperation between solenoid centers

alpha=Wbp/(2d0*L4) !defl. angle delta=arctan(Wbp/(2d0*L4)),
                   !alpha=tan(delta)

Wd=1d-6      !width of detector
Wbp=10d-6    !width of integration region on one side of biprism
Ws=2d-6      !width of integration in solenoid
Wa=1d-6      !width of aperture

N=NINT((d/Wbp)*(2d0*Nbp+1d0))  !number to shift index by to place
                               !beam around biprism
Na=1000
Nbpr=NINT((Rbp/Wbp)*(2d0*Nbp+1d0))

write(6,*) N
dx1=Wa/(2d0*Na+1d0)     !space between points at aperture
dx2=Ws/(2d0*Ns+1d0)     !space between points at solenoid
dx3=Wbp/(2d0*Nbp+1d0)   !space between points at biprism
dx4=Wd/(2d0*Nd+1d0)     !resolution of detector

A=-1.90814E12

call omp_set_num_threads(4)

open(unit=28,file="intensity at solenoid.dat")
open(unit=29,file="intensity.dat")
open(unit=30,file="intensity at BP.dat")

!!!!!!!!!!!!!!!!!!!!!!!!!!!!!!!!!!!!!!!!!!!!!!!!!!!!!!!!!!!!!!!!!!!!!!
!!!Propogating wavefunction from tip to aperture to solenoid!!!
!!!!!!!!!!!!!!!!!!!!!!!!!!!!!!!!!!!!!!!!!!!!!!!!!!!!!!!!!!!!!!!!!!!!!!
write(6,*) 'aperture to solenoid'


do i=-Ns,Ns
            Fr1(i)=0d0  !real part
            Fi1(i)=0d0  !imaginary part
enddo


do i=-Ns,Ns
      xs=i*dx2
      x1(i)=xs

      do j=-Na,Na

                  xa=j*dx1

                  Fi1(i)=Fi1(i)+sin((2d0*Pi/lambda)*        &
                         ((xa**2d0+L1**2d0)**0.5d0+((xs-    &
                         xa)**2d0+L2**2d0)**0.5d0))

                  Fr1(i)=Fr1(i)+cos((2d0*Pi/lambda)*        &
                         ((xa**2d0+L1**2d0)**0.5d0+((xs-    &
                         xa)**2d0+L2**2d0)**0.5d0))
```

```
      enddo
enddo

do i=-Ns,Ns
      P3(i)=(Fi1(i))**2d0+(Fr1(i))**2d0
      write(28,997) i*dx2,P3(i)
enddo

!!!!!!!!!!!!!!!!!!!!!!!!!!!!!!!!!!!!!!!!!!!!!!!!!!!!!!!!!!!!!!!!
!!!propogating wavefunction from solenoid to biprism !!!
!!!!!!!!!!!!!!!!!!!!!!!!!!!!!!!!!!!!!!!!!!!!!!!!!!!!!!!!!!!!!!!!
write(6,*) 'solenoid to biprism'

do spin=0,1
      do i=-Nbp,Nbp
            do nums=0,1
                  Fr2(i,nums,spin)=0d0    !real part
                  Fi2(i,nums,spin)=0d0    !imaginary part
            enddo
      enddo
enddo

do spin=0,1
            do nums=0,1

                  do i=-Nbp,Nbp
                        xbp=i*dx3
                        x2(i)=xbp         !xq

                        do j=-Ns,Ns

                              xs=j*dx2

                              phi=(1d0-2d0*spin)*(1d0-      &
                                  2d0*nums)*muo*mu*L*Ko/    &
                                  (hbar*v) + A*xs**2d0


                              Ki=sin((2d0*Pi/lambda)*((xbp-     &
                                 xs)**2d0+L3**2d0)**0.5d0-phi)

                              Kr=cos((2d0*Pi/lambda)*((xbp-     &
                                 xs)**2d0+L3**2d0)**0.5d0-phi)

                              Fi2(i,nums,spin)=
                                    Fi2(i,nums,spin) +          &
                                    (Ki*Fr1(j)+Kr*Fi1(j))       &

                              Fr2(i,nums,spin)=                 &
                                    Fr2(i,nums,spin)+           &
                                    (Kr*Fr1(j)-Ki*Fi1(j))

                        enddo
                        !write(6,*) Fi2(i,numk,nums),
Fr2(i,numk,nums)
                  enddo
```

```
            enddo
enddo

!!!!!!!!!!!!!!!!!!!!!!!!!!!!!!!!!!!!!!!!!!!!!!!!!!!!!!!!!!!!
!!!propogating wavefunction from biprism to detector !!!
!!!!!!!!!!!!!!!!!!!!!!!!!!!!!!!!!!!!!!!!!!!!!!!!!!!!!!!!!!!!
write(6,*) 'biprism to detector'

do spin=0,1
      do i=-Nd,Nd
            Fr3(i,spin)=0d0   !real part
            Fi3(i,spin)=0d0   !imaginary part
      enddo
enddo

do spin=0,1

      do i=-Nd,Nd
            xd=i*dx4
            x3(i)=xd          !xq
            do j=-(N+Nbp),-(N-Nbp)
                  xbp=j*dx3

                  Ki=sin((2d0*Pi/lambda)*((xd-              &
                     xbp)**2d0+L4**2d0)**0.5d0-alpha*abs(xbp))

                  Kr=cos((2d0*Pi/lambda)*((xd-               &
                     xbp)**2d0+L4**2d0)**0.5d0-alpha*abs(xbp))

                  Fi3(i,spin)=Fi3(i,spin)+(Ki*Fr2(j+N,0,spin)+  &
                              Kr*Fi2(j+N,0,spin))

                  Fr3(i,spin)=Fr3(i,spin)+(Kr*Fr2(j+N,0,spin)-  &
                              Ki*Fi2(j+N,0,spin))
            enddo

            do j=N-Nbp,N+Nbp

                  xbp=j*dx3

                  Ki=sin((2d0*Pi/lambda)*((xd-xbp)**2d0+      &
                     L4**2d0)**0.5d0-alpha*abs(xbp))

                  Kr=cos((2d0*Pi/lambda)*((xd-xbp)**2d0+      &
                     L4**2d0)**0.5d0-alpha*abs(xbp))

                  Fi3(i,spin)=Fi3(i,spin)+(Ki*Fr2(j-N,1,spin)+  &
                              Kr*Fi2(j-N,1,spin))

                  Fr3(i,spin)=Fr3(i,spin)+(Kr*Fr2(j-N,1,spin)-  &
                              Ki*Fi2(j-N,1,spin))

            enddo
      enddo
enddo
write(6,*) 'computing probability'
```

```
      do spin=0,1
            do i=-Nd,Nd
                  P1(i,spin)=(Fr3(i,spin))**2d0+(Fi3(i,spin))**2d0
            enddo
      enddo

      do spin=0,1
            do nums=0,1
                  do i=-Nbp,Nbp
                        P2(i,nums,spin)=(Fi2(i,nums,spin))**2d0 +   &
                                        (Fi2(i,nums,spin))**2d0
                  enddo
            enddo
      enddo

      do i=-Nd,Nd
            write(29,999) x3(i),P1(i,0),P1(i,1)
      enddo

      do i=-Nbp,Nbp
            write(30,998) x2(i),P2(i,0,0),P2(i,0,1),P2(i,1,0),P2(i,1,1)
      enddo

997 format(E12.6,x,E12.6)
998 format(E12.6,x,E12.6,x,E12.6,x,E12.6,x,E12.6)
999 format(E12.6,x,E12.6,x,E12.6)

      close(28)
      close(29)
      close(30)

      end program prog
```

A7 - Stern-Gerlach Mach-Zehnder interferometer

The output of the Stern-Gerlach Mach-Zehnder interferometer described in section 3.3 of chapter 5 is computed. The electron beam is propagated from a point source to a collimating aperture, and then to a solenoid. At the solenoid the beam acquires a spin dependent phase shift and is then propagated to the detection screen. This is repeated for another beam passing through a magnetic field of opposite direction. These two resulting wavefunctions represent the two arms of an interferometer having been separated by Bragg diffraction from a standing wave of light. The two wave functions are combined, and a probability distribution is determined which is then integrated over the detector. This is repeated computed for spin up and spin down for various magnetic field strengths. The result of this calculation may be seen in figure 5.9.

```
program prog
implicit none

parameter(Nd=1000,Ns=1000) !Ng1=100,Ng1c=3
!parameter(gratingnumber=4)
real*8 Pi,lambda,dx,d,dx1,dx2,dx3,dx4,hbar,q,m,L1,L2
real*8 Rbp,Rel,Eel,alpha,Vbp,Wd,Ws,Wa,xbp,xd
real*8 P1(-Nd:Nd,0:80,0:1),Fr1(-Ns:Ns)
real*8 L3,Fr2(-Nd:Nd,0:80,0:1,0:1),Fi2(-Nd:Nd,0:80,0:1,0:1)
real*8 x2(-Nd:Nd),xg
real*8 Ki,Kr,Fi1(-Ns:Ns),x1(-Ns:Ns),P1total(0:80,0:1),A(0:80)
real*8 L4,xs,xa,phi,muo,mu,L,Ko,v
integer nums,numk,Nd,i,j,k,Ns,Na,spin

Pi=3.14d0
hbar=1.054572d-34  !hbar in J*s
q=-1.6d-19
m=9.1094d-31
L1=0.25d0  !distance from FET to aperture
L2=0.005d0 !distance from aperture to solenoid
L3=0.5d0   !distance from solenoid to detector
L=0.01     !length of solenoid
Ko=711.3   !0.1 times the necessary surface current density for
           !pi/2
           !phase shift
v=5d6
muo=4d0*Pi*1d-7
```

```
mu=9.27d-24
lambda=2d0*Pi*hbar/(m*v)


Wd=0.01d0    !width of detector
Ws=2d-6      !width of integration in solenoid
Wa=1d-6      !width of aperture

Na=1000

dx1=Wa/(2d0*Na+1d0)     !space between points at aperture
dx2=Ws/(2d0*Ns+1d0)     !space between points at solenoid
dx3=Wd/(2d0*Nd+1d0)     !space between points at detector

A(0)=0d0
A(1)=-8.92133d10
A(2)=-3.49841d11
A(3)=-7.61686d11
A(4)=-1.29378d12
A(5)=-1.90814d12
A(6)=-2.56438d12
A(7)=-3.22475d12
A(8)=-3.85898d12
A(9)=-4.44841d12
A(10)=-4.98888d12
A(11)=-5.49204d12
A(12)=-5.98496d12
A(13)=-6.50789d12
A(14)=-7.11049d12
A(15)=-7.84676d12
A(16)=-8.76933d12
A(17)=-9.92351d12
A(18)=-1.13419d13
A(19)=-1.304d13
A(20)=-1.50134d13
A(21)=-1.72371d13
A(22)=-1.96664d13
A(23)=-2.22403d13
A(24)=-2.48866d13
A(25)=-2.75279d13
A(26)=-3.00893d13
A(27)=-3.25048d13
A(28)=-3.47246d13
A(29)=-3.67198d13
A(30)=-3.84861d13
A(31)=-4.00446d13
A(32)=-4.14411d13
A(33)=-4.27419d13
A(34)=-4.40287d13
A(35)=-4.53908d13
A(36)=-4.69172d13
A(37)=-4.86883d13
A(38)=-5.07678d13
A(39)=-5.31969d13
A(40)=-5.59893d13
A(41)=-5.91298d13
A(42)=-6.25746d13
```

```
A(43)=-6.62548d13
A(44)=-7.00826d13
A(45)=-7.39582d13
A(46)=-7.77794d13
A(47)=-8.145d13
A(48)=-8.48893d13
A(49)=-8.80391d13
A(50)=-9.08692d13
A(51)=-9.33804d13
A(52)=-9.56046d13
A(53)=-9.76019d13
A(54)=-9.94552d13
A(55)=-1.01263d14
A(56)=-1.0313d14
A(57)=-1.05157d14
A(58)=-1.07434d14
A(59)=-1.10028d14
A(60)=-1.12981d14
A(61)=-1.163d14
A(62)=-1.19965d14
A(63)=-1.23923d14
A(64)=-1.28095d14
A(65)=-1.32387d14
A(66)=-1.36691d14
A(67)=-1.40904d14
A(68)=-1.44929d14
A(69)=-1.4869d14
A(70)=-1.52136d14
A(71)=-1.55244d14
A(72)=-1.58025d14
A(73)=-1.60521d14
A(74)=-1.62799d14
A(75)=-1.64948d14
A(76)=-1.67066d14
A(77)=-1.69256d14
A(78)=-1.71614d14
A(79)=-1.74217d14
A(80)=-1.77122d14


call omp_set_num_threads(4)


open(unit=29,file="intensity.dat")


!!!!!!!!!!!!!!!!!!!!!!!!!!!!!!!!!!!!!!!!!!!!!!!!!!!!!!!!!!!!!!!!!!!!
!!!Propogating wavefunction from tip to aperture to solenoid!!!
!!!!!!!!!!!!!!!!!!!!!!!!!!!!!!!!!!!!!!!!!!!!!!!!!!!!!!!!!!!!!!!!!!!!



do i=-Ns,Ns
            Fr1(i)=0d0  !real part
            Fi1(i)=0d0  !imaginary part
enddo
```

```
      do i=-Ns,Ns
            xs=i*dx2
            x1(i)=xs

            do j=-Na,Na

                  xa=j*dx1

                  Fi1(i)=Fi1(i)+sin((2d0*Pi/lambda)*          &
                        ((xa**2d0+L1**2d0)**0.5d0+((xs-      &
                        xa)**2d0+L2**2d0)**0.5d0))

                  Fr1(i)=Fr1(i)+cos((2d0*Pi/lambda)*          &
                        ((xa**2d0+L1**2d0)**0.5d0+((xs-      &
                        xa)**2d0+L2**2d0)**0.5d0))

            enddo
      enddo


      !!!!!!!!!!!!!!!!!!!!!!!!!!!!!!!!!!!!!!!!!!!!!!!!!!!!!!!!!!!
      !!!propogating wavefunction from solenoid to detector!!!
      !!!!!!!!!!!!!!!!!!!!!!!!!!!!!!!!!!!!!!!!!!!!!!!!!!!!!!!!!!!

      do spin=0,1
            do i=-Nd,Nd
                  do numk=0,80
                        do nums=0,1
                              Fr2(i,numk,nums,spin)=0d0     !real part
                              Fi2(i,numk,nums,spin)=0d0     !imaginary
part
                        enddo
                  enddo
            enddo
      enddo

      do spin=0,1
            do numk=0,80
                  write(6,*) numk
                  do nums=0,1

                        do i=-Nd,Nd
                              xd=i*dx3
                              x2(i)=xd          !xq

                              do j=-Ns,Ns

                                    xs=j*dx2

                                    phi=(1d0-2d0*spin)*(1d0-          &
                                        2d0*nums)*muo*mu*L*numk*Ko/   &
                                        (hbar*v)+A(numk)*xs**2d0

                                    Ki=sin((2d0*Pi/lambda)*((xd-   &
                                       xs)**2d0+L3**2d0)**0.5d0-   &
                                       phi-(1d0-2d0*nums)*Pi/4)
```

```
                                    Kr=cos((2d0*Pi/lambda)*((xd-     &
                                       xs)**2d0+L3**2d0)**0.5d0-     &
                                       phi-(1d0-2d0*nums)*Pi/4)

                                    Fi2(i,numk,nums,spin)=           &
                                       Fi2(i,numk,nums,spin)+        &
                                       (Ki*Fr1(j)+Kr*Fi1(j))

                                    Fr2(i,numk,nums,spin)=           &
                                       Fr2(i,numk,nums,spin)+        &
                                       (Kr*Fr1(j)-Ki*Fi1(j))

                              enddo
                              !write(6,*) Fi2(i,numk,nums),      &
                              !Fr2(i,numk,nums)
                        enddo

                  enddo
            enddo
      enddo

      do spin=0,1
            do numk=0,80
                  do i=-Nd,Nd
                        P1(i,numk,spin)=(Fr2(i,numk,0,spin)+          &
                                         Fr2(i,numk,1,spin))**2d0+    &
                                         (Fi2(i,numk,0,spin)+         &
                                         Fi2(i,numk,1,spin))**2d0
                  enddo
            enddo
      enddo
!     !$OMP parallel private(i) shared(Nq,P2,num)
!     !$OMP do
!     do i=-Nd,Nd
!                 P2(i,num)=(Fr2(i,num)**2d0+Fi2(i,num)**2d0)
!     enddo
!     !$OMP end do
!     !$OMP end parallel


      do spin=0,1
            do i=0,80
                  P1total(i,spin)=0d0
            enddo
      enddo

      do spin=0,1
            do numk=0,80
                  do i=-Nd,Nd

                        P1total(numk,spin)=P1total(numk,spin) +      &
                        P1(i,numk,spin)
                  enddo
            enddo
      enddo
```

```
      do numk=0,80
            write(29,999) numk*Ko,P1total(numk,0),P1total(numk,1)
      enddo
999 format(E12.6,x,E12.6,x,E12.6)

      close(29)
      end program prog
```

A8 - Depolarizer

The probability amplitude of the depolarizer as described in section 2 of chapter 6 is computed for a range of laser pulse lengths. The built in double integral routine DTWODQ is used.

```
program prog
use msimsl
implicit none

integer N
parameter (N = 2500)

real t1,t2
real*8 w,w0,tau,Wint,Pi,m,v,lambda,hbar,k,q,eps0,c,p,A0,Int
common w,w0,tau,Wint,Pi,m,v,lambda,hbar,k,q,eps0,c,p,A0,Int

INTEGER    IRULE, NOUT,i,Ntau
REAL*8     A, B, ERRABSr,ERRABSi, ERRESTr,ERRESTi, ERRREL
REAL*8     Freal,Fimaginary, G, H, RESULTi,RESULTr,mu
EXTERNAL   Freal,Fimaginary, G, H

CALL UMACH (2, NOUT)

open(unit=30,file="Itot.dat")
open(unit=31,file="error.dat")

open(unit=32,file="Itoti.dat")
open(unit=33,file="errori.dat")

t1 = cpsec()

Pi = 2d0*dacos(0d0)
mu = 9.274d-24
m = 9.1094d-31
v = 1d7
lambda = 1064d-9
hbar = 1.0546d-34
k = 2d0*Pi/lambda
q = 1.6d-19
eps0 = 8.8542d-12
c = 3d8
p = m*v
Int   = 1d18

w0 = k*c
w = hbar*k**2d0/(2d0*m)


!factor in front of integral
```

```
      A0 = q*mu*k*p/(4d0*m*hbar**2d0)*(2d0*Int/(c*eps0*w0**2d0))

      !tau = 1d-15 !2d0*6.28d-15

      Wint = (2d0*Pi/w0)*100d0 !6.28d-13  !2*Wint = width of
                                          !integration

!                                 Set limits of integration
      A = -Wint
      B = Wint
!                                 Set error tolerances
      ERRABSr = 1d-8
      ERRABSi = 1d-8
      ERRREL = 0
!                                 Parameter for oscillatory function
      IRULE = 6

      Ntau = 1000   !number of tau data points

      do    i = 1,Ntau

            tau = 5d0*(2d0*Pi/w0)*(dfloat(i)/dfloat(Ntau))

            CALL DTWODQ (Freal, A, B, G, H, ERRABSr, ERRREL,      &
                         IRULE, RESULTr, ERRESTr)

            CALL DTWODQ (Fimaginary, A, B, G, H, ERRABSi,         &
                         ERRREL, IRULE, RESULTi, ERRESTi)


            write(30,999) tau,resultr,resulti

            !estimate of absolute value of error
            write(31,999) tau,ERRESTr,ERRESTi

            !write(32,998) tau,resulti
            !write(33,998) tau,ERRESTi

            !ERRABSr = dabs(RESULTr)*1d-2
            !ERRABSi = dabs(RESULTi)*1d-2

            write(6,*) i
      enddo

      close(30)
      close(31)
      close(32)
      close(33)

998   format(E12.6,x,E12.6)
999   format(E12.6,x,E12.6,x,E12.6)

      t2 = cpsec()

      write(6,*) t2-t1

      END
```

```
      REAL*8 FUNCTION Freal (tp, tpp)            !real part of
integrand
            REAL*8       tp, tpp
            real*8 w,w0,tau,Wint,Pi,m,v,lambda,hbar,k,q,eps0,c,p,A0,Int
            common w,w0,tau,Wint,Pi,m,v,lambda,hbar,k,q,eps0,c,p,A0,Int


            Freal = A0*(dcos((w0 - w)*tp + (-w0 + w)*tpp)*      &
                    dexp(-(tp**2d0 +tpp**2d0)/tau**2d0) +       &
                    dcos((-w0 - w)*tp + (w0 + w)*tpp)*          &
                    dexp(-(tp**2d0 + tpp**2d0)/tau**2d0))

            RETURN
      end

      REAL*8 FUNCTION Fimaginary (tp,tpp)       !imaginary part
            REAL*8 tp, tpp
            real*8 w,w0,tau,Wint,Pi,m,v,lambda,hbar,k,q,eps0,c,p,A0,Int
            common w,w0,tau,Wint,Pi,m,v,lambda,hbar,k,q,eps0,c,p,A0,Int

            Fimaginary = A0*(dsin((w0 - w)*tp + (-w0 + w)*tpp)*     &
                         dexp(-(tp**2d0 + tpp**2d0)/tau**2d0) +     &
                         dsin((-w0 - w)*tp + (w0 + w)*tpp)*         &
                         dexp(-(tp**2d0 + tpp**2d0)/tau**2d0))

            RETURN
      end

      REAL*8 FUNCTION G (tp)        !lower bound of inner integral
            REAL*8 tp
            real*8 w,w0,tau,Wint,Pi,m,v,lambda,hbar,k,q,eps0,c,p,A0,Int
            common w,w0,tau,Wint,Pi,m,v,lambda,hbar,k,q,eps0,c,p,A0,Int

            G = -Wint
            RETURN
    end


      REAL*8 FUNCTION H (tp)        !upper bound of inner integral
            REAL*8 tp
            real*8 w,w0,tau,Wint,Pi,m,v,lambda,hbar,k,q,eps0,c,p,A0,Int
            common w,w0,tau,Wint,Pi,m,v,lambda,hbar,k,q,eps0,c,p,A0,Int

            H = tp
            RETURN
    END
```

A9 - Two color spin-flip K-D effect

The probability amplitude of the two color spin-flip K-D effect as described in section 2 of chapter 6 is computed for a range of laser pulse lengths. The built in double integral routine DTWODQ is used.

```
program prog
use msimsl
implicit none

integer N
parameter (N = 2500)   !2500

real t1,t2
real*8 w,w0,tau,Wint,Pi,m,v,lambda,hbar,k,q,eps0,c,p,A0,Int

common w,w0,tau,Wint,Pi,m,v,lambda,hbar,k,q,eps0,c,p,A0,Int


INTEGER    IRULE, NOUT,i,Ntau
REAL*8     A, B, ERRABSr,ERRABSi, ERRESTr,ERRESTi, ERRREL
REAL*8     Freal,Fimaginary, G, H, RESULTi,RESULTr,mu
EXTERNAL   Freal,Fimaginary, G, H !, DTWODQ, UMACH

CALL UMACH (2, NOUT)

open(unit=30,file="Itot.dat")
open(unit=31,file="error.dat")

open(unit=32,file="Itoti.dat")
open(unit=33,file="errori.dat")

t1 = cpsec()

Pi = 2d0*dacos(0d0)
mu = 9.274d-24
m = 9.1094d-31
v = 1d7
lambda = 1064d-9
hbar = 1.0546d-34
k = 2d0*Pi/lambda
q = 1.6d-19
eps0 = 8.8542d-12
c = 3d8
p = m*v
Int   = 1d18 !8.52093313d10 !6.2996d5 !1d10 !1d16

w0 = k*c  !1.0d15 !tau = 6.28d-15
w = hbar*k**2d0/(2d0*m)
```

```
      !factor in front of integral
      A0 = q**2d0*mu*k/(4d0*2d0**0.5d0*m*hbar**2d0)*         &
           (2d0*Int/(c*eps0*w0**2d0))**(3d0/2d0)


      !tau = 1d-15 !2d0*6.28d-15

      Wint = (2d0*Pi/w0)*100d0      !2*Wint = width of integration


!                                   Set limits of integration
      A = -Wint
      B = Wint
!                                   Set error tolerances
      ERRABSr = 1d-8
      ERRABSi = 1d-8
      ERRREL = 0
!                                   Parameter for oscillatory function
      IRULE = 6

      Ntau = 1000   !number of tau data points

      do    i = 1,Ntau

            tau = 5d0*(2d0*Pi/w0)*(dfloat(i)/dfloat(Ntau))

            CALL DTWODQ (Freal, A, B, G, H, ERRABSr, ERRREL, IRULE,
&
                         RESULTr, ERRESTr)

            CALL DTWODQ (Fimaginary, A, B, G, H, ERRABSi, ERRREL,
&
                         IRULE, RESULTi, ERRESTi)

            write(30,999) tau,resultr,resulti

            !estimate of absolute value of error
            write(31,999) tau,ERRESTr,ERRESTi

            !write(32,998) tau,resulti
            !write(33,998) tau,ERRESTi

            !ERRABSr = dabs(RESULTr)*1d-2
            !ERRABSi = dabs(RESULTi)*1d-2

            write(6,*) i
      enddo

      close(30)
      close(31)
      close(32)
      close(33)

998   format(E12.6,x,E12.6)
999   format(E12.6,x,E12.6,x,E12.6)
```

```
      t2 = cpsec()

      write(6,*) t2-t1

      END


      REAL*8 FUNCTION Freal (tp, tpp)            !real part of
integrand
            REAL*8 tp, tpp
            real*8 w,w0,tau,Wint,Pi,m,v,lambda,hbar,k,q,eps0,c,p,A0,Int
            common w,w0,tau,Wint,Pi,m,v,lambda,hbar,k,q,eps0,c,p,A0,Int

            Freal = A0*(dcos((w0 + 3d0*w)*tp + (-w0 - 3d0*w)*tpp)*    &
                    dexp(-(tp**2d0 + 2d0*tpp**2d0)/tau**2d0) +        &
                    dcos((-w0 + 3d0*w)*tp + (w0 - 3d0*w)*tpp)*        &
                    dexp(-(2d0*tp**2d0 + tpp**2d0)/tau**2d0))
            RETURN
      end

      REAL*8 FUNCTION Fimaginary (tp,tpp)       !imaginary part
            REAL*8 tp, tpp
            real*8 w,w0,tau,Wint,Pi,m,v,lambda,hbar,k,q,eps0,c,p,A0,Int
            common w,w0,tau,Wint,Pi,m,v,lambda,hbar,k,q,eps0,c,p,A0,Int

            Fimaginary=A0*(dsin((w0 + 3d0*w)*tp + (-w0 - 3d0*w)*tpp)* &
                        dexp(-(tp**2d0 + 2d0*tpp**2d0)/tau**2d0) +    &
                        dsin((-w0 + 3d0*w)*tp + (w0 - 3d0*w)*tpp)*    &
                        dexp(-(2d0*tp**2d0 + tpp**2d0)/tau**2d0))
            RETURN
      end

      REAL*8 FUNCTION G (tp)        !lower bound of inner integral
            REAL*8 tp
            real*8 w,w0,tau,Wint,Pi,m,v,lambda,hbar,k,q,eps0,c,p,A0,Int
            common w,w0,tau,Wint,Pi,m,v,lambda,hbar,k,q,eps0,c,p,A0,Int

            G = -Wint
            RETURN
      end


      REAL*8 FUNCTION H (tp)        !upper bound of inner integral
            REAL*8 tp
            real*8 w,w0,tau,Wint,Pi,m,v,lambda,hbar,k,q,eps0,c,p,A0,Int
            common w,w0,tau,Wint,Pi,m,v,lambda,hbar,k,q,eps0,c,p,A0,Int

            H = tp
            RETURN
      END
```

A10 - Two color K-D effect (linear polarization)

The probability amplitude of the regular two color K-D effect is computed for a range of laser pulse lengths. The built in double integral routine DTWODQ is used.

```
program prog
use msimsl
implicit none

integer N
parameter (N = 2500)

real*8 w,w0,tau,Wint,Pi,m,v,lambda,hbar,k,q,eps0,c,p,A0,Int

common w,w0,tau,Wint,Pi,m,v,lambda,hbar,k,q,eps0,c,p,A0,Int



INTEGER    IRULE, NOUT,i,Ntau
REAL*8     A, B, ERRABS, ERRESTr,ERRESTi, ERRREL
REAL*8     Freal,Fimaginary, G, H, RESULTi,RESULTr
EXTERNAL   Freal,Fimaginary, G, H !, DTWODQ, UMACH

CALL UMACH (2, NOUT)

open(unit=30,file="Itot.dat")
open(unit=31,file="error.dat")

Pi = 2d0*dacos(0d0)

m = 9.1094d-31
v = 1d7
lambda = 1064d-9
hbar = 1.0546d-34
k = 2d0*Pi/lambda
q = 1.6d-19
eps0 = 8.8542d-12
c = 3d8
p = m*v
Int   = 1d15

w0 = k*c  !1.0d15 !tau = 6.28d-15
w = hbar*k**2d0/(2d0*m)


!factor in front of integral
A0 = q**3d0*p/(16*m**2d0*hbar**2d0)*           &
    (2d0*Int/(c*eps0*w0**2d0))**(3d0/2d0)

!tau = 1d-15 !2d0*6.28d-15
```

```
      Wint = (2d0*Pi/w0)*100d0      !2*Wint = width of integration


!                                   Set limits of integration
      A = -Wint
      B = Wint
!                                   Set error tolerances
      ERRABS = 1d-9
      ERRREL = 0
                  !Parameter for oscillatory function
      IRULE = 6

      Ntau = 1000    !number of tau data points

      do    i = 1,Ntau

            tau = 5*(2d0*Pi/w0)*(dfloat(i)/dfloat(Ntau))

            CALL DTWODQ (Freal, A, B, G, H, ERRABS, ERRREL, IRULE,   &
                         RESULTr, ERRESTr)

            CALL DTWODQ (Fimaginary, A, B, G, H, ERRABS, ERRREL,     &
                         IRULE, RESULTi, ERRESTi)

            write(30,999) tau,resultr,resulti
            write(31,999) tau,ERRESTr,ERRESTi !estimate of absolute
value of error

            write(6,*) i
      enddo

      close(30)
      close(31)

999   format(E12.6,x,E12.6,x,E12.6)

      END


      REAL*8 FUNCTION Freal (tp, tpp)            !real part of
integrand
            REAL*8 tp, tpp
            real*8 w,w0,tau,Wint,Pi,m,v,lambda,hbar,k,q,eps0,c,p,A0,Int
            common w,w0,tau,Wint,Pi,m,v,lambda,hbar,k,q,eps0,c,p,A0,Int

            Freal = A0*(dcos((2d0*w0 + 4d0*w)*tp +                    &
                    (-2d0*w0 - 4d0*w)*tpp)*                           &
                    dexp(-(2d0*tp**2d0 + tpp**2d0)/tau**2d0) +        &
                    dcos((-2d0*w0 + 4d0*w)*tp + (2d0*w0 - 4d0*w)*tpp)*&
                    dexp(-(tp**2d0 + 2d0*tpp**2d0)/tau**2d0) +        &
                    2d0*dcos((-w0 + 3d0*w)*tp + (w0 - 3d0*w)*tpp)*    &
                    dexp(-(2d0*tp**2d0 + tpp**2d0)/tau**2d0) +        &
                    2d0*dcos((w0 + 3d0*w)*tp + (-w0 - 3d0*w)*tpp)*    &
                    dexp(-(tp**2d0 + 2d0*tpp**2d0)/tau**2d0))
            RETURN
      end
```

```
  REAL*8 FUNCTION Fimaginary (tp,tpp)       !imaginary part
        REAL*8 tp, tpp
        real*8 w,w0,tau,Wint,Pi,m,v,lambda,hbar,k,q,eps0,c,p,A0,Int
        common w,w0,tau,Wint,Pi,m,v,lambda,hbar,k,q,eps0,c,p,A0,Int



   Fimaginary = A0*(dsin((2d0*w0 + 4d0*w)*tp +
              (-2d0*w0 -4d0*w)*tpp)*                                  &
              dexp(-(2d0*tp**2d0 + tpp**2d0)/tau**2d0) +              &
              dsin((-2d0*w0 + 4d0*w)*tp + (2d0*w0 - 4d0*w)*tpp)*      &
              dexp(-(tp**2d0 + 2d0*tpp**2d0)/tau**2d0) +              &
              2d0*dsin((-w0 + 3d0*w)*tp + (w0 - 3d0*w)*tpp)*          &
              dexp(-(2d0*tp**2d0 + tpp**2d0)/tau**2d0) +              &
              2d0*dsin((w0 + 3d0*w)*tp + (-w0 - 3d0*w)*tpp)*          &
              dexp(-(tp**2d0 + 2d0*tpp**2d0)/tau**2d0))

        RETURN
end

  REAL*8 FUNCTION G (tp)        !lower bound of inner integral
        REAL*8 tp
        real*8 w,w0,tau,Wint,Pi,m,v,lambda,hbar,k,q,eps0,c,p,A0,Int
        common w,w0,tau,Wint,Pi,m,v,lambda,hbar,k,q,eps0,c,p,A0,Int

        G = -Wint
        RETURN
end


  REAL*8 FUNCTION H (tp)        !upper bound of inner integral
        REAL*8 tp
        real*8 w,w0,tau,Wint,Pi,m,v,lambda,hbar,k,q,eps0,c,p,A0,Int
        common w,w0,tau,Wint,Pi,m,v,lambda,hbar,k,q,eps0,c,p,A0,Int

        H = tp
        RETURN
END
```

Appendix B - Derivations

B1 - Equations of motion of Feynman paradox from Darwin Lagrangian (Chapter 3 Section 2.2.1)

In order to determine the equations of motion for two interacting charged particles, I used the Darwin Lagrangian

$$L=\frac{1}{2}m_1v_1^2+\frac{1}{2}m_2v_2^2-\frac{q_1q_2}{r}+\frac{q_1q_2}{2rc^2}\left[\vec{v}_1\cdot\vec{v}_2+\frac{(\vec{v}_1\cdot\vec{r})(\vec{v}_2\cdot\vec{r})}{r^2}\right]$$

Where v_1 and v_2 are the velocities of the two particles, m_1 and m_2 are the charges, and q_1 and q_2 are the masses. The position of the particles is give by

$$\vec{r}=\vec{r}_1-\vec{r}_2,\ r=\left|\vec{r}_1-\vec{r}_2\right|$$

In order to obtain the equations of motion I first took the derivatives $\frac{d}{dt}\frac{\partial L}{\partial\vec{v}_1}$, $\frac{d}{dt}\frac{\partial L}{\partial\vec{v}_2}$, $\frac{\partial L}{\partial\vec{r}_1}$, and $\frac{\partial L}{\partial\vec{r}_2}$

$$\vec{P}_1=\frac{\partial L}{\partial\vec{v}_1}=m_1\vec{v}_1+\frac{q_1q_2}{2rc^2}\left[\vec{v}_2+\frac{(\vec{v}_2\cdot\vec{r})\vec{r}}{r^2}\right]$$

$$\vec{P}_2=\frac{\partial L}{\partial\vec{v}_2}=m_2\vec{v}_2+\frac{q_1q_2}{2rc^2}\left[\vec{v}_1+\frac{(\vec{v}_1\cdot\vec{r})\vec{r}}{r^2}\right]$$

$$\frac{d}{dt}\frac{\partial L}{\partial\vec{v}_1}=m_1\vec{a}_1-\frac{q_1q_2\left(\vec{r}\cdot\dot{\vec{r}}\right)}{2c^2r^3}\left[\vec{v}_2+\frac{(\vec{v}_2\cdot\vec{r})\vec{r}}{r^2}\right]$$
$$+\frac{q_1q_2}{2c^2r}\left\{\vec{a}_2-\frac{2(\vec{v}_2\cdot\vec{r})(\vec{r}\cdot\dot{\vec{r}})\vec{r}}{r^4}+\frac{\left[(\vec{a}_2\cdot\vec{r})+(\vec{v}_2\cdot\dot{\vec{r}})\right]\vec{r}+(\vec{v}_2\cdot\vec{r})\dot{\vec{r}}}{r^2}\right\}$$
$$=m_1\vec{a}_1+\frac{q_1q_2}{2c^2r}\left\{\vec{a}_2-\frac{(\vec{r}\cdot\dot{\vec{r}})\vec{v}_2}{r^2}-\frac{3(\vec{v}_2\cdot\vec{r})(\vec{r}\cdot\dot{\vec{r}})\vec{r}}{r^4}+\frac{\left[(\vec{a}_2\cdot\vec{r})+(\vec{v}_2\cdot\dot{\vec{r}})\right]\vec{r}+(\vec{v}_2\cdot\vec{r})\dot{\vec{r}}}{r^2}\right\}$$

$$\frac{d}{dt}\frac{\partial L}{\partial \vec{v}_2} = m_2\vec{a}_2 + \frac{q_1q_2}{2c^2r}\left\{\vec{a}_1 - \frac{(\vec{r}\cdot\dot{\vec{r}})\vec{v}_1}{r^2} - \frac{3(\vec{v}_1\cdot\vec{r})(\vec{r}\cdot\dot{\vec{r}})\vec{r}}{r^4} + \frac{\left[(\vec{a}_1\cdot\vec{r}) + (\vec{v}_1\cdot\dot{\vec{r}})\right]\vec{r} + (\vec{v}_1\cdot\vec{r})\dot{\vec{r}}}{r^2}\right\}$$

$$\frac{\partial L}{\partial \vec{r}_1} = \frac{q_1q_2}{r^3}\vec{r} + \frac{q_1q_2}{2c^2}\left[\frac{-(\vec{v}_1\cdot\vec{v}_2)\vec{r}}{r^3} - \frac{3(\vec{v}_1\cdot\vec{r})(\vec{v}_2\cdot\vec{r})\vec{r}}{r^5} + \frac{(\vec{v}_1\cdot\vec{r})\vec{v}_2 + (\vec{v}_2\cdot\vec{r})\vec{v}_1}{r^3}\right]$$

$$\frac{\partial L}{\partial \vec{r}_2} = -\frac{q_1q_2}{r^3}\vec{r} - \frac{q_1q_2}{2c^2}\left[\frac{-(\vec{v}_1\cdot\vec{v}_2)\vec{r}}{r^3} - \frac{3(\vec{v}_1\cdot\vec{r})(\vec{v}_2\cdot\vec{r})\vec{r}}{r^5} + \frac{(\vec{v}_1\cdot\vec{r})\vec{v}_2 + (\vec{v}_2\cdot\vec{r})\vec{v}_1}{r^3}\right]$$

Plugging these into the Lagrange equations of motion,

$$\frac{d}{dt}\frac{\partial L}{\partial \vec{v}_1} - \frac{\partial L}{\partial \vec{r}_1} = 0$$

$$\frac{d}{dt}\frac{\partial L}{\partial \vec{v}_2} - \frac{\partial L}{\partial \vec{r}_2} = 0$$

I get the following equations:

$$m_1\vec{a}_1 + \frac{q_1q_2}{2c^2r}\left\{\vec{a}_2 - \frac{(\vec{r}\cdot\dot{\vec{r}})\vec{v}_2}{r^2} - \frac{3(\vec{v}_2\cdot\vec{r})(\vec{r}\cdot\dot{\vec{r}})\vec{r}}{r^4} + \frac{\left[(\vec{a}_2\cdot\vec{r}) + (\vec{v}_2\cdot\dot{\vec{r}})\right]\vec{r} + (\vec{v}_2\cdot\vec{r})\dot{\vec{r}}}{r^2}\right\}$$

$$-\frac{q_1q_2}{r^3}\vec{r} - \frac{q_1q_2}{2c^2}\left[\frac{-(\vec{v}_1\cdot\vec{v}_2)\vec{r}}{r^3} - \frac{3(\vec{v}_1\cdot\vec{r})(\vec{v}_2\cdot\vec{r})\vec{r}}{r^5} + \frac{(\vec{v}_1\cdot\vec{r})\vec{v}_2 + (\vec{v}_2\cdot\vec{r})\vec{v}_1}{r^3}\right] = 0$$

$$m_2\vec{a}_2 + \frac{q_1q_2}{2c^2r}\left\{\vec{a}_1 - \frac{(\vec{r}\cdot\dot{\vec{r}})\vec{v}_1}{r^2} - \frac{3(\vec{v}_1\cdot\vec{r})(\vec{r}\cdot\dot{\vec{r}})\vec{r}}{r^4} + \frac{\left[(\vec{a}_1\cdot\vec{r}) + (\vec{v}_1\cdot\dot{\vec{r}})\right]\vec{r} + (\vec{v}_1\cdot\vec{r})\dot{\vec{r}}}{r^2}\right\}$$

$$+\frac{q_1q_2}{r^3}\vec{r} + \frac{q_1q_2}{2c^2}\left[\frac{-(\vec{v}_1\cdot\vec{v}_2)\vec{r}}{r^3} - \frac{3(\vec{v}_1\cdot\vec{r})(\vec{v}_2\cdot\vec{r})\vec{r}}{r^5} + \frac{(\vec{v}_1\cdot\vec{r})\vec{v}_2 + (\vec{v}_2\cdot\vec{r})\vec{v}_1}{r^3}\right] = 0$$

In order to simplify the problem I apply the conditions of the Feynman paradox

$\vec{r}_1 = \vec{0}$, $\vec{r}_2 = r\hat{x}$

$\vec{v}_1 = v\hat{x}$, $\vec{v}_2 = v\hat{y}$

$q_1 = q_2$, $m_1 = m_2$

$\vec{r} = -r\hat{x}$, $\dot{\vec{r}} = v(\hat{x} - \hat{y})$, $\hat{r} = -\hat{x}$

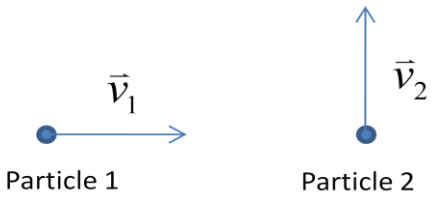

Where $\vec{r}_1$, $\vec{v}_1$, q_1, and m_1 correspond to particle 1 and $\vec{r}_2$, $\vec{v}_2$, q_2, and m_2 correspond to particle 2. By applying these conditions the equations of motion simplify to

$$m\vec{a}_1 + \frac{q^2}{2c^2 r}\left[\vec{a}_2 + \frac{v^2}{r}\hat{y} + \left(\frac{a_{2x}r + v^2}{r}\right)\hat{x}\right] + \frac{q^2}{r^2}\hat{x} - \frac{q^2}{2c^2}\left(-\frac{v^2}{r^2}\hat{y}\right) = 0$$

$$m\vec{a}_2 + \frac{q^2}{2c^2 r}\left[\vec{a}_1 + \frac{v^2}{r}\hat{x} + \frac{3v^2}{r}\hat{x} - \left(\frac{-a_{1x}r + v^2}{r}\right)\hat{x} - \frac{v^2}{r}(\hat{x} - \hat{y})\right] - \frac{q^2}{r^2}\hat{x} - \frac{q^2}{2c^2}\left(\frac{v^2}{r^2}\hat{y}\right) = 0$$

which can be further simplified to

$$m\vec{a}_1 + \frac{q^2}{2c^2 r}\vec{a}_2 + \frac{q^2}{r^2}\hat{x} + \frac{q^2}{2c^2 r}\left[\left(a_{2x} + \frac{v^2}{r}\right)\hat{x} + \frac{2v^2}{r}\hat{y}\right] = 0$$

$$m\vec{a}_2 + \frac{q^2}{2c^2 r}\vec{a}_1 - \frac{q^2}{r^2}\hat{x} + \frac{q^2}{2c^2 r}\left(a_{1x} + \frac{2v^2}{r}\right)\hat{x} = 0$$

Breaking these equations up into components gives the following set of equations

$$ma_{1x} + \frac{q^2}{c^2 r}a_{2x} + \frac{q^2}{r^2}\left(1 + \frac{v^2}{2c^2}\right) = 0$$

$$ma_{1y} + \frac{q^2}{2c^2 r}a_{2y} + \frac{q^2 v^2}{c^2 r^2} = 0$$

$$ma_{2x} + \frac{q^2}{c^2 r}a_{1x} - \frac{q^2}{r^2}\left(1 - \frac{v^2}{c^2}\right) = 0$$

$$ma_{2y} + \frac{q^2}{2c^2 r}a_{1y} = 0$$

the solution to which is

$$a_{1x} = \frac{-\frac{q^2}{mr^2}\left[\left(1+\frac{v^2}{2c^2}\right)+\frac{q^2}{mc^2 r}\left(1-\frac{v^2}{c^2}\right)\right]}{1-\frac{1}{m^2}\left(\frac{q^2}{c^2 r}\right)^2}$$

$$a_{1y} = \frac{-\frac{q^2 v^2}{mc^2 r^2}}{1-\frac{1}{4m^2}\left(\frac{q^2}{c^2 r}\right)^2}$$

$$a_{1x} = \frac{\frac{q^2}{mr^2}\left[\left(1-\frac{v^2}{c^2}\right)+\frac{q^2}{mc^2 r}\left(1+\frac{v^2}{2c^2}\right)\right]}{1-\frac{1}{m^2}\left(\frac{q^2}{c^2 r}\right)^2}$$

$$a_{2y} = \frac{\frac{v^2}{2m^2 r}\left(\frac{q^2}{c^2 r}\right)^2}{1-\frac{1}{4m^2}\left(\frac{q^2}{c^2 r}\right)^2}$$

Since $q^2/mc^2 r \ll v^2/c^2$ (i.e. $q^2/r < mv^2/2$) these can be reduced to the following expressions:

$$a_{1x} \approx -\frac{q^2}{mr^2}\left(1+\frac{v^2}{2c^2}\right) \qquad a_{1y} \approx -\frac{q^2 v^2}{mc^2 r^2}$$

$$a_{2x} \approx \frac{q^2}{mr^2}\left(1-\frac{v^2}{c^2}\right) \qquad a_{2y} \approx 0$$

B2 - Forces on a charged particle and a current loop (Chapter 3 Section 2.2.2)

In order to determine the forces in a system consisting of a point charge and a current loop I start with the following conditions

$$\vec{v}_q = -v_q\hat{x} \qquad \hat{r} = \cos\varphi\hat{x} + \sin\varphi\hat{y} \qquad \hat{x}\times\hat{r} = \sin\varphi\hat{z}$$

where the coordinates and system parameters are shown in figure 2.5. The magnetic dipole moment of the loop may be written in terms of the current and radius ($\mu c = \pi I \varepsilon^2$ in Gaussian units). Thus the force on the loop was determined by integration of the Lorentz force.

$$\vec{F}_\mu = \frac{1}{c}\int \vec{J}\times\vec{B}_q d\tau = \frac{1}{c}\int I\hat{\varphi}\times\vec{B}_q \varepsilon d\varphi = \frac{\mu}{\pi\varepsilon}\int \hat{\varphi}\times\vec{B}_q d\varphi$$

$$\vec{B} = \frac{q}{c}\vec{v}_q\times\frac{\vec{R}}{R^3} = \frac{q}{c}\vec{v}_q\times\frac{\left(\varepsilon\hat{r}-\vec{R}_q\right)}{\left|\varepsilon\hat{r}-\vec{R}_q\right|^3} = -\frac{qv_q}{c}\frac{\left(\varepsilon\sin\varphi\hat{z}+z_q\hat{y}-y_q\hat{z}\right)}{\left|\varepsilon\hat{r}-\vec{R}_q\right|^3}$$

where $\vec{F}_\mu$ and $\vec{B}_q$ are the force on the loop and the magnetic field due to the point charge, respectively. This expression for the magnetic field of the point charge can be simplified by taking a series expansion of Legendre polynomials $\left(\cos\gamma = \frac{\hat{r}\cdot\vec{R}_q}{R_q}\right)$.

$$\frac{1}{\left|\varepsilon\hat{r}-\vec{R}_q\right|^3} = \left(\sum_{l=0}^{\infty}\frac{\varepsilon^l}{R_q^{l+1}}P_l\left(\cos\gamma\right)\right)^3 \approx \frac{1}{R_q^3}\left(P_0\left(\cos\gamma\right)+\frac{\varepsilon}{R_p}P_1\left(\cos\gamma\right)\right)^3$$

$$= \frac{1}{R_q^3}\left(1+\frac{\varepsilon\cos\gamma}{R_q}\right)^3 = \frac{1}{R_q^3}\left(1+\frac{\varepsilon\hat{r}\cdot\vec{R}_q}{R_q^2}\right)^3 \approx \frac{1}{R_q^3}\left(1+\frac{3\varepsilon\hat{r}\cdot\vec{R}_q}{R_q^2}\right)$$

$$= \frac{1}{R_q^3}\left(1+\frac{3\varepsilon\left(x_q\cos\varphi + y_q\sin\varphi\right)}{R_q^2}\right)$$

Making the appropriate substitution the magnetic field due to the moving point charge can be broken up into two terms.

$$\vec{B}_q = -\frac{qv_q}{cR_q^3}\left(\varepsilon\sin\varphi\hat{z} + z_q\hat{y} - y_q\hat{z}\right)\left(1+\frac{3\varepsilon\left(x_q\cos\varphi + y_q\sin\varphi\right)}{R_q^2}\right) = \vec{B}_{qI} + \vec{B}_{qII}$$

$$\vec{B}_{qI} = -\frac{qv_q}{cR_q^3}\left(\varepsilon\sin\varphi\hat{z} + z_q\hat{y} - y_q\hat{z}\right),$$

$$\vec{B}_{qII} = -\frac{qv_q}{cR_q^3}\left(\varepsilon\sin\varphi\hat{z} + z_q\hat{y} - y_q\hat{z}\right)\frac{3\varepsilon\left(x_q\cos\varphi + y_q\sin\varphi\right)}{R_q^2}$$

Substituting these into the Lorentz force expression gives

$$\hat{\varphi}\times\left[\left(\varepsilon\sin\varphi - y_q\right)\hat{z} + z_q\hat{y}\right] = \cos\varphi\left(\varepsilon\sin\varphi - y_q\right)\hat{x} + \sin\varphi\left(\varepsilon\sin\varphi - y_q\right)\hat{y} - z_q\sin\varphi\hat{z}$$

$$\vec{F}_{\mu I} = \frac{\mu}{\pi\varepsilon}\left(-\frac{qv_q}{cR_q^3}\right)\int_0^{2\pi}\left[\cos\varphi\left(\varepsilon\sin\varphi - y_q\right)\hat{x} + \sin\varphi\left(\varepsilon\sin\varphi - y_q\right)\hat{y} - z_q\sin\varphi\hat{z}\right]d\varphi = -\frac{\mu qv_q}{cR_q^3}\hat{y}$$

$$\vec{F}_{\mu II} = \frac{\mu}{\pi\varepsilon}\left(-\frac{3\varepsilon qv_q}{cR_q^5}\right)\int_0^{2\pi}\left(x_q\cos\varphi + y_q\sin\varphi\right)\left[\cos\varphi\left(\varepsilon\sin\varphi - y_q\right)\hat{x}\right]d\varphi$$
$$+\frac{\mu}{\pi\varepsilon}\left(-\frac{3\varepsilon qv_q}{cR_q^5}\right)\int_0^{2\pi}\left(x_q\cos\varphi + y_q\sin\varphi\right)\left[\sin\varphi\left(\varepsilon\sin\varphi - y_q\right)\hat{y} - z_q\sin\varphi\hat{z}\right]d\varphi$$

$$= \frac{3\mu qv_q}{cR_q^5}\left[x_qy_q\hat{x} + y_q^2\hat{y} + y_qz_q\hat{z}\right]$$

$$\vec{F}_\mu = \vec{F}_{\mu I} + \vec{F}_{\mu II} = \frac{\mu qv_q}{cR_q^3}\left[\frac{3\left(x_qy_q\hat{x} + y_q^2\hat{y} + y_qz_q\hat{z}\right)}{R_q^2} - \hat{y}\right]$$

The force acting on the point charge due to the current loop is determined by applying the Lorentz force law as follows

$$\vec{F}_q = \frac{q}{c}\vec{v}_q \times \vec{B}_\mu$$

$$\vec{B}_\mu = \frac{3\vec{R}_q\left(\vec{R}_q \cdot \vec{\mu}\right)}{R_q^5} - \frac{\vec{\mu}}{R_q^3}, \quad \vec{\mu} = \mu\hat{z}$$

where $\vec{F}_q$ and $\vec{B}_\mu$ are the force on the point charge and the magnetic field due to the current loop, respectively. Evaluating the cross product gives

$$\vec{F}_q = \frac{\mu q v_q}{cR_q^3}\left[\frac{3\left(-\hat{x}\times\vec{R}_q\right)z_q}{R_q^2} + \hat{x}\times\hat{z}\right]$$

$$-\hat{x}\times\vec{R}_q = z_q\hat{y} - y_q\hat{z}$$

$$\vec{F}_q = \frac{\mu q v_q}{cR_q^3}\left[\frac{3\left(z_q^2\hat{y} - y_q z_q\hat{z}\right)}{R_q^2} - \hat{y}\right].$$

B3 - Unconstrained Aharonov-Bohm and Aharonov-Casher forces (chapter 3 section 2.2.3)

For the forces acting in the Aharonov-Bohm and Aharonov-Casher Systems in the case of unconstrained motion it is necessary to integrate the force expressions shown in appendix B2. Starting with the Aharonov-Bohm system the magnetic moment of the current loop is taken to be an element for integration to construct an infinitely long solenoid. The magnetic dipole moment associated with a current loop is $\vec{\mu} = IA\hat{z}$ where I is the current and A is the area enclosed. This can be taken as an element on an infinitely long solenoid where the current is $I = Kdz$ and K is the surface current density. The magnetic moment then may be written $\vec{\mu} = KA\hat{z}dz$. The strength of the magnetic field in a solenoid is $B_S = \frac{4\pi}{c}K$ so the magnetic flux enclosed in the solenoid is $\Phi_B = B_S A = \frac{4\pi}{c}KA$. Therefore $KA = \frac{c\Phi_B}{4\pi}$ and the magnetic moment of a current loop can be rewritten for integration into an infinitely long solenoid as follows

$$\vec{\mu} \to \frac{c\Phi_B}{4\pi}\hat{z}dz_\mu.$$

The following integrals must then be taken for the force on the point charge and the force on the solenoid

$$\vec{F}_q = \int_{solenoid} d\vec{F}_q, \quad \vec{F}_s = \int_{solenoid} d\vec{F}_\mu.$$

The integral for the force on the charge may be written

$$\vec{F}_q = \frac{q\Phi_B v_q}{4\pi}\int\left[\frac{3\left(\left(z_q - z_\mu\right)^2 \hat{y} - \left(y_q - y_\mu\right)\left(z_q - z_\mu\right)\hat{z}\right)}{\left[\left(x_q - x_\mu\right)^2 + \left(y_q - y_\mu\right)^2 + \left(z_q - z_\mu\right)^2\right]^{\frac{5}{2}}}\right]dz_\mu$$

$$+\frac{q\Phi_B v_q}{4\pi}\int\left[\frac{-\hat{y}}{\left[\left(x_q - x_\mu\right)^2 + \left(y_q - y_\mu\right)^2 + \left(z_q - z_\mu\right)^2\right]^{\frac{3}{2}}}\right]dz_\mu$$

$$= A\left\{-3\hat{y}\int\frac{Z^2}{\left[\gamma^2 + Z^2\right]^{\frac{5}{2}}}dZ + 3Y\hat{z}\int\frac{Z}{\left[\gamma^2 + Z^2\right]^{\frac{5}{2}}}dZ + \hat{y}\int\frac{1}{\left[\gamma^2 + Z^2\right]^{\frac{3}{2}}}dZ\right\}$$

$$Y = y_q - y_\mu,\ Z = z_q - z_\mu,\ \gamma^2 = \left(x_q - x_\mu\right)^2 + \left(y_q - y_\mu\right)^2,\ A = \frac{q\Phi_B v_q}{4\pi}$$

Evaluating these integrals from $z_\mu = -\infty$ to $z_\mu = \infty$ (i.e. from $Z = \infty$ to $Z = -\infty$) gives

$$\int_{\infty}^{-\infty}\frac{Z^2}{\left[\gamma^2 + Z^2\right]^{\frac{5}{2}}}dZ = -\frac{2}{3\gamma^2},\ \int_{\infty}^{-\infty}\frac{Z}{\left[\gamma^2 + Z^2\right]^{\frac{5}{2}}}dZ = 0,\ \int_{\infty}^{-\infty}\frac{1}{\left[\gamma^2 + Z^2\right]^{\frac{3}{2}}}dZ = -\frac{2}{\gamma^2}$$

Thus the overall integral is zero and $\vec{F}_q = 0.$ The integral for the force on the solenoid is

$$\vec{F}_s = \frac{q\Phi_B v_q}{4\pi}\int\frac{3\left(\left(x_q - x_\mu\right)\left(y_q - y_\mu\right)\hat{x} + \left(y_q - y_\mu\right)^2\hat{y} + \left(y_q - y_\mu\right)\left(z_q - z_\mu\right)\hat{z}\right)}{\left[\left(x_q - x_\mu\right)^2 + \left(y_q - y_\mu\right)^2 + \left(z_q - z_\mu\right)^2\right]^{\frac{5}{2}}}dz_\mu$$

$$-\frac{q\Phi_B v_q}{4\pi}\int\frac{\hat{y}}{\left[\left(x_q - x_\mu\right)^2 + \left(y_q - y_\mu\right)^2 + \left(z_q - z_\mu\right)^2\right]^{\frac{3}{2}}}dz_\mu$$

$$= A\left\{-3\left(XY\hat{x} + Y^2\hat{y}\right)\int\frac{1}{\left[\gamma^2 + Z^2\right]^{\frac{5}{2}}}dZ - 3Y\hat{z}\int\frac{Z}{\left[\gamma^2 + Z^2\right]^{\frac{5}{2}}}dZ + \hat{y}\int\frac{1}{\left[\gamma^2 + Z^2\right]^{\frac{3}{2}}}dZ\right\}$$

$$X = x_q - x_\mu,\ Y = y_q - y_\mu,\ Z = z_q - z_\mu,\ \gamma^2 = \left(x_q - x_\mu\right)^2 + \left(y_q - y_\mu\right)^2,\ A = \frac{q\Phi_B v_q}{4\pi}$$

Evaluating these integrals from $z_\mu = -\infty$ to $z_\mu = \infty$ gives

$$\int_{\infty}^{-\infty} \frac{1}{\left[\gamma^2 + Z^2\right]^{\frac{5}{2}}} dZ = -\frac{4}{3\gamma^4}$$

$$\vec{F}_s = A\left\{4\left(XY\hat{x} + Y^2\hat{y}\right)\frac{1}{\gamma^4} - 2\hat{y}\frac{1}{\gamma^2}\right\}$$

$$= A\left\{\frac{4XY\hat{x} + \left[4Y^2 - 2\left(X^2 + Y^2\right)\right]}{\left(X^2 + Y^2\right)^2}\right\} = A\left\{\frac{4XY\hat{x} - 2\left[X^2 + Y^2\right]}{\left(X^2 + Y^2\right)^2}\right\}$$

$$= \frac{q\Phi_B v_q}{2\pi}\left\{\frac{2\left(x_q - x_s\right)\left(y_q - y_s\right)\hat{x} - \left[\left(x_q - x_s\right)^2 - \left(y_q - y_s\right)^2\right]\hat{y}}{\left[\left(x_q - x_s\right)^2 + \left(y_q - y_s\right)^2\right]^2}\right\}.$$

A very similar derivation is given for the forces in the Aharonov-Casher effect. The point charge is taken to be an element for integration to construct an infinitely long wire.

$$q \to \lambda dz_q$$

The following integrals must be taken for the force on the wire and the magnetic moment

$$\vec{F}_w = \int_{wire} d\vec{F}_q, \quad \vec{F}_\mu = \int_{wire} d\vec{F}_\mu.$$

The Integral for the force on the wire may be written

$$\vec{F}_w = \frac{\lambda\mu v_q}{c}\int\left[\frac{3\left(\left(z_q - z_\mu\right)^2\hat{y} - \left(y_q - y_\mu\right)\left(z_q - z_\mu\right)\hat{z}\right)}{\left[\left(x_q - x_\mu\right)^2 + \left(y_q - y_\mu\right)^2 + \left(z_q - z_\mu\right)^2\right]^{\frac{5}{2}}}\right]dz_q$$

$$+\frac{\lambda\mu v_q}{c}\int\left[\frac{-\hat{y}}{\left[\left(x_q - x_\mu\right)^2 + \left(y_q - y_\mu\right)^2 + \left(z_q - z_\mu\right)^2\right]^{\frac{3}{2}}}\right]dz_q$$

$$= B\left\{3\hat{y}\int \frac{Z^2}{\left[\gamma^2 + Z^2\right]^{\frac{5}{2}}} dZ - 3Y\hat{z}\int \frac{Z}{\left[\gamma^2 + Z^2\right]^{\frac{5}{2}}} dZ - \hat{y}\int \frac{1}{\left[\gamma^2 + Z^2\right]^{\frac{3}{2}}} dZ\right\}$$

$$Y = y_q - y_\mu,\ Z = z_q - z_\mu,\ \gamma^2 = \left(x_q - x_\mu\right)^2 + \left(y_q - y_\mu\right)^2,\ B = \frac{\lambda\mu v_q}{c}$$

Evaluating these integrals from $z_q = -\infty$ to $z_q = \infty$ (i.e. from $Z = -\infty$ to $Z = \infty$) gives

$\vec{F}_w = 0.$ The integral for the force on the magnetic dipole moment is

$$\vec{F}_\mu = \frac{\lambda\mu v_q}{c}\int \frac{3\left(\left(x_q - x_\mu\right)\left(y_q - y_\mu\right)\hat{x} + \left(y_q - y_\mu\right)^2\hat{y} + \left(y_q - y_\mu\right)\left(z_q - z_\mu\right)\hat{z}\right)}{\left[\left(x_q - x_\mu\right)^2 + \left(y_q - y_\mu\right)^2 + \left(z_q - z_\mu\right)^2\right]^{\frac{5}{2}}} dz_q$$

$$-\frac{\lambda\mu v_q}{c}\int \frac{\hat{y}}{\left[\left(x_q - x_\mu\right)^2 + \left(y_q - y_\mu\right)^2 + \left(z_q - z_\mu\right)^2\right]^{\frac{3}{2}}} dz_q$$

$$= B\left\{3\left(XY\hat{x} + Y^2\hat{y}\right)\int \frac{1}{\left[\gamma^2 + Z^2\right]^{\frac{5}{2}}} dZ + 3Y\hat{z}\int \frac{Z}{\left[\gamma^2 + Z^2\right]^{\frac{5}{2}}} dZ - \hat{y}\int \frac{1}{\left[\gamma^2 + Z^2\right]^{\frac{3}{2}}} dZ\right\}$$

$$X = x_q - x_\mu,\ Y = y_q - y_\mu,\ Z = z_q - z_\mu,\ \gamma^2 = \left(x_q - x_\mu\right)^2 + \left(y_q - y_\mu\right)^2,\ B = \frac{\lambda\mu v_q}{c}$$

Evaluating these integrals from $z_q = -\infty$ to $z_q = \infty$ gives

$$\vec{F}_s = B\left\{4\left(XY\hat{x} + Y^2\hat{y}\right)\frac{1}{\gamma^4} - 2\hat{y}\frac{1}{\gamma^2}\right\}$$

$$= B\left\{\frac{4XY\hat{x} + \left[4Y^2 - 2\left(X^2 + Y^2\right)\right]}{\left(X^2 + Y^2\right)^2}\right\} = B\left\{\frac{4XY\hat{x} - 2\left[X^2 + Y^2\right]}{\left(X^2 + Y^2\right)^2}\right\}$$

$$= \frac{2\lambda\mu v_q}{c}\left\{\frac{2\left(x_q - x_s\right)\left(y_q - y_s\right)\hat{x} - \left[\left(x_q - x_s\right)^2 - \left(y_q - y_s\right)^2\right]\hat{y}}{\left[\left(x_q - x_s\right)^2 + \left(y_q - y_s\right)^2\right]^2}\right\}.$$

B4 - Integration of Darwin vector potential for current loop (chapter 3 section 2.3.1)

To determine the magnetic vector potential of a current loop from the Darwin vector potential of a point charge we a system like that shown in figure 2.5 is used in which a rotating ring of charge of radius ε and charge density λ represents a current loop centered at the origin. The charge element is given by

$dq = \lambda \varepsilon d\varphi = \frac{q}{2\pi\varepsilon}\varepsilon d\varphi = \frac{q}{2\pi} d\varphi.$ The vector potential to be integrated (i.e. that of a point charge) is

$$d\vec{A} = \frac{q}{4\pi c R}\left(\vec{v}_I + \frac{\left(\vec{v}_I \cdot \vec{R}\right)\vec{R}}{R^2}\right) d\varphi$$

$$\vec{v} = -v\hat{r}\times\hat{z},\ \ \vec{v}_I = \vec{v}_\mu + \vec{v} = \vec{v}_\mu - v\hat{r}\times\hat{z},\ \ \vec{R} = \vec{R}_P - \varepsilon\hat{r}$$

$$\vec{v}_I \cdot \vec{R} = \left(\vec{v}_\mu - v\hat{r}\times\hat{z}\right)\cdot\left(\vec{R}_P - \varepsilon\hat{r}\right) = \vec{v}_\mu \cdot \vec{R}_P - \varepsilon\hat{r}\cdot\vec{v}_\mu - v\left(\hat{r}\times\hat{z}\right)\cdot\vec{R}_P$$

$$\hat{r} = \cos\varphi\hat{x} + \sin\varphi\hat{y}$$

Where $\vec{v}_I$ is the velocity of the charge element on the current loop relative to the origin, $\vec{v}$ is the velocity of the charge element on the current loop relative to the center of the loop (i.e. the velocity which determines the current in the loop), $\vec{v}_\mu$ is the velocity of the center of the loop, $\vec{R}$ is the position of a field point where the vector potential is calculated relative to a charge element on the loop, $\varepsilon\hat{r}$ is the position of the charge element on the current loop relative to the center of the loop, and $\vec{R}_p$ is the position of the field point relative to the center of the loop. Substituting this into $d\vec{A}$ gives

$$d\vec{A} = \frac{q}{4\pi cR}\left(\vec{v}_\mu - v\hat{r}\times\hat{z} + \frac{\left(\vec{v}_\mu\cdot\vec{R}_P - \varepsilon\hat{r}\cdot\vec{v}_\mu - v\left(\hat{r}\times\hat{z}\right)\cdot\vec{R}_P\right)\left(\vec{R}_P - \varepsilon\hat{r}\right)}{\left|\vec{R}_P - \varepsilon\hat{r}\right|^2}\right)d\varphi$$

$$= \frac{q}{4\pi cR}\left(\vec{v}_\mu + \frac{\left(\vec{v}_\mu\cdot\vec{R}_P\right)\vec{R}_P}{\left|\vec{R}_P - \varepsilon\hat{r}\right|^2}\right)d\varphi$$

$$+\frac{q}{4\pi c}\left(-\frac{v\hat{r}\times\hat{z}}{\left|\vec{R}_P - \varepsilon\hat{r}\right|}\right)d\varphi$$

$$+\frac{q}{4\pi c}\left(\frac{\left(-\varepsilon\left(\vec{v}_\mu\cdot\vec{R}_p\right)\hat{r} - \varepsilon\left(\hat{r}\cdot\vec{v}_\mu\right)\vec{R}_p + \varepsilon^2\left(\hat{r}\cdot\vec{v}_\mu\right)\hat{r} - \left[v\left(\hat{r}\times\hat{z}\right)\cdot\vec{R}_p\right]\vec{R}_p + \varepsilon\left[v\left(\hat{r}\times\hat{z}\right)\cdot\vec{R}_p\right]\hat{r}\right)}{\left|\vec{R}_P - \varepsilon\hat{r}\right|^3}\right)d\varphi$$

$$\frac{1}{\left|\vec{R}_P - \varepsilon\hat{r}\right|} = \sum_{l=0}^{\infty}\frac{\varepsilon^l}{R_p^{l+1}}P_l\left(\frac{\vec{R}_P\cdot\hat{r}}{R_P}\right)$$

The magnetic moment of the current loop can be written as

$\mu c = IA = \lambda v\pi\varepsilon^2 = \frac{q}{2\pi\varepsilon}v\pi\varepsilon^2 = \frac{qv\varepsilon}{2}$, and therefore $v\varepsilon = \frac{2\mu c}{q}$. Substituting this into the expression and taking $\varepsilon \to 0$ simplifies the above expression.

$$d\vec{A} = \frac{q}{4\pi cR_P}\left(\vec{v}_\mu + \frac{\left(\vec{v}_\mu\cdot\vec{R}_P\right)\vec{R}_P}{R_p^2}\right)d\varphi$$

$$+\frac{q}{4\pi c}\left(-\frac{v\hat{r}\times\hat{z}}{R_p}\left(1+\frac{\varepsilon\vec{R}_p\cdot\hat{r}}{R_p^2}\right)+\left(-\frac{\left[v\left(\hat{r}\times\hat{z}\right)\cdot\vec{R}_p\right]\vec{R}_p}{R_p^3}+\frac{\varepsilon\left[v\left(\hat{r}\times\hat{z}\right)\cdot\vec{R}_p\right]\hat{r}}{R_p^3}\right)\left(1+\frac{3\varepsilon\vec{R}_p\cdot\hat{r}}{R_p^2}\right)\right)d\varphi.$$

This of course must then be integrated from $\varphi = 0$ to $\varphi = 2\pi$. The first line gives the familiar vector potential of a charge for the Darwin Lagrangian. The first term in the second line is zero as the integral of $\sin\varphi$ and $\sin\varphi$ from $\varphi = 0$ to $\varphi = 2\pi$ is zero.

$$\vec{A} = \frac{q}{2cR_P}\left(\vec{v}_\mu + \frac{\left(\vec{v}_\mu\cdot\vec{R}_P\right)\vec{R}_P}{R_p^2}\right)$$

$$+\frac{q}{4\pi c}\int_0^{2\pi}\left(-\frac{v\varepsilon\hat{r}\times\hat{z}}{R_p}\left(\frac{\vec{R}_p\cdot\hat{r}}{R_p^2}\right)+\left(-\frac{\left[v\left(\hat{r}\times\hat{z}\right)\cdot\vec{R}_p\right]\vec{R}_p}{R_p^3}+\frac{v\varepsilon\left[\left(\hat{r}\times\hat{z}\right)\cdot\vec{R}_p\right]\hat{r}}{R_p^3}\right)\left(1+\frac{3\varepsilon\vec{R}_p\cdot\hat{r}}{R_p^2}\right)\right)d\varphi$$

$$=\vec{A}_q+\vec{A}_\mu$$

Evaluating the second term in the integral for $\vec{A}_\mu$ gives

$$-\frac{q}{4\pi c}\int_0^{2\pi}\frac{\left[v\left(\hat{r}\times\hat{z}\right)\cdot\vec{R}_p\right]\vec{R}_p}{R_p^3}d\varphi=-\frac{qv}{4\pi cR_p^3}\left\{\left[\int_0^{2\pi}\hat{r}\times\hat{z}d\varphi\right]\cdot\vec{R}_p\right\}\vec{R}_p=0$$

Taking the remaining terms in $\vec{A}_\mu$ which are proportional to $v\varepsilon$ gives

$$\vec{A}_\mu=\frac{q}{4\pi c}\int_0^{2\pi}\left(-\frac{v\varepsilon\hat{r}\times\hat{z}}{R_p}\left(\frac{\vec{R}_p\cdot\hat{r}}{R_p^2}\right)+\left(-\frac{3v\varepsilon\left[\left(\hat{r}\times\hat{z}\right)\cdot\vec{R}_p\right]\vec{R}_p}{R_p^3}\left(\frac{\vec{R}_p\cdot\hat{r}}{R_p^2}\right)+\frac{v\varepsilon\left[\left(\hat{r}\times\hat{z}\right)\cdot\vec{R}_p\right]\hat{r}}{R_p^3}\right)\right)d\varphi$$

$$=\frac{\mu}{2\pi}\int_0^{2\pi}\left(-\frac{\left(\hat{r}\times\hat{z}\right)\left(\vec{R}_p\cdot\hat{r}\right)}{R_p^3}-\frac{3\left[\left(\hat{r}\times\hat{z}\right)\cdot\vec{R}_p\right]\left(\vec{R}_p\cdot\hat{r}\right)\vec{R}_p}{R_p^5}+\frac{\left[\left(\hat{r}\times\hat{z}\right)\cdot\vec{R}_p\right]\hat{r}}{R_p^3}\right)d\varphi$$

$$=\vec{A}_{\mu I}+\vec{A}_{\mu II}+\vec{A}_{\mu III}$$

where $\vec{A}_{\mu I}$, $\vec{A}_{\mu II}$, and $\vec{A}_{\mu III}$ represent the first, second, and third terms in the integral, respectively. Evaluating these integrals gives

$$\vec{A}_{\mu I}=-\frac{\mu}{2\pi}\int_0^{2\pi}\frac{\left(\hat{r}\times\hat{z}\right)\left(\vec{R}_p\cdot\hat{r}\right)}{R_p^3}d\varphi=-\frac{\mu}{2\pi}\int_0^{2\pi}\frac{\left(\sin\varphi\hat{x}-\cos\varphi\hat{y}\right)\left(x_p\cos\varphi+y_p\sin\varphi\right)}{R_p^3}d\varphi$$

$$=-\frac{\mu}{2\pi}\int_0^{2\pi}\frac{\left(\left(x_p\cos\varphi\sin\varphi+y_p\sin^2\varphi\right)\hat{x}-\left(x_p\cos^2\varphi+y_p\cos\varphi\sin\varphi\right)\hat{y}\right)}{R_p^3}d\varphi$$

$$=-\frac{\mu}{2}\frac{\left(y_p\hat{x}-x_p\hat{y}\right)}{R_p^3}=\frac{\mu}{2}\frac{\hat{z}\times\vec{R}_p}{R_p^3}=\frac{\vec{\mu}\times\vec{R}_p}{2R_p^3}$$

$$\vec{A}_{\mu II} = -\frac{\mu}{2\pi}\int_0^{2\pi} \frac{3\left[\left(\hat{r}\times\hat{z}\right)\cdot\vec{R}_p\right]\left(\vec{R}_p\cdot\hat{r}\right)\vec{R}_p}{R_p^5}d\varphi$$

$$= -\frac{\mu\vec{R}_p}{2\pi}\int_0^{2\pi} \frac{3\left[\left(\sin\varphi\hat{x}-\cos\varphi\hat{y}\right)\cdot\left(x_p\hat{x}+y_p\hat{y}+z_p\hat{z}\right)\right]\left(x_p\cos\varphi+y_p\sin\varphi\right)}{R_p^5}d\varphi$$

$$= -\frac{\mu\vec{R}_p}{2\pi}\int_0^{2\pi} \frac{3\left(x_p\sin\varphi-y_p\cos\varphi\right)\left(x_p\cos\varphi+y_p\sin\varphi\right)}{R_p^5}d\varphi$$

$$= -\frac{\mu\vec{R}_p}{2\pi}\int_0^{2\pi} \frac{3\left(\left(x_p^2-y_p^2\right)\sin\varphi\cos\varphi+x_py_p\left(\sin^2\varphi-\cos^2\varphi\right)\right)}{R_p^5}d\varphi = 0$$

$$\vec{A}_{\mu III} = \frac{\mu}{2\pi}\int_0^{2\pi} \frac{\left[\left(\hat{r}\times\hat{z}\right)\cdot\vec{R}_p\right]\hat{r}}{R_p^3}d\varphi$$

$$= \frac{\mu}{2\pi}\int_0^{2\pi} \frac{\left[\left(\sin\varphi\hat{x}-\cos\varphi\hat{y}\right)\cdot\left(x_p\hat{x}+y_p\hat{y}+z_p\hat{z}\right)\right]\left(\cos\varphi\hat{x}+\sin\varphi\hat{y}\right)}{R_p^3}d\varphi$$

$$= \frac{\mu}{2\pi}\int_0^{2\pi} \frac{\left(x_p\sin\varphi-y_p\cos\varphi\right)\left(\cos\varphi\hat{x}+\sin\varphi\hat{y}\right)}{R_p^3}d\varphi$$

$$= \frac{\mu}{2\pi}\int_0^{2\pi} \frac{\left(\left(x_p\sin\varphi\cos\varphi-y_p\cos^2\varphi\right)\hat{x}+\left(x_p\sin^2\varphi-y_p\cos\varphi\sin\varphi\right)\hat{y}\right)}{R_p^3}d\varphi$$

$$= \frac{\mu}{2}\frac{\left(-y_p\hat{x}+x_p\hat{y}\right)}{R_p^3} = \frac{\mu}{2}\frac{\hat{z}\times\vec{R}_p}{R_p^3} = \frac{\vec{\mu}\times\vec{R}_p}{2R_p^3}$$

Adding these three integrals gives the known magnetic vector potential for a magnetic dipole moment.

$$\vec{A}_\mu = \vec{A}_{\mu I} + \vec{A}_{\mu II} + \vec{A}_{\mu III} = \frac{\vec{\mu}\times\vec{R}_p}{R_p^3}$$

If this loop were constructed of two rings of charge, one with $q/2$ and the other with $-q/2$, rotating in opposite directions then it would be a loop with no net charge and a current equal to that of the loop described above. It is a ring with these properties which is described in chapter 2. The magnetic vector potential for such a ring is

$$\vec{A} = \frac{\vec{\mu} \times \vec{R}_p}{R_p^3}.$$

B5 - Integration of Aharonov-Bohm and Aharonov-Casher Lagrangians for constrained motion (chapter 3 section 2.3.1)

In order to determine the interaction Lagrangian for the Aharonov-Bohm and Aharonov-Casher systems in the case of constrained motion, an integral of the interaction Lagrangian for the Mott-Schwinger system is evaluated. This assumes that the solenoid in the Aharonov-Bohm system consists of infinitely many loops that do not interact with each other except to maintain the shape of the solenoid and each one interacts with the passing charge in the way described by the Mott-Schwinger Lagrangian. Likewise the wire in the Aharonov-Casher system consists of infinitely many point charges that do not interact with each other except to maintain the shape of the wire and each one interacts with the passing current loop in the way described by the Mott-Schwinger Lagrangian. The Mott-Schwinger Lagrangian is

$$L_{\text{int}} = \frac{q}{c}\frac{\left(\vec{v}_\mu - \vec{v}_q\right)\cdot\left[\vec{\mu}\times\left(\vec{r}_\mu - \vec{r}_q\right)\right]}{\left|\vec{r}_\mu - \vec{r}_q\right|^3}.$$

In order to integrate this Lagrangian for the Aharonov-Bohm system the magnetic moment of the current loop is taken to be an element for integration to construct an infinitely long solenoid.

$$\vec{\mu} \to \frac{c\Phi_B}{4\pi}\hat{z}dz_\mu$$

Thus the integrated Lagrangian becomes

$$L_{AB} = \int_{solenoid} dL_{MS} = \frac{q\Phi_B}{4\pi}\int_{-\infty}^{\infty}\frac{\left(\vec{v}_\mu - \vec{v}_q\right)\cdot\left[\hat{z}\times\left(\vec{r}_\mu - \vec{r}_q\right)\right]}{\left|\vec{r}_\mu - \vec{r}_q\right|^3}dz_\mu$$

Where L_{AB} and L_{MS} are the Aharonov-Bohm and Mott-Schwinger Lagrangians, respectively. Since $\hat{z}\times\left(\vec{r}_\mu-\vec{r}_q\right)$ has no z_μ dependence this can be written as

$$\vec{\alpha}=\frac{q\Phi_B}{4\pi}\left(\vec{v}_\mu-\vec{v}_q\right)\cdot\left[\hat{z}\times\left(\vec{r}_\mu-\vec{r}_q\right)\right],\ Z=z_\mu-z_q,\ \gamma^2=\left(x_\mu-x_q\right)^2+\left(y_\mu-y_q\right)^2$$

$$L_{AB}=\vec{\alpha}\int_{-\infty}^{\infty}\frac{dZ}{\left(\gamma^2+Z^2\right)^{\frac{3}{2}}}=\frac{2\vec{\alpha}}{\gamma^2}.$$

Similarly the point charge in the Mott-Schwinger system is taken to be an element for integration to construct an infinitely long charged wire in the Aharonov-Casher system.

$$q\to\lambda dz_q.$$

The integrated Lagrangian in this case is

$$L_{AC}=\int_{wire}dL_{MS}=\frac{\lambda}{c}\int_{-\infty}^{\infty}\frac{\left(\vec{v}_\mu-\vec{v}_q\right)\cdot\left[\vec{\mu}\times\left(\vec{r}_\mu-\vec{r}_q\right)\right]}{\left|\vec{r}_\mu-\vec{r}_q\right|^3}dz_q$$

As before $\left(\vec{v}_\mu-\vec{v}_q\right)\cdot\left[\vec{\mu}\times\left(\vec{r}_\mu-\vec{r}_q\right)\right]$ is independent of z_q since $\vec{\mu}=\mu\hat{z}$. Therefore the integral becomes

$$\vec{\beta}=\frac{\lambda}{c}\left(\vec{v}_\mu-\vec{v}_q\right)\cdot\left[\vec{\mu}\times\left(\vec{r}_\mu-\vec{r}_q\right)\right],\ Z=z_\mu-z_q,\ \gamma^2=\left(x_\mu-x_q\right)^2+\left(y_\mu-y_q\right)^2$$

$$L_{AB}=-\vec{\beta}\int_{\infty}^{-\infty}\frac{dZ}{\left(\gamma^2+Z^2\right)^{\frac{3}{2}}}=\frac{2\vec{\beta}}{\gamma^2}.$$

Thus the Aharonov-Bohm and Aharonov-Casher Lagrangians for constrained motion are

$$L_{AB}=\frac{2\vec{\alpha}}{\gamma^2}=\frac{q\Phi_B}{2\pi}\frac{\left(\vec{v}_\mu-\vec{v}_q\right)\cdot\left[\hat{z}\times\left(\vec{r}_\mu-\vec{r}_q\right)\right]}{\left(x_\mu-x_q\right)^2+\left(y_\mu-y_q\right)^2}$$

$$L_{AC} = \frac{2\vec{\beta}}{\gamma^2} = \frac{2\lambda}{c} \frac{\left(\vec{v}_\mu - \vec{v}_q\right) \cdot \left[\vec{\mu} \times \left(\vec{r}_\mu - \vec{r}_q\right)\right]}{\left(x_\mu - x_q\right)^2 + \left(y_\mu - y_q\right)^2}.$$

B6 - Quantum Optics (Chapter 5 section 3.3)

Here the quantum optical analysis of this system based on two momentum states and two spin states is shown in a bit more detail. Consider an unpolarized input state with a downward component of momentum (figure B1) described by the density operator

$$\rho_I = \frac{1}{2}\left(|+\rangle_- \langle +|_- + |-\rangle_- \langle -|_-\right).$$

Where a "+" or "−" inside the bras and kets indicates spin forward or backward while a "+" or "−" subscript indicates an upward or downward component of momentum.

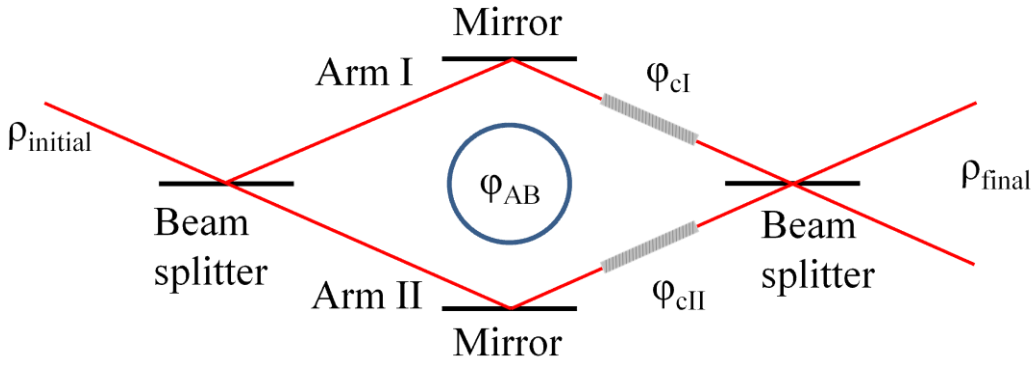

Figure B1

Interferometer Schematic

The operational elements of the Mach-Zehnder interferometer are indicated (for a detailed description see text).

The effect of the beamsplitter described by

$$|+\rangle_- \xrightarrow{BS} \frac{\sqrt{2}}{2}\left(i|+\rangle_+ + |+\rangle_-\right)$$

$$|+\rangle_+ \xrightarrow{BS} \frac{\sqrt{2}}{2}\left(i|+\rangle_- + |+\rangle_+\right),$$

is independent of spin. The effect of the mirror described by

$$|+\rangle_- \xrightarrow{M} i|+\rangle_+$$

$$|+\rangle_+ \xrightarrow{M} i|+\rangle_-,$$

is also independent of spin. The AB phase shift and the phase shift given by the coils is dependent upon which arm of the interferometer the electrons go through. The arms are labeled I and II to track these phaseshifts. The phase shifts given by the coils are chosen to be of equal magnitude and opposite sign. In arm I, the phase shift given by the coil and the AB phase shift are given by

$$|+\rangle_- \xrightarrow{Coil} \exp(i\varphi_c)|+\rangle_-$$

$$|-\rangle_- \xrightarrow{Coil} \exp(-i\varphi_c)|-\rangle_-$$

$$|+\rangle_- \xrightarrow{AB} \exp\left(i\varphi_{AB}/2\right)|+\rangle_-,$$

and in arm II these phase shifts are given by

$$|+\rangle_+ \xrightarrow{Coil} \exp(-i\varphi_c)|+\rangle_+$$

$$|-\rangle_+ \xrightarrow{Coil} \exp(i\varphi_c)|-\rangle_+$$

$$|+\rangle_+ \xrightarrow{AB} \exp\left(-i\varphi_{AB}/2\right)|+\rangle_+,$$

where the AB phase shift is spin independent. Using these operations, the density operator after the first beam splitter is

$$\rho_{II} = \frac{1}{4}\left(|+\rangle_- + i|+\rangle_+\right)\left(\langle+|_- - i\langle+|_+\right) + \frac{1}{4}\left(|-\rangle_- + i|-\rangle_+\right)\left(\langle-|_- - i\langle-|_+\right).$$

The AB phase shift is applied just after the first beamsplitter to give

$$\rho_{III} = \frac{1}{4}\left(\exp\left(-i\varphi_{AB}/2\right)|+\rangle_- + i\exp\left(i\varphi_{AB}/2\right)|+\rangle_+\right)\left(\exp\left(i\varphi_{AB}/2\right)\langle+|_- - i\exp\left(-i\varphi_{AB}/2\right)\langle+|_+\right)$$

$$+\frac{1}{4}\left(\exp\left(-i\varphi_{AB}/2\right)|-\rangle_- + i\exp\left(i\varphi_{AB}/2\right)|-\rangle_+\right)\left(\exp\left(i\varphi_{AB}/2\right)\langle-|_- - i\exp\left(-i\varphi_{AB}/2\right)\langle-|_+\right).$$

The beams then reflect of the mirrors, giving

$$\rho_{IV} = \frac{1}{4}\left(\exp\left(-i\varphi_{AB}/2\right)|+\rangle_+ + i\exp\left(i\varphi_{AB}/2\right)|+\rangle_-\right)\left(\exp\left(i\varphi_{AB}/2\right)\langle+|_+ - i\exp\left(-i\varphi_{AB}/2\right)\langle+|_-\right)$$

$$+\frac{1}{4}\left(\exp\left(-i\varphi_{AB}/2\right)|-\rangle_+ + i\exp\left(i\varphi_{AB}/2\right)|-\rangle_-\right)\left(\exp\left(i\varphi_{AB}/2\right)\langle-|_+ - i\exp\left(-i\varphi_{AB}/2\right)\langle-|_-\right).$$

The density operator after the spin phase coils is

$$\rho_V = \frac{1}{4}\left(\exp\left[-i\left(\varphi_c + \varphi_{AB}/2\right)\right]|+\rangle_+ + i\exp\left[i\left(\varphi_c + \varphi_{AB}/2\right)\right]|+\rangle_-\right)$$

$$\times\left(\exp\left[i\left(\varphi_c + \varphi_{AB}/2\right)\right]\langle+|_+ - i\exp\left[-i\left(\varphi_c + \varphi_{AB}/2\right)\right]\langle+|_-\right)$$

$$+\frac{1}{4}\left(\exp\left[i\left(\varphi_c - \varphi_{AB}/2\right)\right]|-\rangle_+ + i\exp\left[-i\left(\varphi_c - \varphi_{AB}/2\right)\right]|-\rangle_-\right)$$

$$\times\left(\exp\left[-i\left(\varphi_c - \varphi_{AB}/2\right)\right]\langle-|_+ - i\exp\left[i\left(\varphi_c - \varphi_{AB}/2\right)\right]\langle-|_-\right).$$

The final density operator after the last beam splitter is

$$\rho_{VI} = \frac{1}{8}\left\{\exp\left[-i\left(\varphi_c + \varphi_{AB}/2\right)\right]\left(|+\rangle_+ + i|+\rangle_-\right) + i\exp\left[i\left(\varphi_c + \varphi_{AB}/2\right)\right]\left(|+\rangle_- + i|+\rangle_+\right)\right\}$$

$$\times\left\{\exp\left[i\left(\varphi_c + \varphi_{AB}/2\right)\right]\left(\langle+|_+ - i\langle+|_-\right) - i\exp\left[-i\left(\varphi_c + \varphi_{AB}/2\right)\right]\left(\langle+|_- - i\langle+|_+\right)\right\}$$

$$+\frac{1}{8}\left\{\exp\left[i\left(\varphi_c-\varphi_{AB}/2\right)\right]\left(|-\rangle_+ + i|-\rangle_-\right)+i\exp\left[-i\left(\varphi_c-\varphi_{AB}/2\right)\right]\left(|-\rangle_- + i|-\rangle_+\right)\right\}$$

$$\times\left\{\exp\left[-i\left(\varphi_c-\varphi_{AB}/2\right)\right]\left(\langle-|_+ - i\langle-|_-\right)-i\exp\left[i\left(\varphi_c-\varphi_{AB}/2\right)\right]\left(\langle-|_- - i\langle-|_+\right)\right\}.$$

The probability of finding each spin state in each output is given as follows

$$P_{++}=\langle+|_+\,\rho_{VI}\,|+\rangle_+=\frac{1}{2}\sin^2\left(\varphi_c+\varphi_{AB}/2\right)$$

$$P_{-+}=\langle-|_+\,\rho_{VI}\,|-\rangle_+=\frac{1}{2}\sin^2\left(\varphi_c-\varphi_{AB}/2\right)$$

$$P_{+-}=\langle+|_-\,\rho_{VI}\,|+\rangle_-=\frac{1}{2}\cos^2\left(\varphi_c+\varphi_{AB}/2\right)$$

$$P_{--}=\langle-|_-\,\rho_{VI}\,|-\rangle_-=\frac{1}{2}\cos^2\left(\varphi_c-\varphi_{AB}/2\right).$$

B7 - Approximate Perturbative Analysis (Chapter 6 Section 3)

In order to calculate the approximations given in section direct integration of the probability amplitude was performed. In the case of the regular K-D effect calculation of the integral shown in equation (7) of chapter 6 was performed. The matrix element chosen corresponds to the $\frac{q^2A^2}{2m}$ term in the Hamiltonian where $\vec{A}$ is the vector potential corresponding to two counter propagating lasers of frequency ω.

$$\vec{A} = \frac{A_0}{2}\exp\left(\frac{-t^2}{\tau^2}\right)\left(a_L e^{i(kz-\omega t)} + a_L^{\dagger} e^{-i(kz-\omega t)} + a_R e^{-i(kz+\omega t)} + a_R^{\dagger} e^{i(kz+\omega t)}\right)\hat{x}$$

Taking the operator $\frac{q^2A_0^2}{2m}a_L^{\dagger}a_R\exp\left(\frac{-2t^2}{\tau^2} - i2kz\right)$ in the $\frac{q^2A^2}{2m}$ term in the Hamiltonian which is descriptive of a $-2\hbar k$ momentum kick and applying equation (5) gives

$$C_{fi} = \frac{-i}{\hbar}\int_{-\infty}^{\infty} H_{\text{int}}^{fi}(t')dt' = \frac{-iq^2A_0^2}{2m\hbar}\int_{-\infty}^{\infty}\left\langle N+1, N-1, -\hbar k\left|a_L^{\dagger}a_R\exp(-i2kz)\right|N, N, \hbar k\right\rangle\exp\left(\frac{-2t'^2}{\tau^2}\right)dt'$$

$$= \frac{-iq^2A_0^2N}{2m\hbar}\int_{-\infty}^{\infty}\exp\left(\frac{-2t'^2}{\tau^2} + i\omega_{fi}t\right)dt'$$

Since the initial and final state of the electron satisfy the Bragg condition, the frequency difference between the two is zero $(\omega_{fi} = 0)$.

$$C_{fi} = \frac{-iq^2A_0^2N}{2m\hbar}\int_{-\infty}^{\infty}\exp\left(\frac{-2t'^2}{\tau^2}\right)dt' = -\sqrt{\frac{\pi}{2}}\frac{iq^2A_0^2N\tau}{2m\hbar} = -\sqrt{\frac{\pi}{2}}\frac{iq^2I\tau}{\hbar mc\varepsilon_0\omega^2}$$

For the two-color K-D effect the integral shown in equation (8) of chapter 6 was performed. The matrix elements chosen corresponds to the $\frac{q^2A^2}{2m}$ and $\frac{q}{m}\vec{p}\cdot\vec{A}$ terms in

the Hamiltonian where $\vec{A}$ is the vector potential corresponding to two counter propagating lasers of frequencies ω and 2ω.

$$\vec{A}=\frac{A_0}{2}\exp\left(\frac{-t^2}{\tau^2}\right)\left(a_L e^{i(kz-\omega t)}+a_L^{\dagger}e^{-i(kz-\omega t)}+a_R e^{-i2(kz+\omega t)}+a_R^{\dagger}e^{i2(kz+\omega t)}\right)\hat{x}$$

Accounting for all possible combinations of operators contained in the $\frac{q^2A^2}{2m}$ and $\frac{q}{m}\vec{p}\cdot\vec{A}$ terms which give rise to a momentum kick of $-4\hbar k$ results in the probability amplitude

$$C_{fi}=\frac{-q^3A_0^3N^{\frac{3}{2}}p_x}{16m^2\hbar^2}\int_{-\infty}^{\infty}e^{i\left[\left(\frac{2\hbar k^2}{m}+2\omega\right)t'\right]}e^{\frac{-2t'^2}{\tau^2}}\left[\int_{-\infty}^{t'}e^{i\left[\left(\frac{-2\hbar k^2}{m}-2\omega\right)t''\right]}e^{\frac{-t''^2}{\tau^2}}dt''\right]dt'$$

$$-\frac{q^3A_0^3N^{\frac{3}{2}}p_x}{16m^2\hbar^2}\int_{-\infty}^{\infty}e^{i\left[\left(\frac{2\hbar k^2}{m}-2\omega\right)t'\right]}e^{\frac{-t'^2}{\tau^2}}\left[\int_{-\infty}^{t'}e^{i\left[\left(\frac{-2\hbar k^2}{m}+2\omega\right)t''\right]}e^{\frac{-2t''^2}{\tau^2}}dt''\right]dt'$$

$$-2\frac{q^3A_0^3N^{\frac{3}{2}}p_x}{16m^2\hbar^2}\int_{-\infty}^{\infty}e^{i\left[\left(\frac{3\hbar k^2}{2m}-\omega\right)t'\right]}e^{\frac{-2t'^2}{\tau^2}}\left[\int_{-\infty}^{t'}e^{i\left[\left(\frac{-3\hbar k^2}{2m}+\omega\right)t''\right]}e^{\frac{-t''^2}{\tau^2}}dt''\right]dt'$$

$$-2\frac{q^3A_0^3N^{\frac{3}{2}}p_x}{16m^2\hbar^2}\int_{-\infty}^{\infty}e^{i\left[\left(\frac{3\hbar k^2}{2m}+\omega\right)t'\right]}e^{\frac{-t'^2}{\tau^2}}\left[\int_{-\infty}^{t'}e^{i\left[\left(\frac{-3\hbar k^2}{2m}-\omega\right)t''\right]}e^{\frac{-2t''^2}{\tau^2}}dt''\right]dt'$$

In order to evaluate these integrals the approximation $\int_{-\infty}^{t}e^{i\Omega t'}e^{-\frac{t'^2}{\tau^2}}dt'\approx\frac{-i}{\Omega}e^{i\Omega t}e^{-\frac{t^2}{\tau^2}}$ for $\Omega\tau\gg1$ was used. By applying this directly to the integral above the probability amplitude is obtained.

$$C_{fi}\approx\frac{-q^3A_0^3N^{\frac{3}{2}}p_x}{16m^2\hbar^2}\left\{-i7\sqrt{\frac{\pi}{3}}\frac{\tau}{\omega}\frac{\hbar k}{mc}\right\}=i\sqrt{\frac{\pi}{3}}\frac{7q^3p_x\tau}{16\hbar m^3c^2\omega^3}\left(\frac{2I}{c\varepsilon_0}\right)^{\frac{3}{2}}$$

References

Chapter 1

1. W. Ehrenburg and R. E. Siday, "The Refractive Index in Electron Optics and the Principles of Dynamics," Proceedings of the Physical Society (London) **B62**, 8-21 (1949).

2. Y. Aharonov and D. Bohm, "Significance of Electromagnetic Potentials in Quantum Theory," Phys. Rev. **115** (3), 485 (1959).

3. R. G. Chambers, "Shift of an Electron Interference Pattern by Enclosed Magnetic Flux," Physical Review Letters **5** (1), 3-5 (1960).

4. Akira Tonomura, Nobuyuki Osakabe, Tsuyoshi Matsuda, Takeshi Kawasaki, Junji Endo, Shinichiro Yano, and Hiroji Yamada, "Evidence for Aharaonov-Bohm Effect with Magnetic Field Completely Shielded from Electron Wave," Physical Review Letters **56** (8), 792-795 (1986).

5. T. H. Boyer, "Classical Electromagnetic Interaction of a Point Charge and a Magnetic Moment: Considerations Related to the Aharonov-Bohm Phase Shift," Foundations of Physics **32**, 1-39 (2002).

6. A. Caprez, B. Barwick, and H. Batelaan, "Macroscopic test of the Aharonov-Bohm effect," Physical Review Letters **99** (21) (2007).

7. T. H. Boyer, "Comment on experiments related to the Aharonov-Bohm phase shift," Foundations of Physics **38** (6), 498-505 (2008).

8. A. Zeilinger, *Fundamental Aspects of Quantum Theory*, NATO ASI Ser. B. (Plenum, New York, 1985), Vol. 144.

9. Y. Aharonov and A. Casher, "Topological quantum effects for neutral particles," Physical Review Letters **53** (4), 319 (1984).

10. A. Cimmino, G. I. Opat, A. G. Klein, H. Kaiser, S. A. Werner, M. Arif, and R. Clothier, "Observation of the topological Aharonov-Casher phase shift by neutron interferometry," Physical Review Letters **63** (4), 380 (1989).

11. Timothy H. Boyer, "Proposed Aharonov-Casher effect: Another example of an Aharonov-Bohm effect arising from a classical lag," Physical Review A **36** (10), 5083-5086 (1987).

12. S. A. Werner and A. G. Klein, "Observation of Aharonov-Bohm effects by neutron interferometry," J. Phys. A-Math. Theor. **43** (35) (2010).

13. Vaidman, L., “Torque and force on a magnetic dipole.” American Journal of Physics, 1990. **58**(10).

14. Gerlach W and Stern O 1922 “Das magnetische moment des silberatoms.” Z. Phys. 9 353-355

15. Richard Liboff, *Introductory Quantum Mechanics*. (Addison Wesley, 2003), fourth ed.

16. B. Friedrich and D. Herschbach, "Stern and Gerlach: How a bad cigar helped reorient atomic physics," Phys. Today **56** (12), 53-59 (2003).

17. J. Kessler, *Polarized Electrons* (Springer-Verlag, Berlin, 1976).

18. Brillouin L 1928 “Is it possible to test by a direct experiment the hypothesis of the spinning electron.” Proc. Natl. Acad. Sci. 14 755

19. Pauli W 1930 Proc. of the 6th Solvay Conf. 2 Gauthier-Villars, Brussels 1932 183-186, 217-220, 275-280

20. Pauli W 1964 Collected Scientific Papers Kronig R and Weiskopf V F John Wiley and Sons 2

21. Dehmelt H 1990 “Experiments with an isolated subatomic particle at rest.” Rev. Mod. Phys. 62 525-531

22. Gallup G A, Batelaan H and Gay T J 2001 “Quantum mechanical analysis of a longitudinal Stern-Gerlach effect.” Phys. Rev. Lett. 86 4508-4511

Chapter 2

1. F. Pierre, A. B. Gougam, A. Anthore, H. Pothier, D. Esteve and N. O. Birge, Physical Review B **68** (8), 085413 (2003).

2. T. Pfau, S. Spälter, C. Kurtsiefer, C. R. Ekstrom and J. Mlynek, Physical Review Letters **73** (9), 1223-1226 (1994).

3. M. S. Chapman, T. D. Hammond, A. Lenef, J. Schmiedmayer, R. A. Rubenstein, E. Smith and D. E. Pritchard, Physical Review Letters **75** (21), 3783-3787 (1995).

4. D. A. Kokorowski, A. D. Cronin, T. D. Roberts and D. E. Pritchard, Physical Review Letters **86** (11), 2191-2195 (2001).

5. K. Hornberger, S. Uttenthaler, B. Brezger, L. Hackermüller, M. Arndt and A. Zeilinger, Physical Review Letters **90** (16), 160401 (2003).

6. P. Sonnentag and F. Hasselbach, Physical Review Letters **98** (20), 200402 (2007).

7. L. Hackermuller, K. Hornberger, B. Brezger, A. Zeilinger and M. Arndt, Nature **427** (6976), 711-714 (2004).

8. A. Tonomura, Reviews of Modern Physics **59** (3), 639-669 (1987).

9. F. Hasselbach and M. Nicklaus, Physical Review A **48** (1), 143-151 (1993).

10. S. Dimopoulos, P. W. Graham, J. M. Hogan and M. A. Kasevich, Physical Review Letters **98** (11), 111102 (2007).

11. H. Lichte, Philos. Trans. R. Soc. Lond. Ser. A-Math. Phys. Eng. Sci. **360** (1794), 897-920 (2002).

12. P. A. Tipler and R. A. Llewellyn, *Modern Physics*, fourth ed. (2004).

13. R. H. Fowler and L. Nordheim, Proc. R. soc. Lond. Ser. A-Contain. Pap. Math. Phys. Character **119** (781), 173-181 (1928).

14. B. Barwick, C. Corder, J. Strohaber, N. Chandler-Smith, C. J. Uiterwaal and H. Batelaan, New J. Phys. **9**, 142 (2007).

15. P. Hommelhoff, Y. Sortais, A. Aghajani-Talesh and M. Kasevich, Phys. Rev. Lett. **96**, 077401 (2006).

16. E. Joos, in *Decoherence: Theoretical, Experimental, and Conceptual Problems*, edited by P. Blanchard, E. Joos, D. Giulini, C. Kiefer and I.-O. Stamatescu (Springer Berlin Heidelberg, 2000), Vol. 538, pp. 1-17.

17. M. B. Mensky, *Quantum measurements and decoherence: models and phenomenology*. (Kluwer Academic Publishers, 2000).

18. H. G. Krojanski and D. Suter, Physical Review Letters **97** (15), 150503 (2006).

19. N. Tzoar and J. I. Gersten, Physical Review B **8** (12), 5684-5695 (1973).

20. R. E. B. Makinson, Physical Review **75** (12), 1908-1911 (1949).

21. B. Cho, T. Ichimura, R. Shimizu and C. Oshima, Physical Review Letters **92** (24), 246103 (2004).

22. H. H. Hopkins, J. Opt. Soc. Am. **47** (6), 508-525 (1957).

23. G. Pozzi, Optik **77** (2), 69-73 (1987).

24. J. J. Lin and J. P. Bird, J. Phys.-Condes. Matter **14** (18), R501-R596 (2002).

25. J. Rammer and A. Schmid, Physical Review B **34** (2), 1352-1355 (1986).

26. D. Natelson, R. L. Willett, K. W. West and L. N. Pfeiffer, Physical Review Letters **86** (9), 1821-1824 (2001).

27. J. J. Hauser, Physical Review B **10** (7), 2792-2798 (1974).

28. V. F. Gantmakher and L. I. Man, *Electrons and Disorder in Solids*. (Oxford University Press, 2005).

29. B. L. Altshuler and A. G. Aronov, in *Electron-electron interactions in disordered systems*, edited by A. L. Efros and M. Pollak (North-Holland, 1985), Vol. 10.

30. C. W. J. Beenakker and H. v. Houten, arXiv (2004).

31. H. Fukuyama, in *Electron-electron interactions in disordered systems*, edited by A. L. Efros and M. Pollak (North-Holland, 1985), Vol. 10.

32. A. Schmid, Zeitschrift Fur Physik **259** (5), 421-436 (1973).

33. S. Wind, M. J. Rooks, V. Chandrasekhar and D. E. Prober, Physical Review Letters **57** (5), 633-636 (1986).

34. C. Kittel, *Introduction to solid state physics*, Eigth ed. (John Wiley and Sons, Inc, 2005).

35. B. Barwick, G. Gronniger, L. Yuan, S. Liou and H. Batelaan, J. Appl. Phys. **100** (7), 074322 (2006).

Chapter 3

1. Shockley, W. and R.P. James, "'Try Simplest Cases' Discovery of 'Hidden Momentum' Forces on 'Magnetic Currents'." Physical Review Letters, 1967. **18**(20): p. 876.

2. Aharonov, Y. and D. Rohrlich, *Quantum Paradoxes: Quantum Theory for the Perplexed*. 2005: Wiley-VCH Verlag GmbH & Co. KGaA, Weinheim.

3. Ionicioiu, R., "Quantum gates with topological phases." Physical Review A, 2003. **68**(3): p. 034305.

4. Feynman, R.P., R.B. Leighton, and M. Sands, *The Feynman Lectures on Physics*. Vol. II. 1964: California Institute of Technology. pg. 26-5.

5. Caprez, A. and H. Batelaan, “Feynman’s Relativistic Electrodynamics Paradox and the Aharonov-Bohm Effect.” Foundations of Physics, 2009. **39**(3): p. 295-306.

6. Werner, S. and A. Klein, “Observation of Aharonov–Bohm effects by neutron interferometry.” Journal of Physics A: Mathematical and Theoretical, 2010. **43**(354006).

7. Jaen, X., J. Llosa, and A. Molina, “Lagrangian formalism and retarded classical electrodynamics.” Journal of Mathematical Physics, 1989. **30**(7): p. 1502-1504.

8. Mott, N., “The Scattering of Fast Electrons by Atomic Nuclei.” Proceedings of the Royal Society A, 1929. **124**: p. 425-442.

9. Schwinger, J., “On the Polarization of Fast Neutrons.” Physical Review, 1948. **73**(4): p. 407.

10. Möllenstedt, G. and B. W., “Messung der kontinuierlichen Phasenschiebung von Elektronenwellen im kraftfeldfreien Raum durch das magnetische Vektorpotential einer Luftspule.” Naturwissenschaften, 1962. **49**: p. 81.

11. Artamonov, O.M., M. Bode, and J. Kirschner, “The role of elastic electron scattering in coincidence spectroscopy of W(100) in back-reflection geometry.” Surface Science, 1994(307-309): p. 912-916.

12. Tonks, L. and I. Langmuir, “Oscillations in Ionized Gases.” Physical Review, 1929. **33**(2): p. 195-210.

13. Boyer, T.H., “Classical Electromagnetic Interaction of a Point Charge and a Magnetic Moment: Considerations Related to the Aharonov-Bohm Phase Shift.” Foundations of Physics, 2002. **32**: p. 1-39.

14. Boyer, T.H., “Comment on experiments related to the Aharonov-Bohm phase shift.” Foundations of Physics, 2008. **38**(6): p. 498-505.

15. Caprez, A., B. Barwick, and H. Batelaan, “Macroscopic test of the Aharonov-Bohm effect.” Physical Review Letters, 2007. **99**(21).

16. Cimmino, A., et al., “Observation of the topological Aharonov-Casher phase shift by neutron interferometry.” Physical Review Letters, 1989. **63**(4): p. 380.

17. Vaidman, L.,” Torque and force on a magnetic dipole.” American Journal of Physics, 1990. **58**(10).

18. Jackson, J.D., *Classical Electrodynamics*. 3rd ed. 1999, New York: John Wiley & Sons, Inc.

19. Griffiths, D.J., *Introduction to Electrodynamics*, ed. C.F. Zita de Schauensee. 1989, Englewood Cliffs: Prentice-Hall, Inc. 532.

20. Goldstein, H., C. Poole, and J. Safko, *Classical Mechanics, Third Edition*. 2002: Addison Wesley.

21. Dubbers, D. and M.G. Schmidt, "The neutron and its role in cosmology and particle physics." Reviews of Modern Physics, 2011. **83**(4).

22. Chambers, R.G., "Shift of an Electron Interference Pattern by Enclosed Magnetic Flux." Physical Review Letters, 1960. **5**(1): p. 3-5.

23. Osakabe, N., et al., "Experimental confirmation of Aharonov-Bohm effect using a toroidal magnetic field confined by a superconductor." Physical Review A, 1986. **34**(2): p. 815-822.

24. Bachtold, A., et al., "Aharonov-Bohm oscillations in carbon nanotubes." Nature, 1999. **397**(6721): p. 673-675.

25. Feynman, R.P., "Space-time approach to non-relativistic quantum mechanics." Rev. Mod. Phys., 1948. **20**(2): p. 367-387.

26. Berman, P.R., ed. *Atom Interferometry*. 1997, Academic Press.

27. Boyer, T.H., "Classical Electromagnetic Deflections and Lag Effects Associated with Quantum Interference Pattern Shifts: Considerations Related to the Aharonov-Bohm Effect." Physical Review D, 1973. **8**(6): p. 1679-1693.

28. Boyer, T.H., "The force on a magnetic dipole." American Journal of Physics, 1988. **56**(8): p. 688.

29. Anandan, J., "Classical and Quantum Interaction of the Dipole." Physical Review Letters, 2000. **85**(7): p. 1354-1357.

30. Anandan, J., "Electromagnetic effects in the quantum interference of dipoles." Physics Letters A, 1989. **138**(8): p. 347-352.

31. Sangster, K., et al., "Aharonov-Casher phase in an atomic system." Physical Review A, 1995. **51**(3): p. 1776-1786.

32. Badurek, G., et al., "Nondispersive phase of the Aharonov-Bohm effect." Physical Review Letters, 1993. **71**(3): p. 307-311.

33. Peshkin, M. and H.J. Lipkin, "Topology, Locality, and Aharonov-Bohm Effect with Neutrons." Physical Review Letters, 1995. **74**(15): p. 2847-2850.

34. Peshkin, M., “Force-free interactions and nondispersive phase shifts in interferometry.” Foundations of Physics, 1999. **29**(3): p. 481-489.

35. Kruger, M., M. Schenk, and P. Hommelhoff, “Attosecond control of electrons emitted from a nanoscale metal tip.” Nature, 2011. **475**(7354): p. 78-81.

36. Hommelhoff, P., C. Kealhofer, and M.A. Kasevich, “Ultrafast Electron Pulses from a Tungsten Tip Triggered by Low-Power Femtosecond Laser Pulses.” Physical Review Letters, 2006. **97**(24): p. 247402.

37. Hilbert, S.A., et al., “Exploring temporal and rate limits of laser-induced electron emission." Journal of Physics B: Atomic, Molecular and Optical Physics, 2009. **42**(141001).

Chapter 4

1. H. Batelaan and A. Tonomura, “The Aharonov–Bohm effects: Variations on a subtle theme,” Phys. Today 62(9), 38-43, (September 2009).

2. A. Tonomura, N. Osakabe, T. Matsuda, T. Kawasaki, J. Endo, S. Yano, and H. Yamada, “Evidence for Aharonov-Bohm effect with magnetic field completely shielded from electron wave,” Phys. Rev. Lett. 56(8), 792-795, (1986).

3. A. Caprez, B. Barwick, and H. Batelaan, “Macroscopic test of the Aharonov-Bohm effect,” Phys. Rev. Lett. 99, 210401, (2007).

4. T. H. Boyer, “Semiclassical explanation of the Matteucci-Pozzi and Aharonov-Bohm phase shifts,” Foundations of Physics 32, 41-50, (2002).

5. J. R. Nielsen (Ed.), Niels Bohr, Collected Works, Volume 3, The Correspondence Principle (1918–1923), (North-Holland, Amsterdam, 1976).

6. L. Hackermüller, K. Hornberger, B. Brezger, A. Zeilinger, and M. Arndt, “Decoherence of matter waves by thermal emission of radiation,” Nature 427, 711-714, (2004).

7. R. P. Feynman, “Space-time approach to non-relativistic quantum mechanics,” Rev. Mod. Phys. 20, 367–387, (1948).

Chapter 5

1. Gerlach W and Stern O 1922 Das magnetische moment des silberatoms Z. Phys. 9 353-355

2. Pauli W 1930 Proc. of the 6th Solvay Conf. 2 Gauthier-Villars, Brussels 1932 183-186, 217-220, 275-280

3. Pauli W 1964 Collected Scientific Papers Kronig R and Weiskopf V F John Wiley and Sons 2

4. Baym G 1969 Lectures on Quantum Mechanics Benjamin

5. Cohen-Tannoudji C, Diu B and Laloë F 1977 Quantum Mechanics Wiley Interscience

6. Merzbacher E 1970 Quantum Mechanics Wiley 254

7. Mott N F and Massey H S W 1965 The Theory of Atomic Collisions Oxford: Clarendon Press

8. Ohanian H C 1990 Principles of Quantum Mechanics Prentice Hall 1

9. Wheeler J A 1983 Quantum Theory and Measurement Zurek W H University Press

10. Gallup G A, Batelaan H and Gay T J 2001 Quantum mechanical analysis of a longitudinal Stern-Gerlach effect Phys. Rev. Lett. 86 4508-4511

11. Rosenberry M A, Batelaan H, Reyes J P and Gay T J AIP Conf. Proc. 2002 Correlations, Polarization, and Ionization 604 264-269

12. Brillouin L 1928 Is it possible to test by a direct experiment the hypothesis of the spinning electron Proc. Natl. Acad. Sci. 14 755

13. Batelaan H, Gay T J and Schwendiman J J 1997 Stern-Gerlach effect for electron beams Phys. Rev. Lett. 79 4517-4521

14. Feynman R P 1948 Space-time approach to non-relativistic quantum mechanics Rev. Mod. Phys. 20 367-387

15. Jackson J D 1999 Classical Electrodynamics John Wiley & Sons, Inc.

16. Barwick B, Gronniger G, Yuan L, Liou S and Batelaan H 2006 A measurement of electron-wall interactions using transmission diffraction from nano-fabricated gratings J. Appl. Phys. 100 074322

17. Gronniger G, Barwick B, Batelaan H, Savas T, Pritchard D and Cronin A 2005 Electron diffraction from free-standing, metal-coated transmission gratings Appl. Phys. Lett. 87 124104

18. Gao H, Gronniger G, Freimund D, Cronin A and Batelaan H Phase and absorption gratings for electrons 2002 Int. Conf. on Atomic Physics XVIII Sadeghpour H R, Pritchard D E and Heller E J World Scientific

19. Caprez A, Bach R, McGregor S and Batelaan H 2009 A wide-angle electron grating bi-prism beam splitter J. Phys. B 42 165503

20. Hasselbach F and Nicklaus M 1993 Sagnac experiment with electrons: observation of the rotational phase shift of electron waves in vacuum Phys. Rev. A 48 143-151

21. Freimund D L and Batelaan H 2002 Bragg scattering of free electrons using the Kapitza-Dirac effect Phys. Rev. Lett. 89 283602

22. Aharonov Y and Bohm D 1959 Significance of electromagnetic potentials in the quantum theory Phys. Rev. 115 485-491

23. Dehmelt H 1990 Experiments with an isolated subatomic particle at rest Rev. Mod. Phys. 62 525-531

24. Dehmelt H 1988 New continuous Stern-Gerlach effect and a hint of "the" elementary particle Z. Phys. D-Atom Mol. Cl. 10 127-134

Chapter 6

1. P. H. Bucksbaum, D. W. Schumacher and M. Bashkansky, Physical Review Letters **61** (10), 1182-1185 (1988).

2. D. L. Freimund, K. Aflatooni and H. Batelaan, Nature **413**, 142 (2001).

3. M. Gao, H. Jean-Ruel, R. R. Cooney, J. Stampe, M. de Jong, M. Harb, G. Sciaini, G. Moriena and R. J. D. Miller, Opt. Express **20** (11), 12048-12058 (2012).

4. S. Chen, N. D. Powers, I. Ghebregziabher, C. M. Maharjan, C. Liu, G. Golovin, S. Banerjee, J. Zhang, N. Cunningham, A. Moorti, S. Clarke, S. Pozzi and D. P. Umstadter, Physical Review Letters **110** (15), 155003 (2013).

5. B. Barwick, C. Corder, J. Strohaber, N. Chandler-Smith, C. J. Uiterwaal and H. Batelaan, New J. Phys. **9**, 142 (2007).

6. P. Hommelhoff, C. Kealhofer and M. A. Kasevich, Physical Review Letters **97** (24), 247402 (2006).

7. S. A. Hilbert, C. Uiterwaal, B. Barwick, H. Batelaan and A. H. Zewail, Proc. Natl. Acad. Sci. U. S. A. **106** (26), 10558-10563 (2009).

8. P. Baum and A. H. Zewail, Proc. Natl. Acad. Sci. U. S. A. **104** (47), 18409-18414 (2007).

9. S. Ahrens, H. Bauke, C. H. Keitel and C. Müller, Physical Review Letters **109** (4), 043601 (2012).

10. R. Feder, Physical Review Letters **36** (11), 598-600 (1976).

11. P. Baum and A. Zewail, Chem. Phys. Lett. **462** (1-3), 14-17 (2008).

12. T. Kohashi, M. Konoto and K. Koike, J. Electron Microsc. **59** (1), 43-52 (2010).

13. A. H. Zewail, in *Annual Review of Physical Chemistry* (Annual Reviews, Palo Alto, 2006), Vol. 57, pp. 65-103.

14. T. Duden and E. Bauer, J. Electron Microsc. **47** (5), 379-385 (1998).

15. P. Lougovski and H. Batelaan, Physical Review A **84** (2), 023417 (2011).

16. H. Batelaan, Reviews of Modern Physics **79** (3), 929-941 (2007).

17. O. Smirnova, D. L. Freimund, H. Batelaan and M. Ivanov, Physical Review Letters **92** (22), 223601 (2004).

18. T. Nakajima, Y. Matsuo and T. Kobayashi, in *18th International Spin Physics Symposium*, edited by D. G. Crabb, D. B. Day, S. Liuti, X. Zheng, M. Poelker and Y. Prok (American Institute of Physics, Charlottesville, Virginia, 2008), pp. 876-879.

19. N. F. Mott, Proc. R. soc. Lond. Ser. A-Contain. Pap. Math. Phys. Character **124** (794), 425-442 (1929).

20. T. J. Gay, J. Phys. B-At. Mol. Opt. Phys. **16** (18), L553-L556 (1983).

21. H. Batelaan, A. S. Green, B. A. Hitt and T. J. Gay, Physical Review Letters **82** (21), 4216-4219 (1999).

22. T. J. Gay, in *Advances in Atomic, Molecular, and Optical Physics, Vol 57*, edited by E. Arimondo, P. R. Berman and C. C. Lin (Elsevier Academic Press Inc, San Diego, 2009), Vol. 57, pp. 157-247.

23. M. Woods, Int. J. Mod. Phys. A **13** (14), 2517-2524 (1998).

24. U. Fano, Physical Review **178** (1), 131-136 (1969).

25. I. Barth and O. Smirnova, (arXiv:1212.2895v3) (2013).

26. E. Brunkow, N. Clayburn, M. LeDoux and T. Gay, (APS DAMOP, Quebec City, Canada, 2013).

27. presented at the 18th International Spin Physics Symposium Charlottesville, Virginia, 2008 (unpublished).

28. W. Pauli, presented at the Proc. of the 6th Solvay Conf., 1930 (unpublished).

29. W. Pauli, *Collected Scientific Papers*. (John Wiley and Sons, New York, 1964).

30. L. Brillouin, Proc. Natl. Acad. Sci. **14**, 755 (1928).

31. H. Dehmelt, Z. Phys. D-Atom Mol. Cl. **10** (2-3), 127-134 (1988).

32. H. Batelaan, T. J. Gay and J. J. Schwendiman, Phys. Rev. Lett. **79** (23), 4517-4521 (1997).

33. G. A. Gallup, H. Batelaan and T. J. Gay, Phys. Rev. Lett. **86** (20), 4508-4511 (2001).

34. S. McGregor, R. Bach and H. Batelaan, New J. Phys. **13** (2011).

35. D. L. Freimund and H. Batelaan, Laser Phys. **13** (6), 892-896 (2003).

36. J. Anandan, Physical Review Letters **85** (7), 1354-1357 (2000).

37. E. Esarey, P. Sprangle and J. Krall, Physical Review E **52** (5), 5443-5453 (1995).

38. P. H. Bucksbaum, M. Bashkansky and T. J. McIlrath, Physical Review Letters **58** (4), 349-352 (1987).

39. L. Shao, D. Cline, X. Ding, Y. K. Ho, Q. Kong, J. J. Xu, I. Pogorelsky, V. Yakimenko and K. Kusche, Nucl. Instrum. Methods Phys. Res. Sect. A-Accel. Spectrom. Dect. Assoc. Equip. **701**, 25-29 (2013).

40. A. E. Siegman, *Lasers*. (University Science Books, Sausalito, 1986).

Chapter 7

1. A. Tonomura, Electron holography, 2nd, enl. ed., Springer series in optical sciences v. 70 (Springer, Berlin ; New York, 1999), pp. xi, 162 p.

2. L. Marton, J. A. Simpson, and J. A. Suddeth, "Electron Beam Interferometer," Physical Review 90, 490 (1953).

3. L. Marton, J. A. Simpson, and J. A. Suddeth, "An Electron Interferometer," Review of Scientific Instruments 25, 1099 (1954).

4. G. Möllenstedt and H. Düker, "FRESNELscher Interferenzversuch mit einem Biprisma für Elektronenwellen," Naturwissenschaften 42, 41 (1955).

5. G. Gronniger, B. Barwick, and H. Batelaan, "A three grating electron interferometer," New Journal of Physics 8, 224 (2006).

6. A. Cronin and B. McMorran, "Electron interferometry with nanogratings," Phys. Rev. A 74, 061602 (2006).

7. B. J. McMorran and A. D. Cronin, "An electron Talbot interferometer," New Journal of Physics 11, 033021 (2009).

8. R. C. Forrey, A. Dalgarno, and J. Schmiedmayer, "Determining the electron forward-scattering amplitude using electron interferometry," Phys. Rev. A 59, R942 (1999).

9. P. Sonnentag and F. Hasselbach, "Decoherence of Electron Waves Due to Induced Charges Moving Through a Nearby Resistive Material," Braz. J. Phys. 35, 385 (2005).

10. M. Ozcan, "High-sensitivity rotation sensing with atom interferometers using Aharonov-Bohm effect," presented at the Quantum Sensing and Nanophotonic Devices III Conference, San Jose, CA USA, 2006.

11. G. Badurek, H. Weinfurter, R. Gahler, A. Kollmar, S. Wehinger, and A. Zeilinger, "Nondispersive Phase of the Aharonov-Bohm Effect," Physical Review Letters 71, 307 (1993).

12. G. Gronniger, B. Barwick, H. Batelaan, T. Savas, D. Pritchard, and A. Cronin, "Electron diffraction from free-standing, metal-coated transmission gratings," Appl. Phys. Lett. 87, 124104 (2005).

13. T. Hibi and K. Yada, "Electron interference microscopy," in Principles and Techniques of Electron Microscopy, M. A. Hayat, ed. (Van Nostrand, New York, 1976), pp. 312-343.

14. R. P. Feynman and A. R. Hibbs, Quantum Mechanics and Path Integrals (McGraw-Hill Book Company, New York, 1965).

15. B. Barwick, G. Gronniger, L. Yuan, S. Liou, and H. Batelaan, "A measurement of electron-wall interactions using transmission diffraction from nano-fabricated gratings," Journal of Applied Physics 100(7), 074322 (2006).

16. G. Möllenstedt and W. Bayh, "Kontinuierliche Phasenschiebung von Elektronenwellen im kraftfeldfreien Raum durch das magnetische Vektorpotential eines Solenoids," Phys. Blätt. 18, 299 (1962).

17. M. Nicklaus and F. Hasselbach, "Wien Filter: A wave-packet-shifting device for restoring longitudinal coherence in charged-matter-wave interferometers," Phys. Rev. A 48, 152 (1993).

18. P. Sonnentag and F. Hasselbach, "Measurement of Decoherence of Electron Waves and Visualization of the Quantum-Classical Transition," Phys. Rev. Lett. 98, 200402 (2007).

Chapter 8

1. Adam Preston Caprez, "Tests of the Aharonov-Bohm effect" (January 1, 2009). *ETD collection for University of Nebraska - Lincoln.* Paper AAI3350442. http://digitalcommons.unl.edu/dissertations/AAI3350442

2. B. Barwick, G. Gronniger, L. Yuan, S. Liou, and H. Batelaan, "A measurement of electron-wall interactions using transmission diffraction from nano-fabricated gratings," J. Appl. Phys. **100** (7), 074322 (2006).

3. Harald Kiesel, Andreas Renz, and Franz Hasselbach, "Observation of Hanbury Brown−Twiss anticorrelations for free electrons," Nature **418**, 392 (2002).

4 F. Hasselbach, "Progress in electron- and ion-interferometry," Rep. Prog. Phys. **73** (1) (2010).

5. Brett E Barwick, "Coherent control of free electrons" (January 1, 2007). *ETD collection for University of Nebraska - Lincoln.* Paper AAI3252443. http://digitalcommons.unl.edu/dissertations/AAI3252443

6. Franz Hasselbach, "Selected Topics In Charged Particle Interferometry," Scanning Microscopy **11**, 345-366 (1997).

7. Hermann Wollnik, *Optics of charged particles*. (Academic Press, Inc., 1987).